INFORMATION TO USERS

This manuscript has been reproduced from the microfilm master. UMI films the text directly from the original or copy submitted. Thus, some thesis and dissertation copies are in typewriter face, while others may be from any type of computer printer.

The quality of this reproduction is dependent upon the quality of the copy submitted. Broken or indistinct print, colored or poor quality illustrations and photographs, print bleedthrough, substandard margins, and improper alignment can adversely affect reproduction.

In the unlikely event that the author did not send UMI a complete manuscript and there are missing pages, these will be noted. Also, if unauthorized copyright material had to be removed, a note will indicate the deletion.

Oversize materials (e.g., maps, drawings, charts) are reproduced by sectioning the original, beginning at the upper left-hand corner and continuing from left to right in equal sections with small overlaps. Each original is also photographed in one exposure and is included in reduced form at the back of the book.

Photographs included in the original manuscript have been reproduced xerographically in this copy. Higher quality 6" x 9" black and white photographic prints are available for any photographs or illustrations appearing in this copy for an additional charge. Contact UMI directly to order.

UMI

A Bell & Howell Information Company
300 North Zeeb Road, Ann Arbor MI 48106-1346 USA
313/761-4700 800/521-0600

A MULTI-REGION TRANSIENT EROSION MODEL FOR CONCRETE WITH TIME DEPENDENT SURFACE HEAT FLUX

by

Arif Nesimi Kılıç

A Dissertation Submitted to the Faculty of the
DEPARTMENT OF NUCLEAR AND ENERGY ENGINEERING
In Partial Fulfillment of the Requirements
For the Degree of
DOCTOR OF PHILOSOPHY
WITH A MAJOR IN NUCLEAR ENGINEERING
In the Graduate College
THE UNIVERSITY OF ARIZONA

1996

THE UNIVERSITY OF ARIZONA ®
GRADUATE COLLEGE

As members of the Final Examination Committee, we certify that we have read the dissertation prepared by Arif Nesimi Kilic

entitled A Multi-Region Transient Erosion Model for Concrete with Time Dependent Surface Heat Flux

and recommend that it be accepted as fulfilling the dissertation requirement for the Degree of Doctor of Philosophy/Engineering

Robert L. Seale	Robert L. Seale	10/21/96 Date
David L. Hetrick	David L. Hetrick	10/21/96 Date
Barry D. Ganapol	Barry Ganapol	10/21/96 Date
H. C. Perkins	H. C. Perkins	10/21/96 Date
Alfonso Ortega	A Ortega	10/21/96 Date

Final approval and acceptance of this dissertation is contingent upon the candidate's submission of the final copy of the dissertation to the Graduate College.

I hereby certify that I have read this dissertation prepared under my direction and recommend that it be accepted as fulfilling the dissertation requirement.

Robert L. Seale / Robert L. Seale — 27 Nov. 1996
Dissertation Director — Date

STATEMENT BY THE AUTHOR

This dissertation has been submitted in partial fulfillment of requirements for an advanced degree at The University of Arizona and is deposited in the University Library to be made available to borrowers under rules of the library.

Brief quotations from this dissertation are allowable without special permission, provided that accurate acknowledgement of source is made. Requests for permission for extended quotation from or reproduction of this manuscript in whole or in part may be granted by the head of the major department or the Dean of the Graduate College when in his or her judgement the proposed use of the material is in the interest of scholarship. In all other instances, however, permission must be obtained from the author.

SIGNED: 

To my parents

who have helped me to become who I am

"Measure what can be measured,

and make measurable what cannnot be measured."

Galileo Galilei

ACKNOWLEDGEMENTS

I would like to thank my academic advisor Dr. Robert L. Seale who introduced me to this topic, and provided his continued support and overwhelming patience throughout the duration of this endeavor. The assistance and valuable suggestions by Dr. David L. Hetrick, Dr. Barry D. Ganapol, Dr. H. C. Perkins, and Dr. Alfonso Ortega, as the committee members, are also deeply appreciated.

Thanks are due to Kathleen C. Parrish, my supervisor, and Paul F. Crawley, my director, who provided me with support and assistance in preparation of this dissertation, and to Elizabeth Knube for her professional help in editing of the final form of this manuscript. I extend my appreciations to Dr. Jonathan Seely, and Mrs. Seely, and all of my friends who were supportive and helpful.

I am also very greatful to my wife Marlen, and my children Deniz and Celine, for their patience, support, and encouragement not only during the completion of this study, but also during my stay at the University of Arizona, and our life together.

TABLE OF CONTENTS

TABLE OF CONTENTS - *continued*

page

TABLE OF CONTENTS - *continued*

LIST OF FIGURES

LIST OF FIGURES - *continued*

LIST OF FIGURES - *continued*

LIST OF FIGURES - *continued*

LIST OF FIGURES - *continued*

LIST OF FIGURES - *continued*

LIST OF FIGURES - *continued*

LIST OF TABLES

ABSTRACT

A multi-region, transient concrete ablation and decomposition model is developed. The model consists of four regions of concrete containing a thermally affected region, a dry (evaporated and chemically dehydrated) region, and a gas-free (decarboxylated) region with ablated concrete at the melt/concrete interface. Each region has an interface where the latent heat of local decomposition reactions is taken into account as heat sinks due to endothermic characteristics of the reactions. The time dependent temperature profiles, and depth and growth rate of the regions are evaluated by use of the heat balance integral method. Solutions are obtained for surface heat fluxes in forms of constant, $e^{-\lambda t}$, $t^{-\lambda}$, and -At to analyze various melt cooldown schemes. The erosion front progresses with a constant rate proportional to the surface heat flux in case of constant heat flux, and terminates at a finite erosion depth that is logarithmically proportional to the cooldown rate for surface heat flux in forms of $e^{-\lambda t}$ and $t^{-\lambda}$. Sensitivity analyses are performed to investigate the effects of important thermophysical parameters. Larger erosion depth and rate is observed for higher thermal conductivity. Decomposition temperatures are found to be significant in ablation. Model results were compared with previous experiments and models, and determined to be valid and accurate for different types of melt/concrete interaction. The model presented in this study is simple yet very detailed and accurate in simulating the actual molten core/concrete interaction (MCCI) phenomena, and in investigating the concrete reaction to the molten core. It not only can be embodied into the MCCI codes currently being developed, but also can be used to determine the containment integrity, and the fission products released into the environment and to the public as a stand alone code.

CHAPTER 1

INTRODUCTION

1.1. Introduction

Mankind has had over fourty years experience of designing and operating commercial nuclear power stations. The important considerations and responsibilities of nuclear power plant design engineers have always been the public health and safety as well as safe operation of the plant as it is in any industrial process. But the amount of fission product inventory of a large nuclear power plant and the sensitivity of the public, being generally aware of the catastrophic results due to past experiences, nuclear weapons, fallout, etc., add some special responsibilities for the designers. Furthermore, the fact that an accident happening anywhere in the world may affect people elsewhere and a growing general awareness of the effects of the environment on the quality of life have brought nuclear power plants to the focus of public concerns. Although great care is taken in design, fabrication, operation, maintenance, and extensive in-service inspections make today's nuclear power plants safe and reliable, the risk associated with an accident has to be considered more than for any other operational system.

The risk assessment to the public associated with the operation of a nuclear

power plant has been investigated by several nations around the world [1, 2, 54] since the early 70's. These investigations have evaluated the risk of an accident by studying the hypothetical scenarios of the operational failures and their resulting events. All of these investigations aim to protect the public health and safety and the environment by making the probability of abnormal operating conditions and accidents as low as practical. Although this probability can be made extremely low, it cannot be made equal to zero. Therefore, the control of fission products becomes a prime reactor safety consideration.

Fission products build up in the fuel and are kept there by the first barrier, the fuel material and the cladding. Integrity of this barrier can be violated, or in other words, fuel failure can occur under a wide spectrum of situations, ranging from normal operation to severe accidents. A fuel element is defined as failed when the metal cladding, that houses the ceramic fuel elements in most designs, is breached. This allows the fission products such as noble gases and a few other more volatile ones, that are already diffused out of the fuel region, to escape through the cladding. In most nuclear reactors, this escape can be tolerated since a few fuel elements are insignificant considering thousands of independent fuel elements loaded into the reactor. A few failures do not necessitate the shutdown of the reactor. Regulations are established to limit this tolerable amount (for example, in the U.S. maximum allowable fuel element failure is 1% under normal operation [3]) depending on the capacity of the radioactive waste treatment features of the design.

If for any reason the first barrier fails, the fission products are released to the primary coolant system, the second barrier. The primary coolant system encloses the inventory of reactor coolant. The definition of the primary coolant

system depends on the design. It can be a system of coolant loops including the steam generator tubes in indirect cycles, or it can be defined as the reactor cooling portion of working fluid that can be isolated from the turbine-condenser system by automatic isolation valves. The integrity of the second barrier is preserved by safety and relief valves, and installed safety features. A great deal of attention is given in the design, fabrication, and operation to ensure an absolute minimum probability of the major primary coolant system breach. High standards for piping, vessels, and valves increase the reliability of the system against any breaching. Since the operating pressure, temperature, and other system vvariables can exceed the standard design, some number of operation limits and engineering safety features are used for design.

The third fission barrier, which is the last barrier between the fission products and the environment and public, is the containment. The containment serves no functional requirement during normal operations, and even during some accident scenarios. The only function of the containment, unlike the first two barriers which are the vital components of nuclear heat transfer, is to prevent fission products that escape from primary system in the event of an accident from entering the environment and to protect the reactor from external events such as weather, missile impact, and other natural phenomena. Engineering safety features prevent the fission product release beyond regulation from containment under normal operating conditions and during the accidents where the containment integrity is preserved. Failure of the containment is considered in severe accident analysis which focuses on core meltdown. A core meltdown accident may break the integrity of all fission barriers, and therefore, core meltdown accident sequences dominate the risks from an accident in a nuclear power plant.

1.2. Phases of a Meltdown Accident

The design of nuclear power plants and their protection and safety systems is to provide that the reactor core will not melt even in the event of a major accident. The sequence of the events that can lead to a meltdown may be initiated by a variety of very severe (and also, very improbable) accidents, depending on the reactor type. Whatever the initiating accident may be, the core meltdown is caused by failure in removing the sensible and decay heat from the reactor. Cooling failures may range from the total loss of coolant to the failure of the residual heat removal systems. WASH-1400 [1, 50] listed the engineered safety features whose failure may affect the course of reactor meltdown. Figure 1 illustrates the sequence of a loss of coolant accident (LOCA). LOCA may quickly develop into a meltdown since the uncovered fuel rods are heated, by the fission decay heat and by the exothermic zirconium/water reactions, to temperatures well above the normal design limits which breaks the first barrier. The molten core then loses its geometry, which further disables the coolant entry to the core, causing intolerable thermal loading in the core support structure. Under this load the support structure collapses, and the molten core debris migrates to the lower plenum, possibly causing exothermic chemical reactions [4, 5], or explosions when it contacts with residual water. Reactor pressure vessel (RPV) failure could occur with the penetration of hot melt into RPV. This primary vessel melt-through is the last step of in-vessel consequences of a meltdown accident.

When the molten core debris slumps into the reactor cavity, either concrete basemat in pressurized water reactors (PWR) or systems in boiling water reactors (BWR), possible steam explosions which would overpressurize the containment, and water/melt reactions which would provide extra energy to the melt occur. The

molten debris eventually contacts the concrete structure of the containment building. The potential for containment failure at this point is extremely high [50] since the molten core debris attacks and penetrates the concrete foundation. This final molten core/concrete interaction (MCCI) is identified as an important part of the accident sequence. It is not only because of its direct effect on the integrity of the containment building, which is the last barrier to the dispersal of fission products, but also no engineering safety features are available to mitigate the progress.

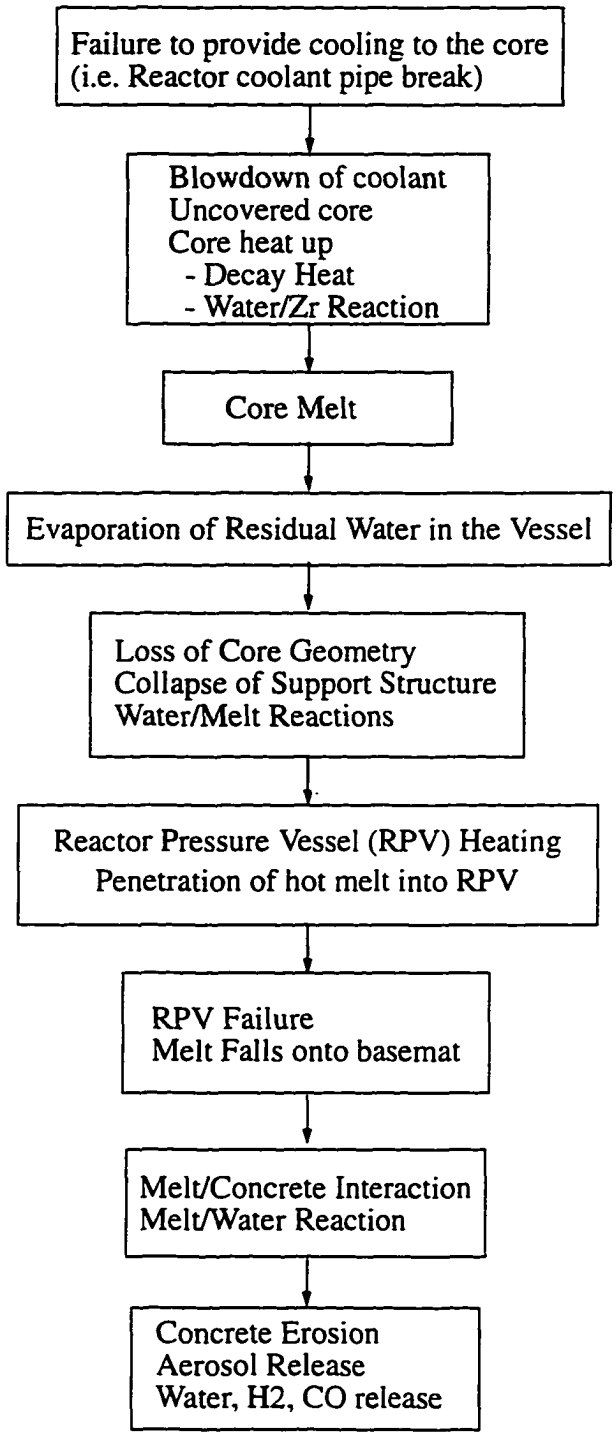

Figure 1: The sequence of a core meltdown.

1.3. Molten Core/Concrete Interaction

Molten core/concrete interactions have major impacts on several safety assessments. The early-time effect is the generation of noncondensable gases from the interaction that may result in an explosion or sudden containment overpressurization. Decomposition of concrete at high temperatures is a substantial contributor of water vapor and carbon dioxide that eventually react with molten metal and tend to be reduced to hydrogen and carbon monoxide. All of these gases cause an overpressurization of containment. Further, hydrogen and carbon monoxide are combustible gases and their ignition could inject additional thermal and mechanical energy into containment. This consequence of MCCI can be identified as "above-ground" impact. The risk associated with noncondensable gases and aerosols is derived from their potential to cause the release of radioactivity to the atmosphere. Since the quantity of these gases released into the containment is directly related to the amount of decomposing concrete, concrete erosion should be analyzed in detail to provide a basis for the design of a safe and reliable containment structure.

The growth and penetration of the molten pool into the decomposing concrete is also a potential risk to the containment integrity due to the long term effect of the molten core/concrete interactions. If the containment basemat fails, a substantial amount of radioactivity could be released to the soil underneath the reactor building, perhaps reaching the underground water system to present high risk to the public. Thus, the containment basemat must be designed to prevent any mechanical failure.

Another use of the MCCI evaluation is to calculate the partition of the

energy release from the molten pool as a part of the post accident heat removal (PAHR) process. The debris coolability also plays an important role in sequence analysis of the risk assessment associated with meltdown accident in LWR [6].

All the impacts of the MCCI indicated above may couple together making the analysis more complex. Overall, these effects add to the evaluation of the decomposition of the concrete, or in other words, to the calculation of the concrete erosion rates and depths. For the determination of the concrete erosion rates and depths, several models have been proposed in the past by several authors since the first detailed report of WASH-1400 [50]. Those models vary from a simple steady state approach to a detailed transient analysis of the phenomena.

1.4. Previous Models of MCCI

A simple but mostly reliable analysis of the MCCI, which is used in today's computer analysis [7, 8, 9, 10, 46] is based on the steady state erosion of concrete. In this model, the erosion rates are predicted based on the first law of thermodynamics, i.e. incoming and outgoing energies and masses are balanced (Figure 2). The surface heat flux that decomposes and ablates the concrete is then balanced by the product of the ablation enthalpy which includes sensible heat of concrete, latent heat of fusion, and chemical energies due to the reactions that decompose concrete ingredients and the rate that this energy is produced by decomposed material. This model is a good approximation for the high temperature phase of the MCCI where the melt is so hot that erosion is very rapid and solidification of the melt does not take place. If solidification occurs or the decomposition rate is slow, steady state calculations are not valid. The model gives an overestimated concrete ablation rate and an underestimated in-depth concrete decomposition rate. This is simply caused by assuming that the concrete temperature remains constant during the process. In the actual case, temperature in concrete is time dependent due to the molten core cooling in time, i.e. decreasing surface heat flux, and heat conduction properties of concrete that are to change because of decomposition of the concrete as water and gas release reactions. Therefore, the steady-state approximation does not provide an exact answer to the actual situation. However, it is a good and simple approach to the problem.

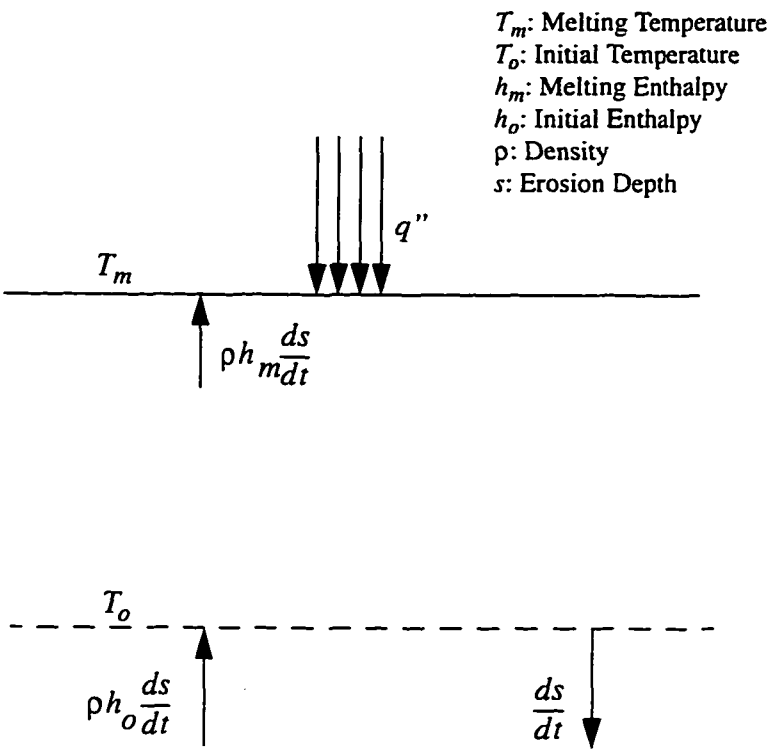

Figure 2: Conceptual Picture of a Steady-State Ablation Model

Transient models for MCCI phenomenon or related subjects such as melting or freezing have been studied in the past by several authors. Landau's [11] analysis for one dimensional melting of solid which is subject to a known constant surface heat flux showed that the velocity of the melting front reached a steady state value when the thermal front penetration rate was equal to the melting front velocity.

Henry [12] assumed an exponential temperature distribution in concrete and derived an expression for a steady state ablation rate after the thermal boundary layer is developed by assuming that all sensible and chemical energies of decomposition reactions are lumped together as a single latent heat. He calculated the amount of time to reach the steady state by substituting the in-depth penetration with one steady state boundary layer thickness which is the ratio of thermal diffusivity to ablation velocity.

Another model that was derived by Corradini [13], a single region transient model, included a detailed approach to the latent heat of fusion and chemical energies due to decomposition by sorting the reactions (Figure 3). All of the chemical energies were also considered as a lumped energy source at the surface of ablation, although they were calculated at each decomposition front. Then, by the use of the integral technique, assuming a polynomial temperature profile in the concrete, he found the concrete ablation velocity in terms of the thermal front depth. His approximation for the boundary condition at the surface is valid if the thermal properties of concrete are constant for each phase of decomposed concrete. Since the concrete is a heterogenous mixture of vaporizable and chemically bounded water, carbon dioxide and refractory oxides, decomposition of each ingredient would create a region with characteristic conduction properties.

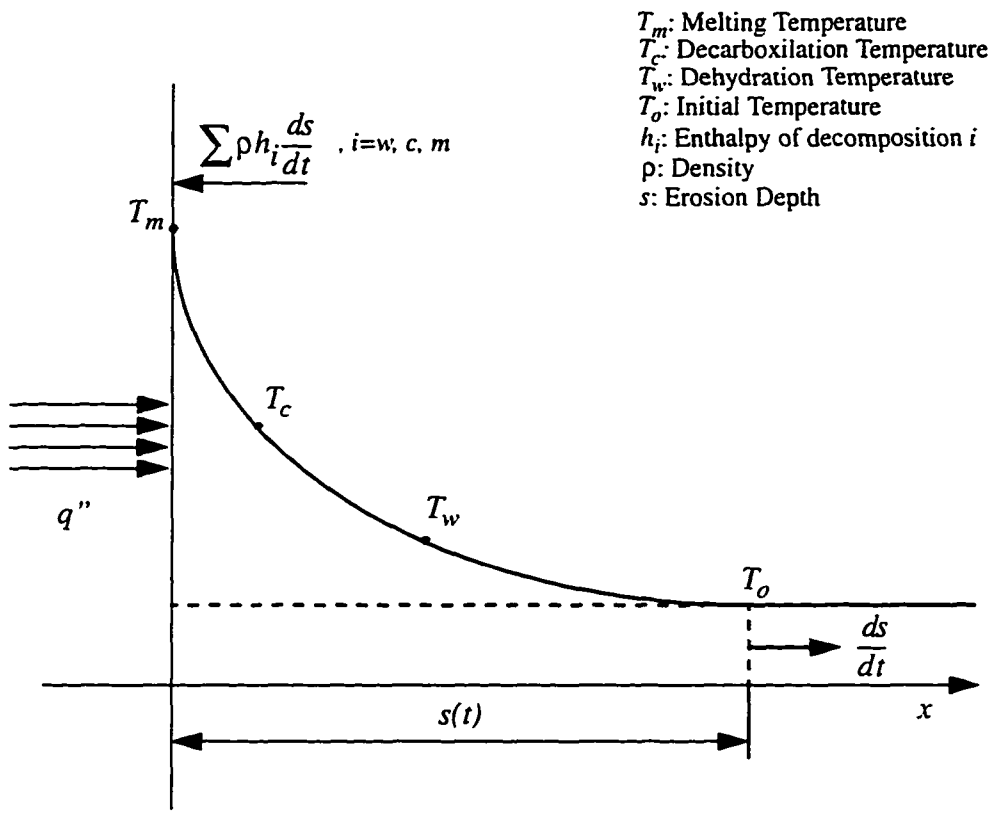

Figure 3: Conceptual Picture of One-Region Transient Ablation Model.

In the previous study by the author [47, 49], a four-region transient model which represented the phase variation in concrete considering thermal property differences in each phase was developed (Figure 4). All of the chemical energies were considered as heat sinks at each decomposition front. Using the integral method, the model determined the temperature profiles for each region, and then calculated the erosion rates and depths. The study found that there was a delay between time to reach steady state for ablation and thermal penetration fronts, that differed from Henry's and Corradini's transient studies. The model also provided the calculation of the thickness, and the growth rate of each region in the decomposed concrete which provided more specific input to the gas and aerosol release codes, and thermally degraded concrete investigations. The study considered a constant surface heat flux, and constant thermophysical properties in each region, and the solutions were limited to those initial conditions.

In actual molten core/concrete or molten metal/concrete interactions, the surface heat flux decreases rapidly due to crust formation and cooling of the debris. Therefore, the four region model can be improved to consider time dependent surface heat flux to represent and simulate the actual phenomena of the MCCI.

Also, the effect of thermophysical properties on the erosion and decomposition rates and depths can be evaluated. These properties differ for concrete based on not only the ingredients or types but also its production, mixing, drying, etc., and affect the concrete reaction to the heat transfer from the melt, and eventually, the ablation of the concrete.

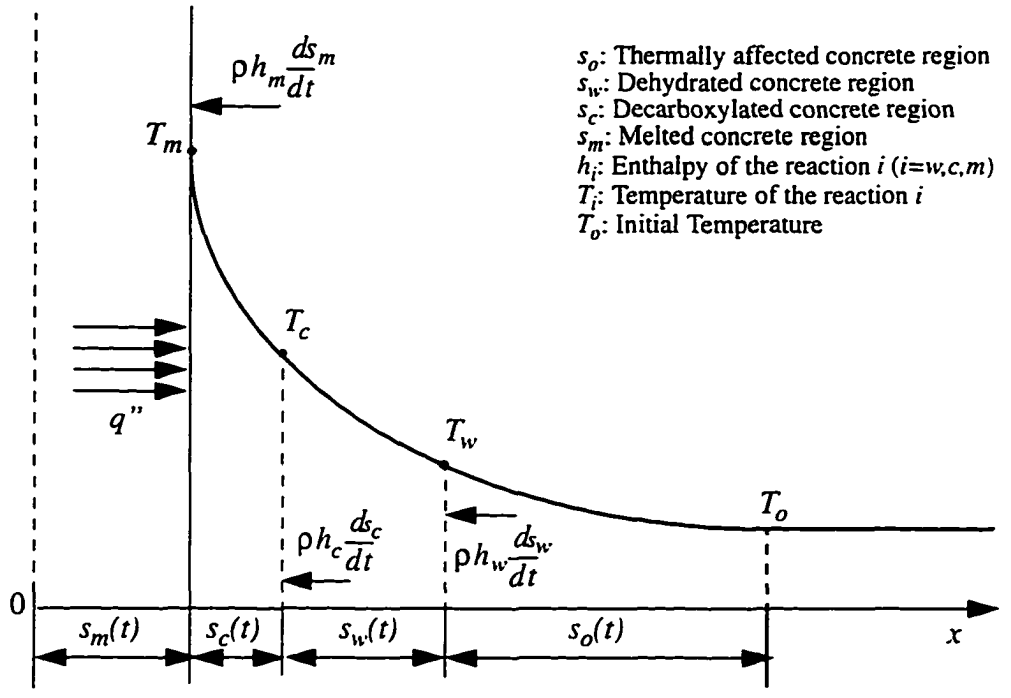

Figure 4: Conceptual picture of four-region transient model with constant surface heat flux and constant thermophysical properties.

CHAPTER 2

MODEL DESCRIPTION AND SOLUTION METHOD

2.1. Introduction

In this study, a multi-region, transient ablation of concrete with a time dependent heat flux at the surface will be considered. The time dependent surface heat flux will represent a superposed melt to concrete heat transfer. By doing so, a normalized decomposition and ablation of the concrete can be investigated since the change in surface heat flux due to cooling of the melt and crust formation in the melt can be evaluated and incorporated to a superimposed model. The effects of the thermophysical properties will also be investigated by a sensitivity study on those parameters.

2.2. Model Description

2.2.1. Concrete Decomposition

Concrete decomposition and ablation can be considered as the melting of a solid caused by a hot solid on the surface. Via this approach, concrete can be represented as a semi-infinite solid subject to a known heat flux on the surface. Heating

of the concrete at the surface increases the surface temperature, and a thermal depth moves into the concrete. Since the concrete is a heterogenous mixture of evaporable and chemically bound water, carbon dioxide and refractory oxides (Calcium oxide, Silicon oxide etc.), those components start to decompose when the temperature reaches their decomposition value [14, 15]. Table 1 presents the decomposition type and temperatures. Thus, as the surface temperature increases, we observe, first, the evaporation of evaporable water followed by the release of chemically bound water and, subsequently, decomposition of carbon dioxide and, finally, refractory oxides. When the refractory oxides decompose, literally, the concrete is considered melted. Therefore, basically three consequent regions of the concrete are observed: temperature affected region, dry concrete region, and a region without carbon dioxide gas, i.e. gas free region.

Table 1: Decomposition Reactions and Temperatures for the Species in Concrete [7]

Species	Decomposition Temperature (K)
Evaporable Water	290-500
Chemically Bounded Water	630-750
Carbon dioxide	870-1253
Refractory Oxides (melting)	1350-1670

2.2.2. Assumptions and Justification

In this study, the following assumptions are made:

1. Temperature varies in only one direction, i.e. a one dimensional problem is considered.

2. The only heat transfer mechanism is conduction, that is assume that no gas film is existing between the hot molten core and the concrete, and energy transfer by mass diffusion is neglected.

3. Phase change occurs at only a single temperature front for each phase and chemically bounded water and evaporable water decompose at the same front.

4. Molten concrete is immediately removed from the surface.

5. Density changes in non-mobile regions during the process are negligible.

The penetration depth in concrete is analyzed for a large surface and very fast transient, therefore a one dimensional solution is good enough to estimate the erosion rate.

"No gas film existence" assumption is an approximation, as well. Experiments [16] also studied the effects of a molten slag-gas film between the hot molten core and the concrete. In some molten core/concrete interaction models [17] this effect is simply neglected by the assumption that the slag is carried away from the surface by a rapid gas flow. In this model, a correction factor for the surface

heat flux is added to take the other mechanism of the heat transfer into account. This factor is determined by a parametric study.

Negligible mass diffusion is another approximation. Since the concrete may behave as a porous medium, both vapor and carbon dioxide gas might diffuse through the medium driven by the pressure gradient, but the speed of the transient and the depths of thermal regions make this assumption a reasonable approximation to the actual situation.

The assumption of phase change occurring at a single temperature front is a very simplified model of the actual physical phenomena. Decomposition of water and gas occurs in a temperature range in reality, and energy absorption in these reactions is widely spread in those ranges. On the other hand, the enthalpies for those reactions are calculated for those temperature values and this does not effect the overall energy balance of the regions significantly. In WASH-1400 [50] it was also assumed that water decomposition takes place at about 900°F, and then melting occurs at 1400-1600°F.

The model by these assumptions is simple but good enough to illustrate the physical phenomena that are important during the transient.

2.2.3. The Multi-Region Transient Decomposition Model

2.2.3.1. Conceptual Model

Under the assumptions and definition of the concrete decomposition, we can divide the transient decomposition of concrete into four consequent physical phenomena:

Pre-evaporation: from initial state until the surface temperature reaches the evaporation temperature of evaporable and chemically bound water.

Dry concrete: the phase between water evaporation and gas decomposition.

CO_2 free (decarboxylated) concrete: from gas decomposition until the melting starts.

Ablation: the erosion of the concrete surface.

Then we will write the governing equation(s) for each region separately for each process described above and solve them with appropriate boundary and initial conditions applied to those regions by use of the heat balance integral technique.

The conceptual picture of the model is shown in Figure 5.

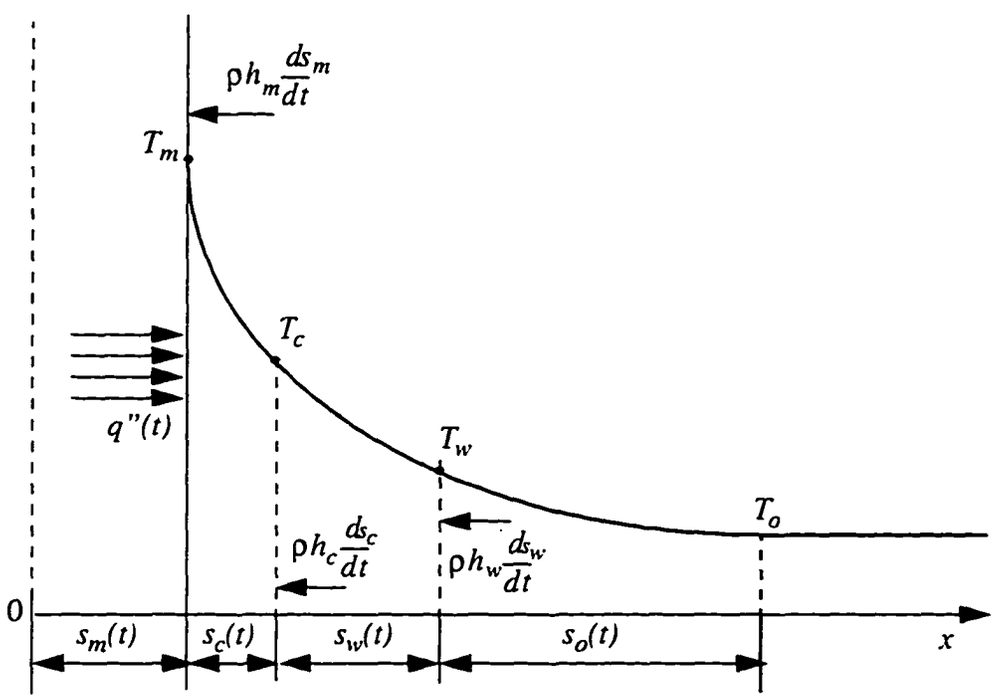

Figure 5: Conceptual picture of four-region transient model with time dependent surface heat flux and constant thermophysical properties.

2.2.3.2. Model Formulation

For the model, governing equations may be written for each region as follows:

$$\frac{\partial^2}{\partial x^2} T_n(x, t) = \frac{1}{\alpha_n} \frac{\partial}{\partial t} T_n(x, t) \qquad (2.2.3.1)$$

where T_n is the temperature of region n (n=1, 2, 3 for thermal, dry and gas-free region respectively)

Boundary conditions can be written at three different kinds of boundaries:

1. At the surface (before melting):

$$k_n \frac{\partial}{\partial x} T_{ns}(0, t) = -q''(t) \qquad (2.2.3.2)$$

where T_{ns} is the temperature of the region next to the surface.

2. At the unaffected concrete boundary:

$$T_1(s_{th}, t) = T_0 \qquad (2.2.3.3)$$

and:

$$\frac{\partial}{\partial x} T_1(s_{th}, t) = 0 \qquad (2.2.3.4)$$

where T_1 is the temperature of the region next to the unaffected concrete,

and T_0 is the unaffected concrete temperature. s_{th} is the distance of the thermal front from the original concrete surface ($\sum s_n$, n=1, 2, 3 for thermal, dry and gas-free region respectively). The thermal boundary layer $s_{th}(t)$ is defined as the distance beyond which, for practical purposes, there is no heat flow. Thus the initial temperature remains unaffected beyond $s_{th}(t)$.

3. At the decomposition interface s_{ij}:

$$T_i(s_{ij}, t) = T_j(s_{ij}, t) = T_{Rij} \tag{2.2.3.5}$$

and:

$$-k_j \frac{\partial}{\partial x} T_j(s_{ij}, t) = -k_i \frac{\partial}{\partial x} T_i(s_{ij}, t) + \rho_i L_{ij} \frac{ds_{ij}}{dt} \tag{2.2.3.6}$$

which is known as Stefan's boundary condition of phase change from phase i to phase j, where L_{ij} is the latent heat of the decomposition reaction, i.e. the enthalpy term, T_{Rij} is the decomposition temperature and s_{ij} is the total distance from the original surface. Note that the first term in the RHS of the Equation 2.2.3.6 becomes the surface heat flux $q''(t)$ after the melting begins.

The initial conditions are set by the thicknesses of each region when a particular decomposition starts.

2.3. Solution Method

As mentioned earlier in this chapter, decomposition and ablation of concrete can be considered as melting of a solid by a surface heat flux.

Solutions of the problems involved with melting or freezing are mostly considered to be in forms of the error function. But, in our model, time dependent boundary conditions prohibit the evaluation of the temperature distribution in forms of the error function or any related functions. Therefore, the solution must be derived by an approximate method.

In this study, Goodman's [21] heat balance integral method is used. This method has been found to be very reliable in engineering applications where exact solution analyses are not applicable and which require a close look at the significance of physical parameters that drive the phenomena where the numerical solutions cannot serve well enough. The same method was used in Corradini's one-phase concrete decomposition model.

2.3.1. Heat Balance Integral Method

Various analytic methods provide exact solutions for the partial differential equations (PDEs) where the equations and their boundary conditions are linear and the geometry is simple enough. Also, for limited numbers of special cases, nonlinear equations can be solved exactly. When the geometries get more complicated and existing boundary conditions are nonlinear, exact solution analyses are not available. Therefore, the solutions of problems are analyzed by the use of some approximate analytical methods or numerical techniques. In some cases numerical solution of the equations cannot be justified. For the problems which require a close look at the significance of physical parameters that drive the physical phenomena, numerical solutions cannot serve well enough. Use of approximate analytical methods for those types of problems provide better understanding of those parameters.

The integral method has been used for the solution of PDEs since the first applications to the boundary layer and energy equations in fluid mechanics by Von Karman et al. [23]. In heat conduction, multi-dimensional steady state and one dimensional transient problems, or the problems involved with temperature dependent properties are approximated in several studies. The one dimensional transient melting problem was analyzed by use of the heat balance integral method. Several investigators [24-28] have used the method for the solution of the one-dimensional transient phase change problems. This is commonly referred to as Stefan's problem, named after J. Stefan who studied the thickness of polar ice [29], with both linear and nonlinear boundary and initial conditions, because of its simplicity and straight-forward approach to the problem. Comparing the results with available exact solutions for a few special cases shows that accuracy of the method is acceptable [30].

The method involves the integration of governing equation(s) over a phenomenological distance, mostly a thermal front that is a function of time, defined by the certain boundary conditions applied to that region. This removes the second degree derivative of the spatial variable in the differential equation and by applying Leibnitz' rule on the derivative of an integral, a first degree, time dependent equation called "the heat balance integral" is found. The next step is to choose a suitable temperature profile for the temperature distribution in space. The most preferred type of profile is a polynomial with the degree of two to four. Polynomials with higher degrees do not improve the accuracy, and require derivation of artificial boundary conditions [47]. Then, by use of the boundary conditions, the coefficients of the polynomial are determined. Replacing this temperature distribution in the heat balance equation gives a first degree ordinary differential equation for the phenomenological distance with time as the independent variable. This

equation is subject to given initial conditions. Solution of this equation can be performed analytically if possible or by use of a simple and reliable numerical method such as Runge-Kutta or another predictor-corrector method, and then this solution is substituted into the temperature profile in order to get temperature distribution as a function of time and space in the media. Since the governing equation is satisfied only on the average, this solution is not exact but simple enough to illustrate the physical phenomena and very useful in the engineering applications.

2.3.2. Application of the Solution Method to the Model

Integrating the governing equation 2.2.3.1 in each region from lower boundary s_l to upper boundary s_u results in:

$$\frac{\partial}{\partial x}T_n(s_u, t) - \frac{\partial}{\partial x}T_n(s_l, t) = \frac{1}{\alpha_n}\int_{s_l}^{s_u}\frac{\partial}{\partial t}T_n(x, t)\,dx \qquad (2.3.2.1)$$

By using Leibnitz' formula, and the boundary conditions, and defining:

$$\theta_n = \int_{s_l}^{s_u} T_n(x, t)\,dx, \qquad (2.3.2.2)$$

heat balance equation(s) can be obtained in forms of:

$$\frac{d\theta_n}{dt} = f_n\left(\frac{ds_n}{dt}, \frac{\partial}{\partial x}T_n(s_{ij}, t), \ldots\right) \qquad (2.3.2.3)$$

Next, a quadratic temperature profile function(s) is selected as:

$$T_n = A_n + B_n x + C_n x^2 \tag{2.3.2.4}$$

These coefficients, which might be the functions of s_n and time itself, are determined by using the boundary conditions, and temperature profiles then can be inserted into Equation(s) 2.3.2.2 to determine θ_n. The resulting function is used in Equation 2.3.2.1 resulting in equations independent of the space variable, and including the thermal region thicknesses, their derivatives, and the physical parameters. These equations can be written in forms of:

$$\frac{ds_n}{dt} = g_n(s_n, s_{n_1}, t) \tag{2.3.2.5}$$

where s_{n_1} represents the other regions than s_n.

Equation 2.3.2.5 actually represents a system of ordinary differential equations. These equations can be solved simultaneously for region thicknesses and their derivatives by using the initial conditions, and a simple numerical technique.

CHAPTER 3

GENERAL SOLUTION

3.1. Introduction

The model defines three regions in the concrete coupled with an ablation front. Each region has an interface where the latent heat of decomposition reaction is taken into account as heat sinks. The governing equation for each region can be derived before and after each decomposition reaction begins. Therefore, the solution will consider four solution systems for each period of time: before the evaporations begins (pre-evaporation), after evaporation but before the decarboxylation begins (dry concrete), after decarboxylation but before melting begins (gas-free concrete), and finally after melting.

3.2. Solution

3.2.1. Pre-evaporation

When hot molten core debris contacts the concrete which has a uniform initial temperature T_i, the problem can be considered as heating of a semi-infinite media with a time dependent surface heat flux for, as illustrated in Figure 6.

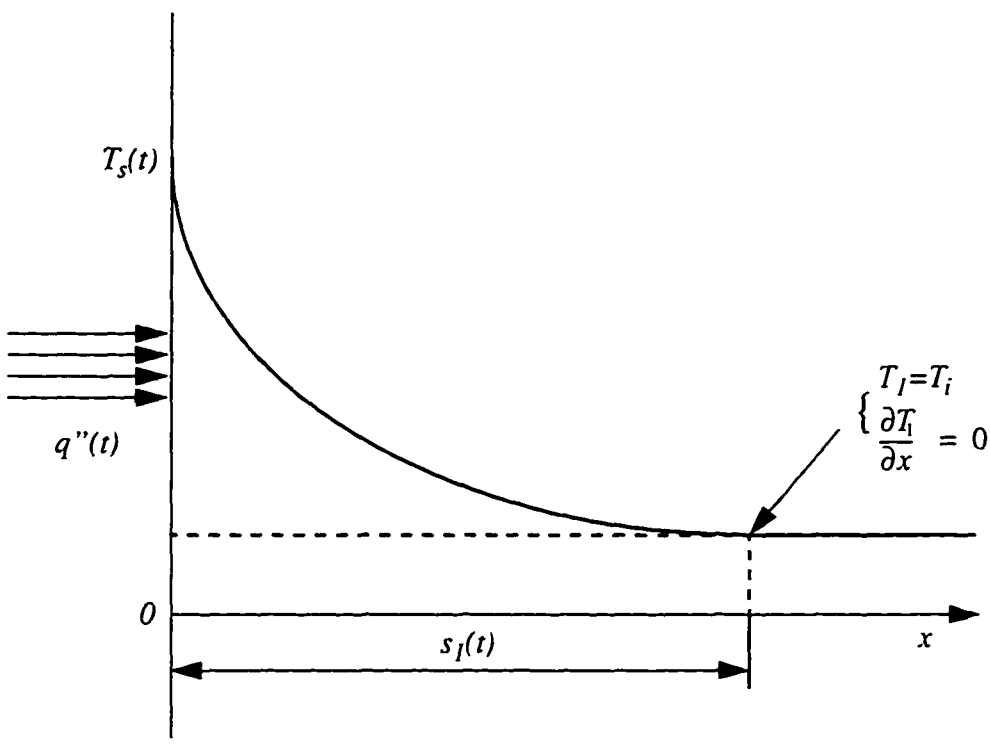

Figure 6: Heating of a semi-infinite media (concrete) by a surface heat flux and the definition of the thermal boundary for pre-evaporation.

For this problem, the thermal boundary layer $s_1(t)$ is defined as the distance beyond which, for practical purposes, there is no heat flow. Thus the initial temperature remains unaffected beyond $s_1(t)$.

The mathematical formulation of this problem is given as the heat diffusion equation with constant thermal properties and no heat generation:

$$\frac{\partial^2}{\partial x^2} T_1(x,t) = \frac{1}{\alpha_1} \frac{\partial}{\partial t} T_1(x,t) \tag{3.2.1.1}$$

and the boundary and initial conditions:

$$k_1 \frac{\partial}{\partial x} T_1(0,t) = -q''(t) \tag{3.2.1.1.a}$$

$$T_1(s_1,t) = T_i \tag{3.2.1.1.b}$$

$$\frac{\partial}{\partial x} T_1(s_1,t) = 0 \tag{3.2.1.1.c}$$

$$s_1(0) = 0 \tag{3.2.1.1.d}$$

Equation 3.2.1.1 can be non-dimensionalized by choosing the dimensionless parameters for temperature:

$$\theta = \frac{T_1 - T_i}{T_i} \tag{3.2.1.2}$$

for space:

$$\bar{x} = \frac{x}{l} \tag{3.2.1.3}$$

and:

$$\bar{s} = \frac{s}{l} \tag{3.2.1.4}$$

and for time:

$$\tau = \frac{t\alpha_1}{l} \equiv \mathrm{Fo} \tag{3.2.1.5}$$

where Fo is the Fourier Number and l is an arbitrary distance that is chosen in terms of initial (known) parameters as:

$$l = \frac{k_1 T_i}{q_0''} \tag{3.2.1.6}$$

where $q_0''=q''(0)$.

Then the governing equation 3.2.1.1 becomes:

$$\frac{\partial^2}{\partial \bar{x}^2}\theta_1(\bar{x},\tau) = \frac{\partial}{\partial \tau}\theta_1(\bar{x},\tau) \tag{3.2.1.7}$$

with the boundary and initial conditions:

$$-\frac{\partial}{\partial \bar{x}}\theta_1(0,\tau) = \frac{q''(\tau)}{q_0''} \tag{3.2.1.7.a}$$

$$\theta_1(\bar{s}_1,\tau) = 0 \tag{3.2.1.7.b}$$

$$\frac{\partial}{\partial \bar{x}}\theta_1(\bar{s}_1,\tau) = 0 \tag{3.2.1.7.c}$$

$$\bar{s}_1(0) = 0 \tag{3.2.1.7.d}$$

By integrating the Equation 3.2.1.7 with respect to the space variable from $\bar{x} = 0$ to $\bar{x} = \bar{s}_1(\tau)$:

$$\int_{\bar{x}=0}^{\bar{x}=\bar{s}_1} \frac{\partial^2 \theta_1}{\partial \bar{x}^2} d\bar{x} = \int_{\bar{x}=0}^{\bar{x}=\bar{s}_1} \frac{\partial \theta_1}{\partial \tau} d\bar{x} \tag{3.2.1.8}$$

or:

$$\left.\frac{\partial \theta_1}{\partial \bar{x}}\right|_{\bar{x}=\bar{s}_1} - \left.\frac{\partial \theta_1}{\partial \bar{x}}\right|_{\bar{x}=0} = \int_{\bar{x}=0}^{\bar{x}=\bar{s}_1} \frac{\partial \theta_1}{\partial \tau} d\bar{x} \tag{3.2.1.9}$$

can be found.

Applying the Leibnitz' rule to the right hand side of the equation results in:

$$\left.\frac{\partial \theta_1}{\partial \bar{x}}\right|_{\bar{x}=\bar{s}_1} - \left.\frac{\partial \theta_1}{\partial \bar{x}}\right|_{\bar{x}=0} = \frac{d}{d\tau} \int_{\bar{x}=0}^{\bar{x}=\bar{s}_1} \theta_1 d\bar{x} - \theta_1\big|_{\bar{x}=\bar{s}_1} \frac{d\bar{s}_1}{d\tau} \tag{3.2.1.10}$$

By defining:

$$\bar{\theta}_1 = \int_{\bar{x}=0}^{\bar{x}=\bar{s}_1(\tau)} \theta_1 d\bar{x} \tag{3.2.1.11}$$

and applying the boundary conditions, the equation 3.2.1.11 becomes:

$$\frac{\partial \bar{\theta}_1}{\partial \tau} = \frac{q''(\tau)}{q_0''} \tag{3.2.1.12}$$

which is the heat balance integral for the problem considered.

Now we can assume either a second degree or a third degree polynomial for the temperature distribution. To choose a polynomial greater than the fourth degree does not improve the accuracy of the solution significantly [47]. Also the boundary conditions for this problem limit us with the maximum a third degree polynomial.

Then a cubic polynomial is chosen for $\theta_1(\bar{x}, \tau)$ in the form of:

$$\theta_1(\bar{x}, \tau) = A + B\bar{x} + C\bar{x}^2 + D\bar{x}^3 \tag{3.2.1.13}$$

where the coefficients might be functions of time.

Three of these coefficients can be determined by the use of three boundary conditions. The fourth boundary condition, that is necessary to determine the last coefficient, can be found by evaluating the governing equation at the edge of the thermal boundary layer $\bar{s}_1(\tau)$. Since $T_1 = T_i = const.$ at $\bar{s}_1(\tau)$, the derivative of the temperature with respect to time vanishes and we obtain the condition as:

$$\left.\frac{\partial^2 \theta_1}{\partial \bar{x}^2}\right|_{x = s_1} = 0 \tag{3.2.1.14}$$

Application of four conditions to the equation 3.2.1.13 yields the tempera-

ture profile in the form of:

$$\theta_1(\bar{x},\tau) = \frac{\bar{s}_1(\tau)}{3}\frac{q''(\tau)}{q_0''}\left(1-\frac{\bar{x}}{\bar{s}_1(\tau)}\right)^3 \tag{3.2.1.15}$$

Introducing this temperature profile into equation 3.2.1.11 results for $\bar{\theta}_1$ as:

$$\bar{\theta}_1 = \frac{1}{12}\frac{q''}{q_0''}\bar{s}_1^2 \tag{3.2.1.16}$$

and replacing this result into the heat balance integral results in following:

$$\frac{q''}{q_0''} = \frac{d}{d\tau}\left(\frac{1}{12}\frac{q''}{q_0''}\bar{s}_1^2\right) \tag{3.2.1.17}$$

or:

$$\bar{s}_1 = \left(\frac{12}{q''}\int_0^\tau q''(\tau')\,d\tau'\right)^{\frac{1}{2}} \tag{3.2.1.18}$$

Then, using the temperature profile in equation 3.2.1.15, the time dependent surface temperature can be found as:

$$\theta_1(0,\tau) = \frac{1}{3}\frac{q''(\tau)}{q_0''}\left(\frac{12}{q''}\int_0^\tau q''(\tau')\,d\tau'\right)^{\frac{1}{2}} \tag{3.2.1.19}$$

3.2.2. Dry Concrete

When the surface temperature reaches the required temperature for water evaporation T_w, water content of the concrete begins to decompose. In the actual case, there are two types of water decomposition: the first one is the dehydration of the evaporable water in the concrete when molecular water from species such as Tobermorite, Ettringite, and $3CaO.2SiO_2.3H_2O$ vaporize [14]. The second type of water decomposition is the chemical break up of the bonds that hold chemically-constituted water, mainly following the reaction for calcium hydroxide as:

$$Ca(OH)_2 \rightarrow CaO + H_2O$$

This reaction occurs when the temperature reaches about 600-750 K while the dehydration is observed between 290 and 500 K. In this study, by considering the speed of the process and the narrow temperature difference between the temperature ranges for dehydration and the chemical decomposition of water, water decomposition is simplified to a single temperature for both processes, and the latent heat corresponding to that temperature that is chosen appropriately. This dehydration can be considered as a chemical decomposition reaction rather than simple water evaporation. Thus, the pressure corresponding to the decomposition temperature may exceed the critical pressure of water at that temperature.

As the surface temperature continues to increase due to the surface heat flux, the temperature front which is assumed to be at the dehydration temperature starts moving into the solid concrete. At this moment, one can define a second phenomenological distance $s_2(t)$ between the dehydration front and the surface. Since the temperature affected concrete distance is also moving, we have two mov-

ing fronts: one which has the constant dehydration temperature, T_w, and the second beyond where no heat flux is observed. Figure 7 illustrates these regions according to their definitions.

During this process, each of these regions has different thermal properties that are assumed constant inside each region. Since the volumetric changes are negligible and the thermal heat capacities are almost constant in those temperature ranges [31], the real assumption is about the thermal conductivity that depends on the temperature more strongly than others, but, still the range of the temperature is not effective enough to make the constant assumption invalid. Besides the constant evaporation temperature, the front $s_2(t)$ has an endothermic reaction which works as a sink for the heat flux in a magnitude of latent heat of water decomposition.

The way to evaluate the solution is to divide the problem into two separate regions divided by the water evaporation front. Formulation for these two regions can then be written by two governing equations:

$$\frac{\partial^2}{\partial x^2} T_1(x,t) = \frac{1}{\alpha_1}\frac{\partial}{\partial t} T_1(x,t) \qquad (3.2.2.1)$$

$$\frac{\partial^2}{\partial x^2} T_2(x,t) = \frac{1}{\alpha_2}\frac{\partial}{\partial t} T_2(x,t) \qquad (3.2.2.2)$$

with the applied boundary and initial conditions:

$$k_2 \frac{\partial}{\partial x} T_2(0,t) = -q''(t) \qquad (3.2.2.2.a)$$

$$T_2(s_2,t) = T_w \qquad (3.2.2.2.b)$$

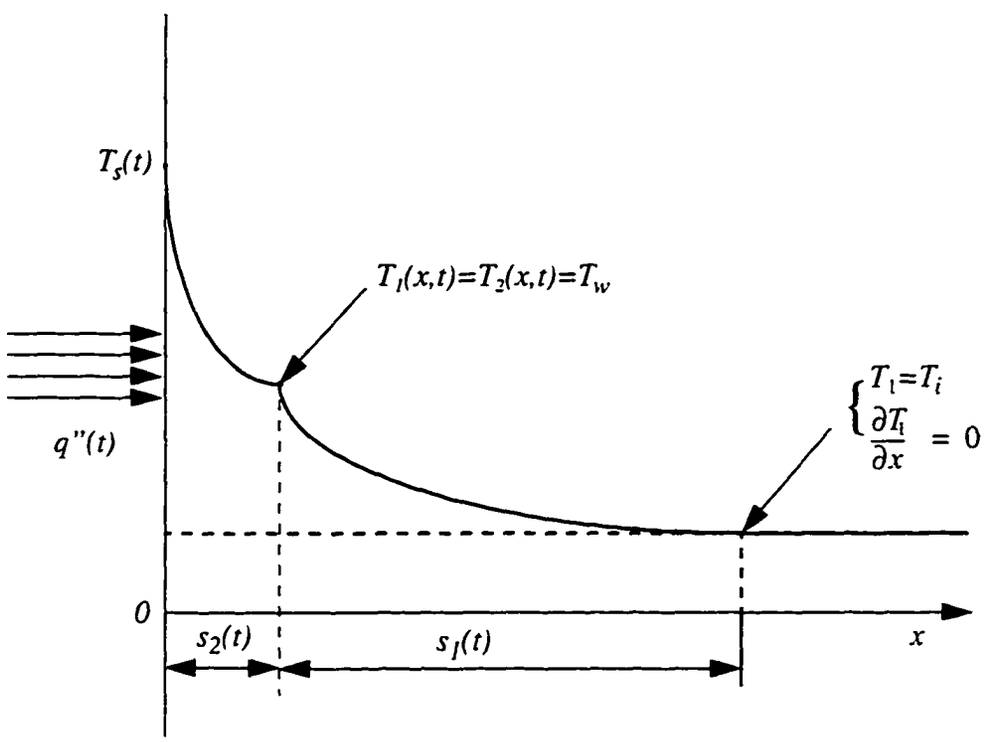

Figure 7: Thermal Layers for Dehydration Phase.

$$T_1(s_2, t) = T_w \tag{3.2.2.2.c}$$

$$T_1(s_2 + s_1, t) = T_i \tag{3.2.2.2.d}$$

$$\frac{\partial}{\partial x} T_1(s_2 + s_1, t) = 0 \tag{3.2.2.2.e}$$

$$-k_2 \frac{\partial}{\partial x} T_2(s_2, t) = -k_1 \frac{\partial}{\partial x} T_1(s_2, t) + \rho L_1 \frac{d}{dt} s_2(t) \tag{3.2.2.2.f}$$

$$s_2(t_w) = 0 \tag{3.2.2.2.g}$$

$$s_1(t_w) = \varepsilon_1 \tag{3.2.2.2.h}$$

where ε_1 is the thermally affected concrete depth when the evaporation begins at time t_w.

Boundary condition 3.2.2.2.f is known as the Stefan's boundary condition which is basically the conservation of energy written at the water decomposition front where L_1 represents the latent heat of evaporation.

Non-dimensionalization can be performed by choosing the parameters as follows:

$$\theta = \frac{T - T_w}{T_w - T_i} \tag{3.2.2.3}$$

$$\bar{x} = \frac{x}{l} \tag{3.2.2.4}$$

$$\bar{s} = \frac{s}{l} \tag{3.2.2.5}$$

and:

$$\tau = \frac{(t - t_w)\,\alpha_1}{l} \tag{3.2.2.6}$$

where l is the same as it is defined in Equation 3.2.1.6.

By these parameters, the governing equations become:

$$\frac{\partial^2}{\partial \bar{x}^2}\theta_1(\bar{x}, \tau) = \frac{\partial}{\partial \tau}\theta_1(\bar{x}, \tau) \tag{3.2.2.7}$$

$$\frac{\partial^2}{\partial \bar{x}^2}\theta_2(\bar{x}, \tau) = \alpha_{12}\frac{\partial}{\partial \tau}\theta_2(\bar{x}, \tau) \tag{3.2.2.8}$$

The dimensionless boundary and initial conditions are:

$$\frac{\partial}{\partial \bar{x}}\theta_2(0, \tau) = \frac{q''(\tau)}{q_0''}\frac{\chi_1}{k_{12}} \tag{3.2.2.8.a}$$

$$\theta_2(\bar{s}_2, \tau) = 0 \tag{3.2.2.8.b}$$

$$\theta_1(\bar{s}_2, \tau) = 0 \tag{3.2.2.8.c}$$

$$\theta_1(\bar{s}_2 + \bar{s}_1, \tau) = -1 \tag{3.2.2.8.d}$$

$$\frac{\partial}{\partial \bar{x}}\theta_1(\bar{s}_2 + \bar{s}_1, \tau) = 0 \tag{3.2.2.8.e}$$

$$k_{12}\frac{\partial}{\partial \bar{x}}\theta_2(\bar{s}_2, \tau) = \frac{\partial}{\partial \bar{x}}\theta_1(\bar{s}_2, \tau) - \frac{1}{St_1}\frac{d}{dt}\bar{s}_2(\tau) \tag{3.2.2.8.f}$$

$$\bar{s}_2(0) = 0 \tag{3.2.2.8.g}$$

$$\bar{s}_1(0) = \varepsilon_1 \tag{3.2.2.8.h}$$

where α_{12} is the dimensionless heat diffusivity that is:

$$\alpha_{12} = \frac{\alpha_1}{\alpha_2} \tag{3.2.2.9}$$

and:

$$k_{12} = \frac{k_2}{k_1} \tag{3.2.2.10}$$

$$\chi_1 = \frac{T_i}{T_w - T_i} \tag{3.2.2.11}$$

$$St_1 = \frac{c_1 (T_w - T_i)}{L_1} \tag{3.2.2.12}$$

In other words, k_{12} is the dimensionless thermal conductivity, χ_1 is the dimensionless heat flux, and St_1 is the Stefan number.

Now we can apply the integral method to both of the governing equations.

By integrating the Equation 3.2.2.7 with respect to the space variable from $\bar{x} = \bar{s}_2(\tau)$ to $\bar{x} = \bar{s}_1(\tau) + \bar{s}_2(\tau)$:

$$\int_{\bar{x}=\bar{s}_2}^{\bar{x}=\bar{s}_1+\bar{s}_2} \frac{\partial^2 \theta_1}{\partial \bar{x}^2} d\bar{x} = \int_{\bar{x}=\bar{s}_2}^{\bar{x}=\bar{s}_1+\bar{s}_2} \frac{\partial \theta_1}{\partial \tau} d\bar{x} \tag{3.2.2.13}$$

or:

$$\left.\frac{\partial \theta_1}{\partial \bar{x}}\right|_{\bar{x}=\bar{s}_1+\bar{s}_2} - \left.\frac{\partial \theta_1}{\partial \bar{x}}\right|_{\bar{x}=\bar{s}_2} = \int_{\bar{x}=\bar{s}_2}^{\bar{x}=\bar{s}_1+\bar{s}_2} \frac{\partial \theta_1}{\partial \tau} d\bar{x} \tag{3.2.2.14}$$

which results in:

$$\left.\frac{\partial\theta_1}{\partial\bar{x}}\right|_{\bar{x}=\bar{s}_1+\bar{s}_2} - \left.\frac{\partial\theta_1}{\partial\bar{x}}\right|_{\bar{x}=\bar{s}_2} = \frac{d}{d\tau}\int_{\bar{x}=\bar{s}_2}^{\bar{x}=\bar{s}_1+\bar{s}_2}\theta_1 d\bar{x} - \theta_1\big|_{\bar{x}=\bar{s}_1+\bar{s}_2}\frac{d}{d\tau}(\bar{s}_1+\bar{s}_2) - \theta_1\big|_{\bar{x}=\bar{s}_2}\frac{d\bar{s}_2}{d\tau} \tag{3.2.2.15}$$

Applying the boundary conditions to the last equation results in:

$$-\left.\frac{\partial\theta_1}{\partial\bar{x}}\right|_{\bar{x}=\bar{s}_2} = \frac{\partial\bar{\theta}_1}{\partial\tau} + \frac{d\bar{s}_1}{d\tau} + \frac{d\bar{s}_2}{d\tau} \tag{3.2.2.16}$$

where:

$$\bar{\theta}_1 = \int_{\bar{x}=\bar{s}_2}^{\bar{x}=\bar{s}_1+\bar{s}_2}\theta_1 d\bar{x} \tag{3.2.2.17}$$

Thus, the heat balance equation for the temperature affected region is:

$$\frac{\partial\bar{\theta}_1}{\partial\tau} = -\left(\left.\frac{\partial\theta_1}{\partial\bar{x}}\right|_{\bar{x}=\bar{s}_2} + \frac{d\bar{s}_1}{d\tau} + \frac{d\bar{s}_2}{d\tau}\right) \tag{3.2.2.18}$$

Integration of Equation 3.2.2.8 from $\bar{x} = 0$ to $\bar{x} = \bar{s}_2(\tau)$ can be performed as:

$$\int_{\bar{x}=0}^{\bar{x}=\bar{s}_2}\frac{\partial^2\theta_2}{\partial\bar{x}^2}d\bar{x} = \alpha_{12}\int_{\bar{x}=0}^{\bar{x}=\bar{s}_2}\frac{\partial\theta_2}{\partial\tau}d\bar{x} \tag{3.2.2.19}$$

that results in:

$$\left.\frac{\partial\theta_2}{\partial\bar{x}}\right|_{\bar{x}=\bar{s}_2} - \left.\frac{\partial\theta_2}{\partial\bar{x}}\right|_{\bar{x}=0} = \alpha_{12}\left(\frac{d}{d\tau}\int_{\bar{x}=0}^{\bar{x}=\bar{s}_2}\theta_2 d\bar{x} - \theta_2|_{\bar{x}=\bar{s}_2}\frac{d\bar{s}_2}{d\tau}\right) \tag{3.2.2.20}$$

With the use of the boundary conditions, the heat balance integral for the dry concrete region can be constructed as:

$$\frac{\partial\bar{\theta}_2}{\partial\tau} = \frac{1}{\alpha_{12}k_{12}}\left(\left.\frac{\partial\theta_1}{\partial\bar{x}}\right|_{\bar{x}=\bar{s}_2} - \chi_1\frac{q''}{q_0''} - \frac{1}{St_1}\frac{d\bar{s}_2}{d\tau}\right) \tag{3.2.2.21}$$

where

$$\bar{\theta}_2 = \int_{\bar{x}=0}^{\bar{x}=\bar{s}_2}\theta_2 d\bar{x} \tag{3.2.2.22}$$

Temperature profiles can be chosen for each region as quadratic polynomials. As was mentioned earlier, the degree can be between two and four. The number of boundary conditions given above require us to select a second degree polynomial. Thus the profiles can be selected as:

$$\theta_1(\bar{x},\tau) = A_1 + B_1[\bar{x} - \bar{s}_2(\tau)] + C_1[\bar{x} - \bar{s}_2(\tau)]^2 \tag{3.2.2.23}$$

and:

$$\theta_2(\bar{x},\tau) = A_2 + B_2[\bar{s}_2(\tau) - \bar{x}] + C_2[\bar{s}_2(\tau) - \bar{x}]^2 \tag{3.2.2.24}$$

By the use of the boundary condition 3.2.2.8.c, 3.2.2.8.d, and 3.2.2.8.e, coefficients in the equation 3.2.2.23 can be found such that:

$$\theta_1(\bar{x},\tau) = -2\left[\frac{\bar{x}-\bar{s}_2(\tau)}{\bar{s}_1(\tau)}\right] + \left[\frac{\bar{x}-\bar{s}_2(\tau)}{\bar{s}_1(\tau)}\right]^2 \tag{3.2.2.25}$$

In equation 3.2.2.23, use of the boundary condition 3.2.2.8.b gives $A_1 = 0$, and applying the boundary conditions 3.2.2.8.a and 3.2.2.8.f results in two equations:

$$-\frac{\chi_1}{k_{12}} = B_2 + 2C_2\bar{s}_2 \tag{3.2.2.26}$$

and:

$$B_2 = \frac{1}{k_{12}}\left[\frac{2}{\bar{s}_1} + \frac{1}{St_1}\frac{d\bar{s}_2}{d\tau}\right] \tag{3.2.2.27}$$

These equations are not convenient to solve for C_2 and B_2 since they result in a first degree, second order ordinary differential equation with one initial condition for $\bar{s}_2(\tau)$. This problem can be overcome by eliminating $\frac{d\bar{s}_2}{d\tau}$ in the latter equation by using the boundary conditions together with the governing equation 3.2.2.8. Since this governing equation is valid everywhere in the region $0 \le \bar{x} \le \bar{s}_2(\tau)$, it can be written at the dry concrete-temperature affected concrete interface as following:

$$\left.\frac{\partial^2\theta_2}{\partial\bar{x}^2}\right|_{\bar{x}=\bar{s}_2} = \alpha_{12}\left.\frac{\partial\theta_2}{\partial\tau}\right|_{\bar{x}=\bar{s}_2} \tag{3.2.2.28}$$

or:

$$\frac{d\bar{s}_2}{d\tau} = 2\frac{C_2}{B_2} \tag{3.2.2.29}$$

Combining this result with the equations 3.2.2.26 and 3.2.2.27 gives the coefficients as following:

$$B_2 = -\left[\frac{M_1 - M_2}{2\alpha_{12}k_{12}St_1}\right]\frac{1}{\bar{s}_2(\tau)} \tag{3.2.2.30}$$

and:

$$C_2 = \left[\frac{M_1 - M_2}{4\alpha_{12}k_{12}St_1} - \frac{\chi_1}{2k_{12}}\frac{q''}{q_0''}\bar{s}_2(\tau)\right]\left[\frac{1}{\bar{s}_2(\tau)}\right]^2 \tag{3.2.2.31}$$

where:

$$M_1 = 1 - 2\alpha_{12}St_1\frac{\bar{s}_2}{\bar{s}_1} \tag{3.2.2.32}$$

and:

$$M_2 = \sqrt{M_1^2 - 4\alpha_{12}St_1\chi_1\frac{q''}{q_0''}\bar{s}_2} \tag{3.2.2.33}$$

Thus, the temperature distribution for the dry concrete region can be written as:

$$\theta_2(\bar{x},\tau) = -\left[\frac{M_1 - M_2}{2\alpha_{12}k_{12}St_1}\right]\left(\frac{\bar{s}_2(\tau) - \bar{x}}{\bar{s}_2(\tau)}\right) + \left[\frac{M_1 - M_2}{4\alpha_{12}k_{12}St_1} - \frac{\chi_1}{2k_{12}}\frac{q''}{q_0''}\bar{s}_2(\tau)\right]\left(\frac{\bar{s}_2(\tau) - \bar{x}}{\bar{s}_2(\tau)}\right)^2 \tag{3.2.2.34}$$

In order to use the heat balance integrals, $\bar{\theta}_1$ and $\bar{\theta}_2$ and their derivatives must be evaluated. By their definitions in Equations 3.2.2.17 and 3.2.2.22, $\bar{\theta}_1$ and $\bar{\theta}_2$ can be found as:

$$\bar{\theta}_1 = -\frac{2}{3}\bar{s}_1(\tau) \tag{3.2.2.35}$$

and:

$$\bar{\theta}_2 = -\frac{1}{6}\bar{s}_2(\tau)\left[\frac{M_1 - M_2}{\alpha_{12}k_{12}St_1} + \frac{\chi_1}{k_{12}}\frac{q''}{q_0''}\bar{s}_2(\tau)\right] \tag{3.2.2.36}$$

and their derivatives can be evaluated as following:

$$\frac{d\bar{\theta}_1}{d\tau} = -\frac{2}{3}\frac{d\bar{s}_1}{d\tau} \tag{3.2.2.37}$$

and:

$$\frac{d\bar{\theta}_2}{d\tau} = \mu_1(1+\gamma_1)\frac{d\bar{s}_2}{d\tau} + \mu_1 M\frac{\bar{s}_2}{\bar{s}_1}\frac{d\bar{s}_2}{d\tau} \tag{3.2.2.38}$$

where:

$$\mu_1 = \frac{M_1 - M_2}{6\alpha_{12}k_{12}St_1} \tag{3.2.2.39}$$

$$\gamma_1 = \frac{M_2^2 + M_1M_2 + M_2 - M_1 + 2}{2M_2} \tag{3.2.2.40}$$

and:

$$M = \frac{M_1 - 1}{M_2} \tag{3.2.2.41}$$

Replacing these results into the heat balance equations results in the following equations:

$$\frac{1}{3}\frac{d\bar{s}_1}{d\tau} + \frac{d\bar{s}_2}{d\tau} = \frac{2}{\bar{s}_1} \tag{3.2.2.42}$$

$$\left[\mu_1 M \frac{\bar{s}_2}{\bar{s}_1}\right]\frac{d\bar{s}_1}{d\tau} + \left[\mu_1 (1+\gamma_1) + \frac{1}{\alpha_{12} k_{12} St_1}\right]\frac{d\bar{s}_2}{d\tau} = -\frac{1}{\alpha_{12} k_{12}}\left[\frac{2}{\bar{s}_1} + \chi_1 \frac{q''}{q_0''}\right] \tag{3.2.2.43}$$

These last two equations can be put into a form as:

$$A_{11}\frac{d\bar{s}_1}{d\tau} + B_{11}\frac{d\bar{s}_2}{d\tau} = C_{11} \tag{3.2.2.43.a}$$

$$A_{22}\frac{d\bar{s}_1}{d\tau} + B_{22}\frac{d\bar{s}_2}{d\tau} = C_{22} \tag{3.2.2.43.b}$$

where:

$$A_{11} = \frac{1}{6} \tag{3.2.2.43.c}$$

$$B_{11} = \frac{1}{2} \tag{3.2.2.43.d}$$

$$C_{11} = \frac{1}{\bar{s}_1(\tau)} \tag{3.2.2.43.e}$$

$$A_{22} = \mu_1 M \frac{\bar{s}_2(\tau)}{\bar{s}_1(\tau)} \tag{3.2.2.43.f}$$

$$B_{22} = \mu_1 (1+\gamma_1) + \frac{1}{\alpha_{12} k_{12} St_1} \tag{3.2.2.43.g}$$

$$C_{22} = -\frac{1}{\alpha_{12} k_{12}}\left[\frac{2}{\bar{s}_1(\tau)} + \chi_1 \frac{q''(\tau)}{q_0''}\right] \tag{3.2.2.43.h}$$

Then, an ordinary differential equation system can be constructed as following:

$$\frac{d\bar{s}_1}{d\tau} = \frac{C_{11}B_{22} - C_{22}B_{11}}{A_{11}B_{22} - A_{22}B_{11}} \tag{3.2.2.44}$$

$$\frac{d\bar{s}_2}{d\tau} = \frac{A_{11}C_{22} - A_{22}C_{11}}{A_{11}B_{22} - A_{22}B_{11}} \tag{3.2.2.45}$$

This system is subject to the initial conditions 3.2.2.8.g and 3.2.2.8.h, and can be solved by using a simple numerical method.

By setting $\bar{x} = 0$ in the equation 3.2.2.34, the change of the surface temperature in time also can be found as:

$$T_s = T_w + \frac{1}{2}(T_w - T_i)\left[3\mu_1 - \chi_1 \frac{q''(\tau)}{q_0''} \frac{\bar{s}_2(\tau)}{k_{12}}\right] \tag{3.2.2.46}$$

3.2.3. Gas-free Concrete

Another decomposition in the concrete is the decarboxylation that is observed at temperatures higher than water evaporation. The temperature range for this decomposition process is about 850-1250 K. Depending on the concrete composition, calcareous aggregates such as *calcite*, *magnetite* and *dolomite* dissociate into an oxide and CO_2 by following the reactions:

$$CaCO_3 \rightarrow CaO + CO_2$$
$$MgCO_3 \rightarrow MgO + CO_2$$
$$CaMg(CO_3)_2 \rightarrow CaO + MgO + 2CO_2$$

Although calcium carbonate decomposes at 1160 K at 1 atm. pressure, partial decompositions can take place at temperatures as low as 900 K [14].

Since this decomposition causes as much change in material properties as the temperature effect, the media must be divided into three regions that have different thermal properties. This brings another phenomenological distance, s_3, associated with another governing equation into the calculations for the new region as shown in Figure 8. Thus, the mathematical formulation is as follows:

$$\frac{\partial^2}{\partial x^2} T_1(x,t) = \frac{1}{\alpha_1} \frac{\partial}{\partial t} T_1(x,t) \qquad (3.2.3.1)$$

$$\frac{\partial^2}{\partial x^2} T_2(x,t) = \frac{1}{\alpha_2} \frac{\partial}{\partial t} T_2(x,t) \qquad (3.2.3.2)$$

$$\frac{\partial^2}{\partial x^2} T_3(x,t) = \frac{1}{\alpha_3} \frac{\partial}{\partial t} T_3(x,t) \qquad (3.2.3.3)$$

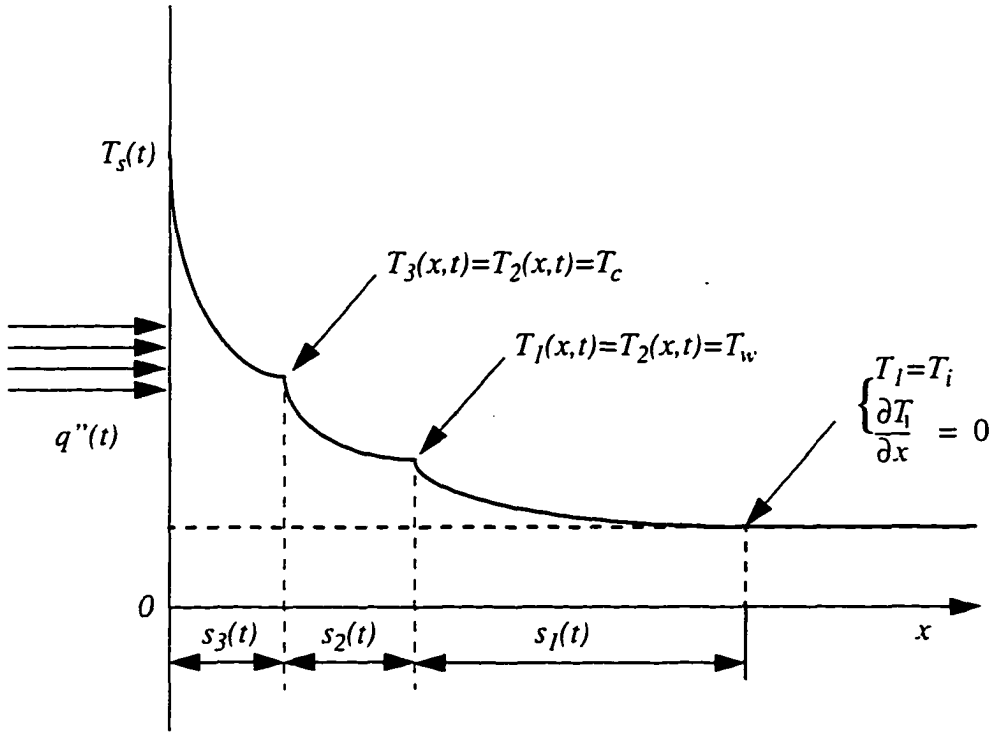

Figure 8: Thermal Layers for Decarboxylation (Gas-Free) Phase.

with the applied boundary and initial conditions:

$$k_3 \frac{\partial}{\partial x} T_3(0, t) = -q''(t) \quad (3.2.3.3.a)$$

$$T_3(s_3, t) = T_c \quad (3.2.3.3.b)$$

$$T_2(s_3, t) = T_c \quad (3.2.3.3.c)$$

$$T_2(s_3 + s_2, t) = T_w \quad (3.2.3.3.d)$$

$$T_1(s_3 + s_2, t) = T_w \quad (3.2.3.3.e)$$

$$T_1(s_3 + s_2 + s_1, t) = T_i \quad (3.2.3.3.f)$$

$$\frac{\partial}{\partial x} T_1(s_3 + s_2 + s_1, t) = 0 \quad (3.2.3.3.g)$$

$$-k_3 \frac{\partial}{\partial x} T_3(s_3, t) = -k_2 \frac{\partial}{\partial x} T_2(s_3, t) + \rho L_2 \frac{d}{dt} s_3(t) \quad (3.2.3.3.h)$$

$$-k_2 \frac{\partial}{\partial x} T_2(s_3 + s_2, t) = -k_1 \frac{\partial}{\partial x} T_1(s_3 + s_2, t) + \rho L_1 \frac{d}{dt} [s_2(t) + s_3(t)] \quad (3.2.3.3.i)$$

$$s_3(t_c) = 0 \quad (3.2.3.3.j)$$

$$s_2(t_c) = \delta_1 \quad (3.2.3.3.k)$$

$$s_1(t_c) = \varepsilon_2 \quad (3.2.3.3.l)$$

Again, Equation 3.2.3.3.h and 3.2.3.3.i are the Stefan's boundary conditions for water evaporation and gas decomposition interfaces, and ε_2 and δ_1 are the thermally effected and dry concrete thicknesses when the gas decomposition begins at time t_c.

Dimensionless parameters for this case are then:

$$\theta = \frac{T - T_c}{T_c - T_w} \tag{3.2.3.4}$$

$$\bar{x} = \frac{x}{l} \tag{3.2.3.5}$$

$$\bar{s} = \frac{s}{l} \tag{3.2.3.6}$$

and:

$$\tau = \frac{(t - t_c)\,\alpha_1}{l^2} \tag{3.2.3.7}$$

where l is again the same as it is defined in Equation 3.2.1.6.

Thus, the dimensionless governing equations are:

$$\frac{\partial^2}{\partial \bar{x}^2}\theta_1(\bar{x}, \tau) = \frac{\partial}{\partial \tau}\theta_1(\bar{x}, \tau) \tag{3.2.3.8}$$

$$\frac{\partial^2}{\partial \bar{x}^2}\theta_2(\bar{x}, \tau) = \alpha_{12}\frac{\partial}{\partial \tau}\theta_2(\bar{x}, \tau) \tag{3.2.3.9}$$

$$\frac{\partial^2}{\partial \bar{x}^2}\theta_3(\bar{x}, \tau) = \alpha_{13}\frac{\partial}{\partial \tau}\theta_3(\bar{x}, \tau) \tag{3.2.3.10}$$

The dimensionless boundary and initial conditions for these governing equations are:

$$\frac{\partial}{\partial \bar{x}}\theta_3(0, \tau) = \frac{q''(\tau)}{q_0''}\frac{\chi_2}{k_{13}} \tag{3.2.3.10.a}$$

$$\theta_3(\bar{s}_3, \tau) = 0 \tag{3.2.3.10.b}$$

$$\theta_2(\bar{s}_3, \tau) = 0 \tag{3.2.3.10.c}$$

$$\theta_2(\bar{s}_2 + \bar{s}_3, \tau) = -1 \tag{3.2.3.10.d}$$

$$\theta_1(\bar{s}_2 + \bar{s}_3, \tau) = -1 \tag{3.2.3.10.e}$$

$$\theta_1(\bar{s}_1 + \bar{s}_2 + \bar{s}_3, \tau) = \theta_0 \tag{3.2.3.10.f}$$

$$\frac{\partial}{\partial \bar{x}}\theta_1(\bar{s}_1 + \bar{s}_2 + \bar{s}_3, \tau) = 0 \tag{3.2.3.10.g}$$

$$k_{13}\frac{\partial}{\partial \bar{x}}\theta_3(\bar{s}_3, \tau) = k_{12}\frac{\partial}{\partial \bar{x}}\theta_2(\bar{s}_3, \tau) - \frac{1}{St_2}\frac{d\bar{s}_3}{d\tau} \tag{3.2.3.10.h}$$

$$k_{12}\frac{\partial}{\partial \bar{x}}\theta_2(\bar{s}_2 + \bar{s}_3, \tau) = \frac{\partial}{\partial \bar{x}}\theta_1(\bar{s}_2 + \bar{s}_3, \tau) - L_{12}\frac{1}{St_2}\frac{d}{d\tau}(\bar{s}_2 + \bar{s}_3) \tag{3.2.3.10.i}$$

$$\bar{s}_3(0) = 0 \tag{3.2.3.10.j}$$

$$\bar{s}_2(0) = \bar{\delta}_1 \tag{3.2.3.10.k}$$

$$\bar{s}_1(0) = \bar{\varepsilon}_2 \tag{3.2.3.10.l}$$

where:

$$\alpha_{13} = \frac{\alpha_1}{\alpha_3} \tag{3.2.3.11}$$

$$k_{13} = \frac{k_3}{k_1} \tag{3.2.3.12}$$

$$\chi_2 = -\frac{T_i}{T_c - T_w} \tag{3.2.3.13}$$

$$St_2 = \frac{c_1(T_c - T_w)}{L_2} \tag{3.2.3.14}$$

$$L_{12} = \frac{L_1}{L_2} \tag{3.2.3.15}$$

L_{12}, defined in the last equation, is the dimensionless latent heat.

Applying the integral method to the equations 3.2.3.8, 3.2.3.9, and 3.2.3.10 results as the heat balance equations for each region as follows:

For the temperature affected region:

$$\frac{\partial}{\partial\tau}\bar{\theta}_1 = -\frac{\partial\theta_1}{\partial\bar{x}}\bigg|_{\bar{x}=\bar{s}_2+\bar{s}_3} + \theta_0\frac{d\bar{s}_1}{d\tau} + (1+\theta_0)\frac{d\bar{s}_2}{d\tau} + (1+\theta_0)\frac{d\bar{s}_3}{d\tau} \tag{3.2.3.16}$$

where:

$$\bar{\theta}_1 = \int_{\bar{x}=\bar{s}_2+\bar{s}_3}^{\bar{x}=\bar{s}_1+\bar{s}_2+\bar{s}_3} \theta_1 d\bar{x} \tag{3.2.3.17}$$

For the dehydrated concrete region:

$$\frac{\partial\bar{\theta}_2}{\partial\tau} = \frac{1}{\alpha_{12}}\left(\frac{\partial\theta_2}{\partial\bar{x}}\bigg|_{\bar{x}=\bar{s}_2+\bar{s}_3} + \frac{\partial\theta_2}{\partial\bar{x}}\bigg|_{\bar{x}=\bar{s}_3} - \frac{d\bar{s}_3}{d\tau} - \frac{d\bar{s}_2}{d\tau}\right) \tag{3.2.3.18}$$

where:

$$\bar{\theta}_2 = \int_{\bar{x}=\bar{s}_3}^{\bar{x}=\bar{s}_2+\bar{s}_3} \theta_2 d\bar{x} \tag{3.2.3.19}$$

For the CO_2 free concrete region:

$$\frac{\partial \bar{\theta}_3}{\partial \tau} = \frac{1}{\alpha_{13} k_{13}} \left(k_{12} \frac{\partial \theta_2}{\partial \bar{x}} \bigg|_{\bar{x} = \bar{s}_3} - \chi_2 \frac{q''}{q_0''} - \frac{1}{St_2} \frac{d\bar{s}_3}{d\tau} \right) \tag{3.2.3.20}$$

where:

$$\bar{\theta}_3 = \int_{\bar{x}=0}^{\bar{x}=\bar{s}_3} \theta_3 d\bar{x} \tag{3.2.3.21}$$

Temperature profiles can be chosen for each region as:

$$\theta_1(\bar{x}, \tau) = A_1 + B_1 [\bar{x} - (\bar{s}_2 + \bar{s}_3)] + C_1 [\bar{x} - (\bar{s}_2 + \bar{s}_3)]^2 \tag{3.2.3.22}$$

$$\theta_2(\bar{x}, \tau) = A_2 + B_2 [(\bar{s}_2 + \bar{s}_3) - \bar{x}] + C_2 [(\bar{s}_2 + \bar{s}_3) - \bar{x}]^2 \tag{3.2.3.23}$$

and:

$$\theta_3(\bar{x}, \tau) = A_3 + B_3 [\bar{s}_3 - \bar{x}] + C_3 [\bar{s}_3 - \bar{x}]^2 \tag{3.2.3.24}$$

By the use of the boundary conditions, coefficients in the equation 3.2.3.22 can be found such that:

$$\theta_1(\bar{x}, \tau) = -1 + 2(1 + \theta_0) \left[\frac{\bar{x} - (\bar{s}_2 + \bar{s}_3)}{\bar{s}_1} \right] - (1 + \theta_0) \left[\frac{\bar{x} - (\bar{s}_2 + \bar{s}_3)}{\bar{s}_1} \right]^2 \tag{3.2.3.25}$$

If the boundary conditions 3.2.3.10.c, 3.2.3.10.d, and 3.2.3.10.i are used together with the governing equation 3.2.3.9, the temperature distribution for the dry concrete region can be found as:

$$\theta_2(\bar{x},\tau) = 1-\left[\frac{M_1'-M_2'}{\alpha_{12}k_{12}St_2}\right]\left(\frac{(\bar{s}_2+\bar{s}_3)-\bar{x}}{\bar{s}_2}\right)+\left[1+\frac{M_1'-M_2'}{\alpha_{12}k_{12}St_2}\right]\left(\frac{(\bar{s}_2+\bar{s}_3)-\bar{x}}{\bar{s}_2}\right)^2 \tag{3.2.3.26}$$

where:

$$M_1' = (1+\theta_0)\,\alpha_{12}St_2\frac{\bar{s}_2}{\bar{s}_1}+L_{12} \tag{3.2.3.27}$$

and:

$$M_2' = \sqrt{M_1'^2+2\alpha_{12}k_{12}St_2L_{12}} \tag{3.2.3.28}$$

In order to find the temperature distribution in the gas-free region, the boundary conditions 3.2.3.10.a, 3.2.3.10.b, and 3.2.3.10.h can be used together with the governing equation 3.2.3.10 that results as:

$$\theta_3(\bar{x},\tau) = -\left[\frac{N_1'-N_2'}{2\alpha_{13}k_{13}St_2}\right]\left(\frac{\bar{s}_3-\bar{x}}{\bar{s}_3}\right)+\left[\frac{N_1'-N_2'}{4\alpha_{12}k_{12}St_1}-\frac{\chi_2}{2k_{12}}\frac{q''}{q_0''}\bar{s}_3\right]\left(\frac{\bar{s}_3-\bar{x}}{\bar{s}_3}\right)^2 \tag{3.2.3.29}$$

where:

$$N_1' = 1-2\alpha_{13}k_{12}St_2\frac{\bar{s}_3}{\bar{s}_2}\left[1+\frac{M_1'-M_2'}{2\alpha_{12}k_{12}St_2}\right] \tag{3.2.3.30}$$

and:

$$N_2' = \sqrt{N_1'^2-4\alpha_{13}St_2\chi_2\frac{q''}{q_0''}\bar{s}_3} \tag{3.2.3.31}$$

After finding this temperature distribution, $\bar{\theta}_1$, $\bar{\theta}_2$, and $\bar{\theta}_3$ then can be evaluated by their definitions in Equations 3.2.3.17, 3.2.3.19, and 3.2.3.21 as follows:

$$\bar{\theta}_1 = \left[\frac{2}{3}(\theta_0 + 1) - 1\right]\bar{s}_1(\tau) \tag{3.2.3.32}$$

$$\bar{\theta}_2 = -\frac{2}{3}\left[1 + \frac{M_1' - M_2'}{4\alpha_{12}k_{12}St_2}\right]\bar{s}_2(\tau) \tag{3.2.3.33}$$

and:

$$\bar{\theta}_2 = -\frac{1}{6}\left[\frac{N_1' - N_2'}{\alpha_{13}k_{13}St_2} + \frac{\chi_2}{k_{13}}\frac{q''}{q_0''}\bar{s}_3(\tau)\right]\bar{s}_3(\tau) \tag{3.2.3.34}$$

Their derivatives then can be found as:

$$\frac{d\bar{\theta}_1}{d\tau} = \left[\frac{2}{3}(\theta_0 + 1) - 1\right]\frac{d\bar{s}_1}{d\tau} \tag{3.2.3.35}$$

$$\frac{d\bar{\theta}_2}{d\tau} = \left[\mu_2(1 - M') - \frac{2}{3}\right]\frac{d\bar{s}_2}{d\tau} + \mu_2 M'\frac{\bar{s}_2}{\bar{s}_1}\frac{d\bar{s}_1}{d\tau} \tag{3.2.3.36}$$

and:

$$\frac{d\bar{\theta}_3}{d\tau} = \mu_3(1 + \gamma_2)\frac{d\bar{s}_3}{d\tau} - \mu_3 N(M_L M' - 1)\frac{\bar{s}_3}{\bar{s}_2}\frac{d\bar{s}_2}{d\tau} + \mu_3 N M_L M\frac{\bar{s}_3}{\bar{s}_1}\frac{d\bar{s}_1}{d\tau} + \mu_3 Q\frac{\bar{s}_3}{q''}\frac{d}{d\tau}q'' \tag{3.2.3.37}$$

where:

$$\mu_2 = \frac{M_1' - M_2'}{6\alpha_{12}k_{12}St_2} \tag{3.2.3.38}$$

$$M' = \frac{M_1' - L_{12}}{M_2'} \tag{3.2.3.39}$$

$$\mu_3 = \frac{N_2' - N_1'}{6\alpha_{13}k_{13}St_2} \tag{3.2.3.40}$$

$$\gamma_2 = \frac{N_2'^2 + N_1'N_2' + N_2' - N_1' + 2}{2N_2'} \tag{3.2.3.41}$$

$$N = \frac{N_1' - 1}{N_2'} \tag{3.2.3.42}$$

$$M_L = \frac{M'}{M_2' + M_1' - 1} \tag{3.2.3.43}$$

and:

$$Q = \left(1 + \frac{N_2'}{2}\right)\left(\frac{N_1' + N_2'}{2N_2'}\right) \tag{3.2.3.44}$$

Replacing these results into the heat balance equations results in the following equations:

$$\frac{1}{3}\frac{d\bar{s}_1}{d\tau} + \frac{d\bar{s}_2}{d\tau} + \frac{d\bar{s}_3}{d\tau} = \frac{2}{\bar{s}_1} \tag{3.2.3.45}$$

$$\mu_2 M'\left(\frac{\bar{s}_2}{\bar{s}_1}\frac{d\bar{s}_1}{d\tau}\right) + \left[\mu_2(1 - M') + \frac{1}{3}\right]\frac{d\bar{s}_2}{d\tau} + \frac{d\bar{s}_3}{d\tau} = \frac{1}{\alpha_{12}\bar{s}_2}(1 - 6\mu_2) \tag{3.2.3.46}$$

$$\mu_3 N M_L M\frac{\bar{s}_3}{\bar{s}_1}\frac{d\bar{s}_1}{d\tau} - \mu_3 N(M_L M' - 1)\frac{\bar{s}_3}{\bar{s}_2}\frac{d\bar{s}_2}{d\tau} + \left[\mu_3(1 + \gamma_2) + \frac{1}{\alpha_{13}k_{13}St_2}\right]\frac{d\bar{s}_3}{d\tau} =$$

$$\frac{2}{\alpha_{13}k_{13}\bar{s}_2}\left[k_{12}(3\mu_2 - 1) - \frac{\chi_2}{2}\frac{q''}{q_0''}\bar{s}_2(\tau)\right] - \mu_3 Q\bar{s}_3\frac{1}{q''}\frac{d}{d\tau}q'' \tag{3.2.3.47}$$

(3.2.3.48)

Putting these equations into the form of an ordinary differential equation system gives three equations to be solved simultaneously:

$$\frac{d\bar{s}_1}{d\tau} = \frac{D_{11}'(C_{33}'B_{22}' - C_{22}'B_{33}') - B_{11}'(C_{33}'D_{22}' - C_{22}'D_{33}') + C_{11}'(B_{33}'D_{22}' - B_{22}'D_{33}')}{DetX} \quad (3.2.3.49)$$

$$\frac{d\bar{s}_2}{d\tau} = \frac{A_{11}'(C_{33}'D_{22}' - C_{22}'D_{33}') - D_{11}'(C_{33}'A_{22}' - C_{22}'A_{33}') + C_{11}'(D_{33}'A_{22}' - D_{22}'A_{33}')}{DetX} \quad (3.2.3.50)$$

$$\frac{d\bar{s}_1}{d\tau} = \frac{A_{11}'(D_{33}'B_{22}' - D_{22}'B_{33}') - B_{11}'(D_{33}'A_{22}' - D_{22}'A_{33}') + D_{11}'(B_{33}'A_{22}' - B_{22}'A_{33}')}{DetX} \quad (3.2.3.51)$$

where:

$$A_{11}' = \frac{1}{3} \quad (3.2.3.51.a)$$

$$B_{11}' = 1 \quad (3.2.3.51.b)$$

$$C_{11}' = 1 \quad (3.2.3.51.c)$$

$$D_{11}' = \frac{2}{\bar{s}_1(\tau)} \quad (3.2.3.51.d)$$

$$A_{22}' = \mu_2 M' \frac{\bar{s}_2(\tau)}{\bar{s}_1(\tau)} \quad (3.2.3.51.e)$$

$$B_{22}' = \mu_2(1 - M') + \frac{1}{3} \quad (3.2.3.51.f)$$

$$C_{22}' = 1 \quad (3.2.3.51.g)$$

$$D_{22}' = \frac{2}{\alpha_{12}\bar{s}_2(\tau)}(1 - 6\mu_2) \quad (3.2.3.51.h)$$

$$A_{33}' = \mu_3 N M_L M \frac{\bar{s}_3}{\bar{s}_1} \quad (3.2.3.51.i)$$

$$B_{33}' = -\mu_3 N(M_L M' - 1)\frac{\bar{s}_3}{\bar{s}_2} \quad (3.2.3.51.j)$$

$$C_{33}' = \mu_3(1 + \gamma_2) + \frac{1}{\alpha_{13}k_{13}St_2} \quad (3.2.3.51.k)$$

$$D_{33}' = \frac{2}{\alpha_{13} k_{13} \bar{s}_2}\left[k_{12}(3\mu_2 - 1) - \frac{\chi_2}{2}\frac{q''}{q_0''}\bar{s}_2(\tau)\right] - \mu_3 Q \bar{s}_3 \frac{1}{q''}\frac{d}{d\tau}q'' \qquad (3.2.3.51.l)$$

and:

$$DetX = A_{11}'(C_{33}'B_{22}' - C_{22}'B_{33}') - B_{11}'(C_{33}'A_{22}' - C_{22}'A_{33}') + C_{11}'(B_{33}'A_{22}' - B_{22}'A_{33}') \qquad (3.2.3.51.m)$$

The solutions of this system with the initial conditions 3.2.3.10.j, 3.2.3.10.k, and 3.2.3.10.l gives the front velocities and the depth with respect to time.

The surface temperature variation by time can be evaluated by setting $\bar{x} = 0$ in the equation 3.2.3.29:

$$T_s = T_w + \frac{1}{2}(T_c - T_w)\left[3\mu_3 - \chi_2 \frac{q''(\tau)}{q_0''}\frac{\bar{s}_3(\tau)}{k_{13}}\right] \qquad (3.2.3.52)$$

3.2.4. Ablation

The next phase to follow the gas release from the concrete is the ablation or total melting of the concrete. Applied heat flux on the surface causes increasing surface temperature. When this temperature is high enough, the refractory oxides start to decompose. Since concrete is a mixture of several compounds, and liquidus and solidus temperatures by which the melting point is calculated are different for different mixtures, the temperature at which melting starts varies. The range of these temperatures is from about 1500 K to 1900 K (for Basaltic Aggregate this range is between 1350 K and 1670 K while Limestone Aggregate-Command Sand has a range of 1420-1670 K). Although there is no way to define a precise temperature for ablation, because the ablated material may not be completely molten, the choice of a single temperature for ablation front has no effect on overall conservation of energy since the calculated decomposition enthalpies are appropriate for that temperature.

We will also assume that molten compounds will be transferred immediately from the surface by gas flow. This is very simplified yet a good representation of the actual MCCI phenomena, and the assumption has been consistent with present molten core/concrete interaction models.

To analyze this phase of the MCCI transient model, we will define a new region that exists hypothetically between the original molten core/concrete interface and the moving melting front. By this definition, the melting interface will have two boundary conditions which are: the heat flux and the melting temperature. The boundary conditions at the original interface would indeed vanish. This region is shown in Figure 9. Thus, the process is governed by three equations that

are the same as in gas free concrete but they are valid over the new distances as follows:

$$\frac{\partial^2}{\partial x^2}T_1(x,t) = \frac{1}{\alpha_1}\frac{\partial}{\partial t}T_1(x,t) \quad (3.2.4.1)$$

$$\frac{\partial^2}{\partial x^2}T_2(x,t) = \frac{1}{\alpha_2}\frac{\partial}{\partial t}T_2(x,t) \quad (3.2.4.2)$$

$$\frac{\partial^2}{\partial x^2}T_3(x,t) = \frac{1}{\alpha_3}\frac{\partial}{\partial t}T_3(x,t) \quad (3.2.4.3)$$

with the applied boundary and initial conditions:

$$T_3(s,t) = T_m \quad (3.2.4.3.a)$$

$$T_3(s+s_3,t) = T_c \quad (3.2.4.3.b)$$

$$T_2(s+s_3,t) = T_c \quad (3.2.4.3.c)$$

$$T_2(s+s_3+s_2,t) = T_w \quad (3.2.4.3.d)$$

$$T_1(s+s_3+s_2,t) = T_w \quad (3.2.4.3.e)$$

$$T_1(s+s_3+s_2+s_1,t) = T_i \quad (3.2.4.3.f)$$

$$\frac{\partial}{\partial x}T_1(s+s_3+s_2+s_1,t) = 0 \quad (3.2.4.3.g)$$

$$-k_3\frac{\partial}{\partial x}T_3(s,t) = -q''(t) + \rho L_3\frac{ds}{dt} \quad (3.2.4.3.h)$$

$$-k_3\frac{\partial}{\partial x}T_3(s+s_3,t) = -k_2\frac{\partial}{\partial x}T_2(s+s_3,t) + \rho L_2\frac{d}{dt}[s+s_3] \quad (3.2.4.3.i)$$

$$-k_2\frac{\partial}{\partial x}T_2(s+s_3+s_2,t) = -k_1\frac{\partial}{\partial x}T_1(s+s_3+s_2,t) + \rho L_1\frac{d}{dt}[s+s_3+s_2] \quad (3.2.4.3.j)$$

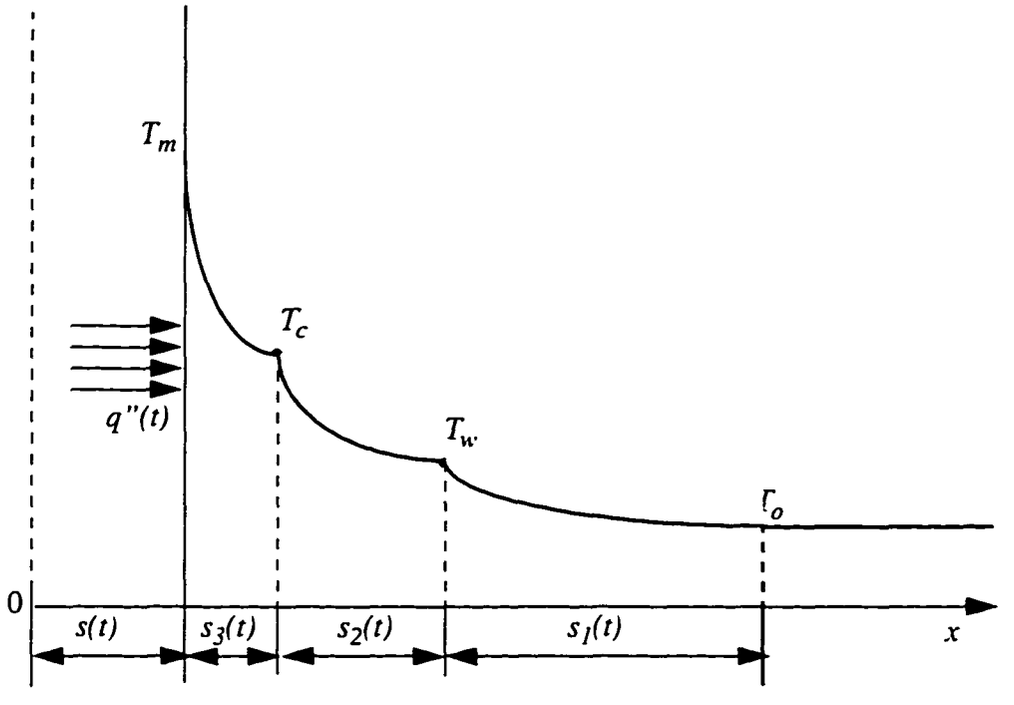

Figure 9: Thermal Layers for Ablation Phase.

$$s(t_m) = 0 \tag{3.2.4.3.k}$$

$$s_3(t_m) = \eta \tag{3.2.4.3.l}$$

$$s_2(t_m) = \delta_2 \tag{3.2.4.3.m}$$

$$s_1(t_m) = \varepsilon_3 \tag{3.2.4.3.n}$$

Again, Equation 3.2.4.3.h, 3.2.4.3.i, and 3.2.4.3.j are the Stefan's boundary conditions for water evaporation, gas decomposition, and melting interfaces and η, ε_3, and δ_2 are the gas-free, thermally affected, and dry concrete thicknesses when the erosion of the concrete begins.

Dimensionless parameters for this case are then:

$$\theta = \frac{T - T_m}{T_m - T_c} \tag{3.2.4.4}$$

$$\bar{x} = \frac{x}{l} \tag{3.2.4.5}$$

$$\bar{s} = \frac{s}{l} \tag{3.2.4.6}$$

and:

$$\tau = \frac{(t - t_m)\,\alpha_1}{l^2} \tag{3.2.4.7}$$

where l is again the same as it is defined in Equation 3.2.1.6.

Thus, the dimensionless governing equations are:

$$\frac{\partial^2}{\partial \bar{x}^2}\theta_1(\bar{x},\tau) = \frac{\partial}{\partial \tau}\theta_1(\bar{x},\tau) \tag{3.2.4.8}$$

$$\frac{\partial^2}{\partial \bar{x}^2}\theta_2(\bar{x},\tau) = \alpha_{12}\frac{\partial}{\partial \tau}\theta_2(\bar{x},\tau) \tag{3.2.4.9}$$

$$\frac{\partial^2}{\partial \bar{x}^2}\theta_3(\bar{x},\tau) = \alpha_{13}\frac{\partial}{\partial \tau}\theta_3(\bar{x},\tau) \tag{3.2.4.10}$$

The dimensionless boundary and initial conditions for these governing equations are:

$$\theta_3(\bar{s},\tau) = 0 \tag{3.2.4.10.a}$$

$$\theta_3(\bar{s}_3+\bar{s},\tau) = -1 \tag{3.2.4.10.b}$$

$$\theta_2(\bar{s}_3+\bar{s},\tau) = -1 \tag{3.2.4.10.c}$$

$$\theta_2(\bar{s}_2+\bar{s}_3+\bar{s},\tau) = \theta_w \tag{3.2.4.10.d}$$

$$\theta_1(\bar{s}_2+\bar{s}_3+\bar{s},\tau) = \theta_w \tag{3.2.4.10.e}$$

$$\theta_1(\bar{s}_1+\bar{s}_2+\bar{s}_3+\bar{s},\tau) = \theta_0 \tag{3.2.4.10.f}$$

$$\frac{\partial}{\partial \bar{x}}\theta_1(\bar{s}_1+\bar{s}_2+\bar{s}_3+\bar{s},\tau) = 0 \tag{3.2.4.10.g}$$

$$k_{13}\frac{\partial}{\partial \bar{x}}\theta_3(\bar{s},\tau) = \frac{q''}{q_0}\chi_3 + \frac{1}{St_3}\frac{d}{d\tau}\bar{s} \tag{3.2.4.10.h}$$

$$k_{13}\frac{\partial}{\partial \bar{x}}\theta_3(\bar{s}_3+\bar{s},\tau) = k_{12}\frac{\partial}{\partial \bar{x}}\theta_2(\bar{s}_3+\bar{s},\tau) - L_{23}\frac{1}{St_3}\frac{d}{d\tau}(\bar{s}_3+\bar{s}) \tag{3.2.4.10.i}$$

$$k_{12}\frac{\partial}{\partial \bar{x}}\theta_2(\bar{s}_2+\bar{s}_3+\bar{s},\tau) = \frac{\partial}{\partial \bar{x}}\theta_1(\bar{s}_2+\bar{s}_3+\bar{s},\tau) - L_{13}\frac{1}{St_3}\frac{d}{d\tau}(\bar{s}_2+\bar{s}_3+\bar{s}) \tag{3.2.4.10.j}$$

$$\bar{s}(0) = 0 \tag{3.2.4.10.k}$$

$$\bar{s}_3(0) = \eta \tag{3.2.4.10.l}$$

$$\bar{s}_2(0) = \delta_2 \tag{3.2.4.10.m}$$

$$\bar{s}_1(0) = \varepsilon_3 \tag{3.2.4.10.n}$$

where:

$$\chi_3 = -\frac{T_i}{T_m - T_c} \tag{3.2.4.11}$$

$$St_3 = \frac{c_1 (T_m - T_c)}{L_3} \tag{3.2.4.12}$$

$$L_{23} = \frac{L_2}{L_3} \tag{3.2.4.13}$$

Applying the integral method to the equations 3.2.4.8, 3.2.4.9, and 3.2.4.10 results as the heat balance equations for each region as follows:

For the temperature affected region:

$$\frac{\partial}{\partial \tau}\bar{\theta}_1 = -\frac{\partial \theta_1}{\partial \bar{x}}\bigg|_{\bar{x} = \bar{s}_2 + \bar{s}_3 + \bar{s}} + \theta_0 \frac{d\bar{s}_1}{d\tau} + (\theta_0 - \theta_w)\left[\frac{d}{d\tau}\bar{s} + \frac{d\bar{s}_3}{d\tau} + \frac{d\bar{s}_2}{d\tau}\right] \tag{3.2.4.14}$$

where:

$$\bar{\theta}_1 = \int_{\bar{x} = \bar{s}_2 + \bar{s}_3 + \bar{s}}^{\bar{x} = \bar{s}_1 + \bar{s}_2 + \bar{s}_3 + \bar{s}} \theta_1 d\bar{x} \tag{3.2.4.15}$$

For the dehydrated concrete region:

$$\frac{\partial \bar{\theta}_2}{\partial \bar{\tau}} = \frac{1}{\alpha_{12}}\left[\left.\frac{\partial \theta_2}{\partial \bar{x}}\right|_{\bar{x}=\bar{s}_2+\bar{s}_3+\bar{s}} - \left.\frac{\partial \theta_2}{\partial \bar{x}}\right|_{\bar{x}=\bar{s}_3+\bar{s}}\right] + \theta_w \frac{d\bar{s}_2}{d\bar{\tau}} + (1+\theta_w)\left(\frac{d\bar{s}_2}{d\bar{\tau}} + \frac{d\bar{s}_3}{d\bar{\tau}}\right) \quad (3.2.4.16)$$

where:

$$\bar{\theta}_2 = \int_{\bar{x}=\bar{s}_3+\bar{s}}^{\bar{x}=\bar{s}_2+\bar{s}_3+\bar{s}} \theta_2 d\bar{x} \quad (3.2.4.17)$$

For the CO_2 free concrete region:

$$\frac{\partial \bar{\theta}_2}{\partial \bar{\tau}} = \frac{1}{\alpha_{13}}\left[\left.\frac{\partial \theta_3}{\partial \bar{x}}\right|_{\bar{x}=\bar{s}_3+\bar{s}} - \left.\frac{\partial \theta_3}{\partial \bar{x}}\right|_{\bar{x}=\bar{s}}\right] - \left(\frac{d}{d\bar{\tau}}\bar{s} + \frac{d\bar{s}_3}{d\bar{\tau}}\right) \quad (3.2.4.18)$$

where

$$\bar{\theta}_3 = \int_{\bar{x}=\bar{s}}^{\bar{x}=\bar{s}_3+\bar{s}} \theta_3 d\bar{x} \quad (3.2.4.19)$$

Temperature profiles can be chosen for each region as:

$$\theta_1(\bar{x},\tau) = A_1 + B_1[\bar{x} - (\bar{s}_2+\bar{s}_3+\bar{s})] + C_1[\bar{x} - (\bar{s}_2+\bar{s}_3+\bar{s})]^2 \quad (3.2.4.20)$$

$$\theta_2(\bar{x},\tau) = A_2 + B_2[(\bar{s}_2+\bar{s}_3+\bar{s}) - \bar{x}] + C_2[(\bar{s}_2+\bar{s}_3+\bar{s}) - \bar{x}]^2 \quad (3.2.4.21)$$

and:

$$\theta_3(\bar{x},\tau) = A_3 + B_3[\bar{s}_3 + \bar{s} - \bar{x}] + C_3[\bar{s}_3 + \bar{s} - \bar{x}]^2 \qquad (3.2.4.22)$$

By the use of the boundary condition 3.2.4.10.e, 3.2.4.10.f, and 3.2.4.10.g, coefficients in the equation 3.2.4.20 can be found such that:

$$\theta_1(\bar{x},\tau) = \theta_w - 2(\theta_w - \theta_i)\left[\frac{\bar{x} - (\bar{s}_2 + \bar{s}_3 + \bar{s})}{\bar{s}_1}\right] + (\theta_w - \theta_i)\left[\frac{\bar{x} - (\bar{s}_2 + \bar{s}_3 + \bar{s})}{\bar{s}_1}\right]^2 \qquad (3.2.4.23)$$

By using the same method, the temperature distribution for the dry concrete region can be found as:

$$\theta_2(\bar{x},\tau) = \theta_w - \left[\frac{M_1'' - M_2''}{\alpha_{12}k_{12}St_3}\right]\left(\frac{(\bar{s}_2 + \bar{s}_3 + \bar{s}) - \bar{x}}{\bar{s}_2}\right) + \left[1 + \theta_w + \frac{M_1'' - M_2''}{\alpha_{12}k_{12}St_3}\right]\left(\frac{(\bar{s}_2 + \bar{s}_3 + \bar{s}) - \bar{x}}{\bar{s}_2}\right)^2 \qquad (3.2.4.24)$$

where:

$$M_1'' = L_{13} - (\theta_w - \theta_i)\,\alpha_{12}St_3\frac{\bar{s}_2}{\bar{s}_1} \qquad (3.2.4.25)$$

and:

$$M_2'' = \sqrt{M_1''^2 - 2\alpha_{12}k_{12}St_3L_{13}(1 + \theta_w)} \qquad (3.2.4.26)$$

The temperature distribution in the gas-free region can be determined as described in Section 3.2.3 as:

$$\theta_3(\bar{x},\tau) = -1-\left[\frac{N_1''-N_2''}{\alpha_{13}k_{13}St_3}\right]\left(\frac{\bar{s}_3+\bar{s}-\bar{x}}{\bar{s}_3}\right)+\left[\frac{N_1''-N_2''}{\alpha_{13}k_{13}St_2}+1\right]\left(\frac{\bar{s}_3+\bar{s}-\bar{x}}{\bar{s}_3}\right)^2 \quad (3.2.4.27)$$

where:

$$N_1'' = L_{13}-\alpha_{13}k_{12}St_3\frac{\bar{s}_3}{\bar{s}_2}\left[\frac{M_1''-M_2''}{2\alpha_{12}k_{12}St_3}-(1+\theta_w)\right] \quad (3.2.4.28)$$

and:

$$N_2'' = \sqrt{N_1''^2+2\alpha_{13}k_{13}St_3L_{23}} \quad (3.2.4.29)$$

After finding this temperature distribution, $\bar{\theta}_1$, $\bar{\theta}_2$, and $\bar{\theta}_3$ then can be evaluated by their definitions as following:

$$\bar{\theta}_1 = \frac{1}{3}\bar{s}_1(\tau)\,(\theta_w+2\theta_i) \quad (3.2.4.30)$$

$$\bar{\theta}_2 = \left[\frac{2}{3}(1+\theta_w)-1-\frac{M_1''-M_2''}{6\alpha_{12}k_{12}St_3}\right]\bar{s}_2(\tau) \quad (3.2.4.31)$$

and:

$$\bar{\theta}_3 = -\frac{2}{3}\left[\frac{N_1''-N_2''}{4\alpha_{13}k_{13}St_3}+1\right]\bar{s}_3(\tau) \quad (3.2.4.32)$$

Their derivatives then can be found as:

$$\frac{d\bar{\theta}_1}{d\tau} = \frac{1}{3}(\theta_w+2\theta_i)\frac{d\bar{s}_1}{d\tau} \quad (3.2.4.33)$$

$$\frac{d\bar{\theta}_2}{d\tau} = \left[\frac{2}{L}\mu_3\left(1+\frac{L_{13}}{2M_2''}\right)-1\right]\frac{d\bar{s}_2}{d\tau}+\mu_3 M_L\frac{\bar{s}_2}{\bar{s}_1}\frac{d\bar{s}_1}{d\tau} \tag{3.2.4.34}$$

where:

$$\mu_3 = \frac{M_1''-M_2''}{6\alpha_{12}k_{12}St_3} \tag{3.2.4.35}$$

$$M_L = \frac{M_1''-L_{13}}{M_2''} \tag{3.2.4.36}$$

$$L = \frac{L_{13}}{M_1''+M_2''-L_{13}} \tag{3.2.4.37}$$

and:

$$\frac{d\bar{\theta}_3}{d\tau} = \left(\mu_4(N_L-1)-\frac{2}{3}\right)\frac{d\bar{s}_3}{d\tau}-\left(\mu_4 N_L(LM_L-1)\frac{\bar{s}_3}{\bar{s}_2}\right)\frac{d\bar{s}_2}{d\tau}-\mu_4 N_L M_L L\frac{\bar{s}_3}{\bar{s}_1}\frac{d\bar{s}_1}{d\tau} \tag{3.2.4.38}$$

where:

$$\mu_4 = \frac{N_1''-N_2''}{6\alpha_{13}k_{13}St_3} \tag{3.2.4.39}$$

$$N_L = \frac{N_1''-L_{23}}{N_2''} \tag{3.2.4.40}$$

Replacing these results into the heat balance equations results in the following equations:

$$\frac{1}{3}\frac{d\bar{s}_1}{d\tau}+\frac{d\bar{s}_2}{d\tau}+\frac{d\bar{s}_3}{d\tau}+\frac{d}{d\tau}\bar{s} = \frac{2}{\bar{s}_1} \tag{3.2.4.41}$$

$$-\frac{1}{3}M_L\frac{L}{L+1}\left(\frac{\bar{s}_2 d\bar{s}_1}{\bar{s}_1 d\tau}\right)+\left[\frac{2}{3}\frac{1}{1+L}\left(1-M_L+\frac{1}{2}\frac{M_1''}{M_2''}\right)-1\right]\frac{d\bar{s}_2}{d\tau}-\frac{d\bar{s}_3}{d\tau}-\frac{d}{d\tau}\bar{s}=\frac{2}{\alpha_{12}\bar{s}_2}\left(\frac{L-1}{L+1}\right) \tag{3.2.4.42}$$

$$-\mu_4 N_L M_L L\frac{\bar{s}_3 d\bar{s}_1}{\bar{s}_1 d\tau}-\mu_4 N_L (M_L L-1)\frac{\bar{s}_3 d\bar{s}_2}{\bar{s}_2 d\tau}+\left[\mu_4 (N_L-1)+\frac{1}{3}\right]\frac{d\bar{s}_3}{d\tau}+\frac{d}{d\tau}\bar{s}=$$

$$\frac{2}{\alpha_{13}\bar{s}_3}(1+6\mu_4) \tag{3.2.4.43}$$

In order to build a differential equation system for four regions, these last three equations must be combined with the equation 3.2.4.10.h that also can be written as:

$$\frac{d}{d\tau}\bar{s}=-\frac{2k_{13}St_3}{\bar{s}_3}(1+3\mu_4)-\chi_3\frac{q''}{q_0}St_3 \tag{3.2.4.44}$$

Equations 3.2.4.41 through 3.2.4.44 can be written in a form that is the same as in Equations 3.2.3.49 through 3.2.3.51 with the new coefficients as following:

$$A_{11}' = \frac{1}{3} \tag{3.2.4.44.a}$$

$$B_{11}' = 1 \tag{3.2.4.44.b}$$

$$C_{11}' = 1 \tag{3.2.4.44.c}$$

$$D_{11}' = \frac{2}{\bar{s}_1}+\frac{2k_{13}St_3}{\bar{s}_3}(1+3\mu_4)+\chi_3\frac{q''}{q_0}St_3 \tag{3.2.4.44.d}$$

$$A_{22}' = \frac{1}{3}M_L\frac{L}{L+1}\frac{\bar{s}_2}{\bar{s}_1} \tag{3.2.4.44.e}$$

$$B_{22}' = \frac{1}{3}\frac{1}{1+L}\left(\frac{M_1''}{M_2''} - M_L - (1+L)\right) \qquad (3.2.4.44.f)$$

$$C_{22}' = -1 \qquad (3.2.4.44.g)$$

$$D_{22}' = \frac{2}{\alpha_{12}\bar{s}_2}\left(\frac{L-1}{L+1}\right) - \frac{2k_{13}St_3}{\bar{s}_3}(1+3\mu_4) - \chi_3\frac{q''}{q_0}St_3 \qquad (3.2.4.44.h)$$

$$A_{33}' = \mu_4 N_L M_L L\frac{\bar{s}_3}{\bar{s}_1} \qquad (3.2.4.44.i)$$

$$B_{33}' = -\mu_4 N_L (M_L L - 1)\frac{\bar{s}_3}{\bar{s}_2} \qquad (3.2.4.44.j)$$

$$C_{33}' = \mu_4 (N_L - 1) + \frac{1}{3} \qquad (3.2.4.44.k)$$

$$D_{33}' = -\frac{2}{\alpha_{13}\bar{s}_3}(1+6\mu_4) - \frac{2k_{13}St_3}{\bar{s}_3}(1+3\mu_4) - \chi_3\frac{q''}{q_0}St_3 \qquad (3.2.4.44.l)$$

The solutions of this system with the initial conditions 3.2.4.10.k, 3.2.4.10.l, 3.2.4.10.m, and 3.2.4.10.n, give the front velocities and the depth as functions of time.

CHAPTER 4

RESULTS AND DISCUSSION

4.1. Introduction

During the molten core/concrete interaction, the driving force for the ablation rate and depth, and CO, H_2 and H_2O release is the rate at which heat is transferred to the concrete. The heat flux to the concrete depends on how fast the debris is cooled and how fast the heat is transported into the concrete. The phenomena that have the influence on the progression of a core/concrete interaction are (but not limited to): heat transfer to the concrete and to the containment atmosphere from the debris, heat conduction in the concrete, gas release from the concrete and corresponding changes in concrete thermal properties, reduction of those gases as they pass through the debris, transport of molten concrete/released gas mixture, crust formation as the debris cools down, fission product redistribution within the debris, decay heat source term, and aerosol production. A correct thermal modelling of a MCCI requires an a priori knowledge of the magnitude of the energy source from the debris, and thermal conduction properties of the concrete.

Besides the surface heat flux, the other data that is required to be known to evaluate the progress of the melting depth and rate, and gas production, and fur-

thermore the thermal integrity of the concrete containment basemat is the heat conduction within the concrete itself. The heat conduction is greatly influenced by the thermal properties of the concrete, and the chemical decomposition of its constituents. The magnitude of the influence depends on the type, preparation, and manufacturing of the concrete. Since the concrete is a heterogenous mixture, in most cases it is very difficult to know and generalize its properties.

In this section, first, the concrete properties are examined to be used for the evaluation of the effects of the heat flux and thermal properties. Then, the heat flux into the concrete is modelled as a surface heat flux that would simulate any combination of the phenomena listed above. The dimensionless solution given in the previous chapter, enables the application of the general solution to the different magnitudes and cooling down characteristic of the heat flux into the concrete.

As a result of previous experiments, it is more likely that the heat flux time variation into the concrete can be lumped into two basic forms: $e^{-\lambda t}$, and $t^{-\lambda}$. Therefore, the effects of the surface heat fluxes in these forms (for different λs) are evaluated together with the constant heat flux case that serves to illustrate the verification of the model by comparison to the previous models and experiments performed with constant heat source. An example that can be extended beyond the MCCI. a linearly decreasing heat flux case, is also modelled. This case is more applicable to the melting of binary alloys which would be a topic of a different kind than the MCCI.

Finally, the effects of the concrete thermal properties and the effects of chemical decomposition reactions are evaluated to provide a normalized solution for different concrete types.

4.2. Concrete Properties:

The first fact about concrete is that it is a heterogenous mixture of very different compounds. The composition is mostly known but mixing and curing processes result in complex and sometimes unpredictable structures. Therefore, the properties are mostly evaluated empirically and then generalized. In this study, the general properties of concrete are examined and applied to represent the most common concrete types in nuclear power plant constructions, as well as the experiments performed to evaluate concrete response to high heat fluxes and molten debris.

Two major types of concrete mostly used in nuclear power plant containment building basemat are basaltic and limestone. These concretes were also evaluated in the other models and experiments that this study is compared with.

General behaviors of concrete have been studied for many purposes from civil engineering to thermal sciences [14, 31-40]. Thermal behavior of concrete at high temperatures, which we are interested in, has been investigated since the beginning of this century mainly for the purpose of fire protection of concrete structures. Later studies on the properties of concrete at elevated temperatures included also the heat flow into concrete constructions in nuclear power stations where the temperatures would be well above the temperatures in a building fire. The first publication of these investigations was the Boulder Canyon Report [31]. This report presented the existence of large scale variation in thermal properties of concrete with respect to temperature. Harmathy [33] published a theoretical approach to thermal properties of concrete at high temperatures and derived relationships between the composition of concrete and thermal properties. Bažant [14]

reviewed all literature on the concrete at elevated temperatures from physical and chemical changes to mechanical and thermal properties.

The thermal properties that are considered to be significant are density, heat capacity and thermal conductivity. Temperature effect on these properties must be included in the model since the basic idea of separating concrete into regions was based on the decomposition temperatures. The assumption was made so that the temperature fronts divide the regions, and thermal properties are constant in each region but differ from one region to another.

Among these properties, the density can be calculated by the composition data and experimental results of temperature effect on the concrete composition. Studies show that density of concrete does not vary significantly with temperature. Harmathy [31] shows that bulk density decreases from about 1420 kg/m^3 at 30°C to about 1280 kg/m^3 at 800°C and then increases to about 1360 kg/m^3 at 1000°C for a cement paste with a water/cement ratio of 0.50. Other studies [32-40] also show that the density shows small or no variation with temperature and for limestone and basaltic concretes it can be assumed constant at approximately 2400-2500 kg/m^3 for both types of concrete in the range of temperature considered during a molten core/concrete interaction.

The specific heat of concrete is complicated and difficult to calculate since it is not only related to the composition, but also to chemical energies and structural changes of ingredients. Harmathy's calculations showed that the specific heat changes between 0.2 cal/grK and 0.4 cal/grK but it also included a peak of 1.0 cal/grK around 500°C for apparent heat capacity [31]. Bazant's [14] study suggests that the heat capacity is almost constant in 0-1300 K temperature range and its

value can be chosen between 840 and 1260 J/kgK. Petzold and Röhrs [32] investigated the heat capacity for various concrete types and agreed on a general value of 1260 J/kgK at 1400°C. Corradini [13] used 1230 J/kgK value for limestone and 1520 J/kgK for basaltic concrete in his one-region transient model.

Among the thermal properties of concrete, thermal conductivity is the one which most depends on the temperature. Although it is more complex than other properties, with the known thermal conductivities of each constituents and the volume of the pores it can be calculated as a certain combination of these thermal conductivities. There has been many research on thermal conductivity of concrete and its aggregates. While in some types of concrete change in thermal conductivity is not very significant, it can be very large in magnitude for the most commonly used concretes. Especially in case of high temperature gradients, convective heat flux due to the migration of moisture can become very significant which results in a large temperature effect on thermal conductivity. A good approximation for thermal conductivity of concrete is a linear decrease with increasing temperature. The slope shows large variation for different types of concrete. This linear relationship is also assumed in this model together with the assumption of constant thermal conductivities in each region. This, as was discussed before, would not cause a significant error in the calculations since the solution technique is valid for each region on the average.

The thermal diffusivity depends on temperature in the same manner as the thermal conductivity since it is derived from density and heat capacity, which are assumed to be constant, and the thermal conductivity. Figure 10 illustrates this variation of thermal diffusivity as well as it gives an idea about temperature dependence of the thermal conductivity.

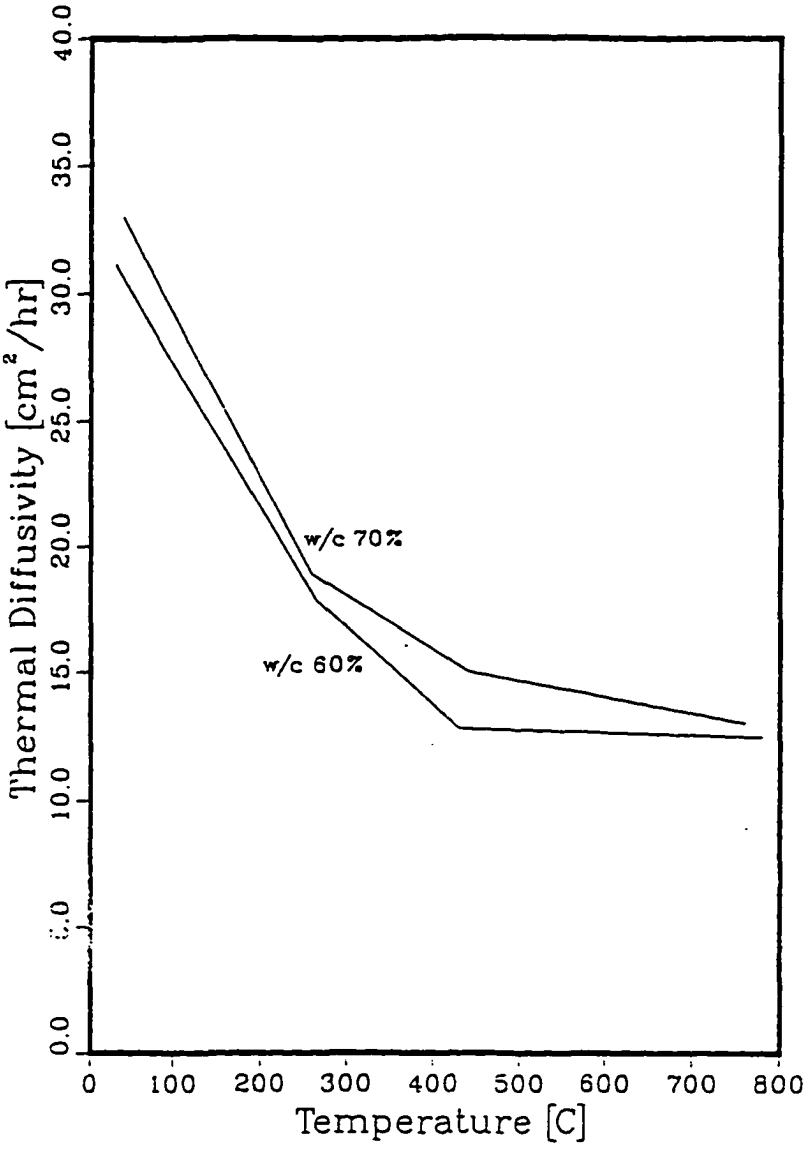

Figure 10: Thermal Diffusivity of Concrete [35].

For the decomposition enthalpies and temperatures, chemical changes in aggregates must be taken into account. Since concrete is an heterogenous mixture of many aggregates and reactions to bring these constituents are very different, calculating the chemical energies are very complex. On the other hand, classifying all these reactions into basic decomposition reactions simplifies the calculations. The main reaction is the dehydration of water content in the concrete. This also can be divided into two steps which are the dehydration of evaporable water and then chemical water where the latter one can be considered as a chemical decomposition reaction rather than simple water evaporation. As it was mentioned earlier, these reactions together with the CO_2 decomposition and decomposition of refractory oxides are basic reactions observed during the decomposition process of concrete. The experimental data provides us energies involved with those reactions. Figure 11 illustrates these reactions, their enthalpies of decomposition and temperatures for limestone concrete. Although these reactions occur in some temperature ranges, they can be simplified as if they occurred at a single temperature. Calculated enthalpies that are appropriate to those temperatures give us the amounts of heat loss in those reactions. Therefore, the choice of the temperature as long as they are in the range of reaction, does not affect the overall energy balance.

Summary of the thermal properties that are used in this study is given in Table 2.

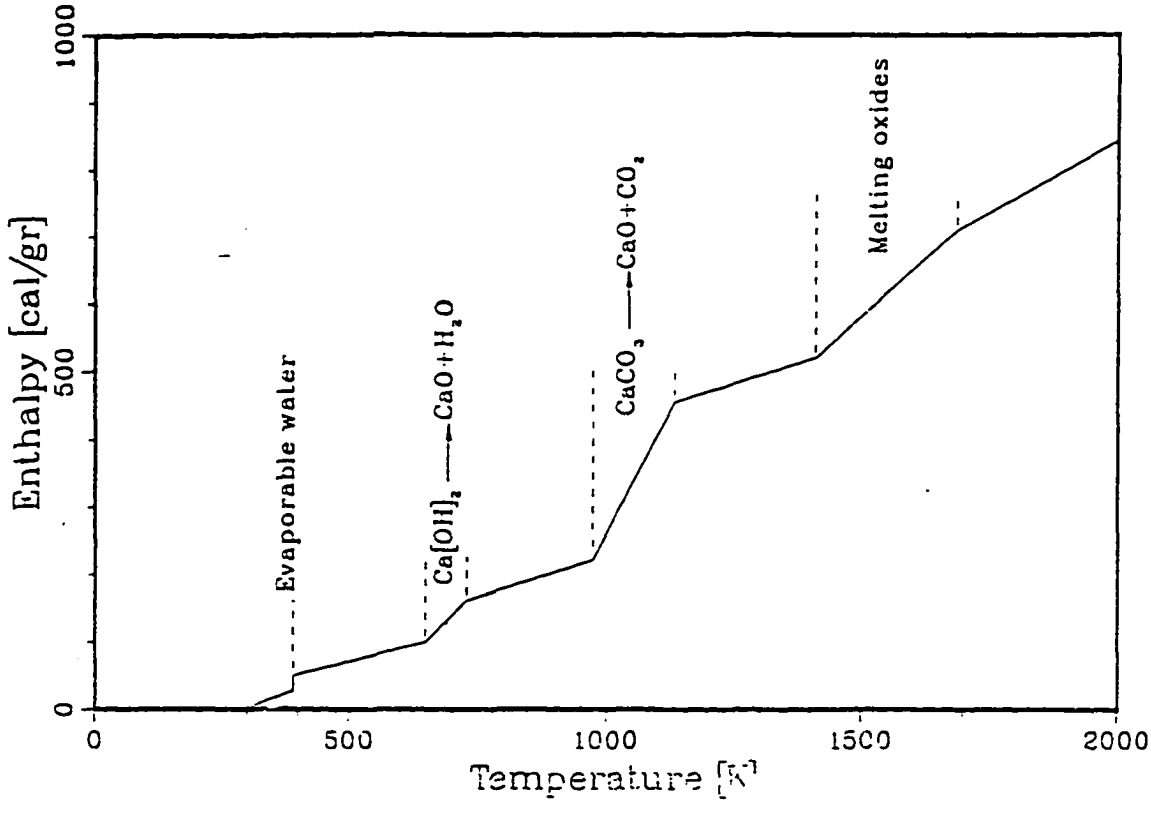

Figure 11: Decomposition Enthalpies of Concrete[47]

Table 2: Limestone Concrete Properties Used in the General Solution.

Parameter	Value
Density (kg/m^3)	2500
Specific Heat (kJ/kgK)	1.23
Initial Thermal Conductivity of Concrete (W/mK)	1.5
Thermal Conductivity of Dry Concrete (W/mK)	1.1
Thermal Conductivity of Decarboxylated Concrete (W/mK)	0.8
Decomposition Enthalpy of Dehydration (MJ/kg)	0.2578
Decomposition Enthalpy of Decarboxylation (MJ/kg)	0.9906
Decomposition Enthalpy of Oxide Decomposition (melting) (MJ/kg)	0.2835
Decomposition Temperature of Water (K)	690
Decomposition Temperature of Carbon dioxide (K)	1060
Decomposition Temperature of Oxides (K)	1670

4.3. Results for Different Forms of Surface Heat Flux

4.3.1. Constant Surface Heat Flux

The concrete ablation when it is subjected to a constant surface heat flux has been the basic and common topic for many MCCI models and experiments. The assumption of constant heat flux in the mathematical analyses simplifies the model but in most cases is good enough to illustrate the physical phenomena. It is also useful to examine the effects of the physical properties that are important. The same reasons are also applicable to the experimental work that is performed to obtain qualitative information on the important phenomena during the interaction. These experiments use more prototypical materials that are mostly internally heated and sustained through induction or joule heating.

In a previous study [47], a similar model was used to evaluate the concrete ablation when it is subject to a constant surface heat flux. From the general solution that was obtained in the previous chapter, the terms involving the derivative of the surface heat flux cancels out, reducing the differential equations to the ones that are derived in the Reference 47. The results are obtained in the similar fashion. Figures 12 and 13 present the results for the concrete ablation and ablation rate, respectively. They also illustrate the growth and the growth rate of heated, dry, and gas-free concrete regions. Table 3 shows the dimensionless results for sequence of events and important values that can be used to calculate the ablation and decomposition rates and region depths to be used in gas, water, and aerosol release and concrete erosion rates and depths for any surface heat flux and initial concrete thermophysical properties.

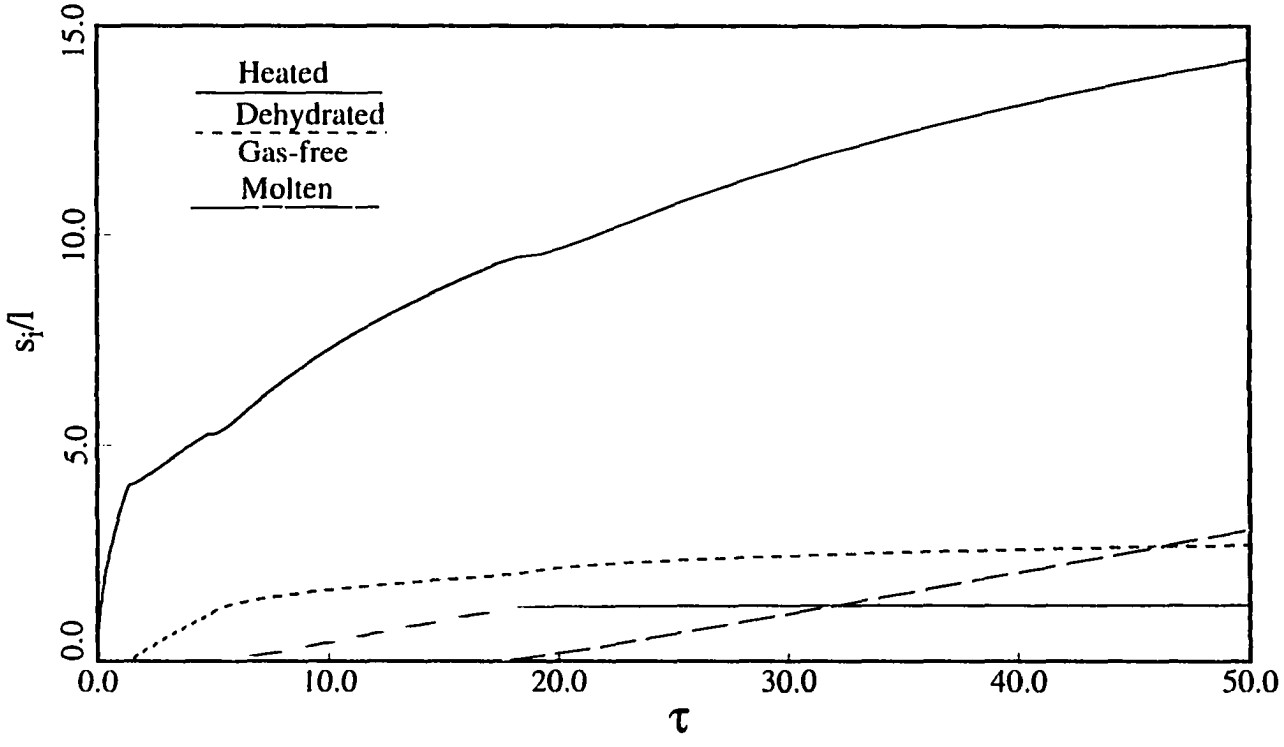

Figure 12: Penetration depth and growth of the regions for constant surface heat flux.

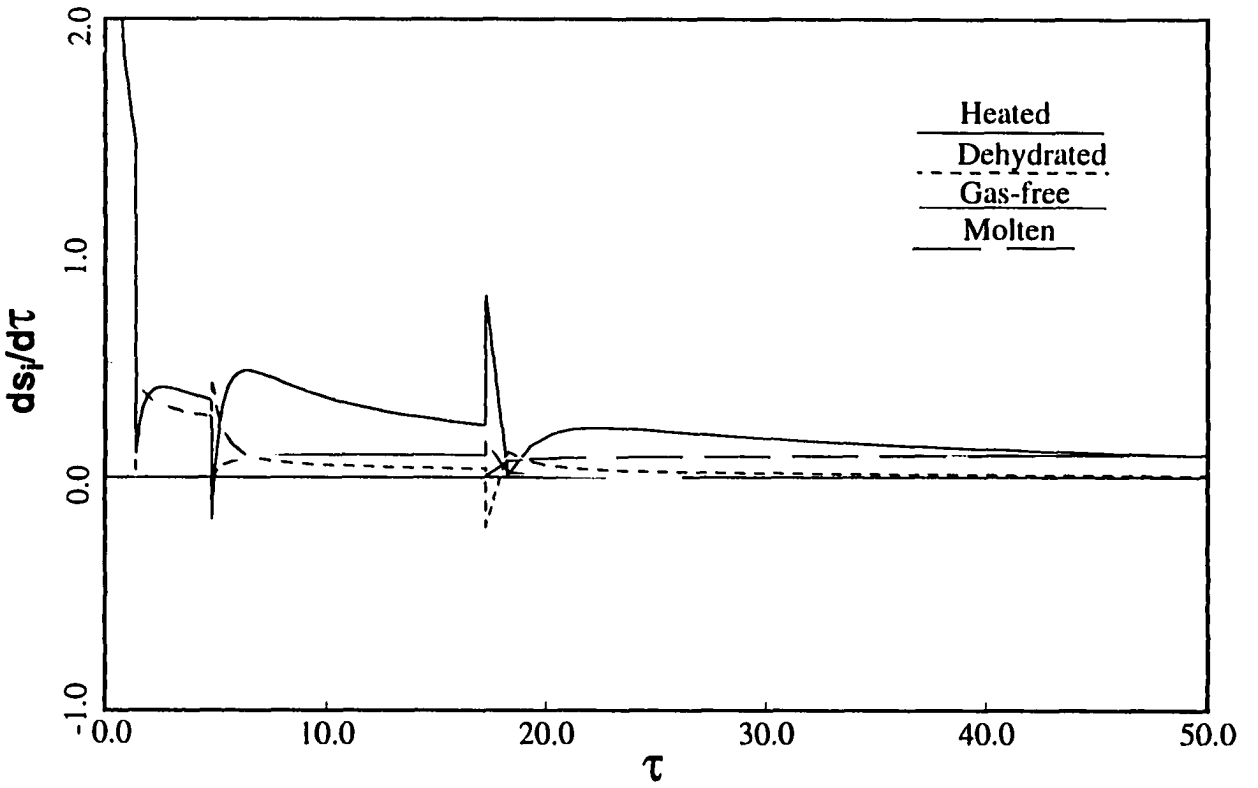

Figure 13: Ablation velocity and the growth rates of the regions for constant surface heat flux.

Table 3: Summary of the Steady State Calculations (Limestone concrete)

Event	Result
Beginning of Dehydration	Fo=1.38
Beginning of CO_2 Release	Fo=4.82
Beginning of Melting	Fo=17.24
Steady State Ablation Rate	0.10
Melting Front Reaches SS Ablation Rate	Fo=148.8
Thermal Front Reaches SS Thickness	Fo=349.5
CO_2 Free Region Reaches SS Thickness	Fo=47.4
Dehydrated Region Reaches SS Thickness	Fo=177.9
SS Thickness of Thermally Affected Region	13.26
SS Thickness of Dry Region	2.08
SS Thickness of CO_2 Free Region	1.95

The main results that can be obtained from the constant surface heat flux case is that the heated, dry and gas-free concrete regions reach a steady state thickness while the ablation continues at a constant rate that is proportional to the magnitude of the heat flux and initial thermal conductivity of the concrete. This is important to evaluate the gas and aerosol release rates from the MCCI. The rate of gas and aerosol production reach a steady state value while the eroded concrete region continues to grow.

The transient modelling of the concrete decomposition, and affected regions shows that the steady state models of the MCCI overestimate the erosion rate and underestimate the in-depth concrete decomposition rate especially when the heat flux is low and the decomposition rate is slow. This model provides the growth rate of each region and ablation rate for fast decomposition and/or low heat fluxes. Figures 14 and 15 compare the results of the model with the CORCON model [46] which is based on the steady state erosion assumption. The overestimation of the rate and depth by the steady state approach may result in thirty times more concrete volume eroding while the gas and water release virtually stay the same. This is especially true in an actual MCCI when the low heat fluxes are more representative of the actual case when the debris cools down and the crust formation occurs over a longer period of time.

Another result of the constant surface heat flux with a multi-region, transient modelling of the decomposed concrete region is that the erosion rate reaches its steady state velocity, while the thermal front still continues to move faster than that velocity. Therefore, the one-region models which evaluate the ablation rate by the velocity of the thermal front do not include this delay, and overestimate the ablation rate. This delay is due to the effects of different thermal diffusivities in

different regions, and the depth of those regions coupled with the location and magnitude of the endothermic decomposition reactions taking place in the concrete. Since this model also calculates the effect of the sensible heat stored in the concrete beyond the ablation front, the prediction for the ablation distance was closer to the steady state amount that is calculated in the one region model.

The model also enables us to obtain the other information that is useful to calculate the gas, water, and aerosol release rates and amounts, such as the temperature affected, dehydrated and decarboxylated region growth and growth rates, and the time that those reactions are observed for different magnitudes of the surface heat flux. These are derived from the results given in Table 3 and are listed in Table 4.

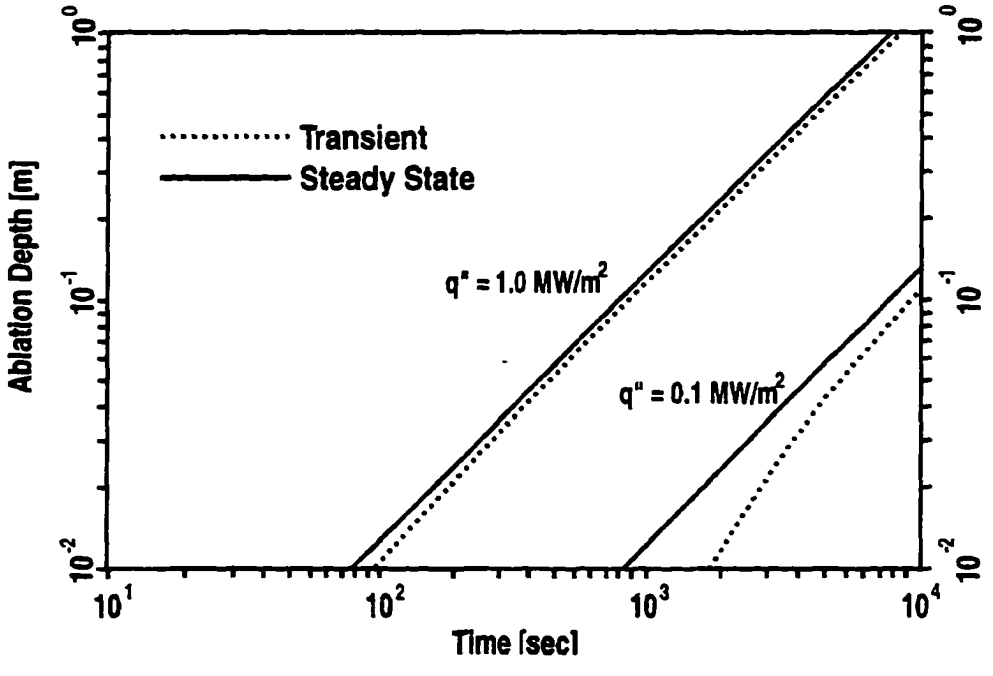

Figure 14: Comparison of Penetration Depth with Steady State Model.

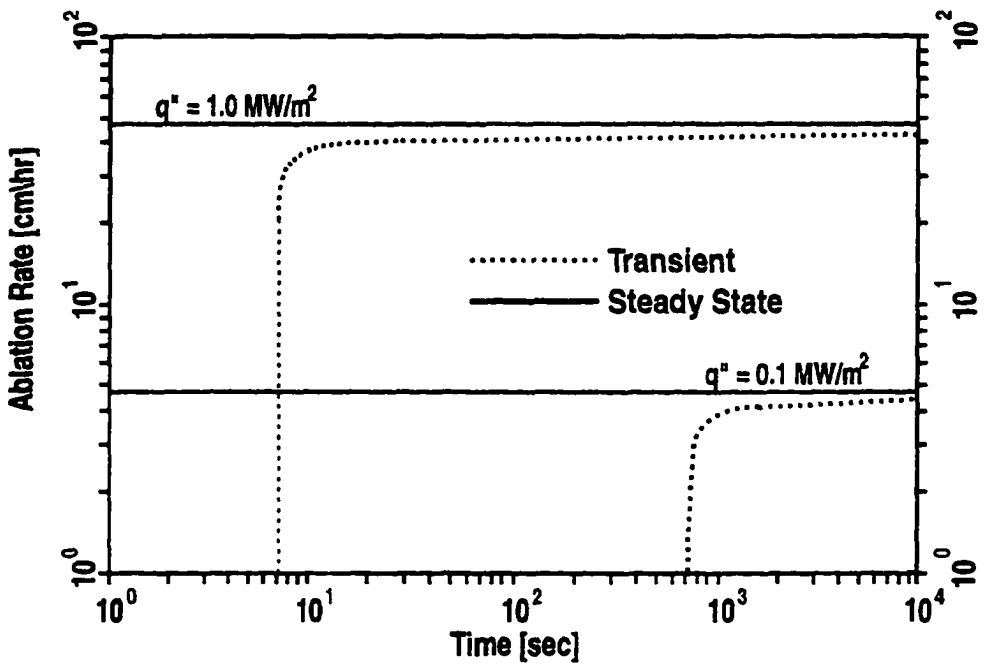

Figure 15: Comparison of Penetration Rate with Steady State Model.

Table 4: Results for Different Magnitudes of Surface Heat Flux

Event	q"=0.03 MW/m^2	q"=3.00 MW/m^2
Beginning of Dehydration (sec)	5448.8	0.545
Beginning of CO_2 Release (sec)	19268.2	1.927
Beginning of Melting (sec)	57172.8	5.717
Steady State Ablation Rate (cm/hr)	0.537	53.7

4.3.2. Time Dependent Surface Heat Flux

In an actual MCCI interaction, the surface heat flux that the concrete is subject to is not constant. This is mainly due to the decreasing decay heat in the molten debris, the cooling of the debris by heat transfer to the concrete and to the containment atmosphere, and crust formation within the debris. The heat flux to the concrete decreases in time which will result in the termination of concrete erosion process naturally. The time required for the termination of concrete ablation is important in order to ensure against a "Chine Syndrome" type of accident.

In this model, it is possible to evaluate the concrete erosion depth and rate together with the dehydrated and decarboxylated concrete regions growth and growth rate when the heat fluxes are low enough where the concrete erosion eventually comes to a halt. For this, the time dependent heat flux boundary conditions can be used in general solutions given in Chapter 3.

The form of surface heat flux decrease can be extracted from the previous experiments which used simulant materials and were aimed at developing models for isolated aspects of the interaction (e. g. convective heat transfer in a bubbling pool, or water/steam reactions). Those are the transient tests in which molten material was teemed into concrete crucibles. Most used melts composed of steel or thermite, while others used molten UO_2. The general characteristics of these experiments showed that the heat flux to the concrete decreases in time, and can be simulated in a form of exponential decay. Therefore, in the following two sections, the results for two different forms of surface heat flux will be presented: in form of $e^{-\lambda t}$ and $t^{-\lambda}$.

Although the rate of cooling (or decrease in the surface temperature) in and actual MCCI case would be represented by a surface heat flux in the form of the ones given above, the linearly decreasing surface heat flux case is presented here for the informational purposes. This type of surface heat flux is more applicable to the melting/solidification of the binary alloys and melting/freezing problems involving water and other liquids.

4.3.2.1. Surface Heat Flux in Forms of $e^{-\lambda t}$

When the terms that include the heat flux and its derivatives are substituted in the general solution, the differential equations still can be solved using the same method used in the constant heat flux. Although the solution method remains the same, the time steps used in the numerical solution must be evaluated carefully in order to prevent unstable solutions.

The results are obtained for different decay constants (again keeping the parameters dimensionless) to establish a normalized solutions that can be applicable to the different initial surface heat flux and thermophysical parameters of the concrete. These results for the ablation depths and rates for different debris cooling rate are presented in Figures 18 and 19. Figures 20 through 37 present the progress of each region and their growth rate before and after the erosion begins for different decay rates, and Figures 38 through 40 show the progress of the surface temperature before melting begins.

As can be seen, the effect of the decay rate is insignificant during the thermal penetration and the dehydration, and negligible during the CO_2 release phase. This is due to the short period of time in which they occur, and during that period

of time, the effect of the decrease in the surface heat flux is not visible. The agreement between the constant heat flux and the time dependent heat flux results are visible in that period of time.

After the erosion of concrete begins, and time progresses to show the effects of the decreasing heat flux, two main results are observed:

1. The ablation front velocity reaches a peak and then starts decreasing to zero, where the ablation stops, due to the decreasing surface heat flux. As expected, the time required to terminate the erosion depends on how fast the surface heat flux decreases. Table 5 lists the time when the erosion stops and erosion thicknesses for different decay rates. The maximum eroded concrete thickness and time when the erosion terminates are found to be logarithmically proportional to the decay constant. Figures 16 and 17 show the relationship between the decay rate (cooldown rate of the debris) and the maximum eroded concrete depth and time. The initial peak in the erosion rate is due to the balance between the surface heat flux and the endothermic ablation reaction. When the latent heat of ablation overcomes the surface heat flux, the ablation rate starts decreasing. For faster decay in the surface heat flux, the peak rate is lower and earlier. The magnitude of the peak is not significant in terms of the long term rate since the time it occurs is too early in the event.

2. Although the erosion front depth reaches a finite value due to the heat supply being continued but not enough to sustain melting, this heat is transferred to in-depth concrete, continuously increasing the thermally affected, dehydrated, and decarboxylated regions.

These two results of decreasing surface heat flux are totally opposite of what resulted in constant heat flux, where the erosion front eventually grows with a constant growth rate, and the other regions remain at constant thicknesses. The models that calculate the erosion rate based on the thermal front velocity would greatly overestimate the eroded volume of the concrete, since the thermal front and the other regions grow even after the erosion stops. Also, the models that assume that there is no gas, water, and aerosol release after the erosion stops underestimate the amount of those species released from the concrete since their production still continues even at a higher rate after the erosion stops.

Table 5: Summary of Results for Surface Heat Flux in Forms of $e^{-\lambda t}$

Event	λ=0.03	λ=0.05	λ=0.1	λ=0.3	λ=0.5
Beginning of Evaporation (Fo)	1.377	1.377	1.378	1.380	1.383
Thermal Region Thickness When Evaporation Begins	4.065	4.066	4.067	4.071	4.076
Beginning of CO2 Release (Fo)	4.810	4.811	4.816	4.833	4.851
Thermal Region Thickness When Decarboxylation Begins	5.275	5.276	5.279	5.292	5.305
Dry Region Thickness When Decarboxylation Begins	1.083	1.083	1.083	1.084	1.086
Beginning of Melting (Fo)	17.27	17.29	17.35	17.59	17.84
Thermal Region Thickness When Melting Begins	9.299	9.305	9.322	9.390	9.461
Dry Region Thickness When Melting Begins	1.989	1.991	1.995	2.013	2.034
CO2 Free Region Thickness When Melting Begins	1.183	1.184	1.185	1.188	1.198
End of Concrete Erosion (Fo)	29628	16481	7361	1989	1064
Eroded Concrete Thickness	821.08	480.55	229.14	67.01	36.30

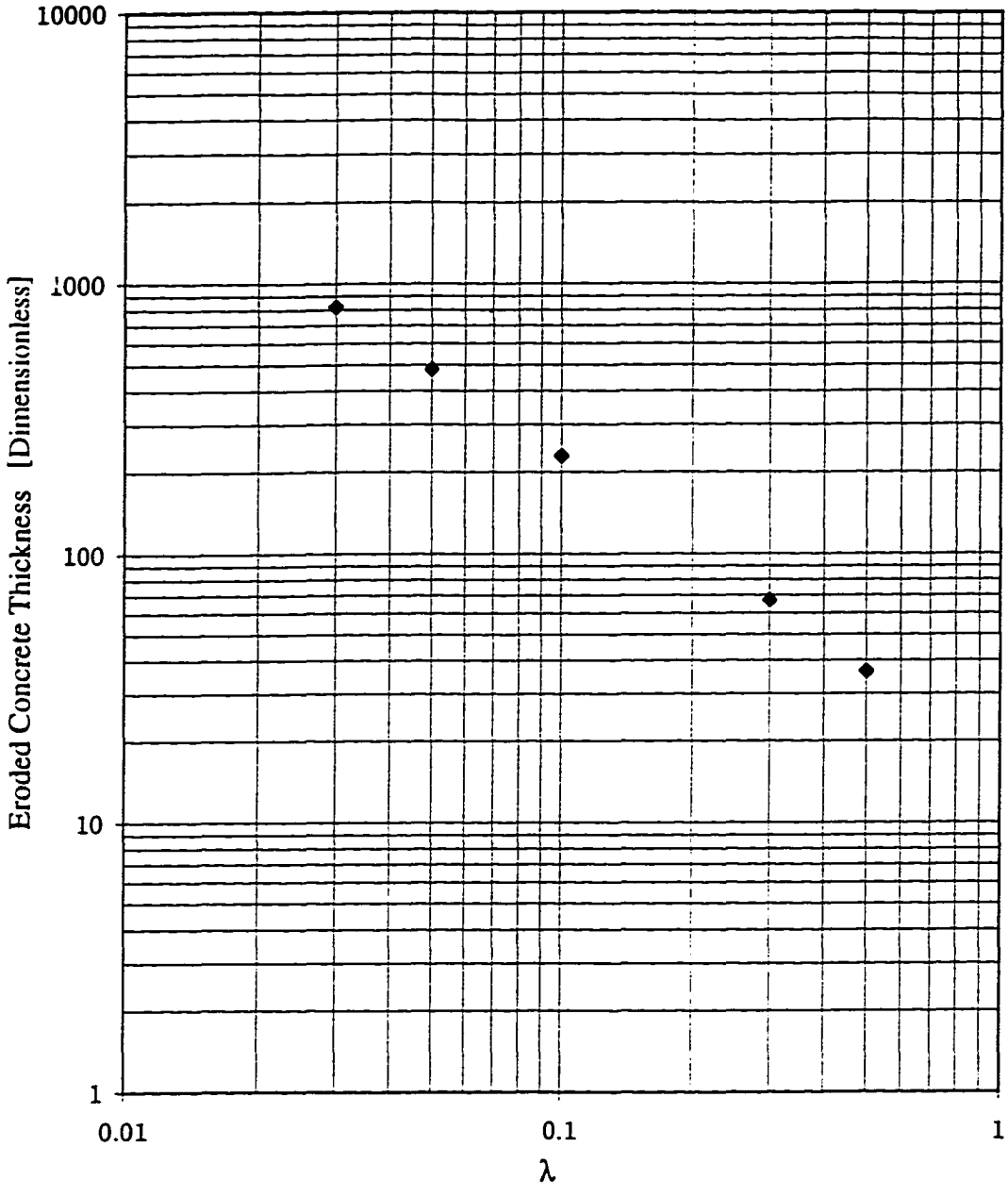

Figure 16: Relationship between the cooldown rate and maximum eroded depth

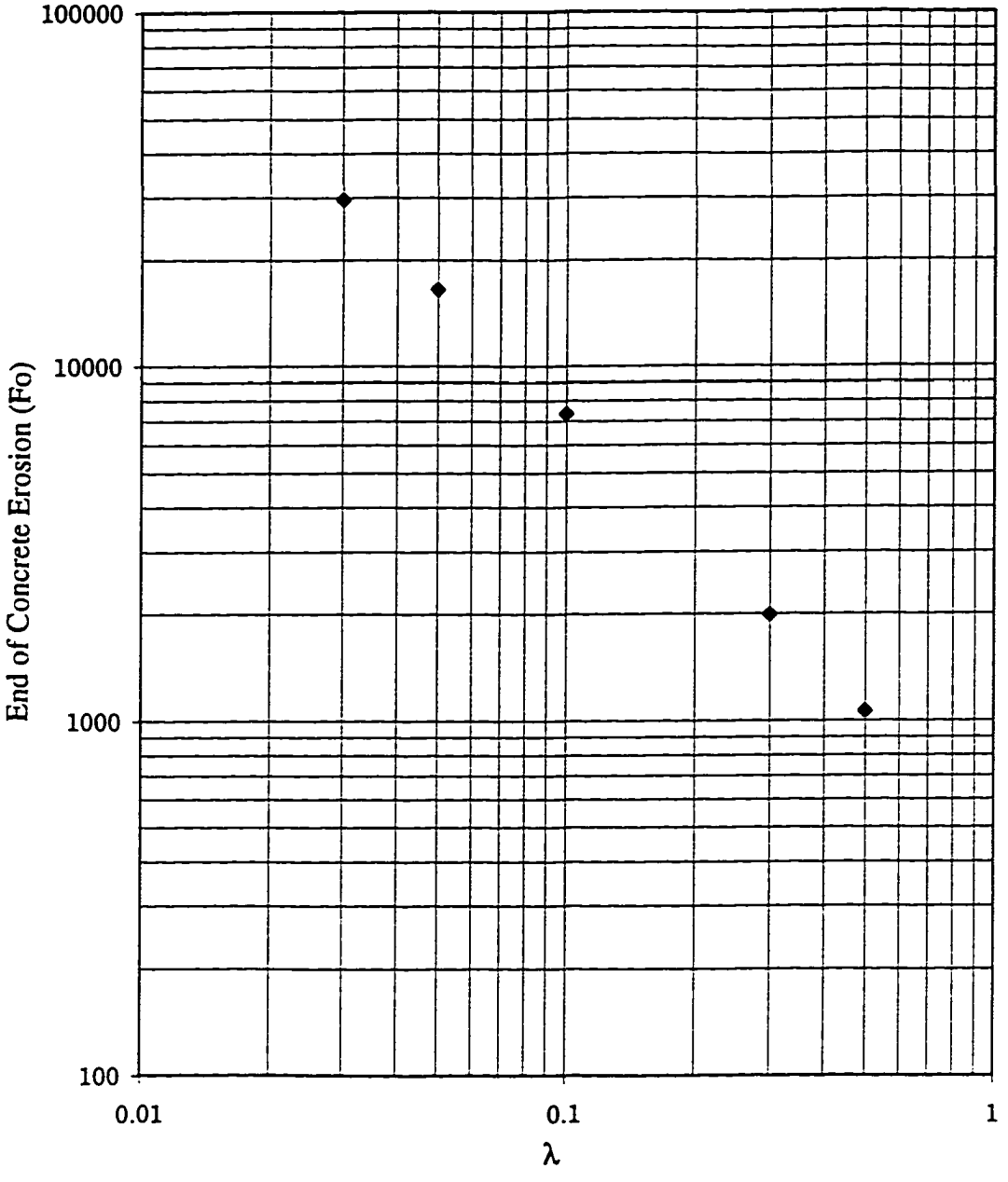

Figure 17: Relationship between the cooldown rate and time to terminate erosion

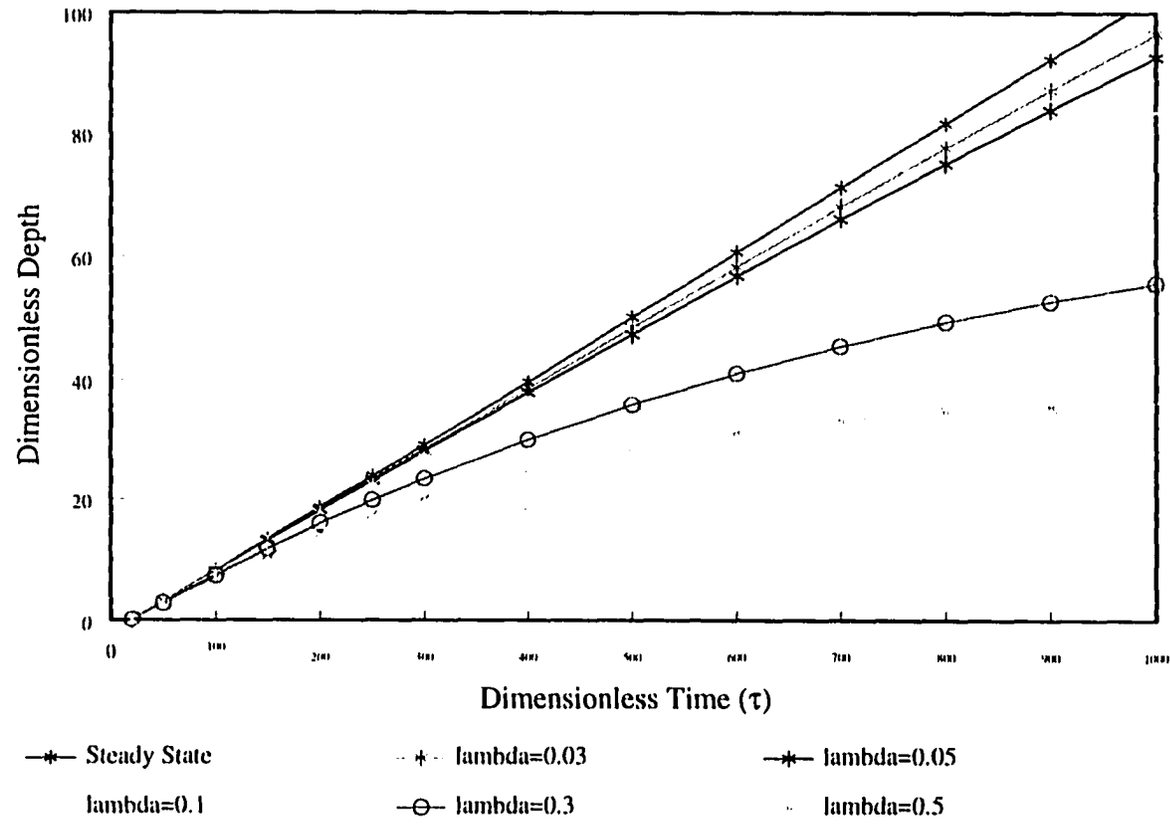

Figure 18: Erosion Growth for $q=q_0e^{-\lambda\tau}$

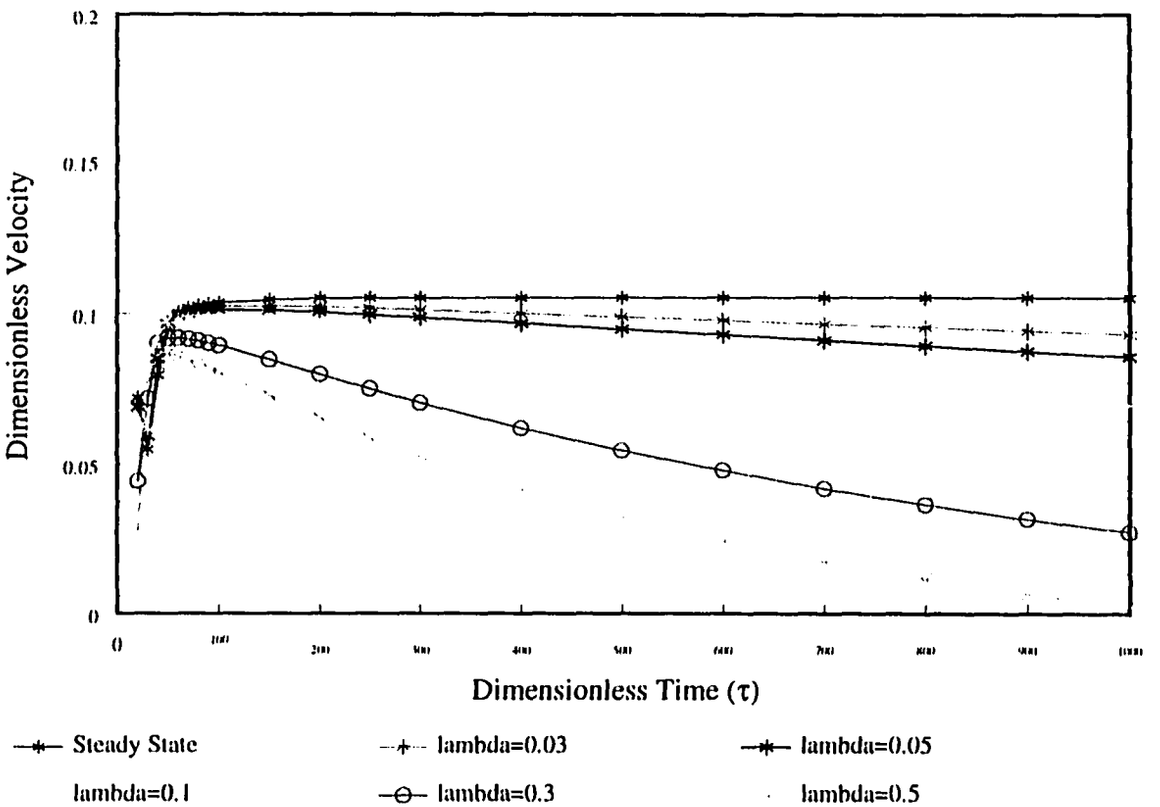

Figure 19: Erosion Growth Rate for $q=q_0e^{-\lambda\tau}$

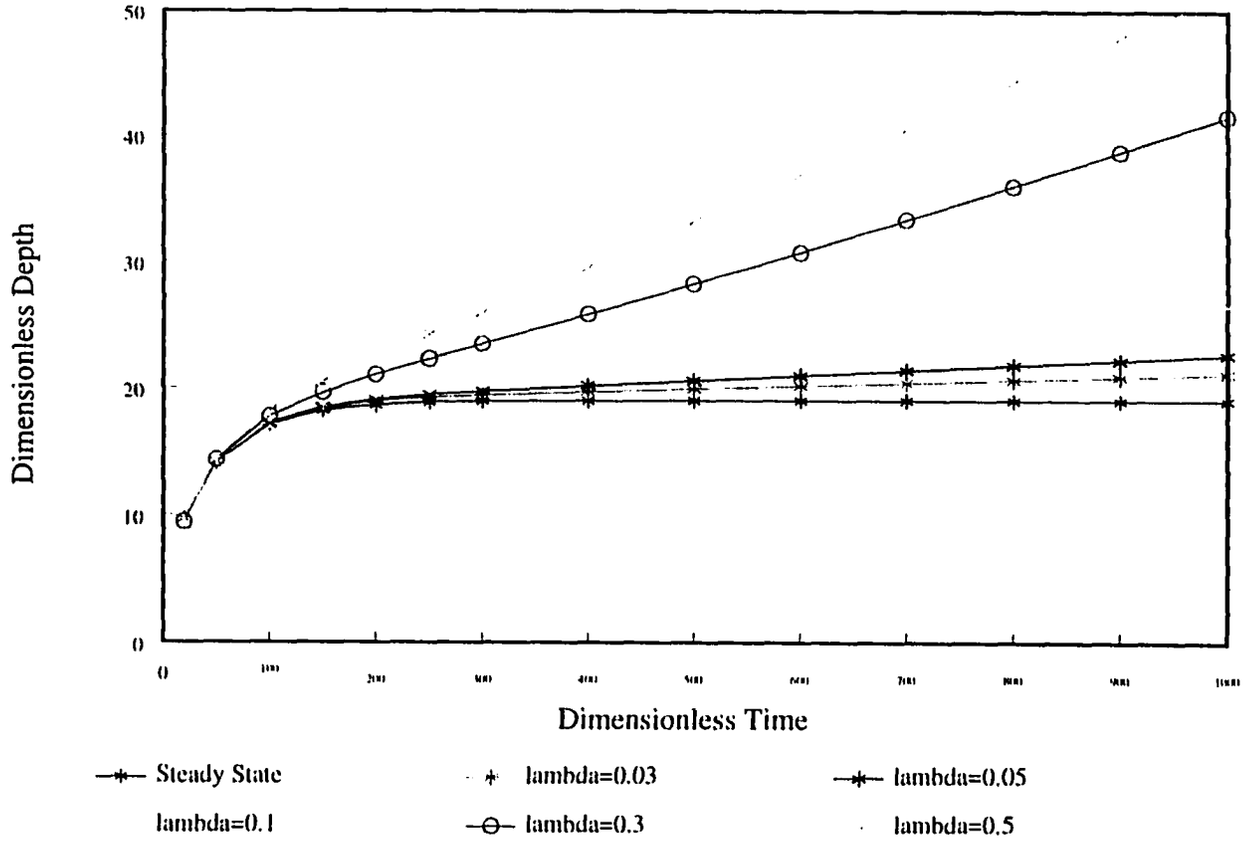

Figure 20: Heated Region Growth During Melting for $q=q_0e^{-\lambda\tau}$

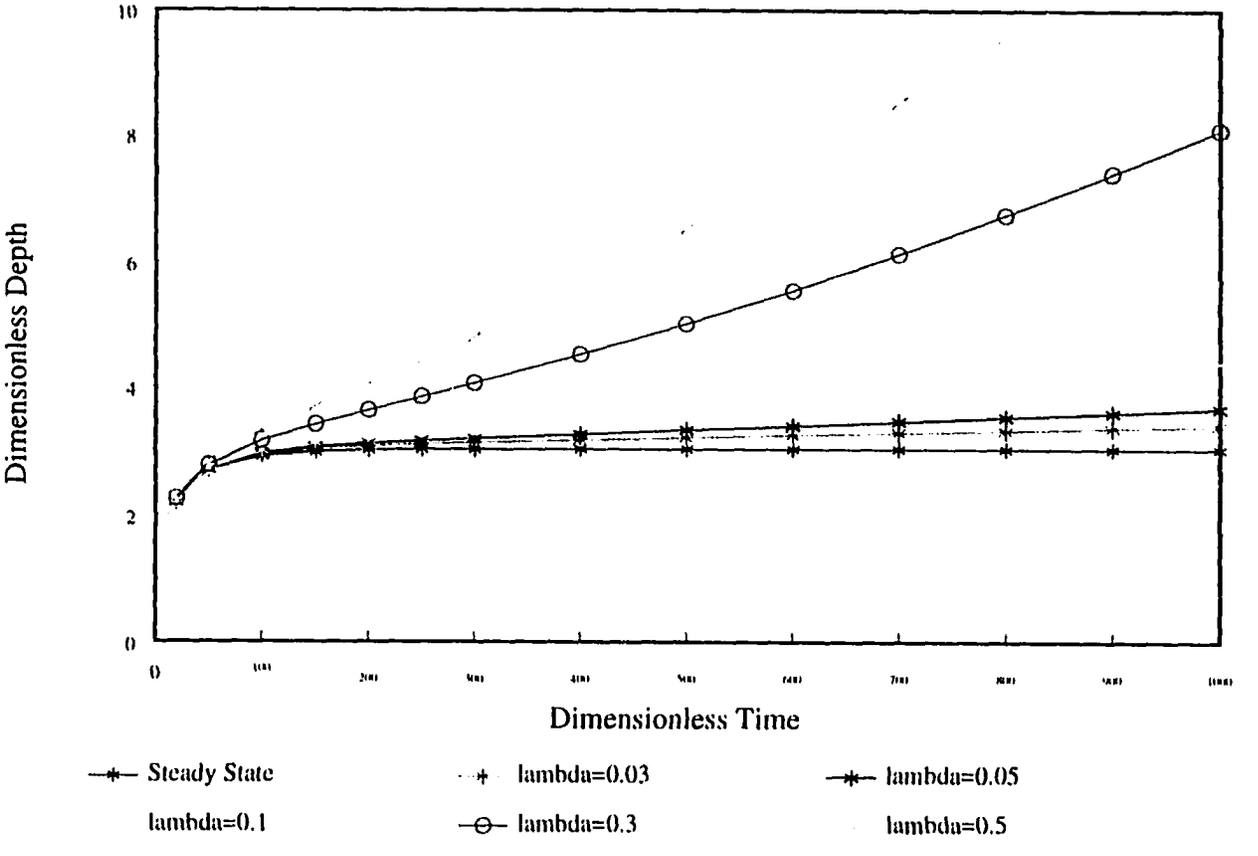

Figure 21: Dry Region Growth During Melting for $q=q_0e^{-\lambda\tau}$

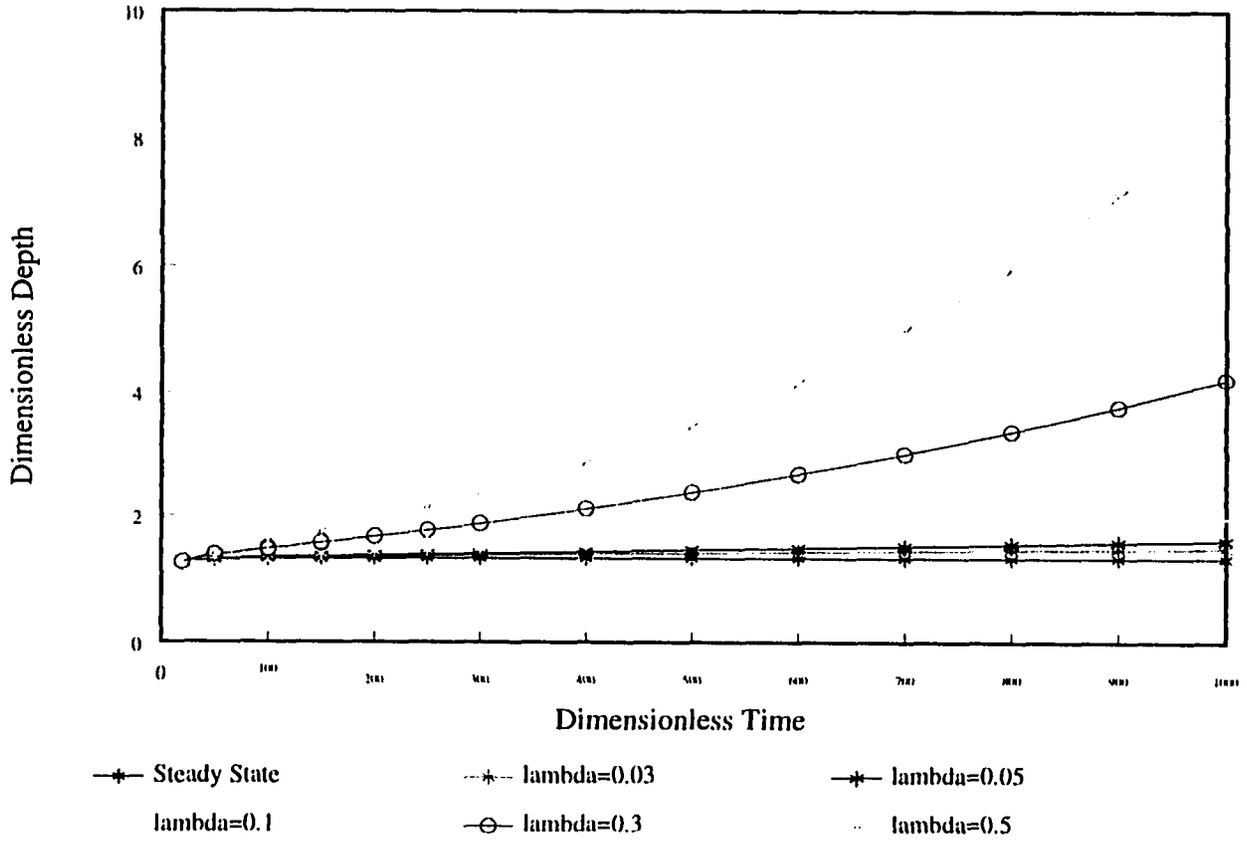

Figure 22: CO_2-Free Region Growth During Melting for $q=q_0e^{-\lambda\tau}$

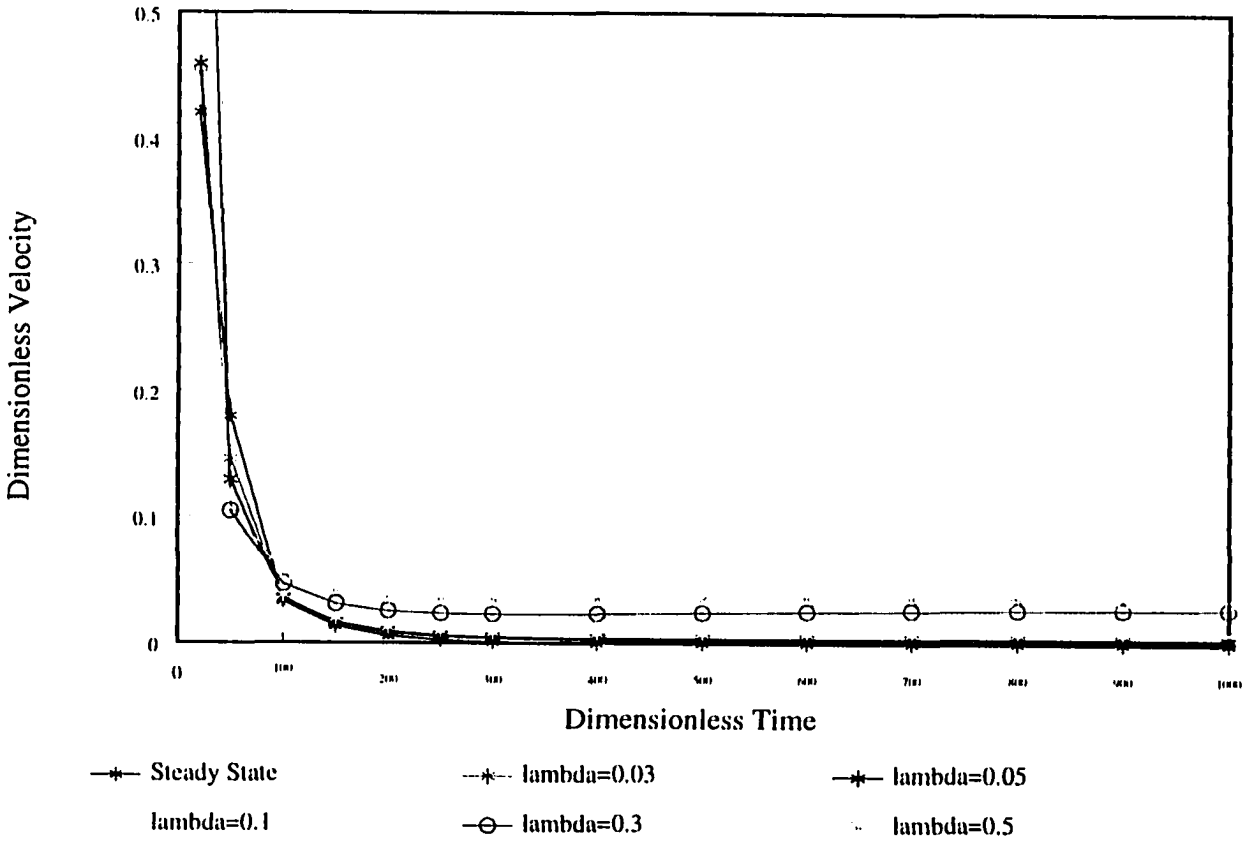

Figure 23: Heated Region Growth Rate During Melting for $q=q_0e^{-\lambda\tau}$

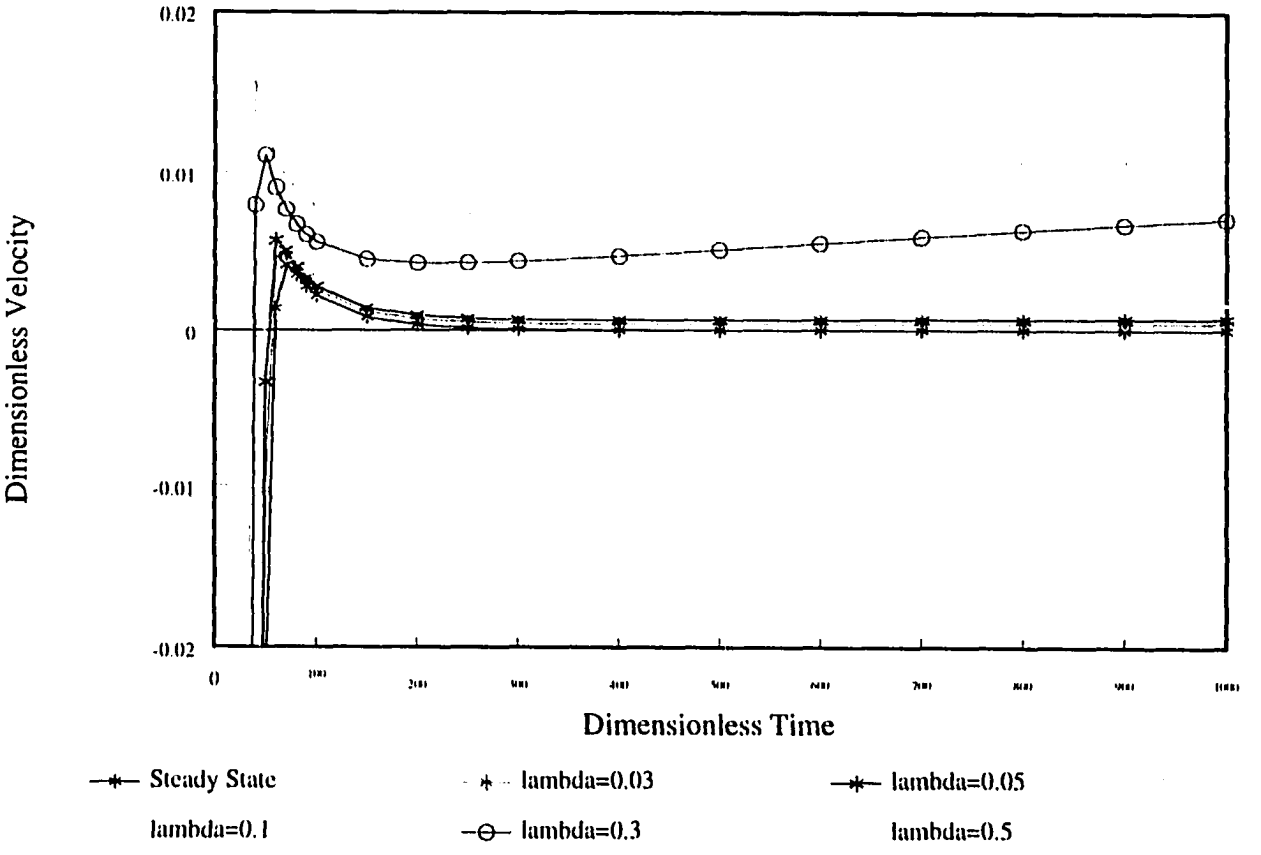

Figure 24: Dry Region Growth Rate During Melting for $q=q_0e^{-\lambda\tau}$

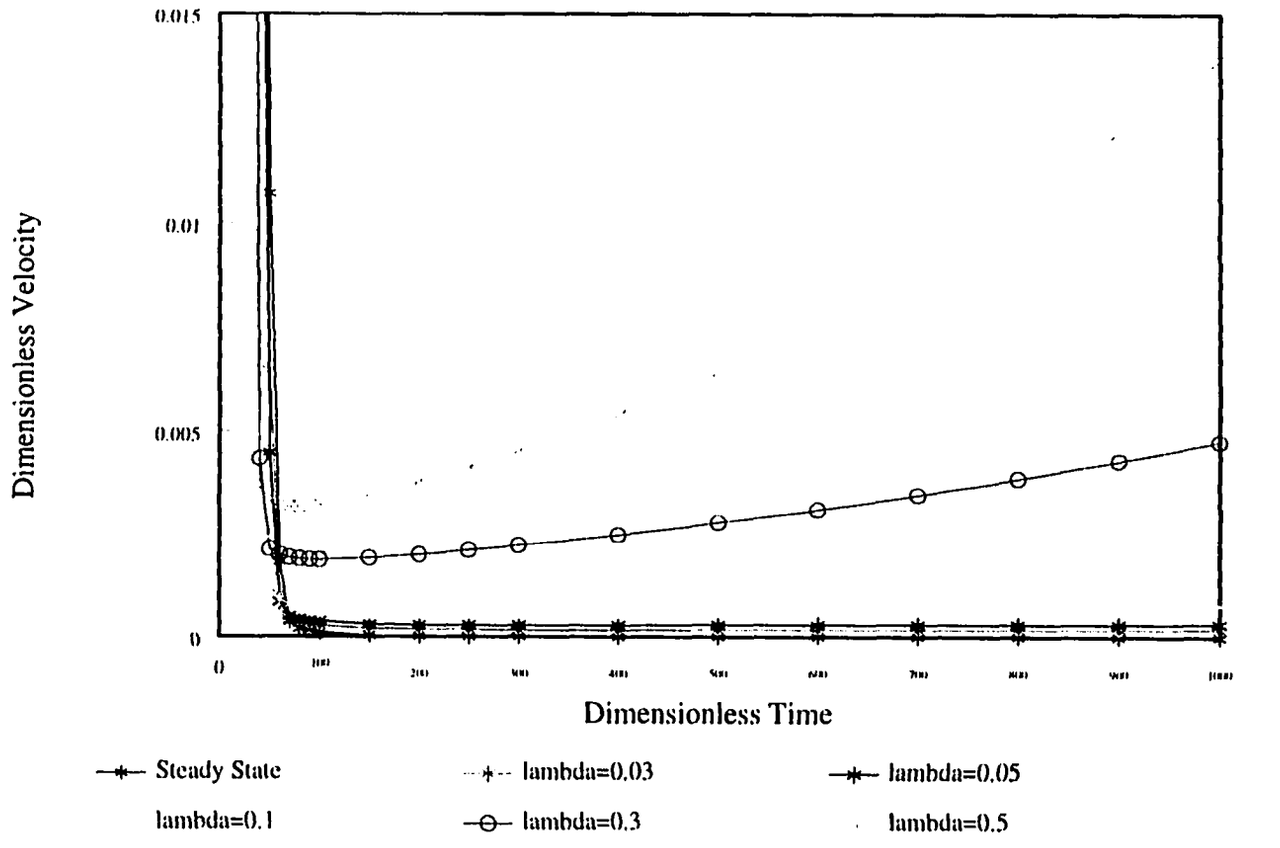

Figure 25: CO_2-Free Region Growth Rate During Melting for $q=q_0e^{-\lambda\tau}$

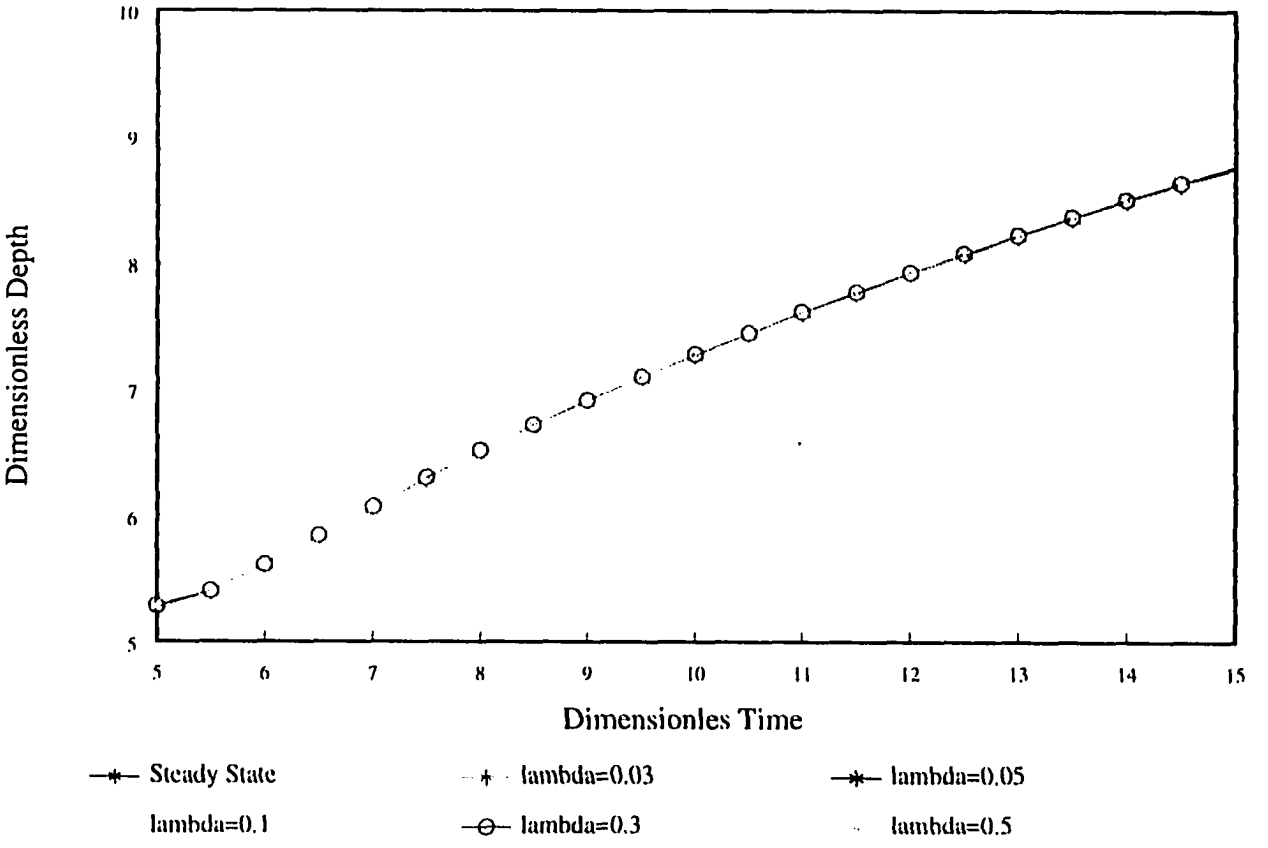

Figure 26: Heated Region Growth During CO_2 Release for $q=q_0e^{-\lambda\tau}$

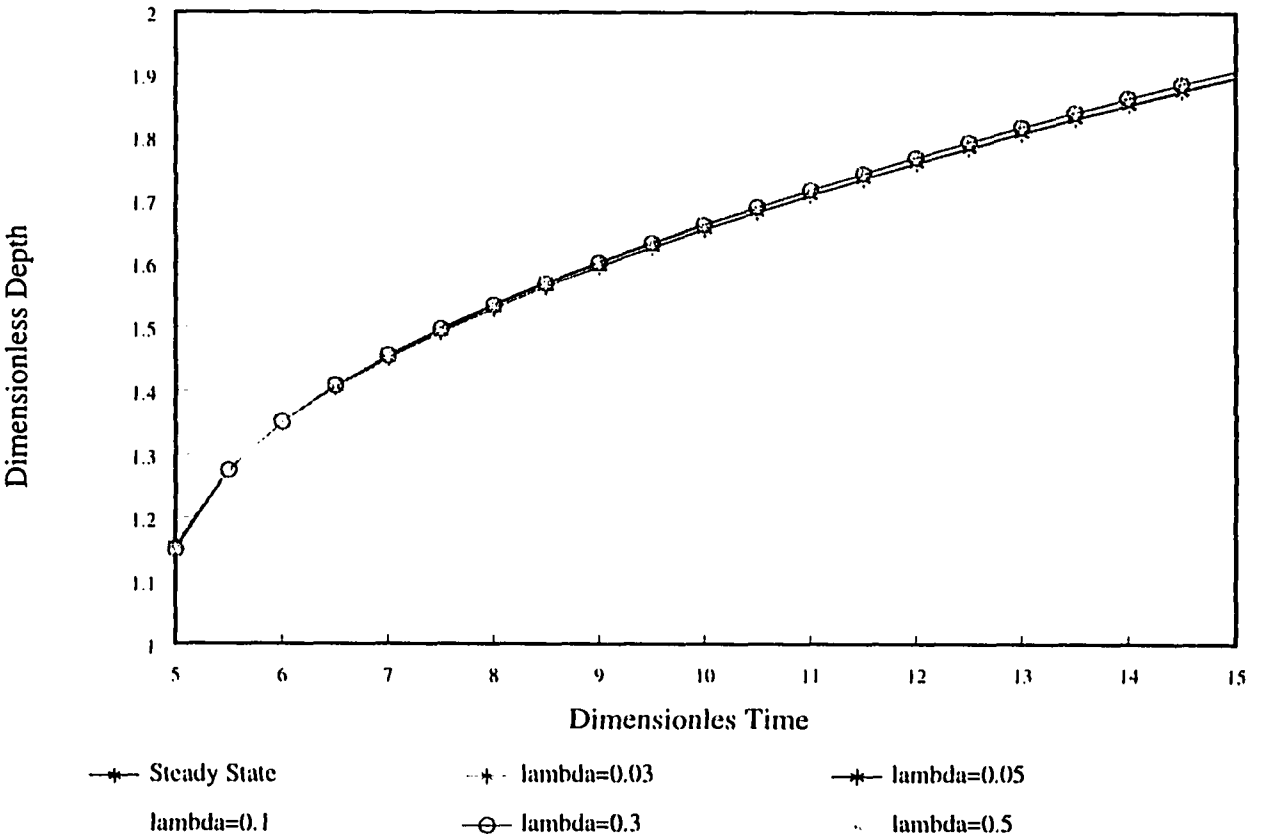

Figure 27: Dry Region Growth During CO_2 Release for $q=q_0e^{-\lambda\tau}$

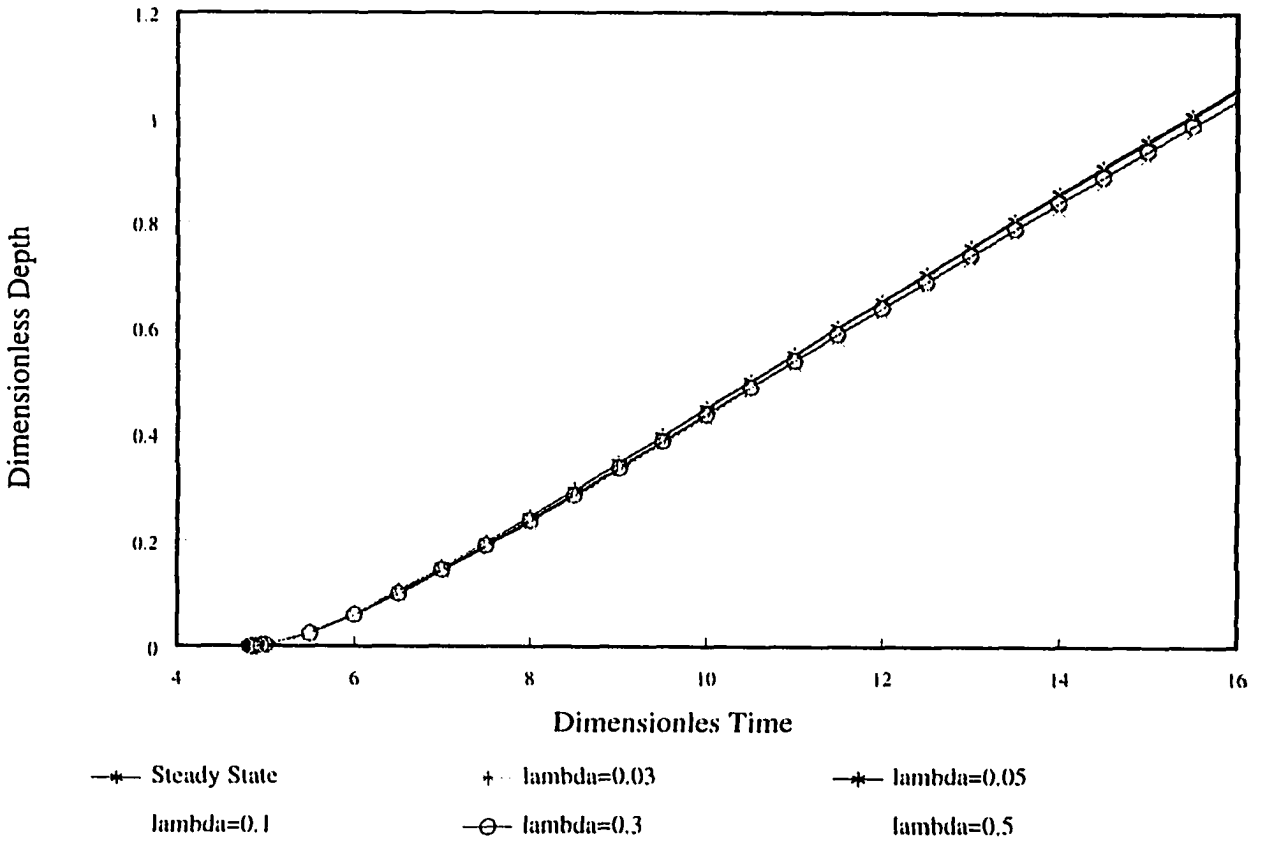

Figure 28: CO_2-Free Region Growth During CO_2 Release for $q=q_0e^{-\lambda\tau}$

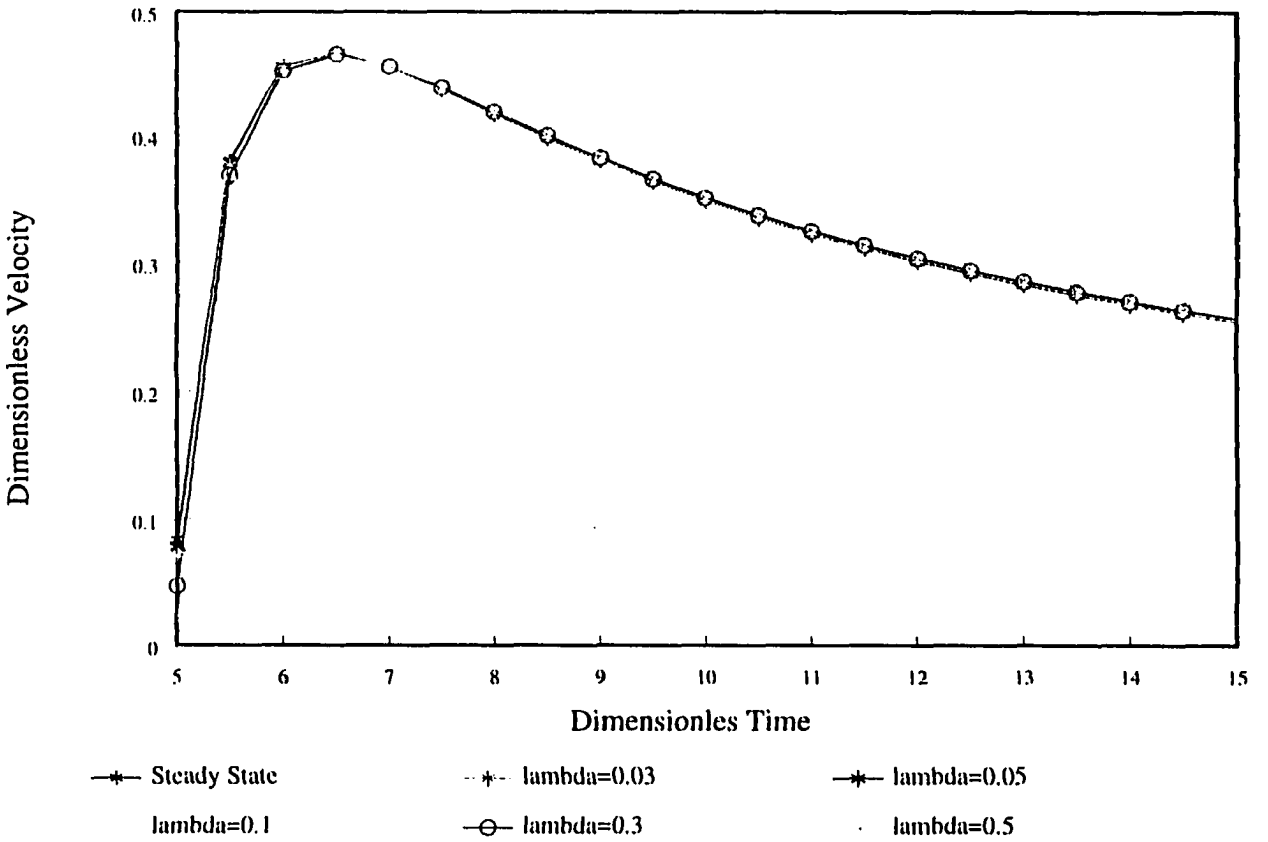

Figure 29: Heated Region Growth Rate During CO_2 Release for $q=q_0e^{-\lambda\tau}$

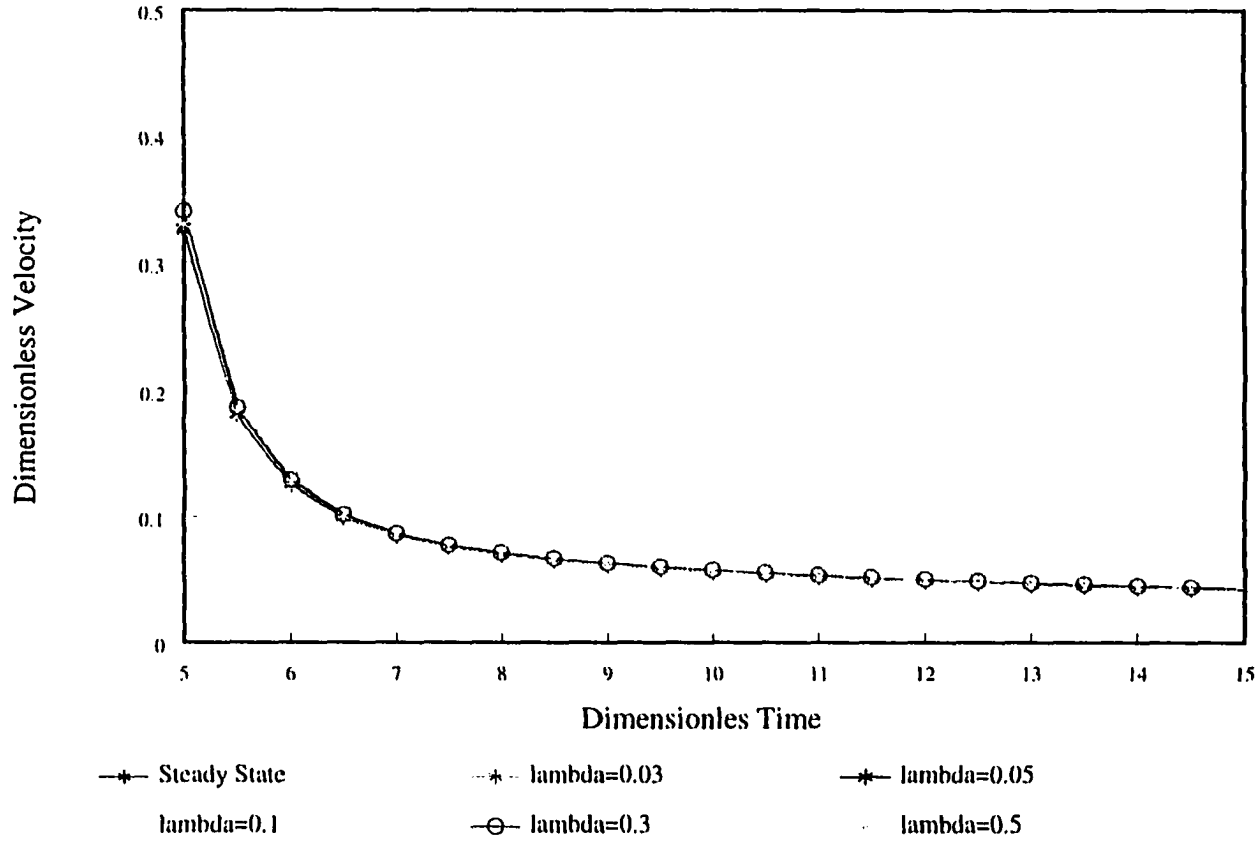

Figure 30: Dry Region Growth Rate During CO_2 Release for $q=q_0e^{-\lambda\tau}$

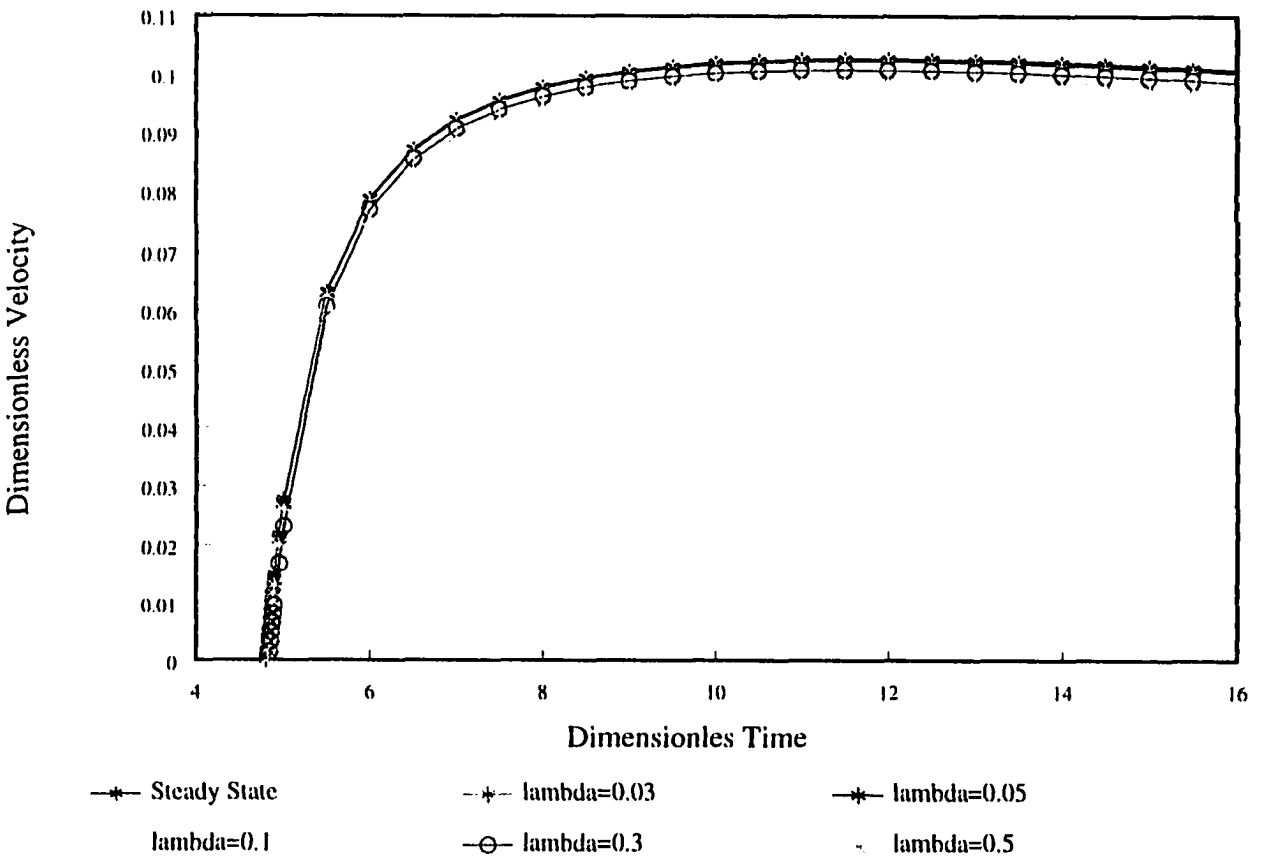

Figure 31: CO_2-Free Region Growth During CO_2 Release for $q=q_0e^{-\lambda\tau}$

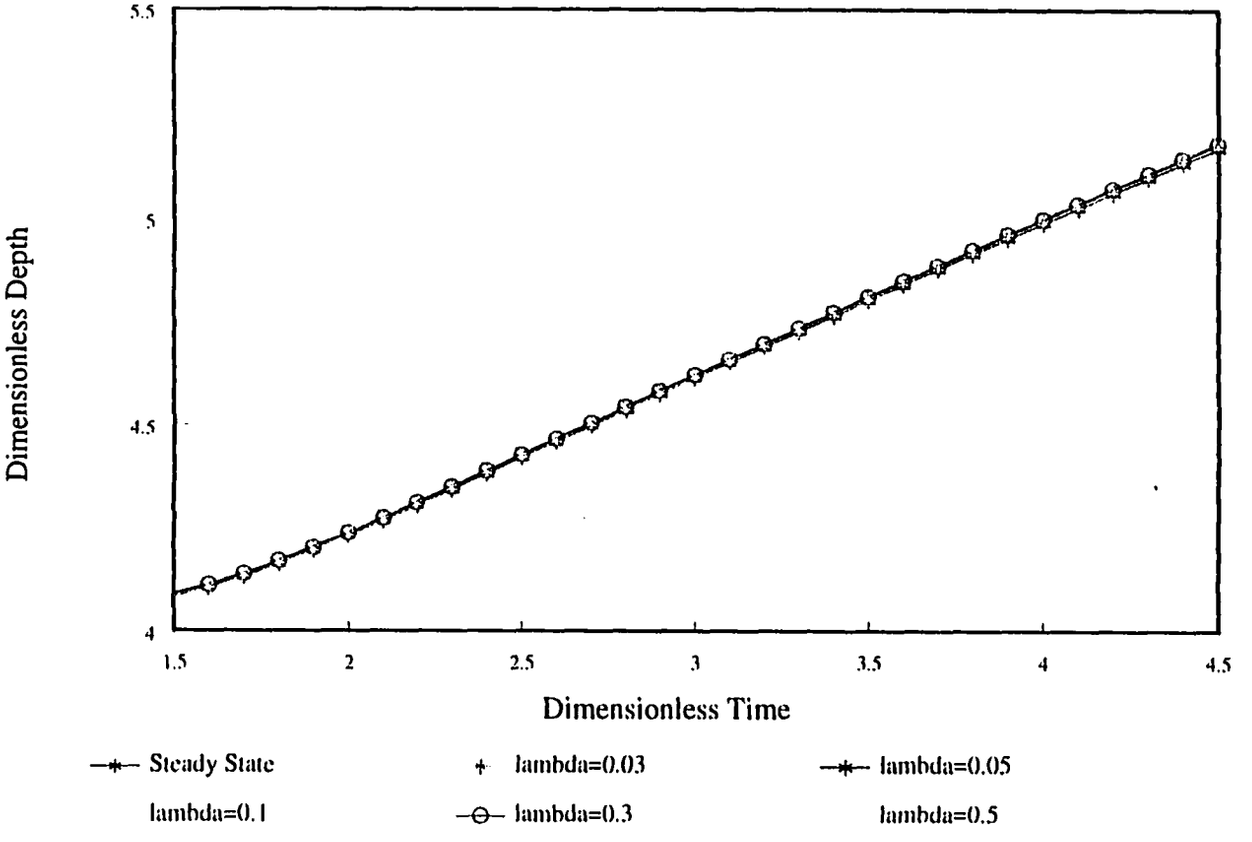

Figure 32: Heated Region Growth During Evaporation for $q=q_0e^{-\lambda\tau}$

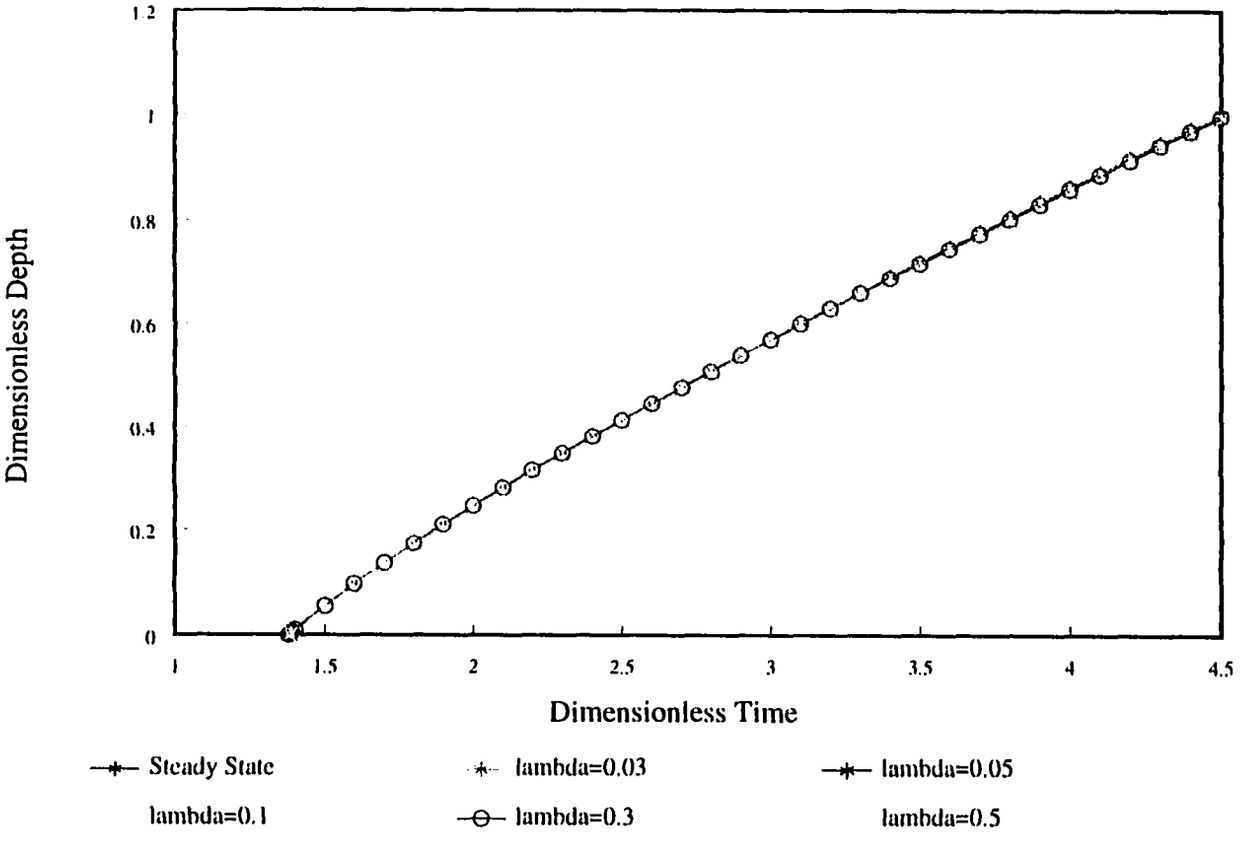

Figure 33: Dry Region Growth During Evaporation for $q=q_{(0)}e^{-\lambda\tau}$

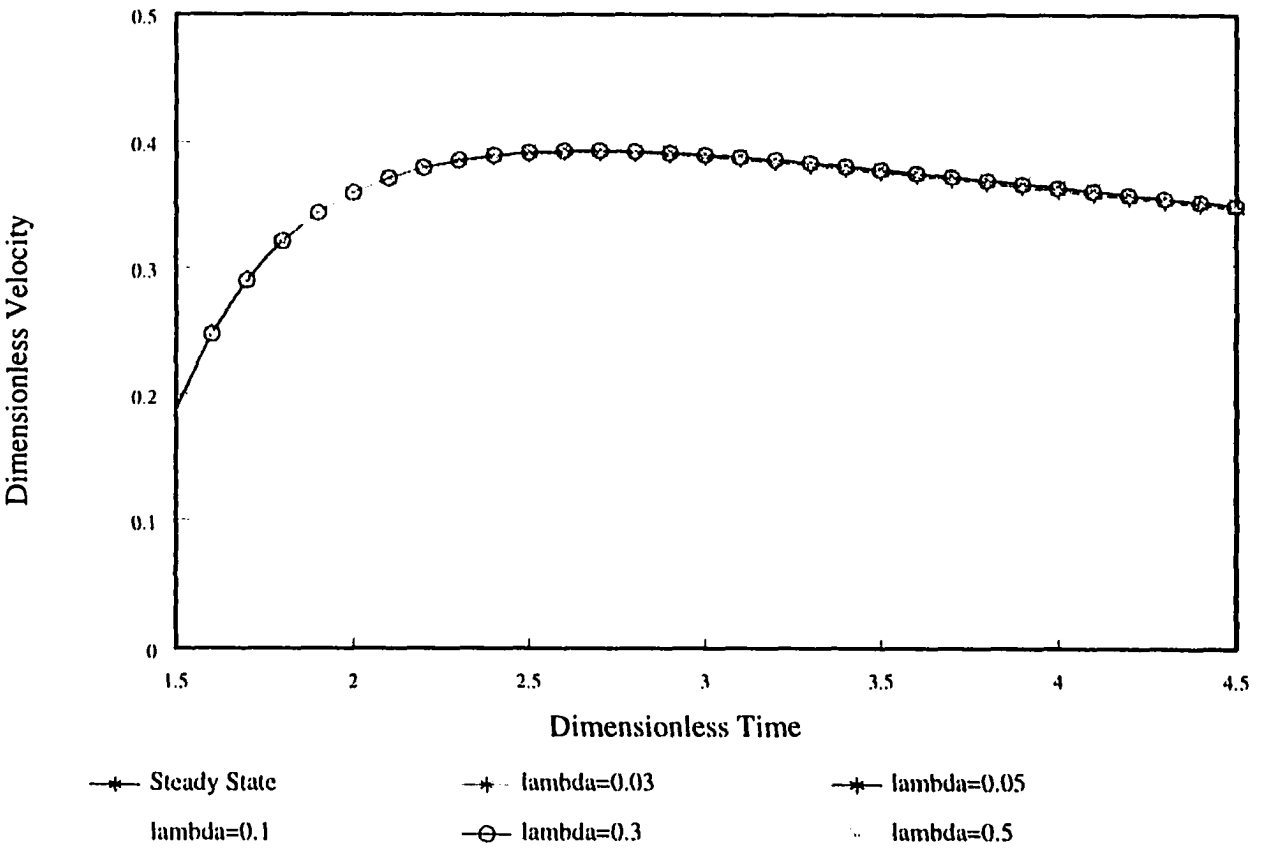

Figure 34: Heated Region Growth Rate During Evaporation for $q=q_0e^{-\lambda\tau}$

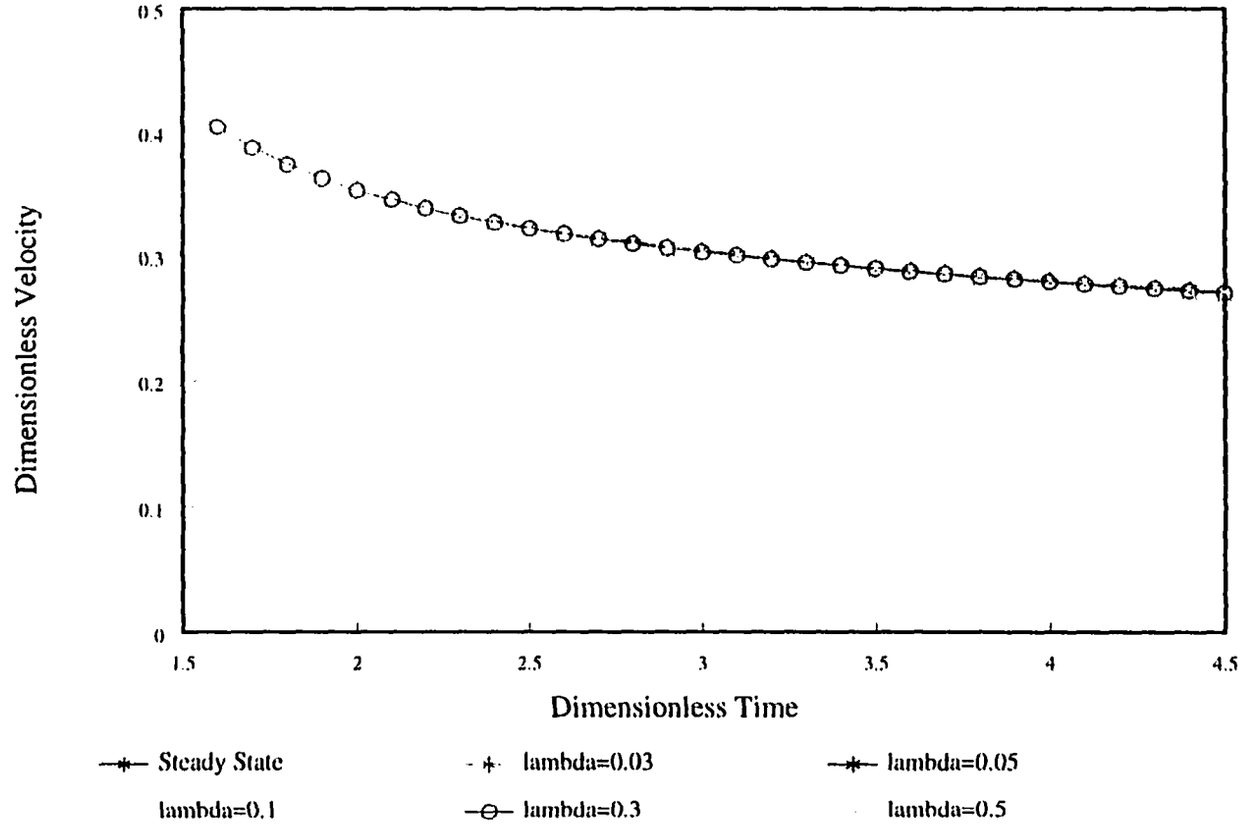

Figure 35: Dry Region Growth Rate During Evaporation for $q=q_0e^{-\lambda\tau}$

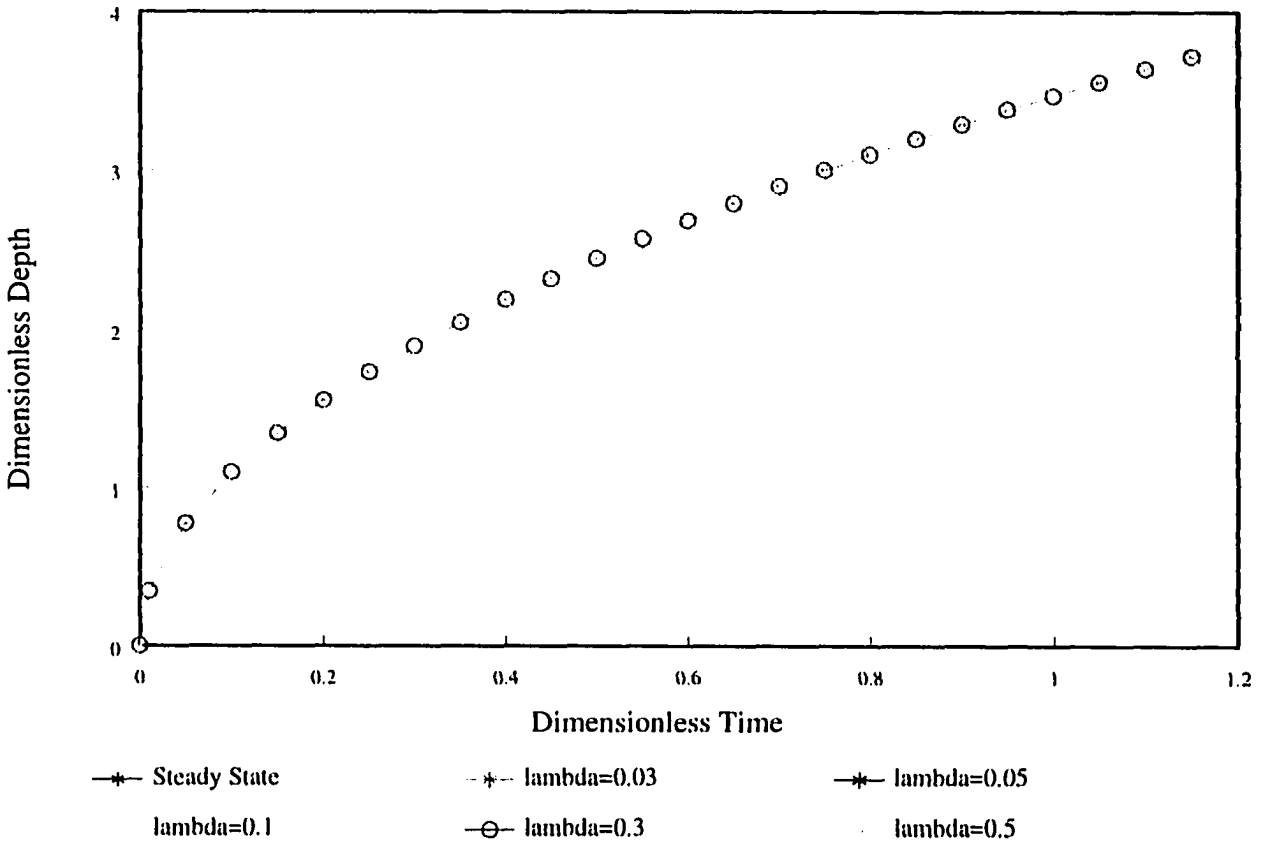

Figure 36: Heated Region Growth During Heating for $q=q_0e^{-\lambda\tau}$

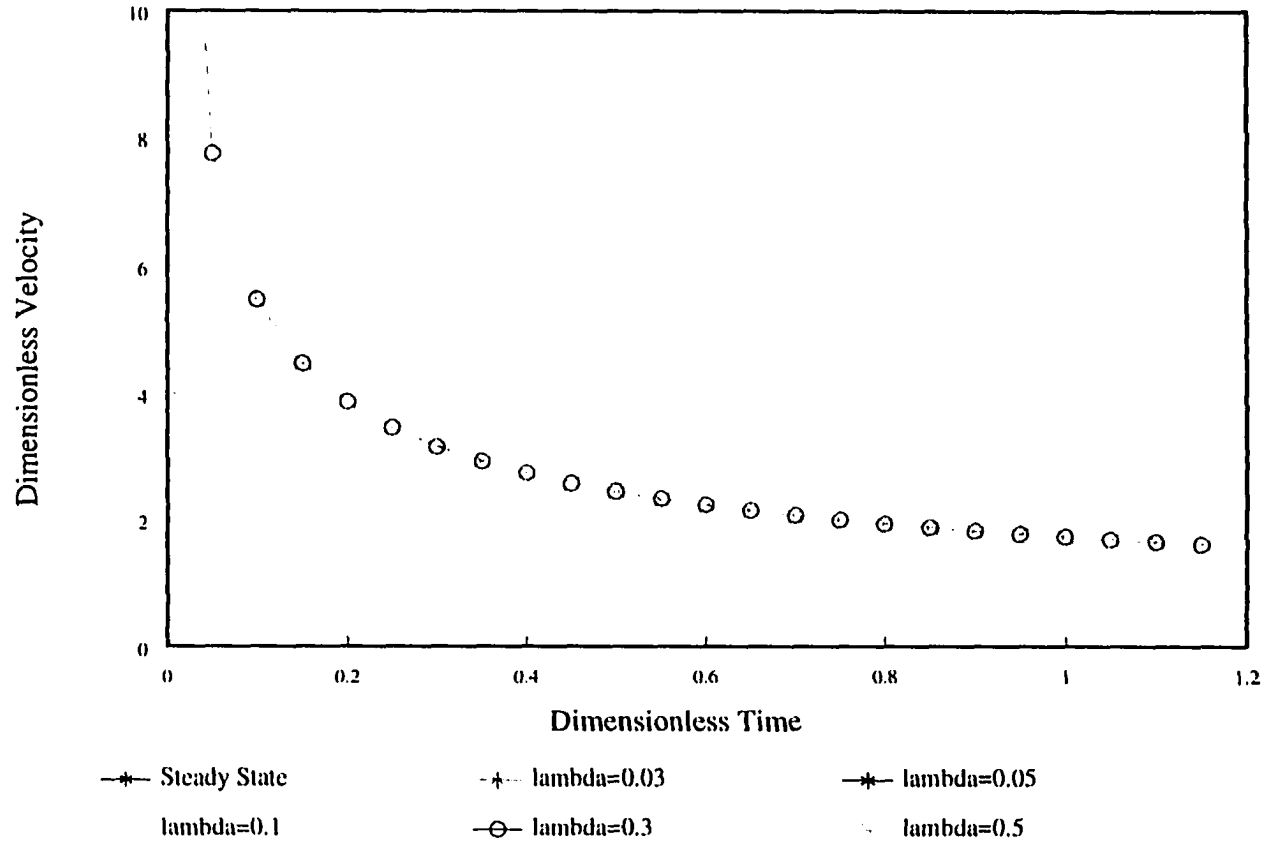

Figure 37: Heated Region Growth Rate During Heating for $q=q_0e^{-\lambda\tau}$

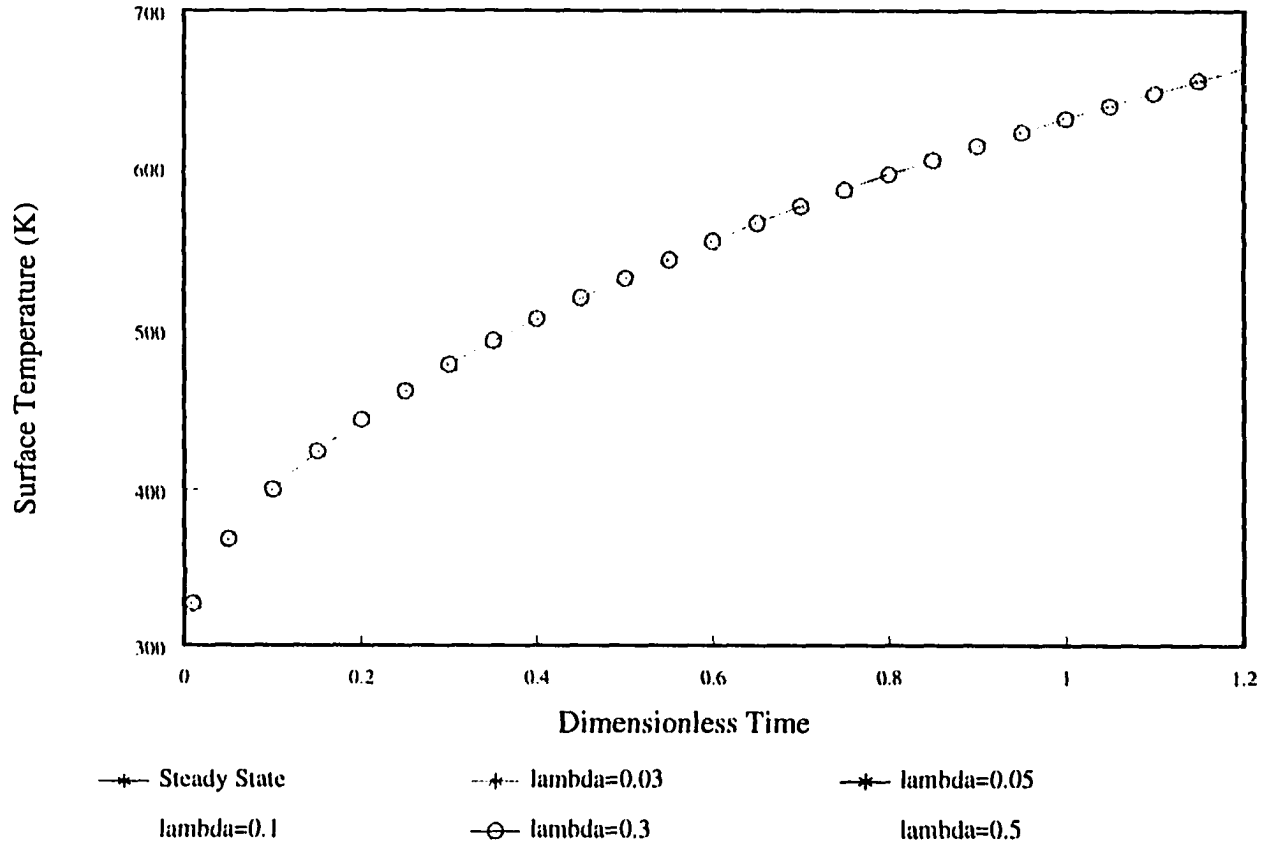

Figure 38: Surface Temperature Before Evaporation for $q=q_0e^{-\lambda\tau}$

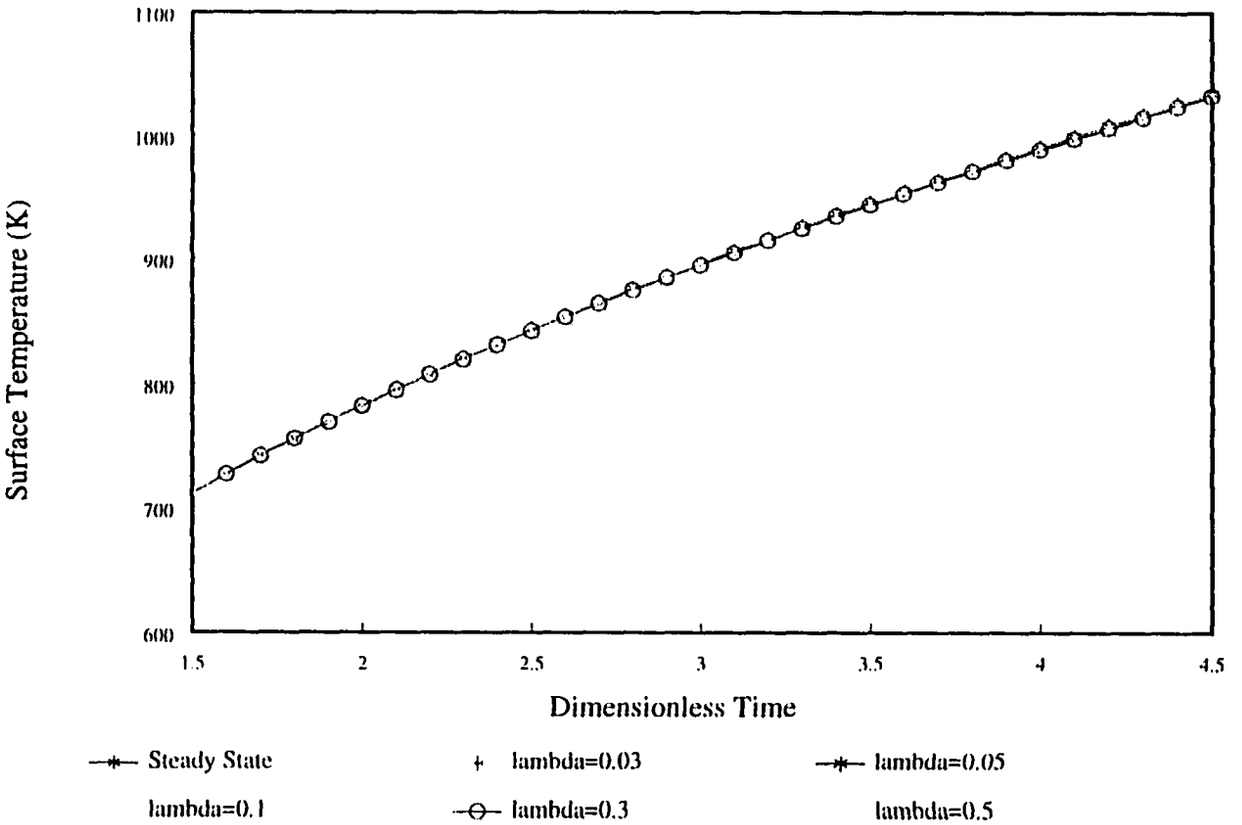

Figure 39: Surface Temperature During Evaporation for $q=q_0e^{-\lambda\tau}$

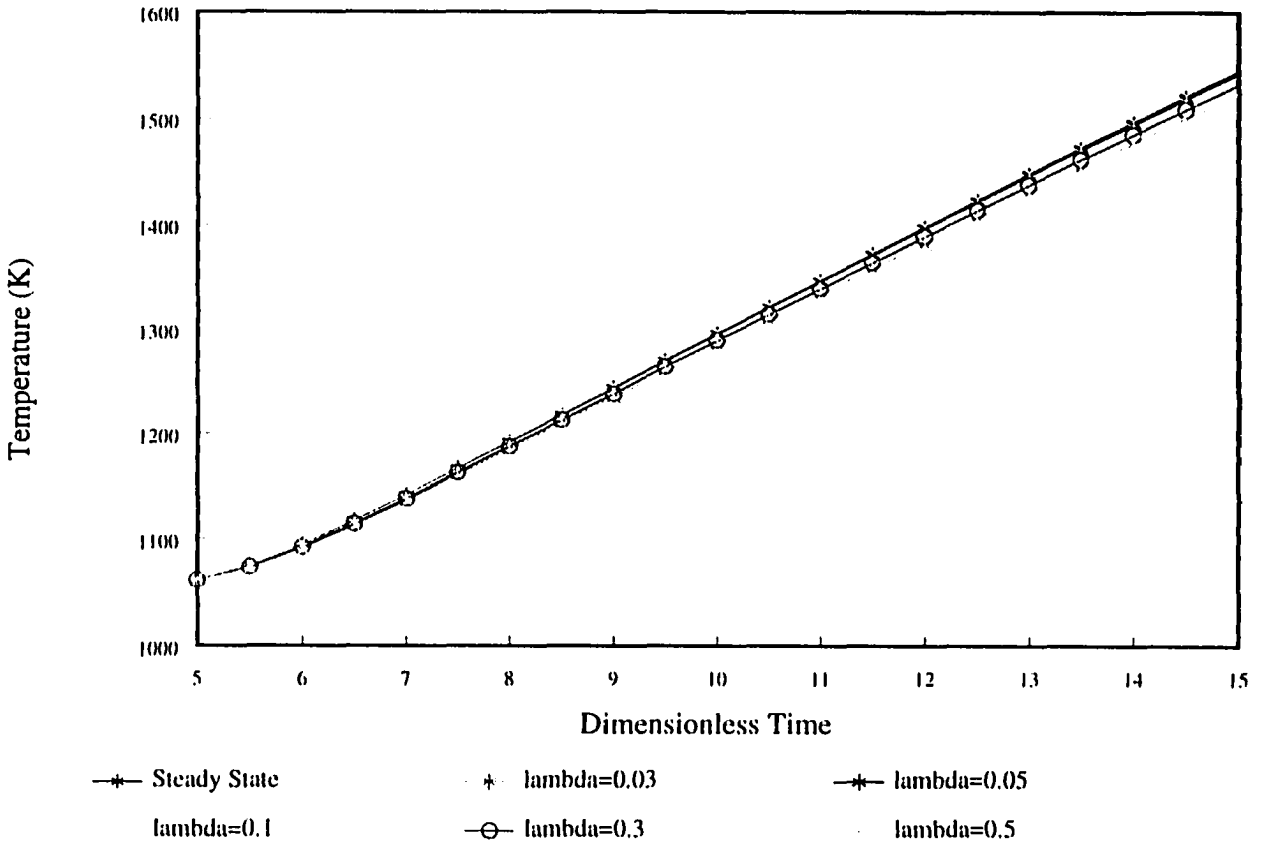

Figure 40: Surface Temperature During CO_2 Release for $q=q_0e^{-\lambda\tau}$

4.3.2.2. Surface Heat Flux in Forms of $t^{-\lambda}$

For the surface heat fluxes in forms of $t^{-\lambda}$, the general solutions in Chapter 3 can be used. The problem with the short term solution can be solved by carefully setting the time steps for this case.

As it is in the surface heat flux in forms of $e^{-\lambda t}$, there are no or negligible effects of the cooling in the shorter times when the dehydration and gas release from the concrete take place, although the surface heat flux decrease is faster and this result in more visible effects on the growth and growth rates of the regions during the gas release. This faster decay in the short time period is more visible when the erosion starts. Since the surface heat flux is lower than what it was for the previous case, the peak at the erosion rate that occurred in that case does not occur for this case. On the other hand, in the longer times, the decay is slower than the previous case and approaches an asymptotic value which translates into a slower but still increasing erosion. As a result, it can be concluded that, for the surface heat flux in forms of $t^{-\lambda}$, the erosion theoretically does not stop although it approaches an asymptotic rate. Also, the growth of the other regions approaches their asymptotic rates. The results for the erosion depths and rates for the surface heat flux in forms of $t^{-\lambda}$ are presented in Figures 41 and 42. Figures 43 through 60 present the progress of each region and their growth rate before and after the erosion begins for different decay rates, and Figures 61 through 63 show the progress of the surface temperature before melting begins.

One interpretation of the results is that different than the previous case: The gas, water, and aerosol release from the concrete does not increase in time, while the erosion rate does not terminate. This type of cooling is also probable in the

actual molten core concrete interactions, and should be examined carefully to determine the required thickness of the concrete basemat to prevent failure.

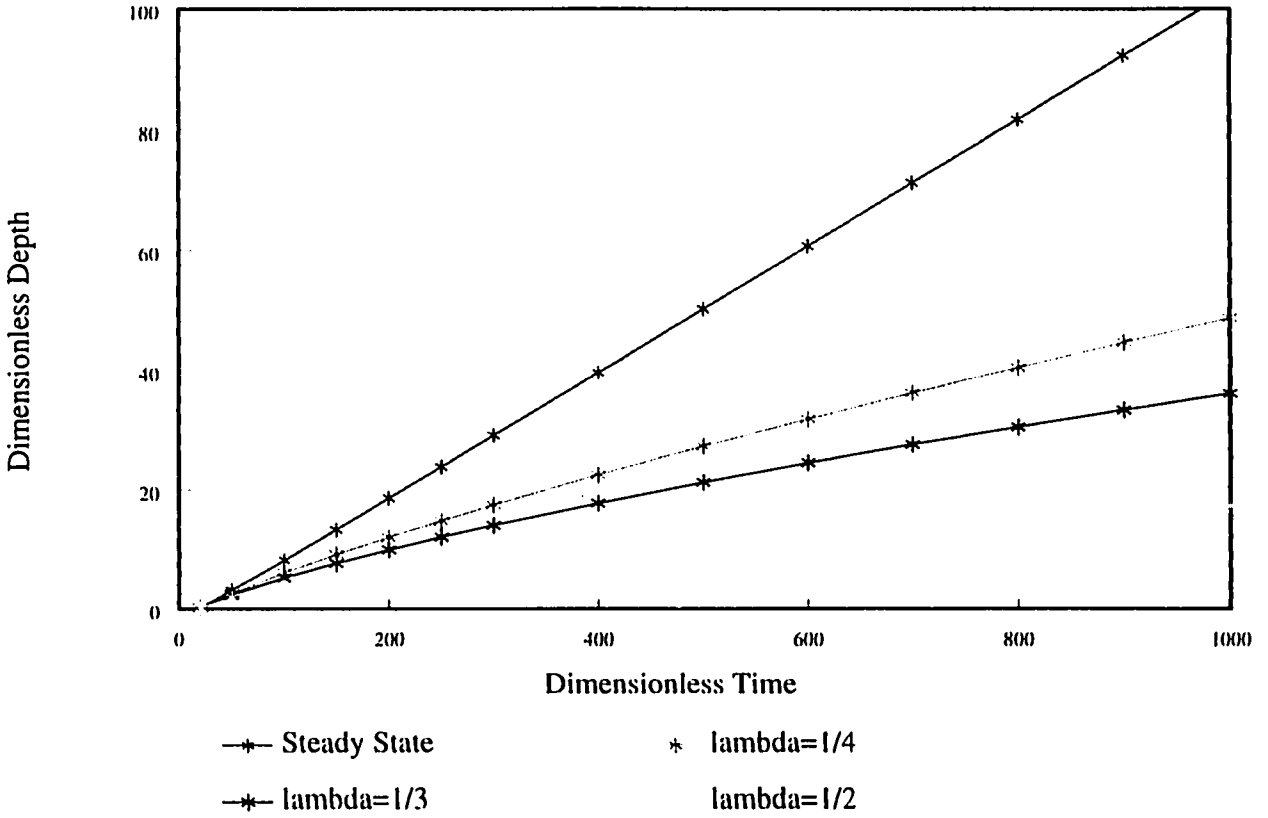

Figure 41: Erosion Growth for $q=q_0t^{-\lambda}$

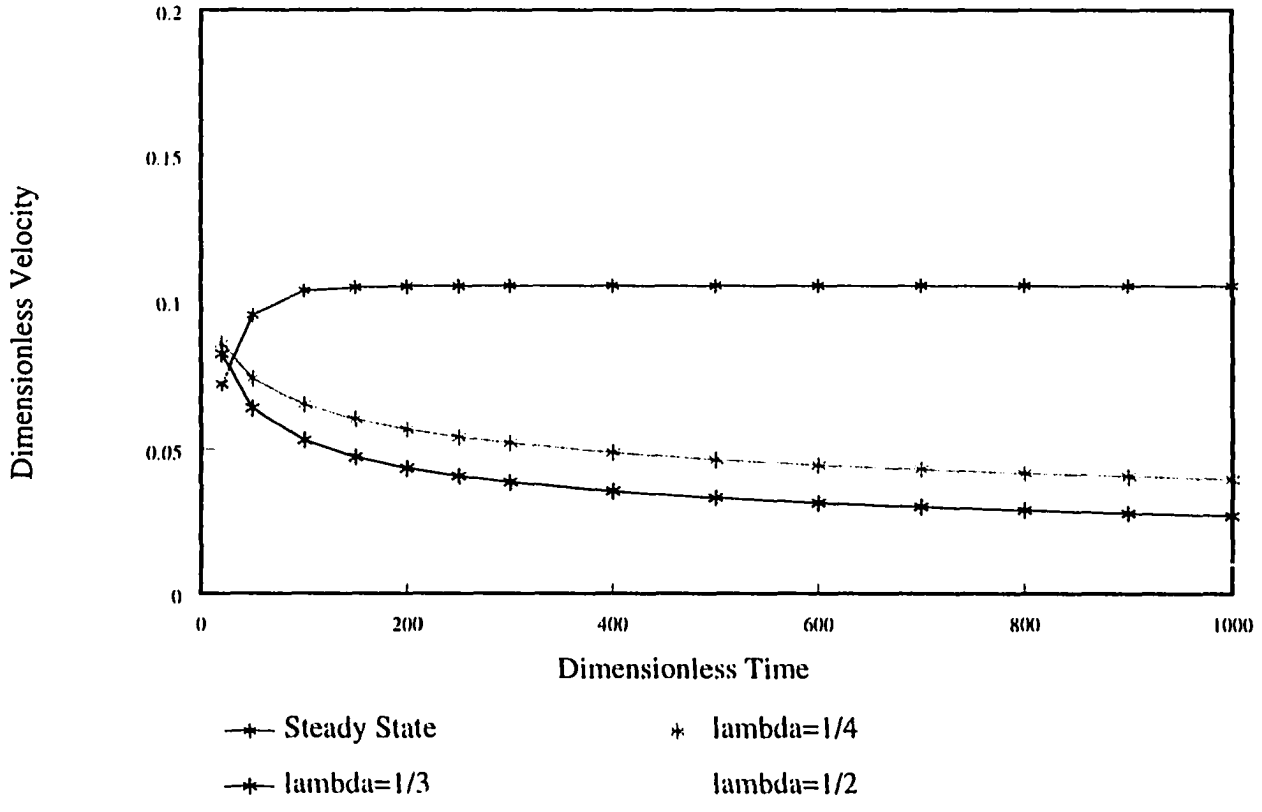

Figure 42: Erosion Growth Rate for $q=q_0t^{-\lambda}$

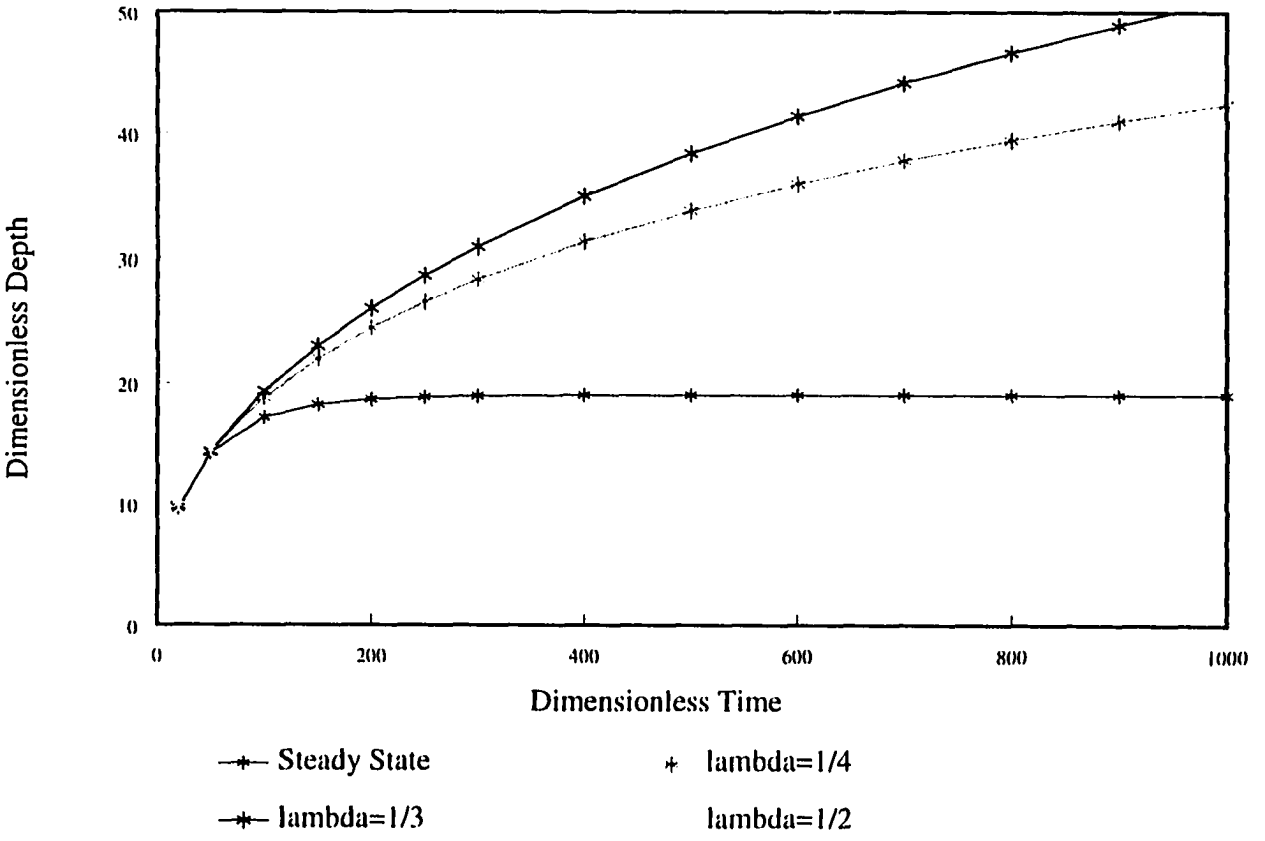

Figure 43: Heated Region Growth During Melting for $q=q_0t^{-\lambda}$

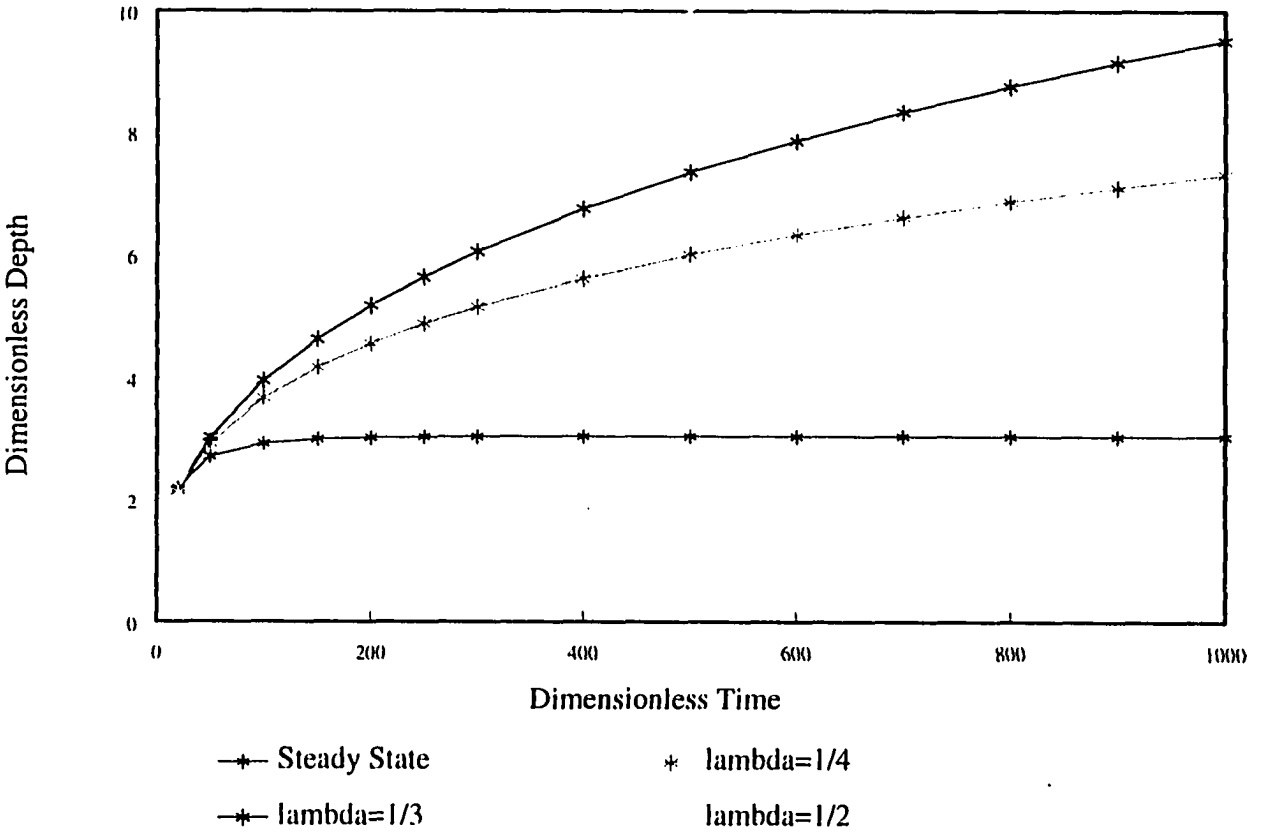

Figure 44: Dry Region Growth During Melting for $q=q_0t^{-\lambda}$

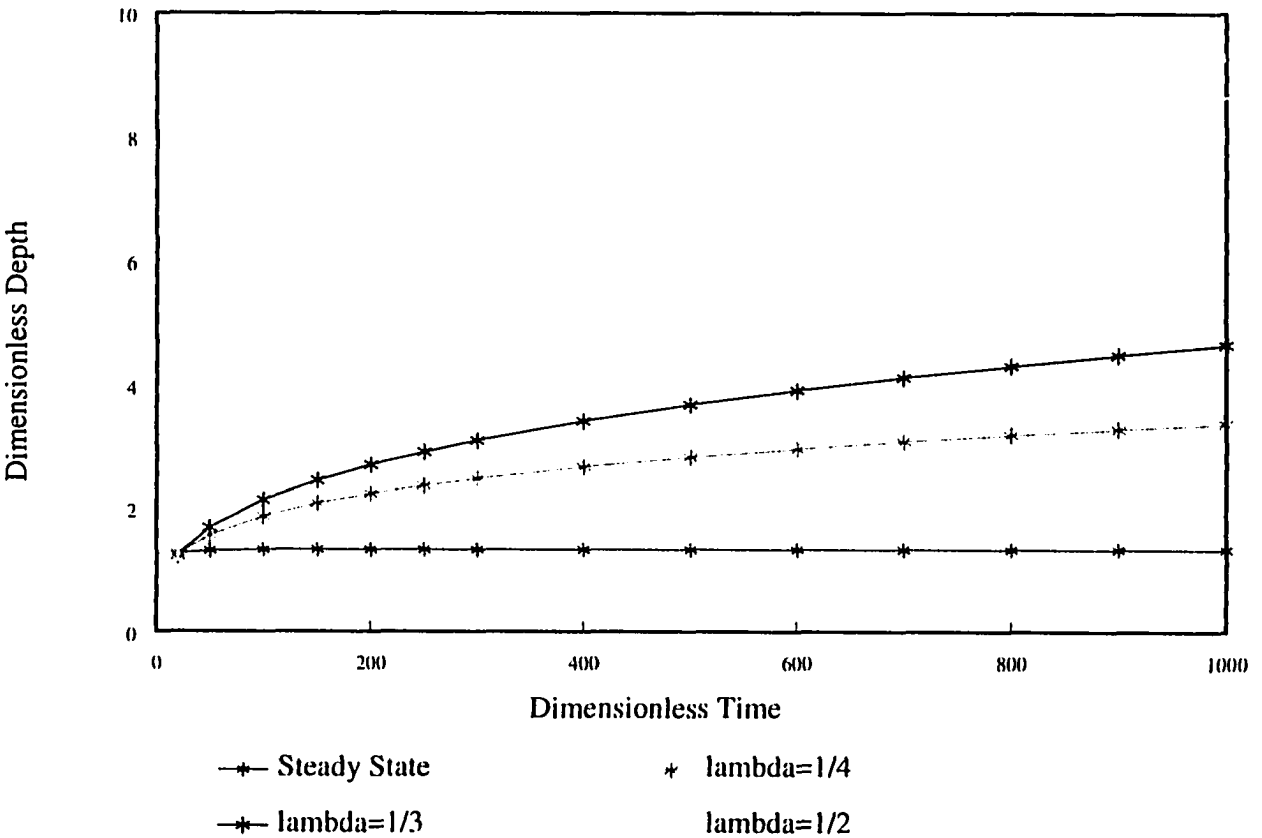

Figure 45: CO_2-Free Region Growth During Melting for $q=q_0t^{-\lambda}$

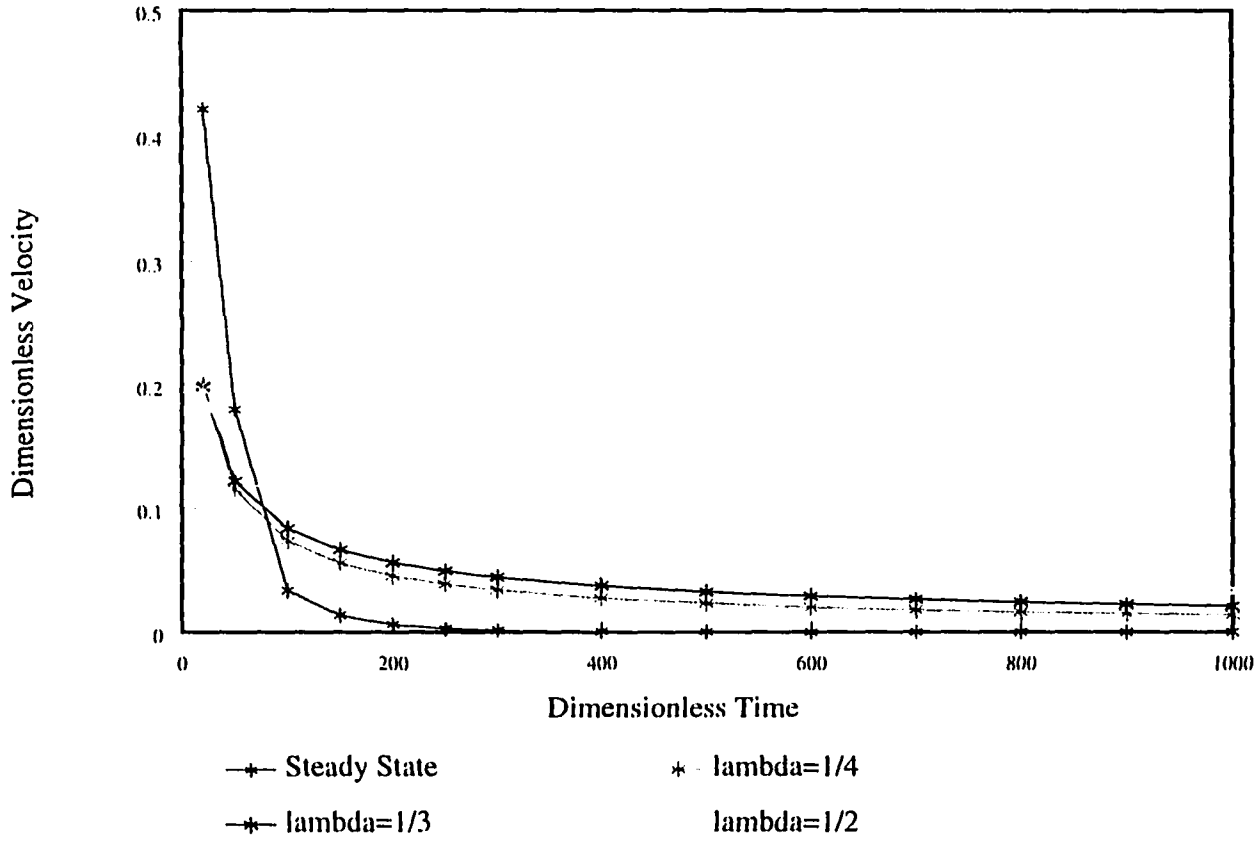

Figure 46: Heated Region Growth Rate During Melting for $q=q_0t^{-\lambda}$

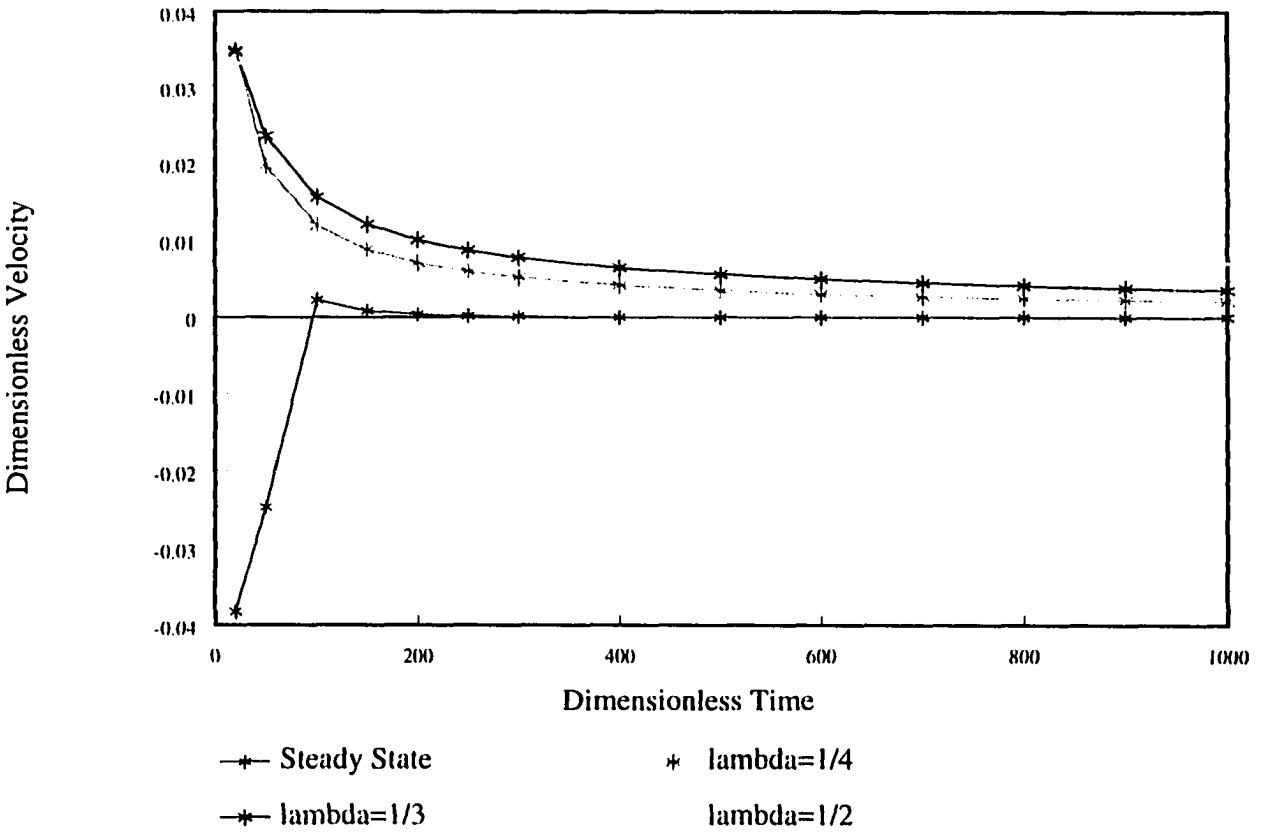

Figure 47: Dry Region Growth Rate During Melting for $q=q_0t^{-\lambda}$

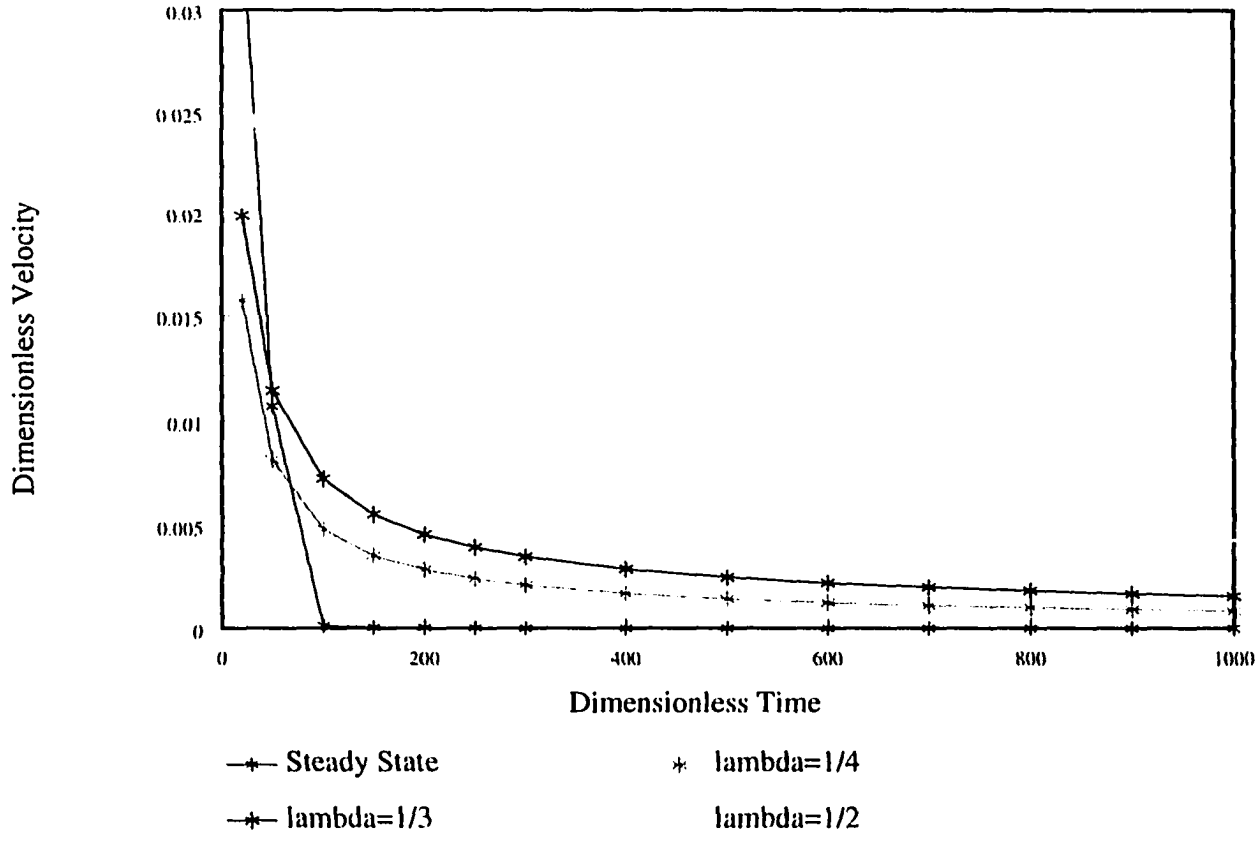

Figure 48: CO_2-Free Region Growth Rate During Melting for $q=q_0t^{-\lambda}$

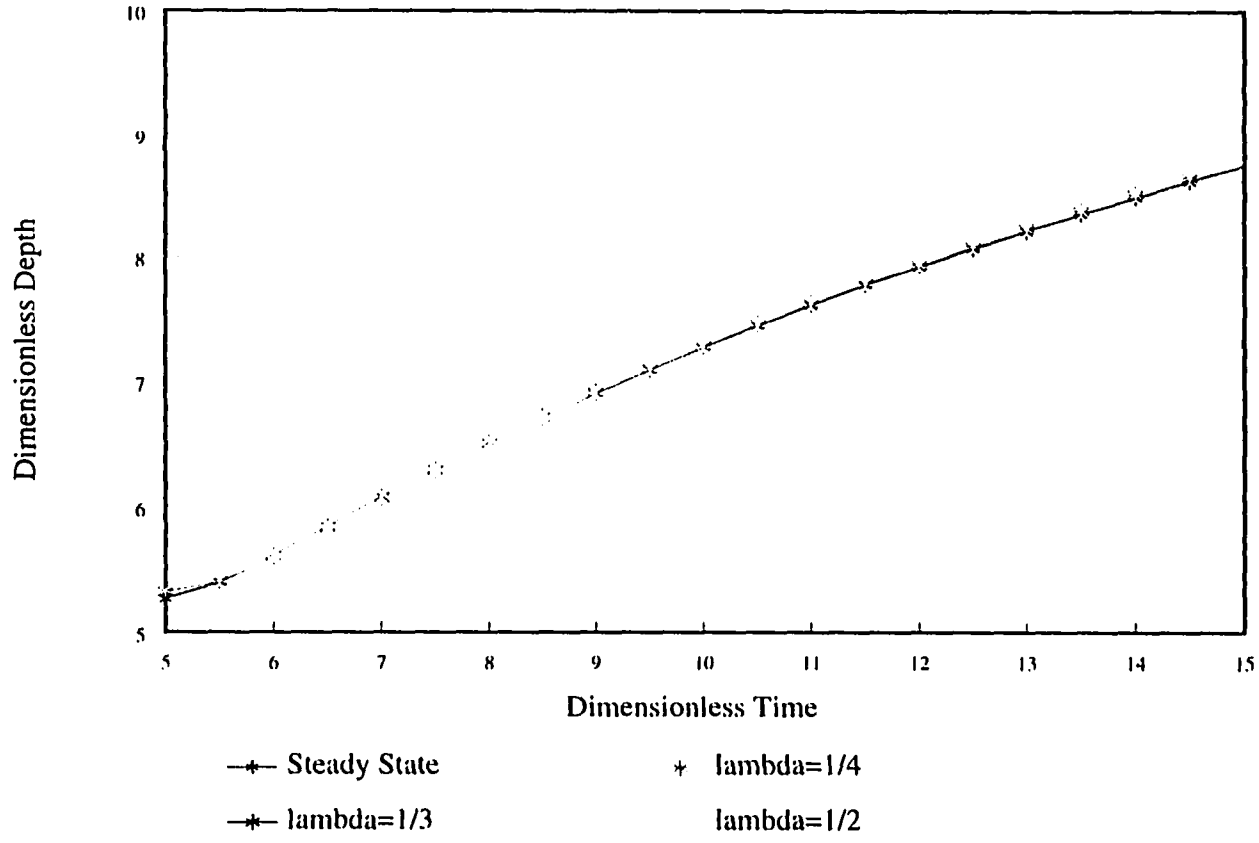

Figure 49: Heated Region Growth During CO_2 Release for $q=q_0t^{-\lambda}$

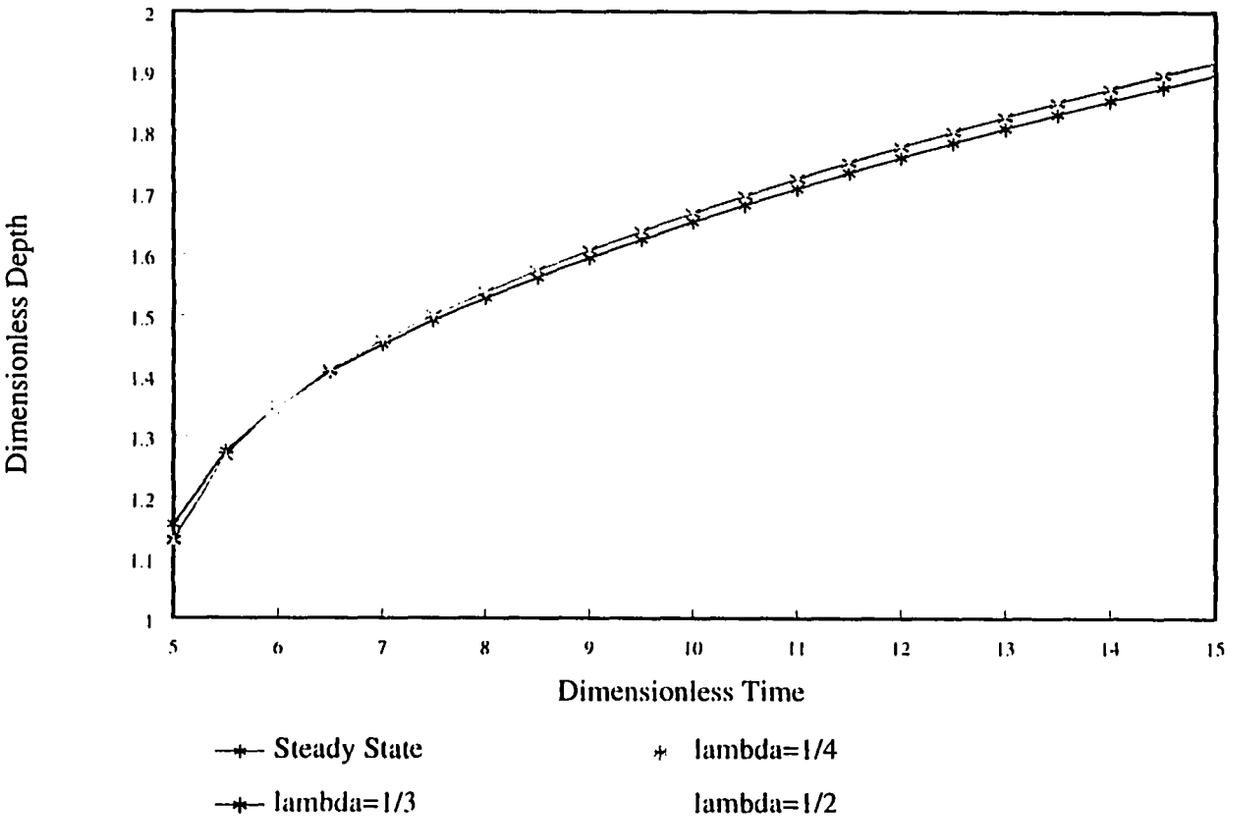

Figure 50: Dry Region Growth During CO_2 Release for $q=q_0t^{-\lambda}$

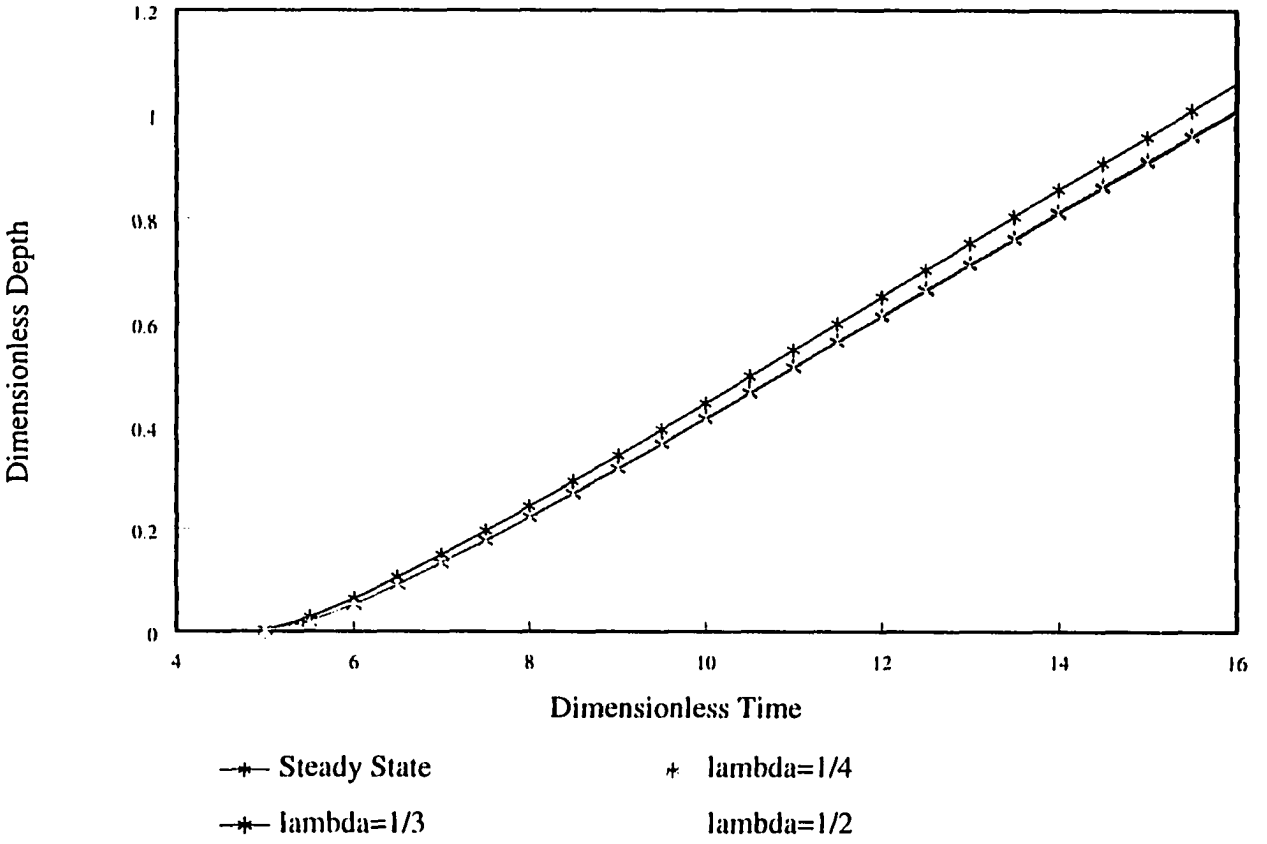

Figure 51: CO_2-Free Region Growth During CO_2 Release for $q=q_0t^{-\lambda}$

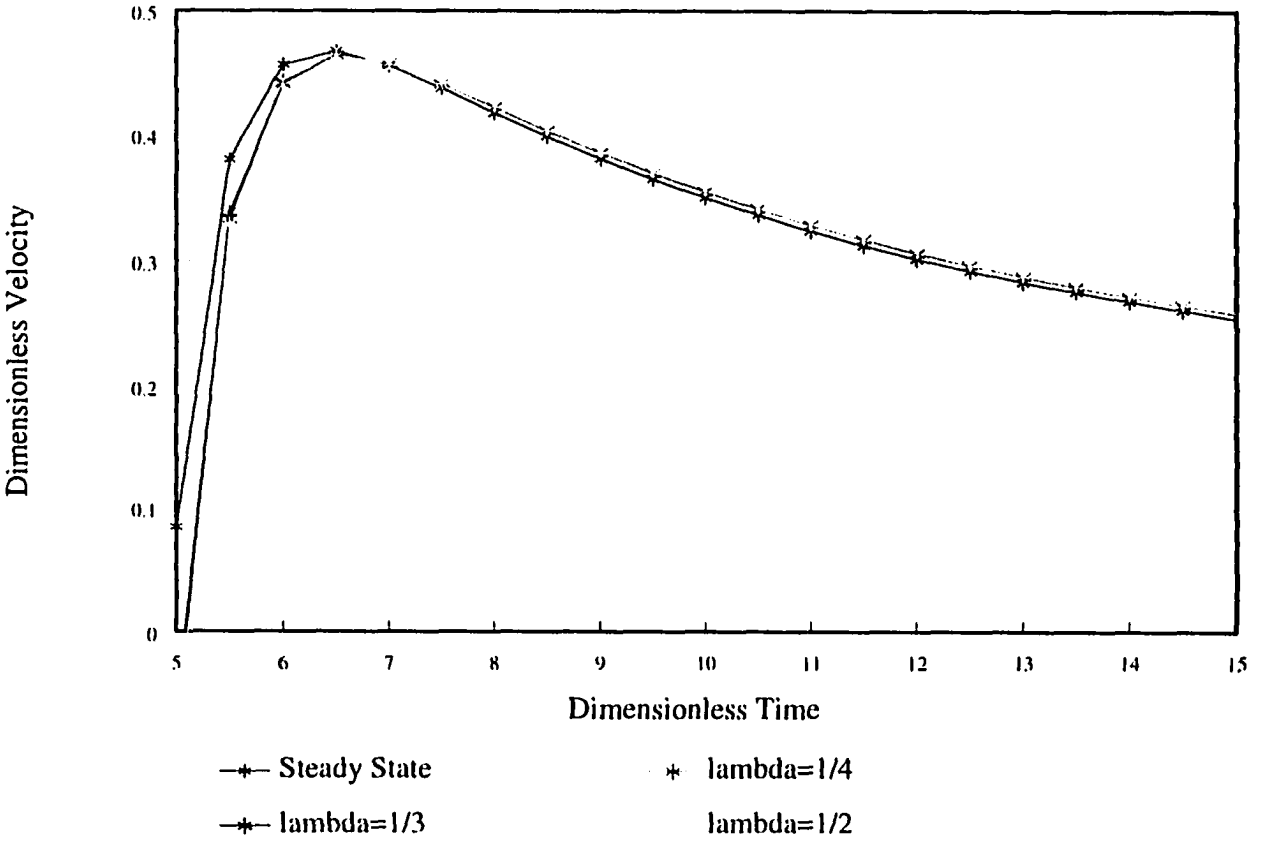

Figure 52: Heated Region Growth Rate During CO_2 Release for $q=q_0t^{-\lambda}$

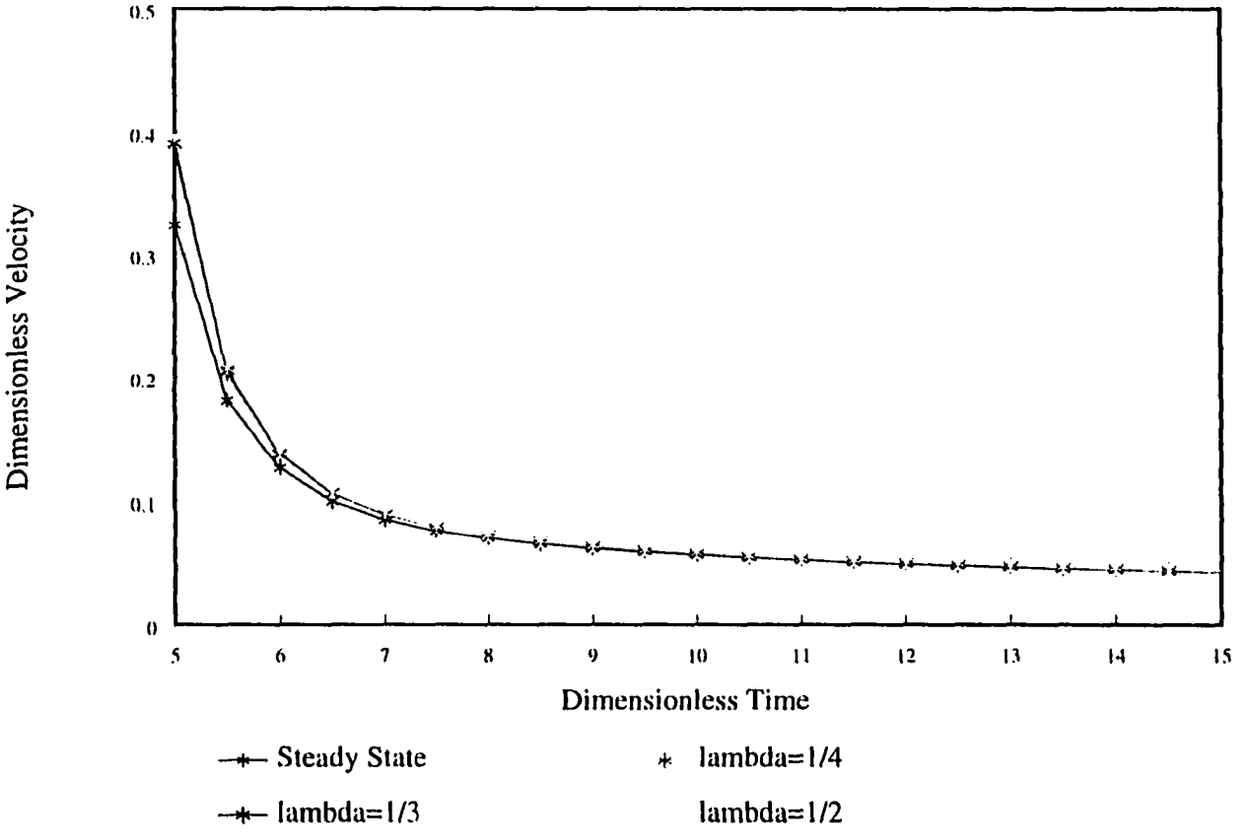

Figure 53: Dry Region Growth During CO_2 Release for $q=q_0t^{-\lambda}$

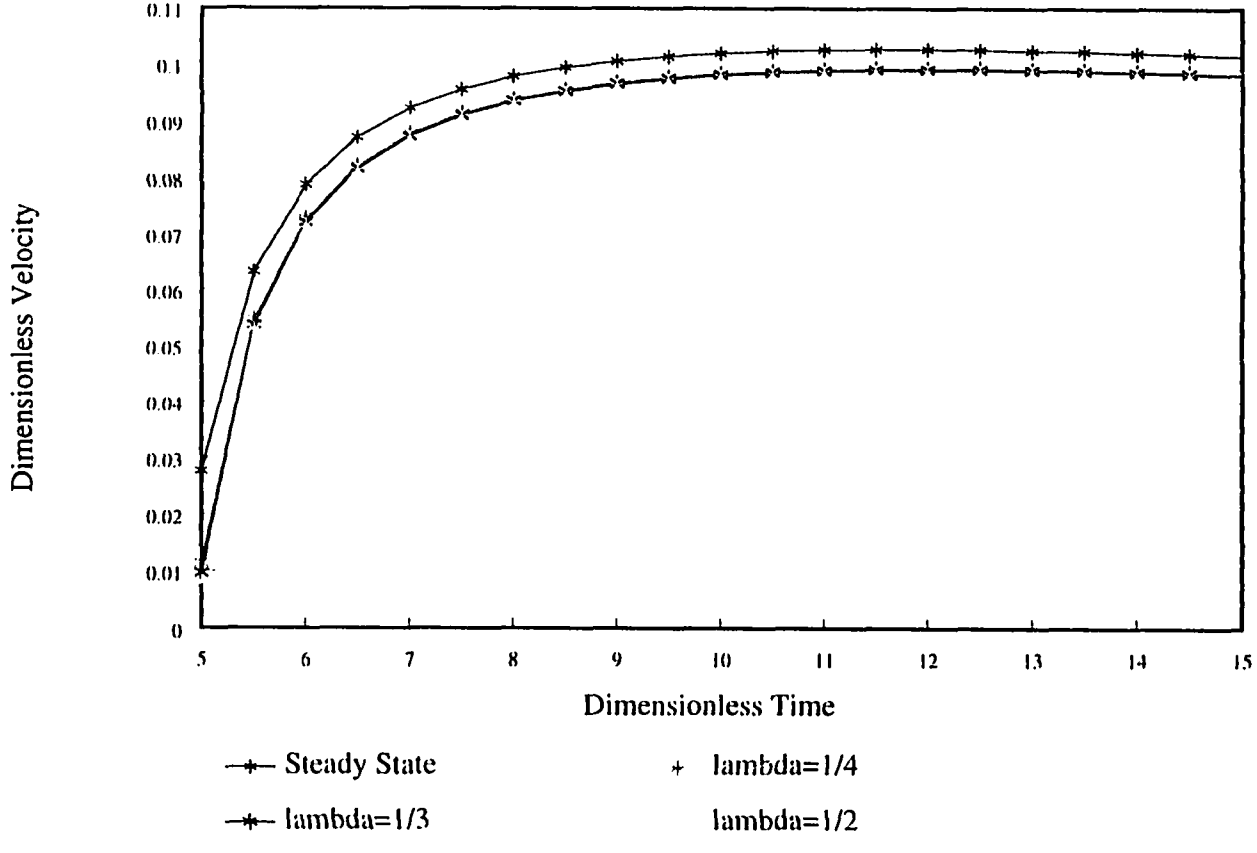

Figure 54: CO_2-Free Region Growth Rate During CO_2 Release for $q=q_0t^{-\lambda}$

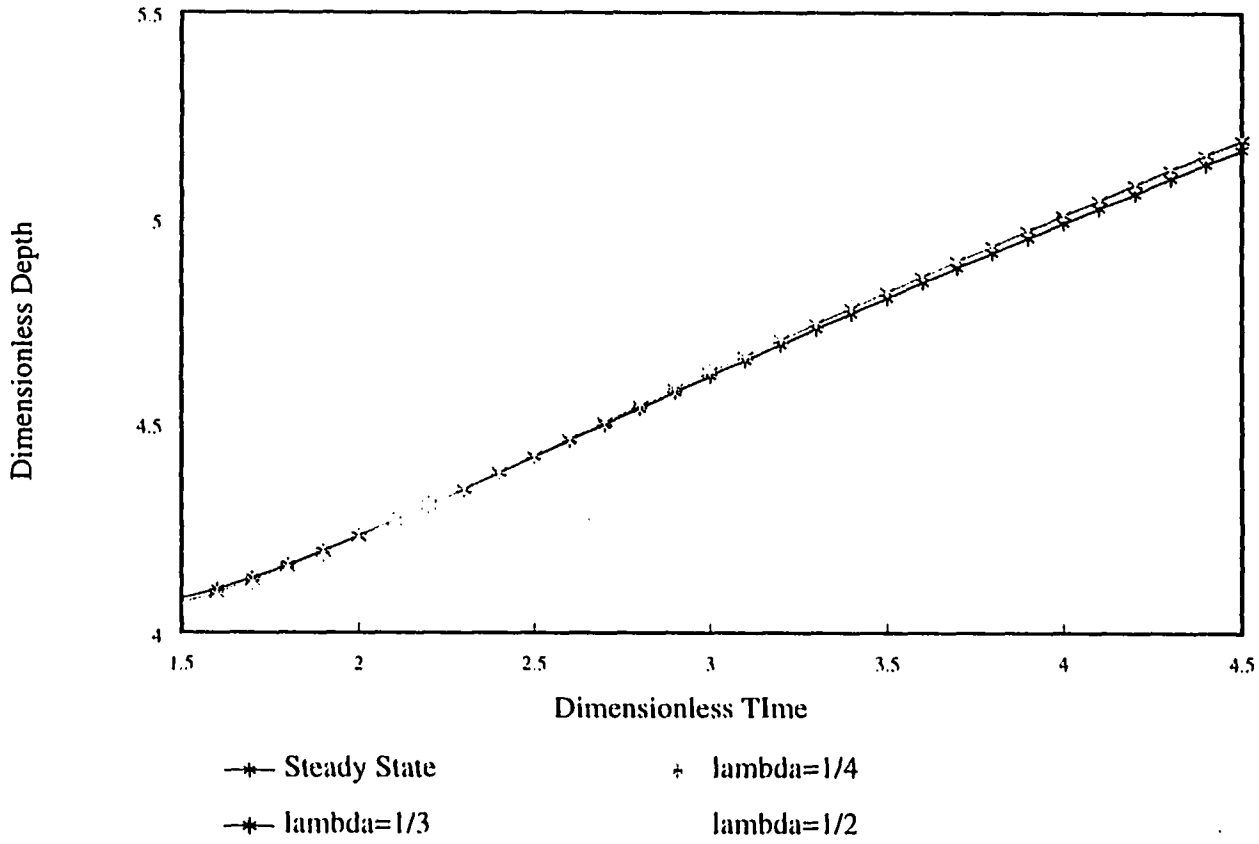

Figure 55: Heated Region Growth During Evaporation for $q=q_0t^{-\lambda}$

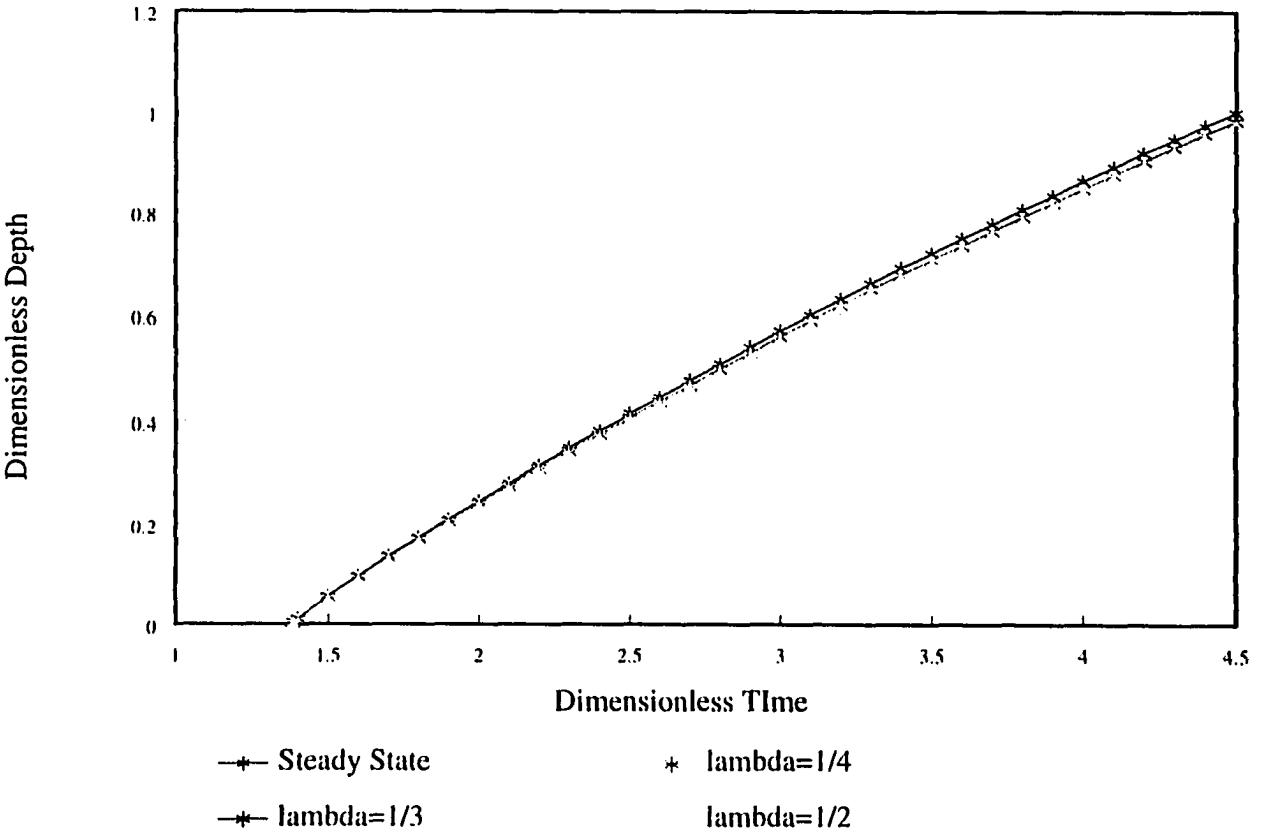

Figure 56: Dry Region Growth During Evaporation for $q=q_0t^{-\lambda}$

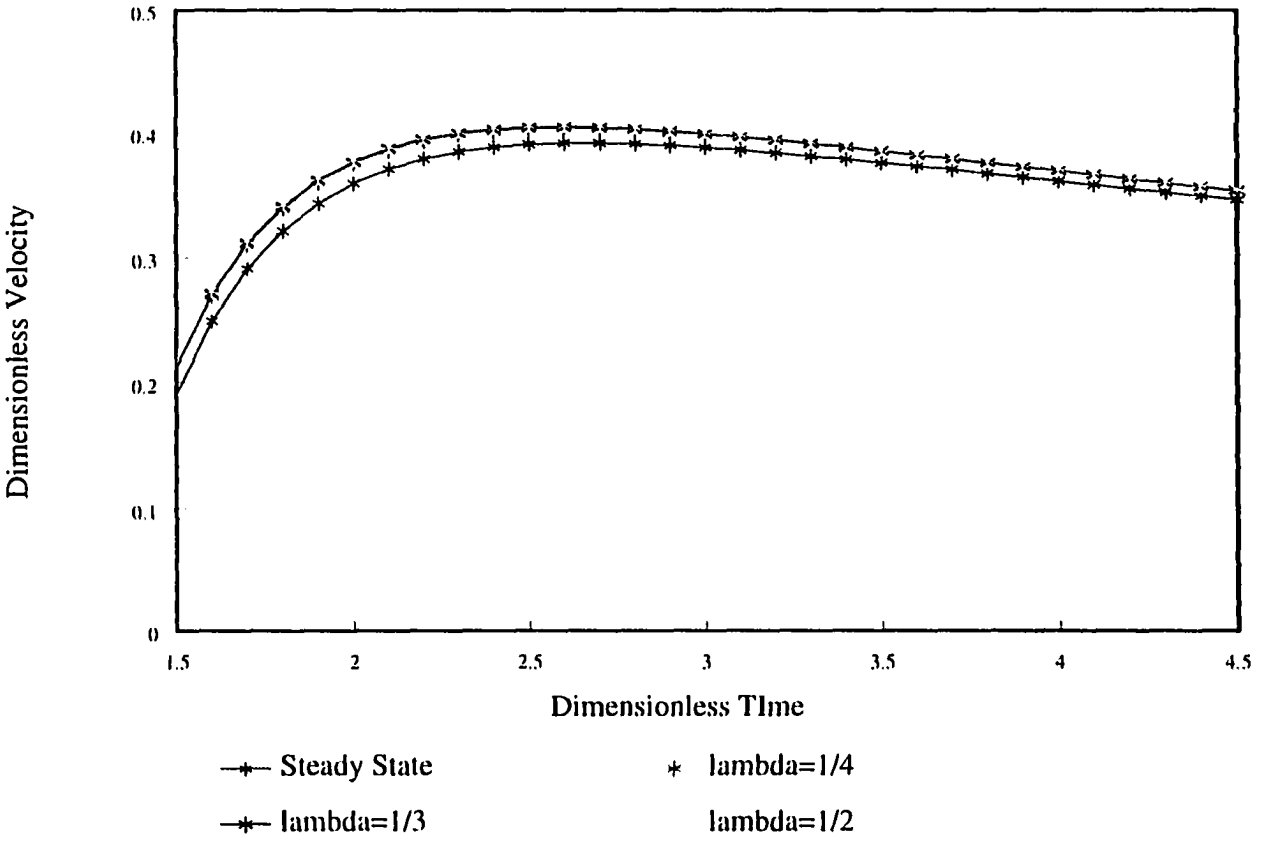

Figure 57: Heated Region Growth Rate During Evaporation for $q=q_0t^{-\lambda}$

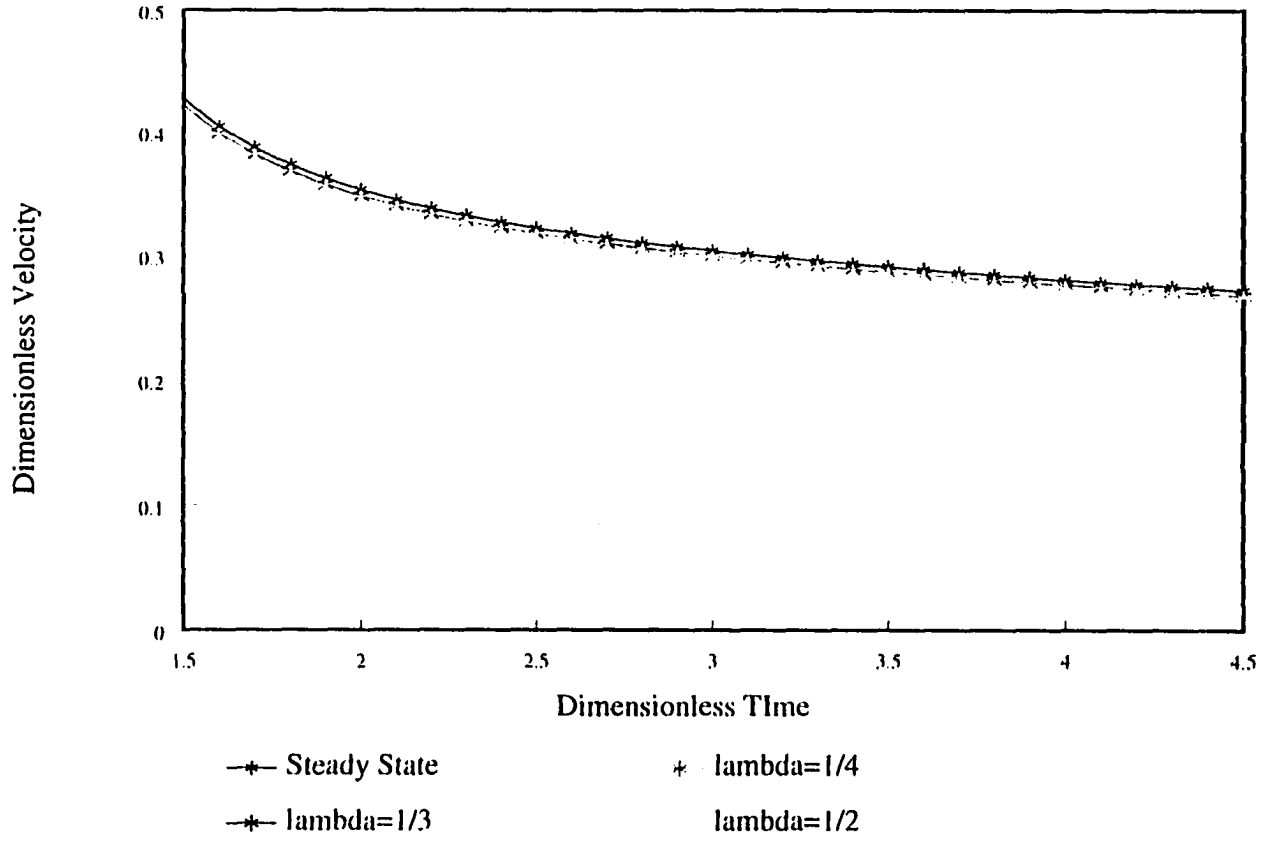

Figure 58: Dry Region Growth Rate During Evaporation for $q=q_0t^{-\lambda}$

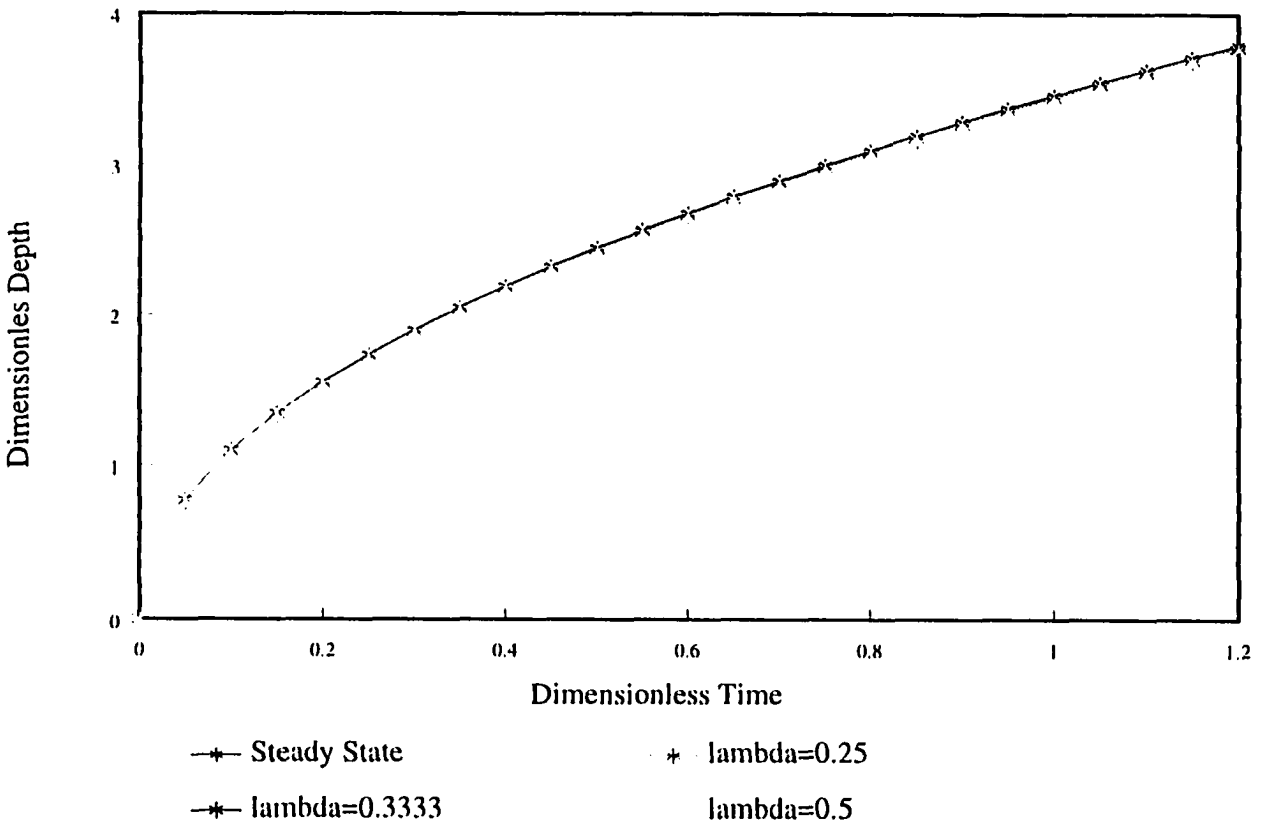

Figure 59: Heated Region Growth During Heating for $q=q_0t^{-\lambda}$

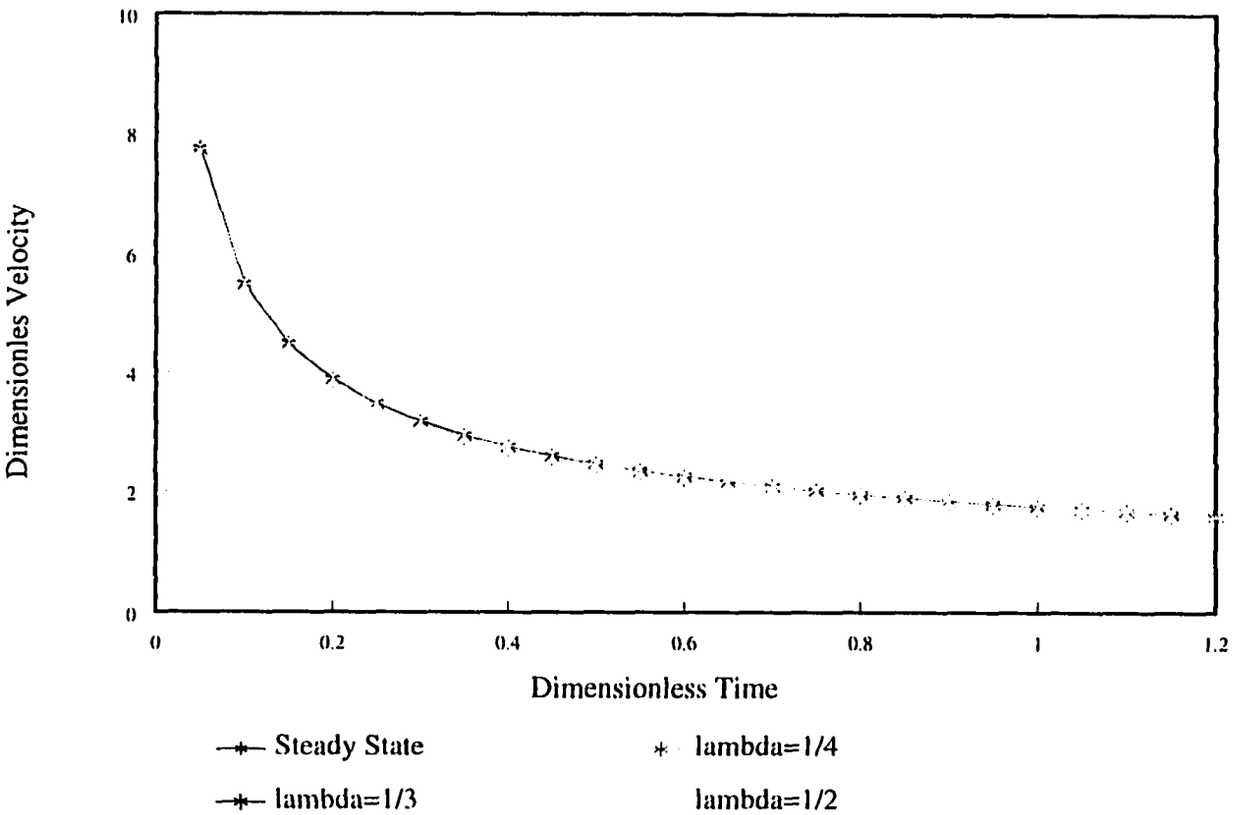

Figure 60: Heated Region Growth Rate During Evaporation for $q=q_0 t^{-\lambda}$

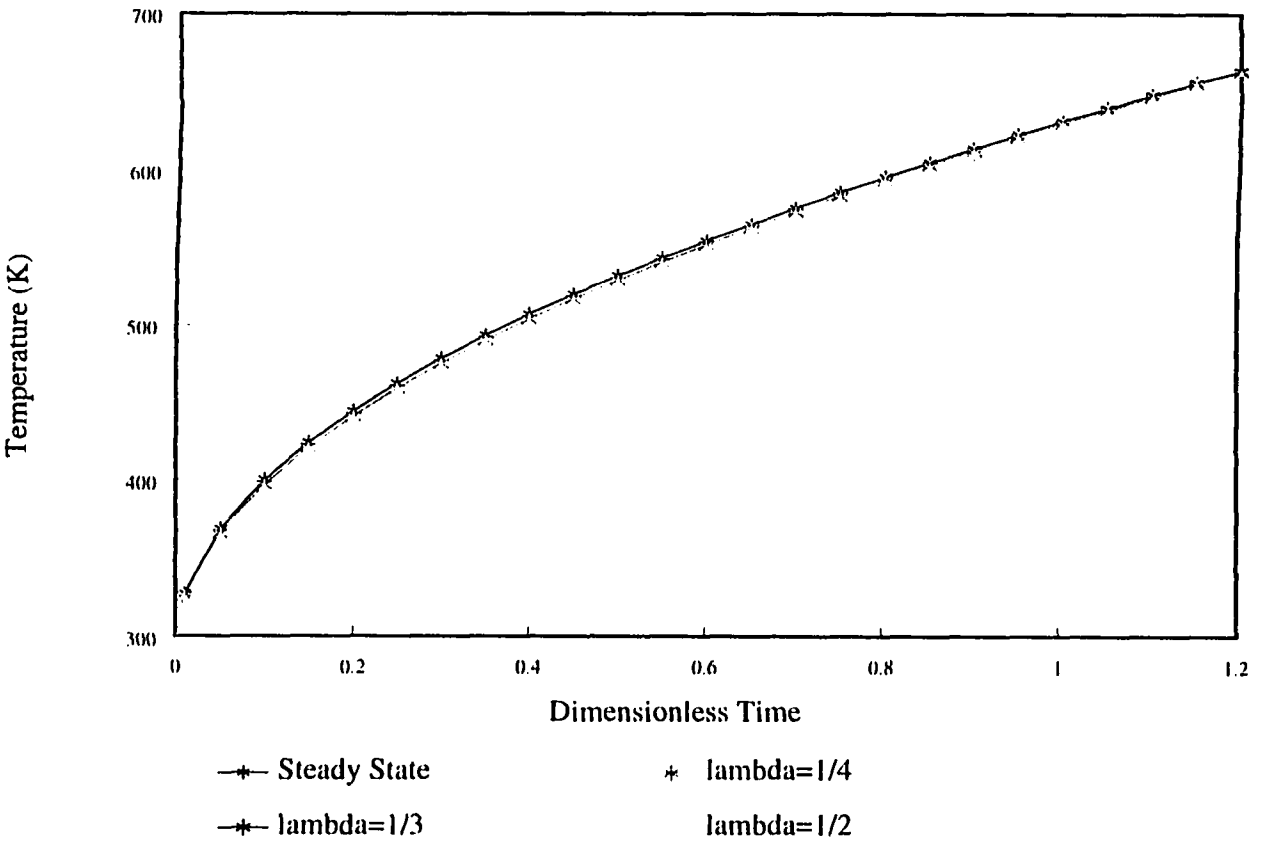

Figure 61: Surface Temperature During Heating for $q=q_0t^{-\lambda}$

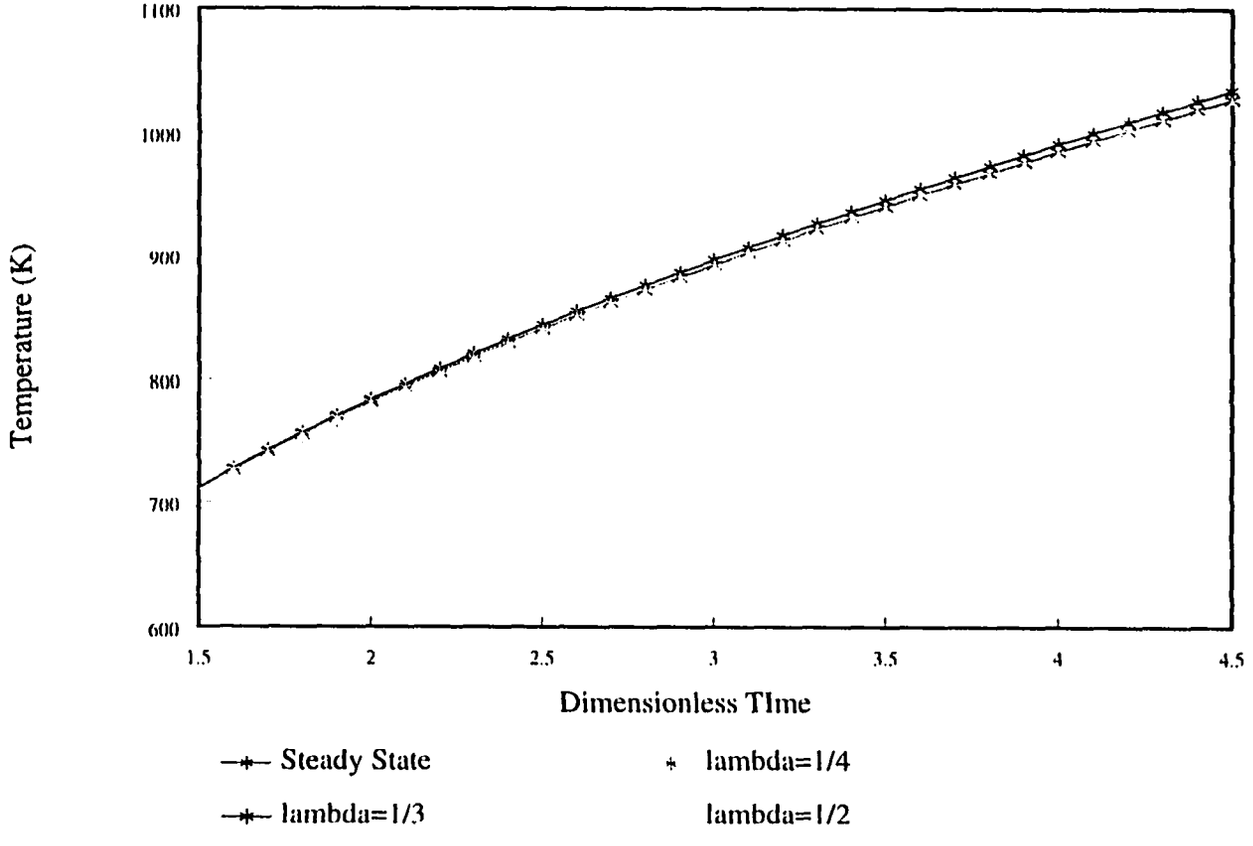

Figure 62: Surface Temperature During Evaporation for $q=q_0t^{-\lambda}$

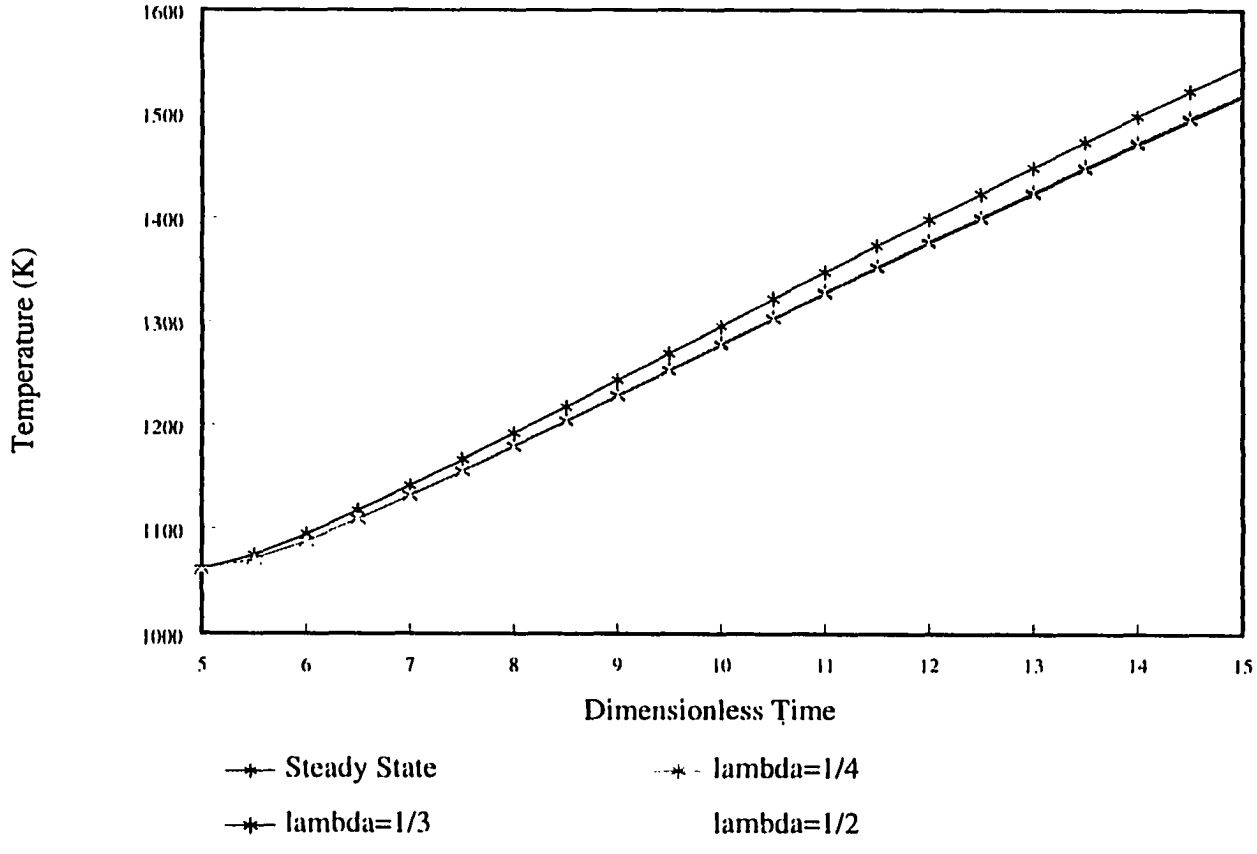

Figure 63: Surface Temperature During CO_2 Release for $q=q_0t^{-\lambda}$

4.3.2.3. Linearly Decreasing Surface Heat Flux

Although the rate of cooling (or decrease in the surface temperature) in an actual MCCI case would be represented by a surface heat flux in forms of the ones given above, the linearly decreasing surface heat flux case is presented here for the informational purposes. This type of surface heat flux is more applicable to the melting/solidification of the binary alloys and melting/freezing problems involving water and other liquids.

As can be seen from the results given in Figures 64 and 65, the linearly decreasing surface heat flux has no or little effect on the erosion rate and depth, and growth and growth rate of the other regions. This is mainly due to the time required for the heat flux to decay below the latent heat of each decomposition reactions is much longer, and the thermal diffusivity of the concrete compensates the additional heat provided to the concrete.

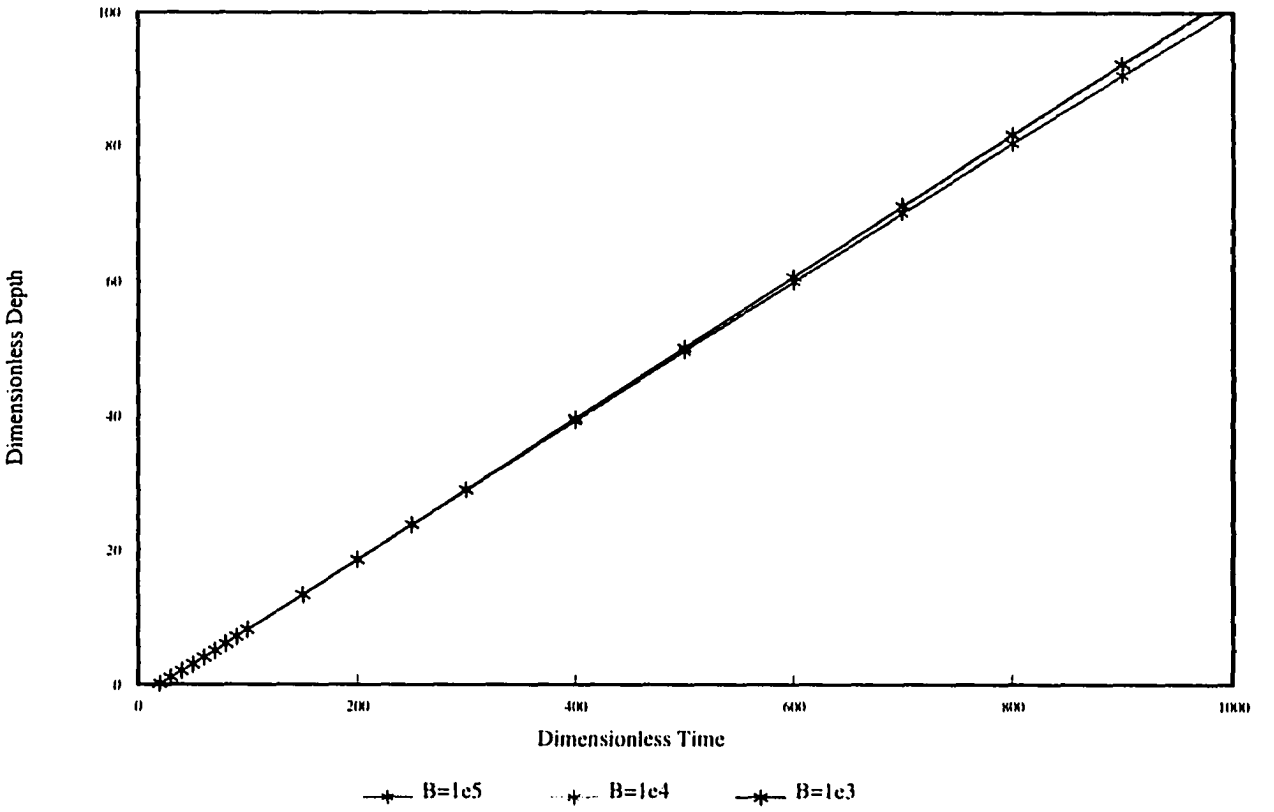

Figure 64: Erosion Growth for $q=q_0-Bt$

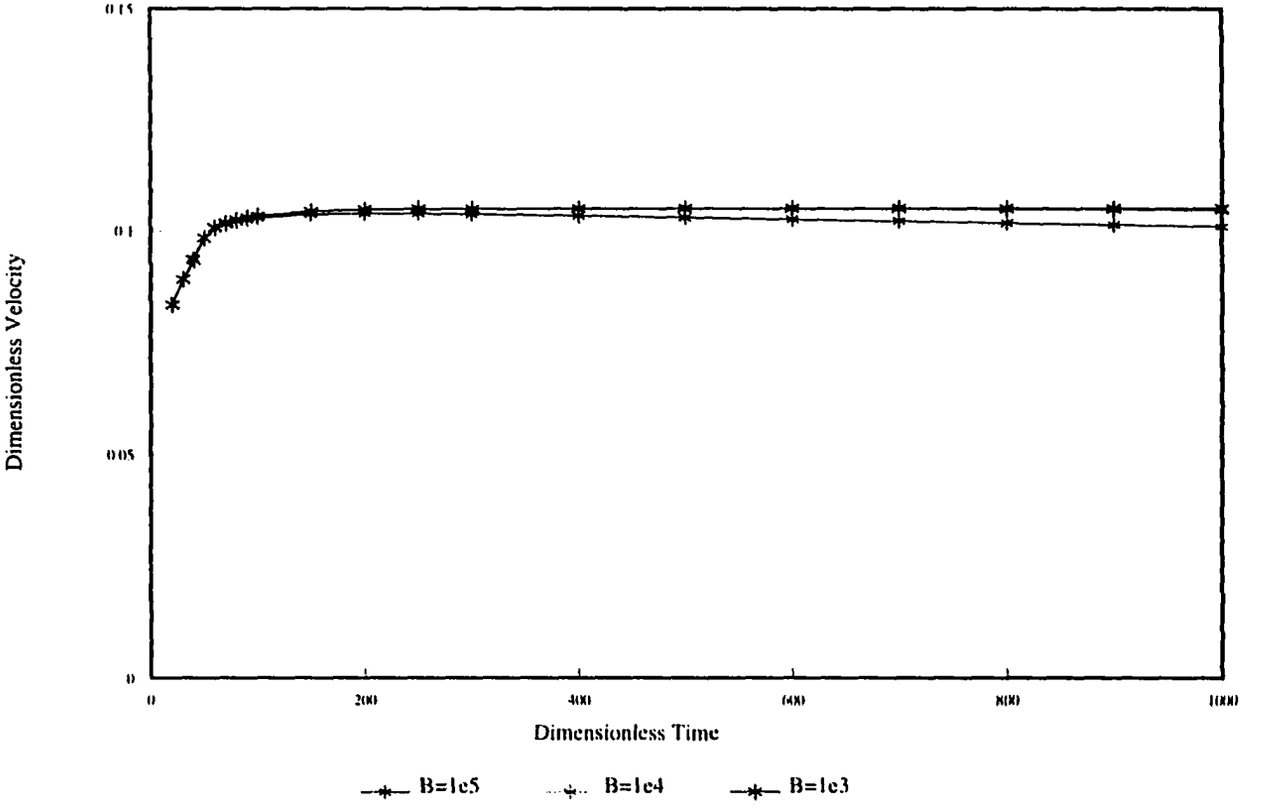

Figure 65: Erosion Growth Rate for $q=q_0-Bt$

4.3.3. Comparison with Melt/Concrete Interaction Experiments

The multi-region transient concrete erosion/decomposition model can be used not only in conjunction with larger core/concrete interaction and aerosol release models such as CORCON [7], WECHSL [10], or VANESA [9], but also to predict concrete erosion and decomposition as a stand alone code. The solution to the concrete decomposition and ablation has been reduced to a simple method, and thus it can be solved in a simple spreadsheet in a shorter calculation time and without requiring large codes. In the following subsections, the results from using the code alone are compared with to date concrete erosion and decomposition experiments and models that include both constant and time dependent surface heat fluxes. Those experiments have investigated cases where both the melting concrete is removed immediately, and more realistic representations of the MCCI where interactions take place in a cavity structure with melt remaining in contact with eroded and decomposed concrete. Most of all available experiments have been performed in Sandia National Laboratories in the U.S.A. and KfK Laboratories in Germany. Comparing the model with the data from those experiments that were performed to investigate the specific cases such as solidification, water existence, and chemical energy contribution is also important since good agreement with the experimental data would prove that the model can be applied to all types of molten core/concrete interactions.

Table 6 presents a summary of the experiments that are used for comparison and validation of the model derived in this study. The summary of the results and this validation is given later in this section.

Table 6: Experiments Used for Verification of Multi-region Erosion Model

Test	Heat Flux Type	Remarks
Radiant Heat Test 3-15	constant	vertical surface; radiant heat flux
Radiant Heat Test 7-4	constant	
Radiant Heat Test 8-31	constant	
Radiant Heat Test 10-26	constant	
Radiant Heat Test 12-32	constant	
BETA V0.2	constant	interaction in a cavity; sustained heat flux
BETA V0.3	constant+exponential decay	interaction in a cavity; high heat flux, cooldown
BETA V1.3	exponential decay	interaction in a cavity; cooldown; oxidic melt effect investigated
BETA V1.8	constant+exponential decay	interaction in a cavity; very high heat flux, cooldown
BETA V2.1	constant	interaction in a cavity; solidification of melt investigated
SWISS-1	constant	interaction in cavity; sustained heat flux; water introduced to interaction to study overlying water pool effect
SWISS-2	constant	
TURC1SS	exponential decay	interaction in cavity; natural cooldown
TURC1T	exponential decay	

4.3.3.1. Constant Surface Heat Flux Experiments

Sandia's Radiant Heat Tests:

One of the earliest experiments that was conducted to observe detailed concrete erosion and decomposition phenomena was performed at Sandia National Laboratories by Muir [16]. Although the experiments included both plasma jet and radiant heat tests, the interest in this study is only the latter one which does not couple the effects of pressure and spallation with quiescent erosion.

The tests were performed by exposing cylindrical concrete specimens with 15 cm diameter and 8 cm height to a constant surface heat flux in a radiant heat facility. The surface of the specimens were mounted vertically so that the molten concrete debris flowed off the surface as the concrete melted. The concrete used in the test included both limestone and basaltic types which are the most common types of concrete used in the nuclear power plant construction. Out of 12 radiant test that were performed, and listed in Table 7, only 5 were analyzed here since the others either did not result in concrete erosion, or failed to provide data.

The results from the general solutions given earlier in this chapter were obtained for limestone concrete with the properties given in Table 2. When Muir's test results are compared with the basaltic concrete, the properties that are applicable to basaltic concrete are used. These basaltic concrete properties listed in Table 8 are also used for the model comparison with other tests that used basaltic concrete later in this chapter.

Table 7: Sandia Radiant Heat Tests [16]

Test No	Concrete Type	Incident Heat Flux (W/m2)	Test Time (min)	Remarks
RH1-2	L	116	4.94	Large variations in heat flux after 2.7min, no data
RH2-6	L	116	5.19	No thermocouple data obtained; test terminated prematurely
RH3-15	L	118	3.86	Equipment failure-test terminated prematurely
RH4-25	B	105	8.33	Thermocouple data questionable; no data given
RH5-21	L	102	9.82	Power control malfunctioning; no data given
RH6-5	L	103	10.10	Center heater element failed; no data given
RH7-4	L	105	8.56	Arcing between electrodes; test terminated prematurely
RH8-31	B	104	8.05	Arcing between electrodes; test terminated prematurely
RH9-12	L	103	9.17	Test terminated early; no data given
RH10-26	B	104	11.17	-
RH11-16	L	32	59.80	No ablation; questionable thermocouple data
RH12-32	B	64	29.80	Questionable thermocouple data

Table 8: Basaltic Concrete Properties Used in the Model

Parameter	Value
Density (kg/m^3)	2500
Specific Heat (kJ/kgK)	1.52
Initial Thermal Conductivity of Concrete (W/mK)	1.5
Thermal Conductivity of Dry Concrete (W/mK)	1.1
Thermal Conductivity of Decarboxylated Concrete (W/mK)	1.0
Decomposition Enthalpy of Evaporation (MJ/kg)	0.3417
Decomposition Enthalpy of Decarboxylation (MJ/kg)	0.0381
Decomposition Enthalpy of Oxide Decomposition (melting) (MJ/kg)	0.3864
Decomposition Temperature of Water (K)	690
Decomposition Temperature of Carbon dioxide (K)	1060
Decomposition Temperature of Oxides (K)	1670

The erosion rates derived from the test data are compared with the results of the model developed in this study, and are tabulated in Table 9. The results the model calculated agrees very well with the experimental data. The lack of agreement in the results of the test RH8-31 was analyzed by Corradini [13], and it was concluded as an unnoted difference in concrete or erosion behavior. The experimental specimen that was used in that test was similar to that used in the other two tests RH12-32 and RH10-26. The difference might have been caused by an error in the thermocouple data from which the ablation velocities are derived. Muir discussed the placement of thermocouples and their propagation and found that the error in thermocouple depths found by radiograph was about +/- 0.15 cm which can cause a significant error.

As is shown in Table 9, the net surface heat flux is lower than the incident flux. This reduction in the incident heat flux, according to Muir's results, is due to the combined effects of emitted radiation (approximately 13 to 53 percent), convective blockage (about 1 to 9 percent), and energy absorption by the gas and melt flows (varying from 0 to 2 percent).

Comparing the results from the model with the visual and photographic observation of the Muir's experiments shows that they are in good agreement. Each test performed had characteristic cyclic surface color changes of the surface of the concrete. This was noted as "... from normal gray to light gray, to dark gray, to very dark gray, to very light gray, and finally to very dark gray (almost black)..." [16]. This can be analyzed as the phases of concrete decomposition. For the heat flux of 1.2 MW/m^2, the final dark appearance of the surface and flow down of the first melt was observed at about 27 seconds for limestone while it was at 42 seconds for basaltic concrete. The model predicted the melting to occur at 35 seconds

for limestone and 38 seconds for the basaltic concrete. The small difference in these times can be explained as the range of the melting process of concrete. The model assumes a single melting temperature. In the actual melting process, this is a range of 1300-1700 K.

The same test results were also used to compare another concrete erosion (single region transient) model developed by Corradini [13] which was described in Chapter 1 of this study. The results from that model are also included in Table 9.

The multi-region model predicted closer ablation velocities to measured ones than to ones that were calculated in Corradini's one region transient model. This difference is mainly because of different thermal diffusivities in the different decomposed concrete regions and the depth of those regions, since the multi-region model calculates also the effects of the sensible heat stored in the concrete beyond the erosion front. As it mentioned in Section 4.3.1, the delay between the times when the melting front and the thermal front reach their steady state erosion velocity causes an overestimation of the erosion velocity if the thermal front velocity is used for the erosion velocity. This difference can be seen when the results of the single and multi-region models are compared in Table 9.

Table 9: Comparison of Constant Heat Flux Results with Muir's Experiments [16] and One-Region Transient Model [13].

			Velocities (cm/hr)		
Test ID	Incident q" (MW/m^2) [16]	Surface q" (MW/m^2) [13]	RHT [16]	One-region [13]	Multi-region
RH3-15	1.18	0.441	17.5	18.5	17.67
RH7-4	1.05	0.392	17.0	16.7	16.52
RH8-31	1.04	0.228	16.0	11.5	10.92
RH10-26	1.04	0.228	11.0	11.5	10.92
RH12-32	0.64	0.141	6.5	6.9	6.76

BETA Tests:

The BETA (Beton-Schmelz-Anlage) experiments were conducted at Karlsruhe Nuclear Research Center (KfK) to investigate the melt/concrete interactions in a large-scale melt facility using internally heated simulated core melts [60, 85]. The experiments covered a wide range of temperatures and power rates typical of accident conditions. Table 10 lists the experiments conducted in the BETA test program.The BETA V0, V1 and V2 test groups used silicate concrete, while limestone type concrete is used in the V3 test group. The experiments continued with the V4 and V5 series, but only the first three series are used for comparison and validation of the multi-region erosion and decomposition model of this study, since the results from those three series were available to the author.

The BETA tests were conducted by pouring a melt, typically consists of 300 kg of a metal phase and 200 kg of an oxide phase, into a cylindrical concrete crucible with an initial diameter of 38 cm. In the crucible, the melt was heated electrically by an induction coil. Depending on the purpose of the experiment, the initial composition and the pouring temperature of the melts, as well as the power in the melt are defined and measured during the experiment. Some of the experiments were conducted to study the melt/concrete interaction at high temperatures, meaning crust formation is not influential, while some studied the effect of solidification process in the melt. Although the V0 group was conducted to test the equipment and measurement systems, their results provided useful data, as well. In this subsection, the data from the BETA experiments that can be represented as constant melt power experiments, which are the BETA V0.2 and V2.1, will be compared with the model's results. Time dependent surface heat flux type of interaction will be studied in the next chapter.

Table 10: BETA large-scale experiments (before 2/22/1986) [60, 85]

Experiment No	Melt Type	Power (kW)	Remarks
V0.1	Iron	0	Test of the facility
V0.2	Iron	400	Test of the facility
V0.3	Iron+Oxide	1700	Test of the facility
V1.1	Iron	Pulsed	Pouring failed
V1.2	Iron+Oxide	Pulsed	Lorentz forces
V1.3	Steel+Oxide	1000	
V1.4	Steel	0	Transient
V1.5	Steel	450	
V1.6	Steel+Oxide	1000	
V1.7	Steel+Oxide	1700	
V1.8	Steel+Oxide	1900	No dispersion
V1.9	Steel+Oxide	400-200	CaO added
V2.1	Steel+Oxide	120-150	
V2.2	Steel+Oxide	50-90	CaO added
V2.3	Steel+Oxide	240	CaO added
V3.1	Steel+Oxide	1700-2500	Limestone concrete; heating only between 0-66 sec
V3.2	Steel+Oxide	400-1000	Limestone concrete: heated 30 min
V3.3	Steel+Oxide	400-600	Limestone concrete: 60 min. heating
V4.1	Steel+Oxide	1000-300	600 mm. crucible diameter, 550 kg steel, 300 kg oxide with CaO

BETA V0.2 Experiment: This experiment, V0.2, together with V0.3 was the first sustained heating experiment and it was similar to the experiments in the test matrix [60]. The melt in the V0.2 experiment consisted of 300 kg of steel and the concrete crucible was silicate. The melt was heated to sustain the melt power around 400 kW, almost constant over some 40 minutes, with the exception of three power peaks between 1700 and 2100 seconds, which were applied to the test equipment, and a short power failure at 600 seconds (Figure 66).

The experiment is modelled using the constant incident heat flux at 400 kW per unit concrete surface (0.1136 m^2) which is reduced by approximately 62.5 percent to calculate the net surface heat flux (~150 kW) to include radiation, convection, and gas flow effects. The properties for the basaltic concrete were used to model the concrete decomposition. Figures 67 and 68 present the experimental data and the model results, respectively. The approximate erosion rate that was derived from the experimental data was 0.18 mm/sec, while the model calculated an erosion rate of 0.1796 mm/sec for 150 kW net surface heat flux, showing that the model is applicable and accurate for the cases when the eroded concrete is not removed from the interface, which is the actual case during a MCCI.

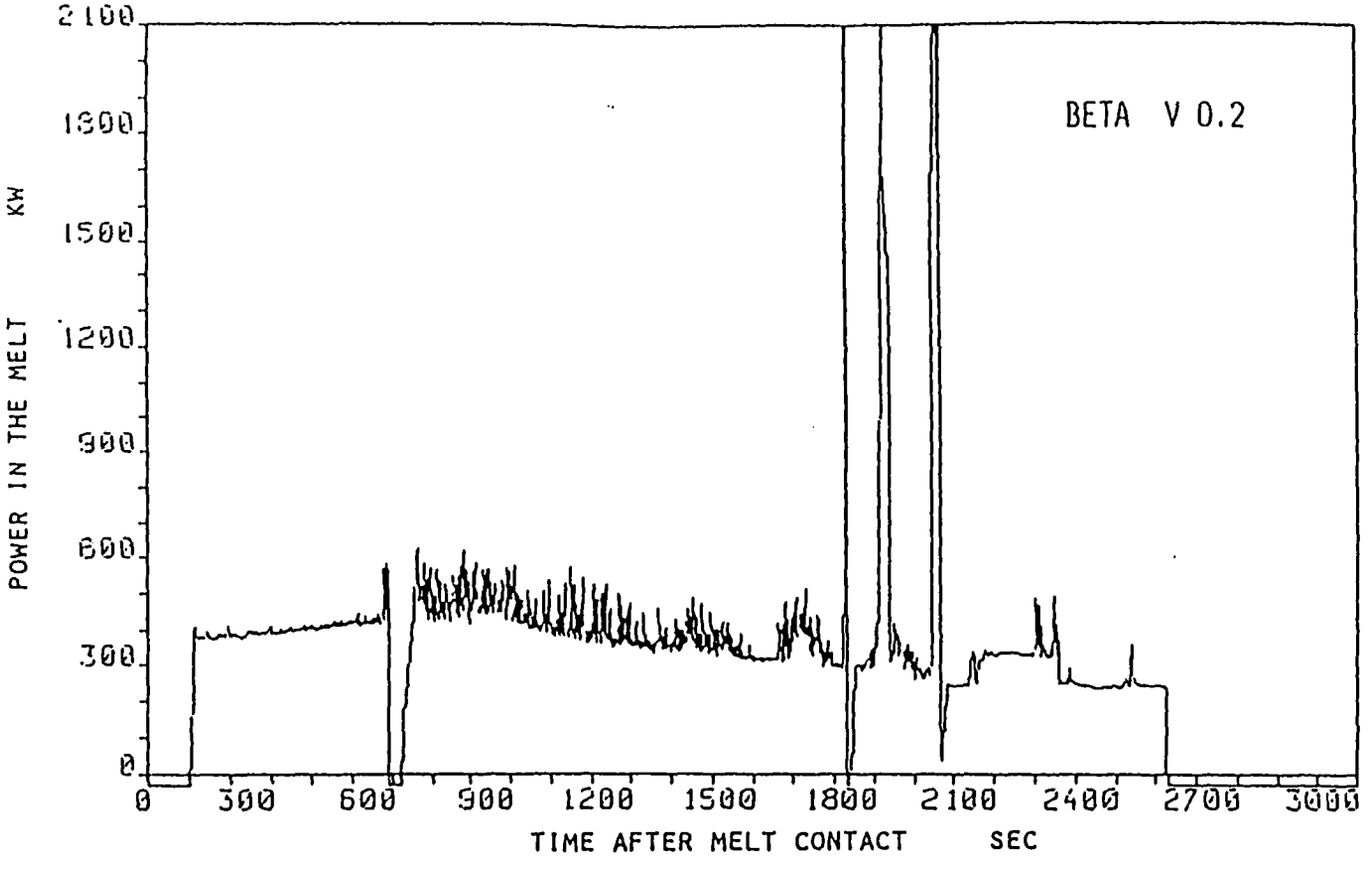

Figure 66: Melt Power for BETA V0.2 Test [60]

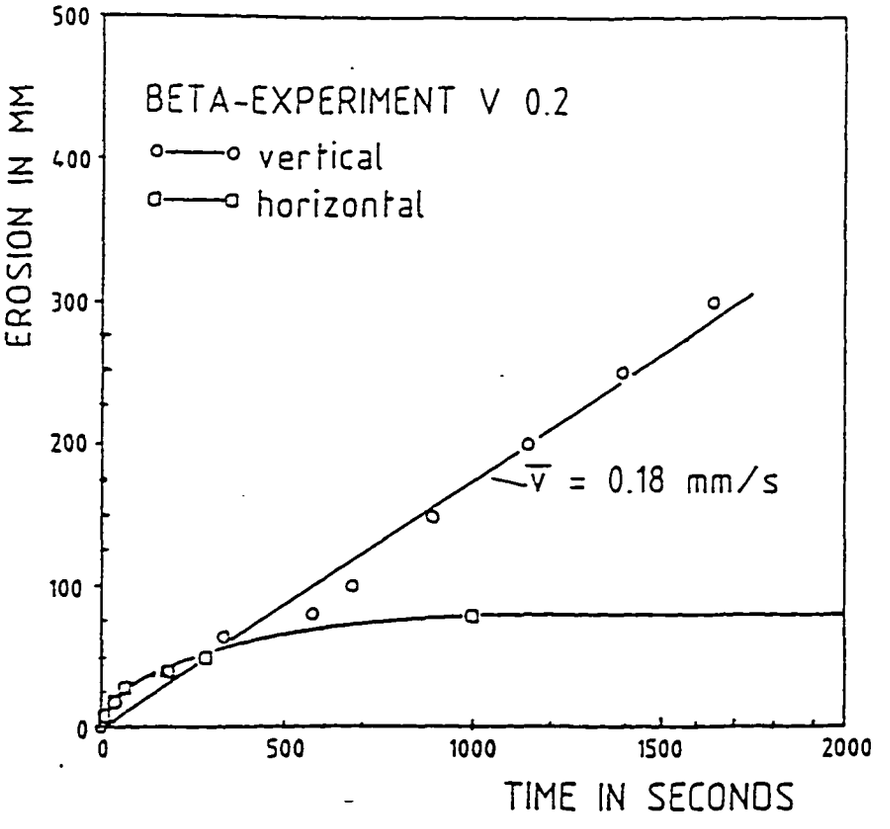

Figure 67: Erosion Depth Observed in BETA V0.2 Test

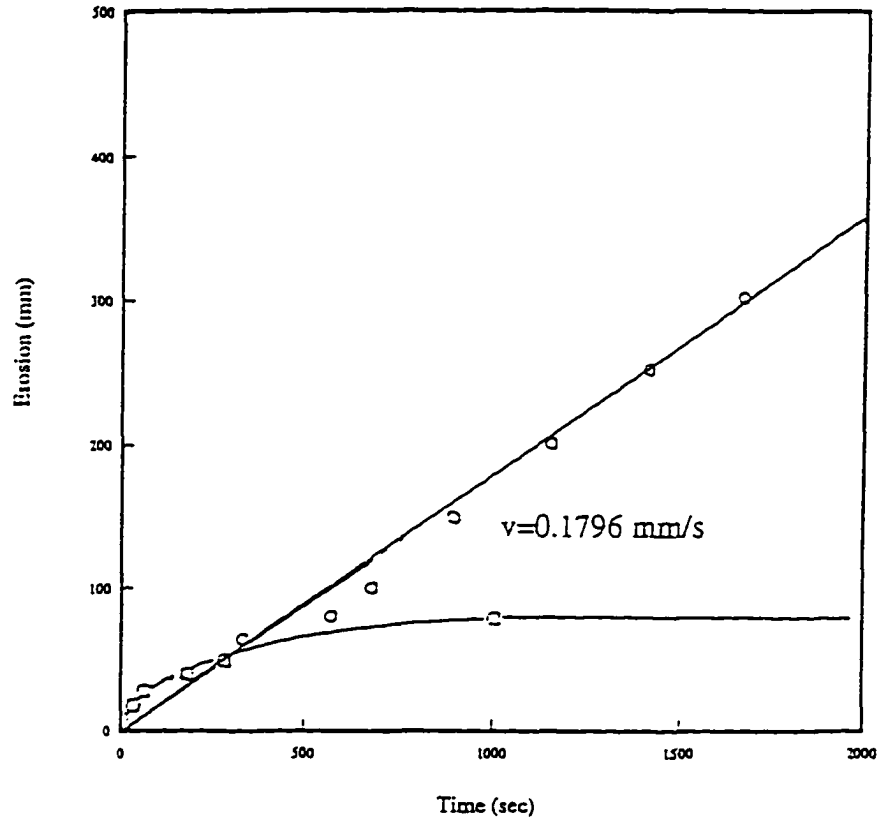

Figure 68: Predicted Erosion Depth by the Model for BETA V0.2 Test

BETA V2.1 Experiment: This experiment was performed to study the effect of the solidification process in the melt with applied lower power level [84]. The melt consisting of 300 kg of steel with 10% nickel and 150 kg of oxide (70% Al_2O_3, 30% SiO_2) was poured at 2000°C. The melt power was sustained at only 120 kW for over 100 minutes (Figure 69). This simulated the situation existing in a core meltdown accident for a long period of time.

The experiment is modelled again for basaltic concrete with a net surface heat flux which is about 37 percent of the incident flux. Figure 70 and 71 show the experimental data and calculated results for the erosion front. The approximate erosion rate that was derived from the experimental data was approximately 0.06 mm/sec while the model calculated an erosion rate of 0.0628 mm/sec for 150 kW net surface heat flux.

From the comparison of the model results with these two BETA constant heat flux experiment data, it can be said that the model is very accurate in calculating the erosion rates and depths for both high heat fluxes when erosion is fast, and low heat fluxes when erosion is slower and the melt solidification affects the concrete erosion and decomposition.

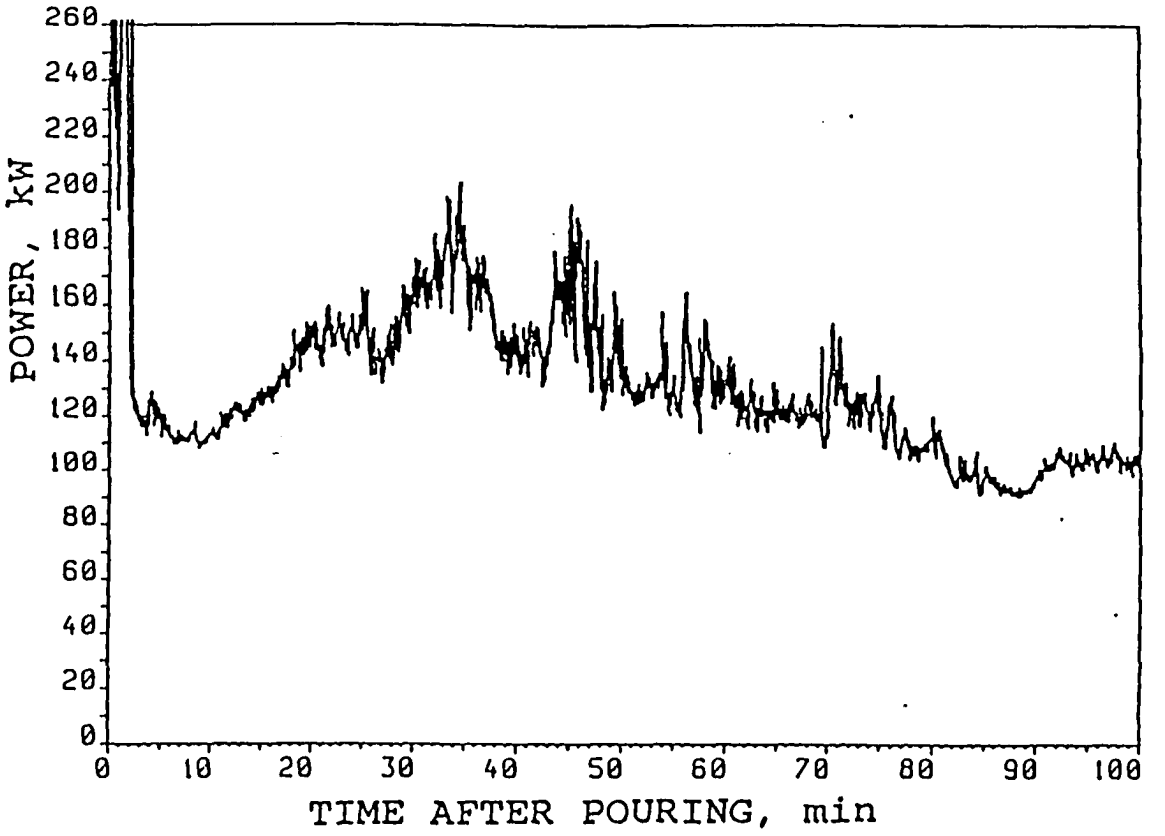

Figure 69: Melt Power for BETA V2.1 Test [84]

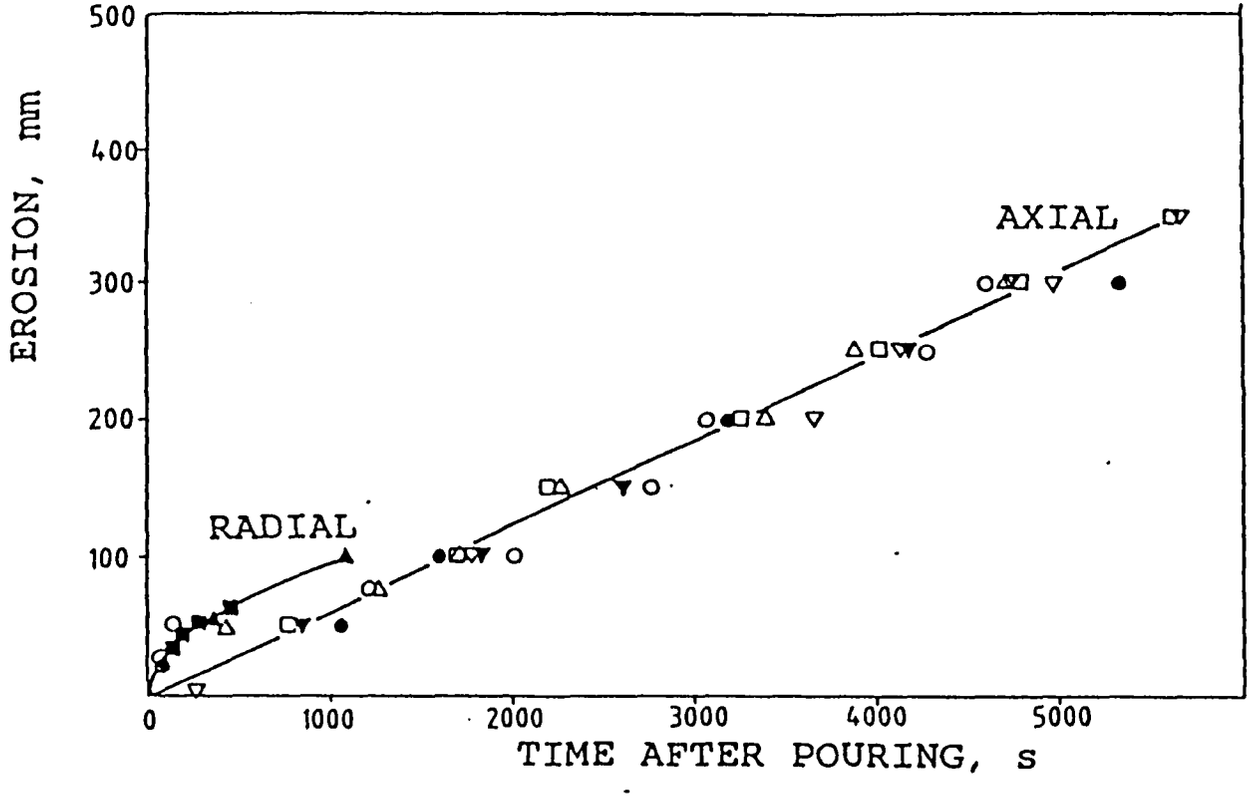

Figure 70: Erosion Depth Observed in BETA V2.1 Test

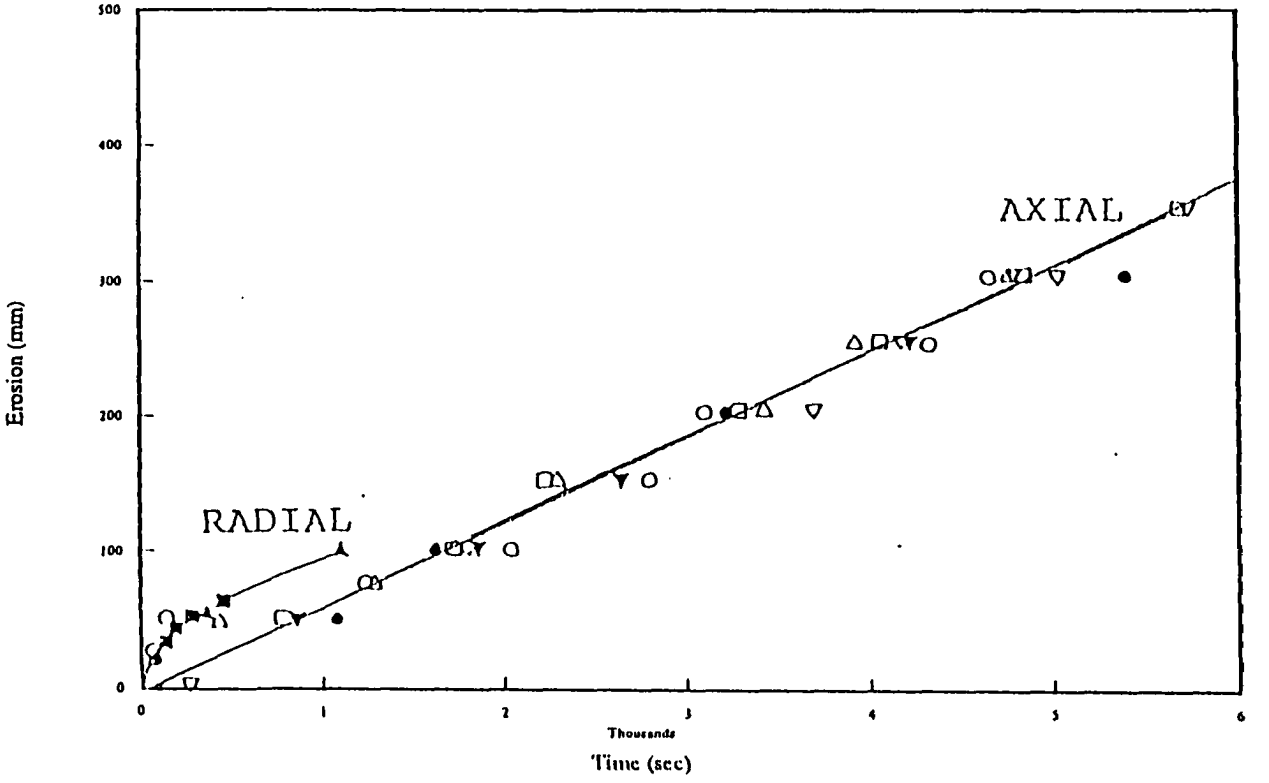

Figure 71: Predicted Erosion Depth by the Model for BETA V2.1 Test

SWISS Experiments:

SWISS1 and 2 tests were conducted at Sandia National Laboratories to examine the effects of an overlying water pool on high temperature melt interactions with concrete [83]. These tests were carried out with a melt of about 46 kg of type 304 stainless steel deposited onto a 21.6 cm diameter disk of limestone/common sand concrete. In the SWISS-1 test, water was added on top of the melt after about 12 cm of concrete had eroded. In the SWISS-2 test, water was added approximately 1 minute after the melt was deposited onto the concrete in order to accomplish the water addition before the concrete erosion started. Interactions were sustained for approximately 40 minutes in both tests.

The tests are modelled by using the constant heat flux case solutions of this study. The incident heat fluxes are calculated as ~70 kW based on the constant debris powers given in Figures 72 and 73, and the delivered debris mass of 44.6 kg for SWISS-1 and 44.2 kg for SWISS-2. The net surface heat fluxes are calculated using 62.5 percent reduction in the incident heat flux. The limestone concrete properties of Table 2 are used for the concrete.

The results for the erosion front from the SWISS-1 and SWISS-2 data are presented in Figure 74. Comparing the multi-region concrete decomposition model results given in Figure 75 show that the model overestimates the erosion depth when a 62.5 percent reduction of the incident flux is applied. Figure 76 shows the erosion front location based on a 2/3 reduction in the incident heat flux, and on corrected melt power for SWISS-1 between 10 and 15 minutes. In that case, the model predicts the erosion rate and depth closer to the experimental results than the case with 62.5 percent incident to net heat flux ratio case. The average erosion

rates derived from the data were 30.0 +/- 2.0 cm/hr for the SWISS-1 and 29.2+/-2.8 cm/hr for the SWISS-2 tests. The multi region model calculated the velocity (one for both tests, since 70 kW incident flux is used for both) as 28.6 cm/hr.

In the SWISS tests, the wet-dry front (i.e. dehydration front) was also investigated by using the thermocouple data for 400 K temperature isoterm. Figure 76 also presents the 400 K isotherm depth calculated by the model to be compared with the "wet/dry interface location" data from the SWISS-1 and SWISS-2 experiments given in Figure 77. The agreement of both shows that the model predicts not only the erosion front but also the dry region thicknesses accurately.

Another conclusion drawn from the tests was that the existence of the water during the melt/concrete interaction does not affect the erosion process of the concrete. This shows that the model is also applicable to the core/concrete interactions with water existence.

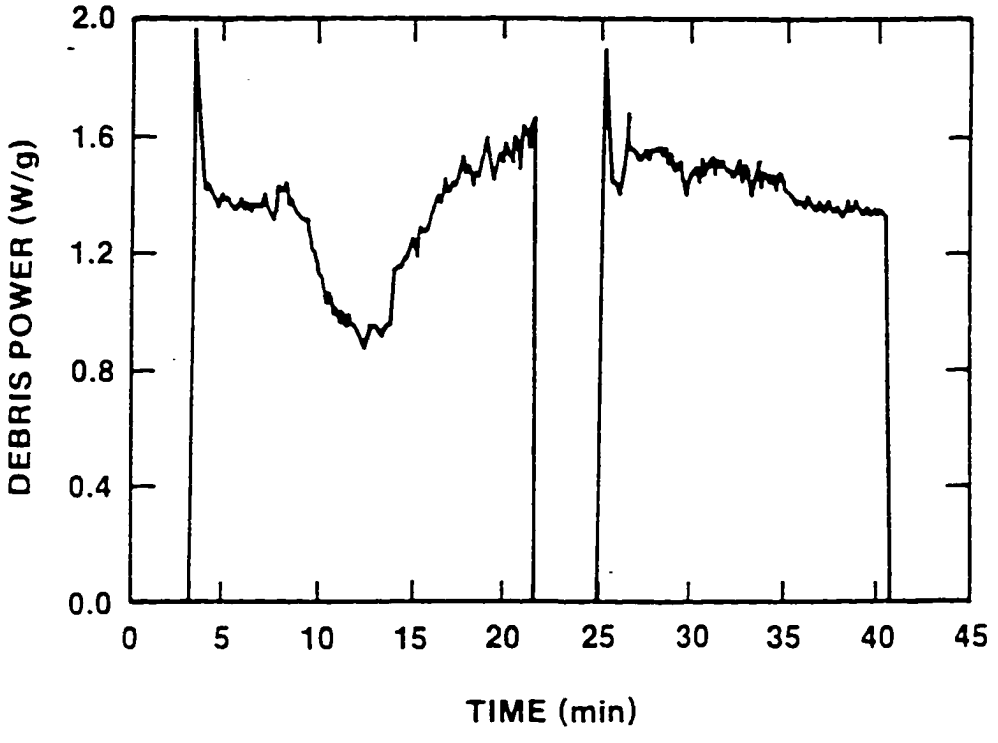

Figure 72: Melt Power for SWISS-1 Test [83]

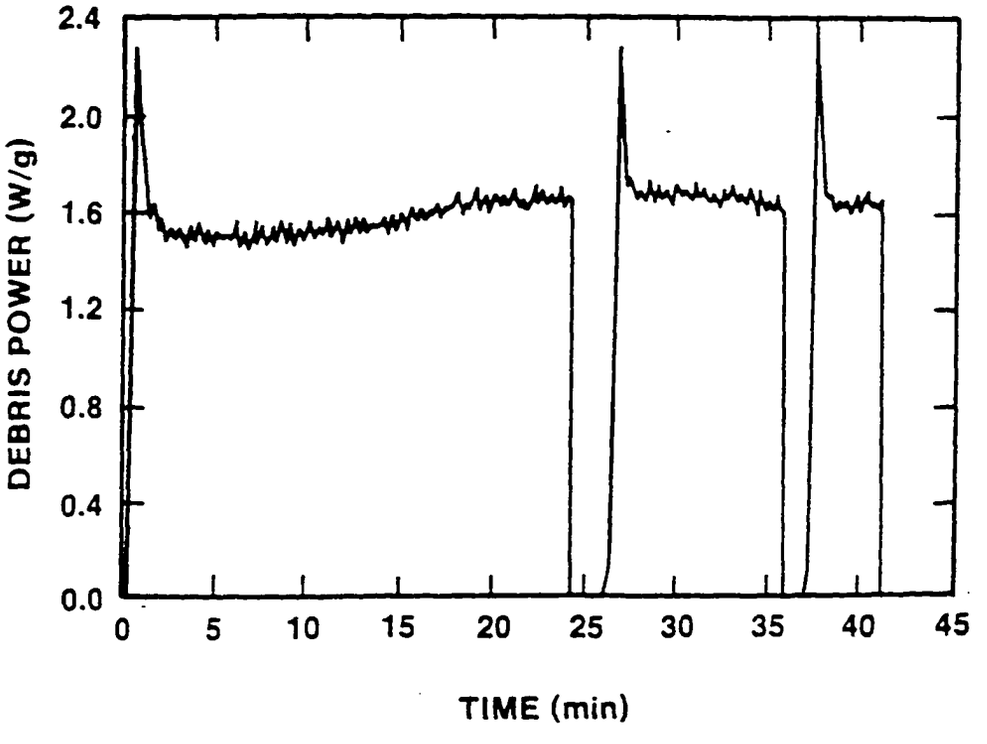

Figure 73: Melt Power for SWISS-2 Test [83]

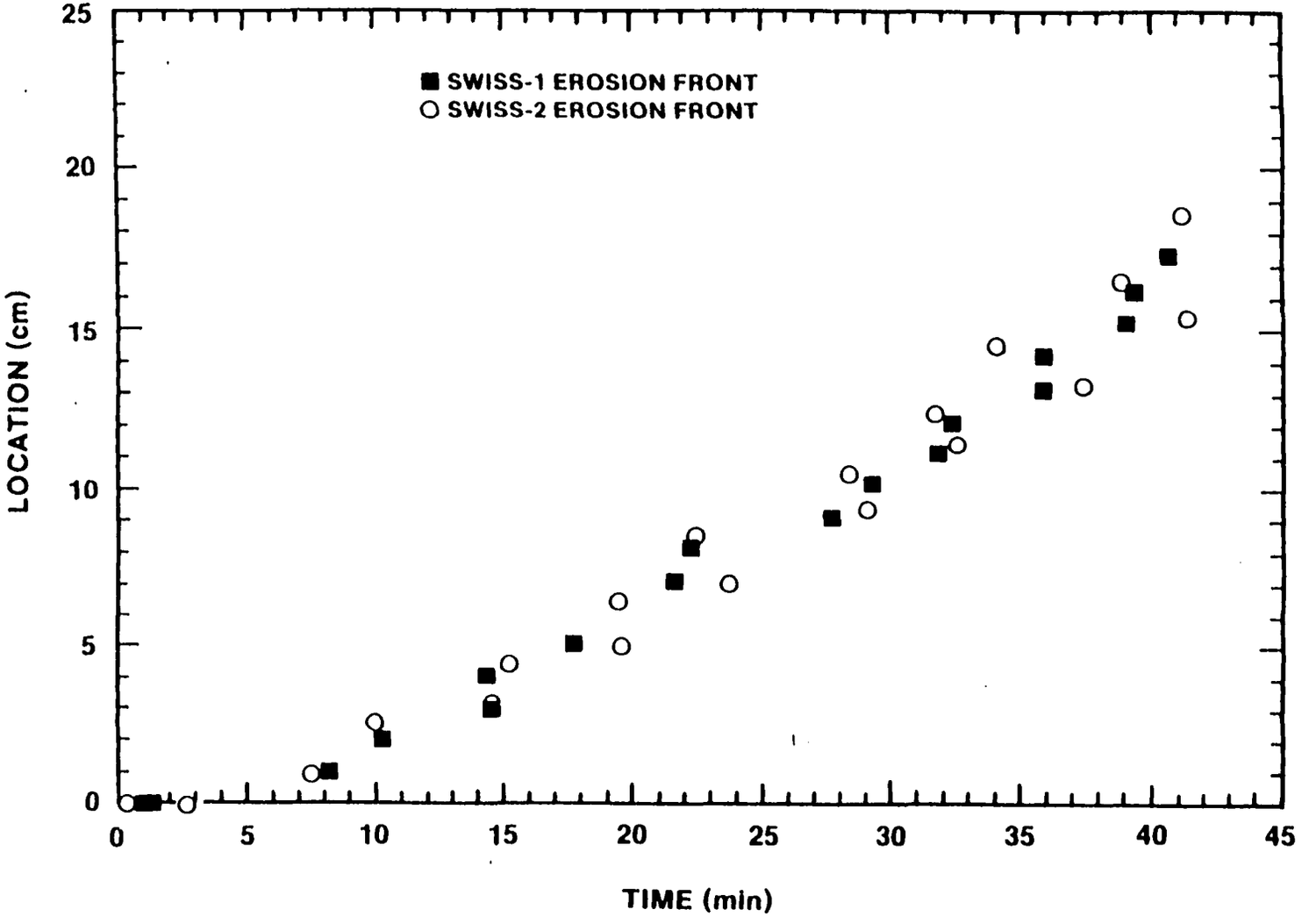

Figure 74: SWISS-1 and SWISS-2 Test Erosion Depth

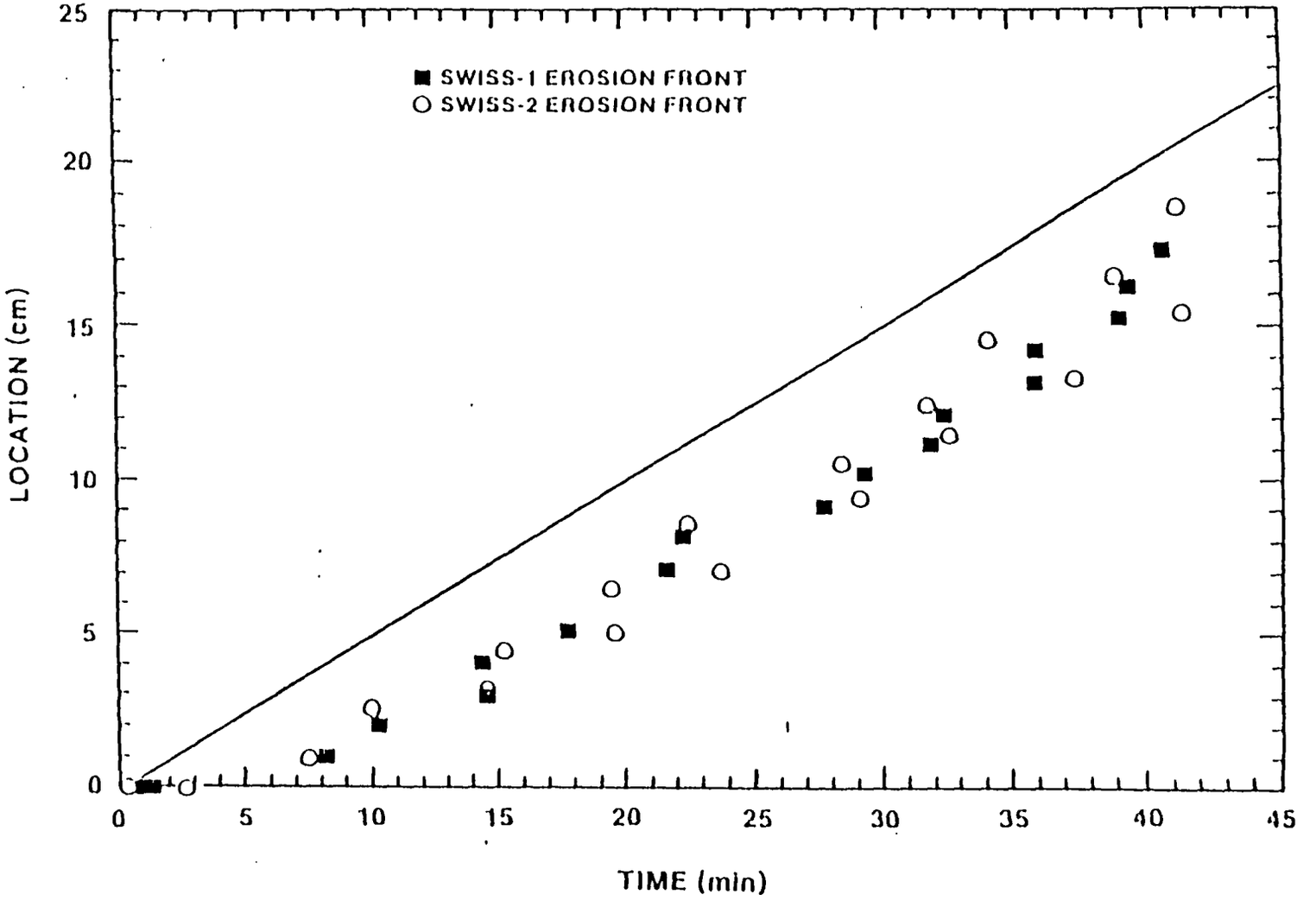

Figure 75: SWISS-1 and SWISS-2 Predicted Erosion Depth by the Model

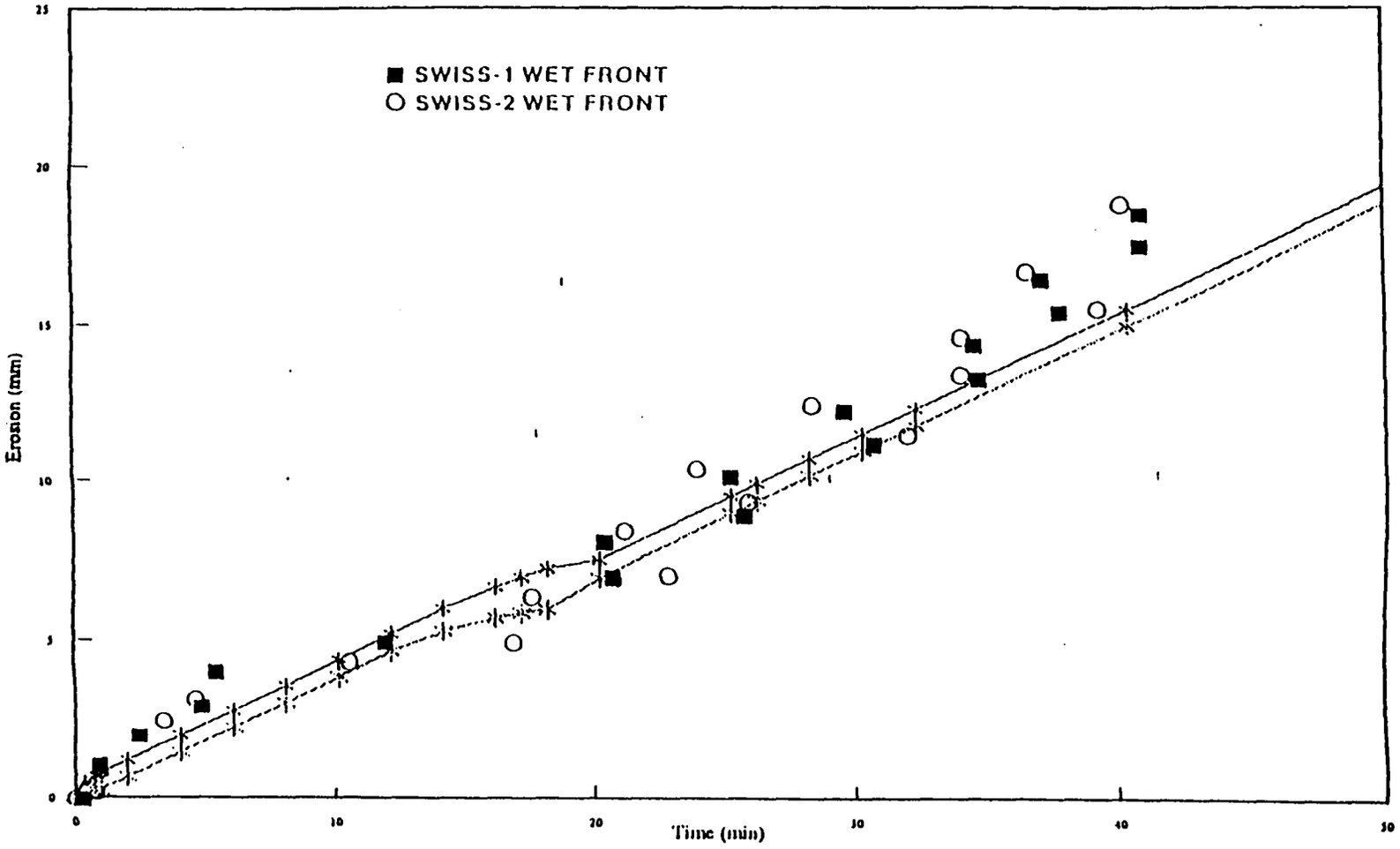

Figure 76: SWISS Test Erosion and Wet/Dry Front Predictions by the Model with $Q_{surface}=0.33xQ_{incident}$

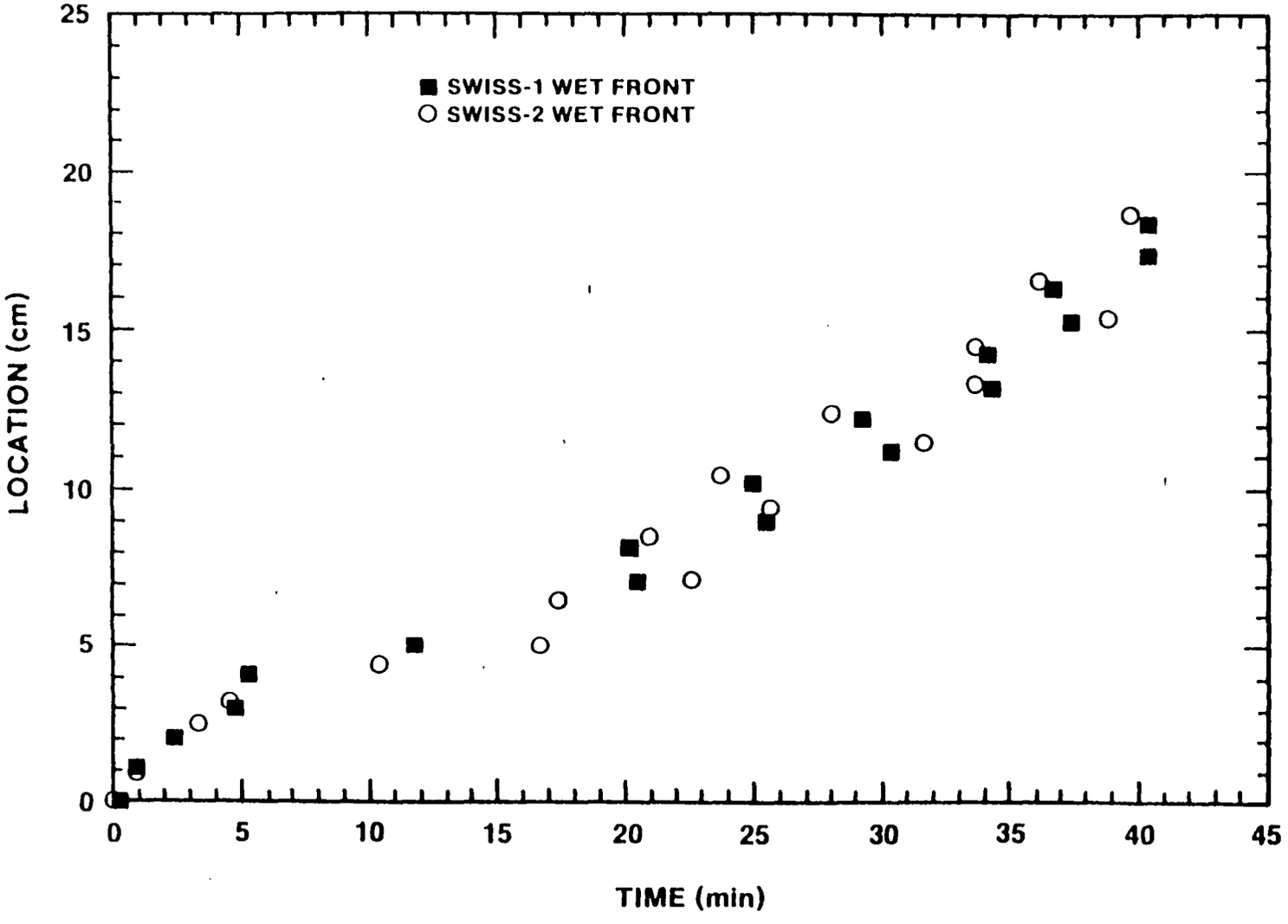

Figure 77: SWISS-1 and SWISS-2 Wet/Dry Front Locations

4.3.3.2. Time Dependent Surface Heat Flux Experiments

4.3.3.2.1. BETA Experiments

The BETA experiments conducted at KfK were given in Table 10 where the constant heat flux solution was compared with two of those experiments. Since most of the BETA experiments were conducted to represent an actual melt/concrete interaction phenomena, the heat fluxes to the concrete were functions of time in those series of experiments. With the available literature, three BETA experiments are selected for the verification and validation of the multi-region core/concrete interaction model with a time dependent surface flux: V0.3, V1.3 and V1.8.

BETA V0.3 Experiment: This experiment, as explained earlier, was performed to test the equipment and measurement devices, but was similar to the test matrix experiments, and provided useful and valid data [60]. It proved that continuous heating of a 300 kg steel melt with a maximum net input power of 1700 kW is achieved for the later tests.

Based on the power in melt curve given in Figure 78, the model for this test can be set as a constant surface heat flux problem between 0 sec and 200 sec with 1700 kW melt power, and approximate exponential decay between 200 sec and 750 sec with 200 kW at 750 sec. By using the solution for the heat flux in forms of $e^{-\lambda t}$ in this chapter, the erosion rate and depths can be predicted. Figure 79 shows the experimental data while Figure 80 shows the model prediction for the erosion. Comparison of these two shows that the model underestimates the concrete erosion observed in the experiment. Since the early time of the experiment is a high constant heat flux case, the erosion should reach its steady state rate before the cooldown, and according to Figure 79 this rate is about the same as the average

erosion rate. Thus, one can consider the magnitude of the initial surface heat flux to be responsible for the difference between the model and the experiment erosion rates since the erosion rate is directly proportional to the magnitude of the initial surface heat flux. Since the incident heat flux was calculated by reducing the incident heat flux by 62.5 percent, one way to investigate the results is to perform a parametric study on this reduction factor. By changing the surface to incident heat flux ratio, the erosion rate is re-calculated and the results are presented in Figure 81. Since the model is not linear, the erosion rate doe not change linearly with the surface heat flux ratio. A reduction factor of 52.5 percent matches with the experimental results (~1 mm/sec erosion rate in the experiment vs. 1.083 mm/sec predicted by the model based on 52.5% reduction factor). This shows that a larger portion of the incident heat flux affects the concrete when the heat flux is very high. Therefore, from this point on, a correlation for the reduction factor will be used as 37.5 percent for the incident heat fluxes that are less than 10 MW/m^2, and 52.5 percent for those greater than 10 MW/m^2.

The difference between the incident to net heat flux ratio can be due to the effects of various parameters. According to Muir, the most effective reduction mechanisms are the emitted radiation and the convection. Reviewing Muir's results shows that the ratio of net to incident heat flux is ~37.5 percent for an incident flux of 1.18 MW/m^2. This ratio is down to ~22 percent for incident heat flux of 0.64 MW/m^2. Using the argument of ratio of the net to incident heat flux being larger for larger surface heat fluxes, the higher ratio that gives closer results to the experimental results can be explained. This has been the topic of several studies, but is not included in the scope of this study. However, it is recommended to improve the model by adding the calculation of radiation and convection heat transfer effects to determine the incident to net surface heat flux ratio.

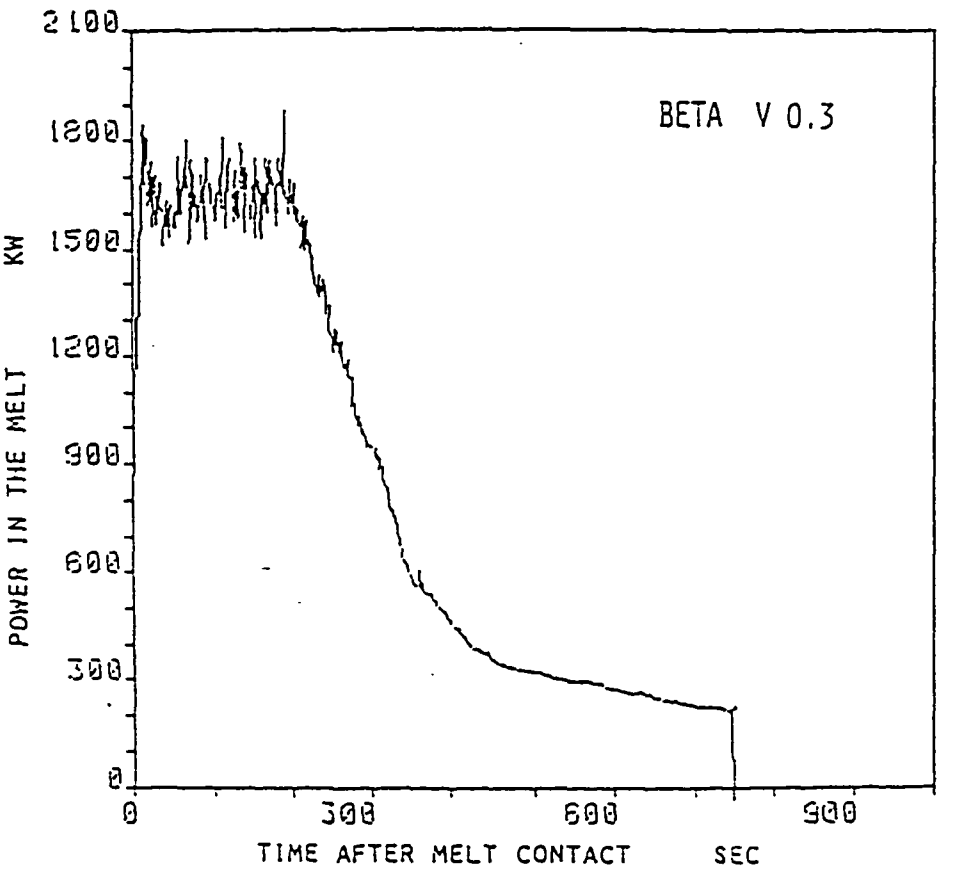

Figure 78: Melt Power for BETA V0.3 Test

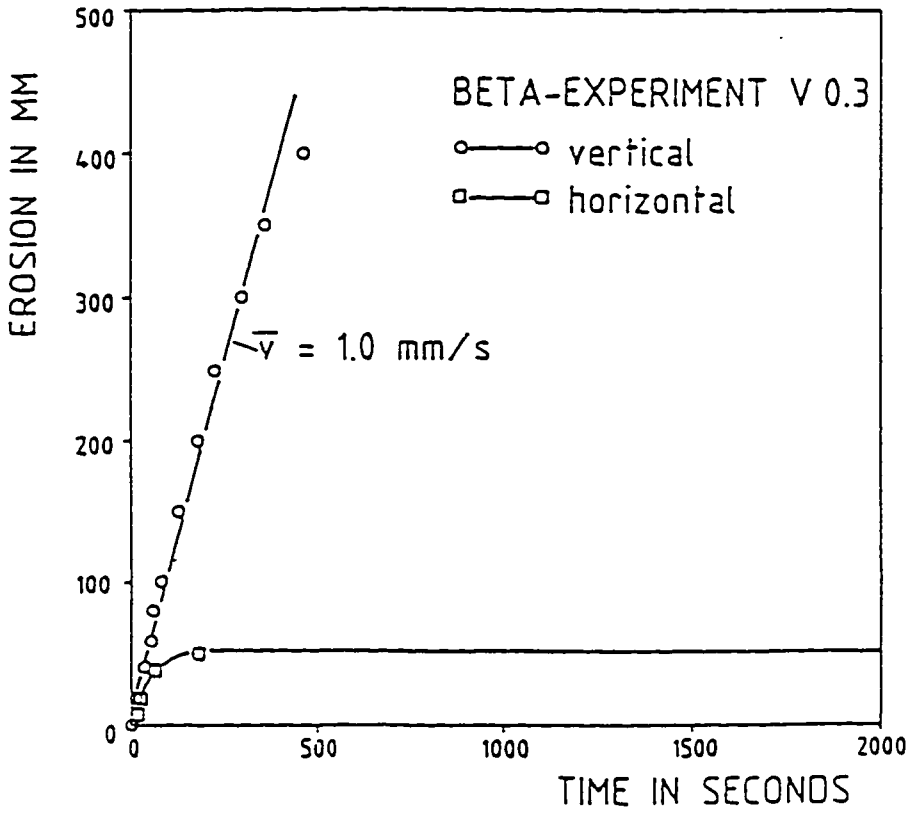

Figure 79: Erosion Depth Observed in BETA V0.3 Test

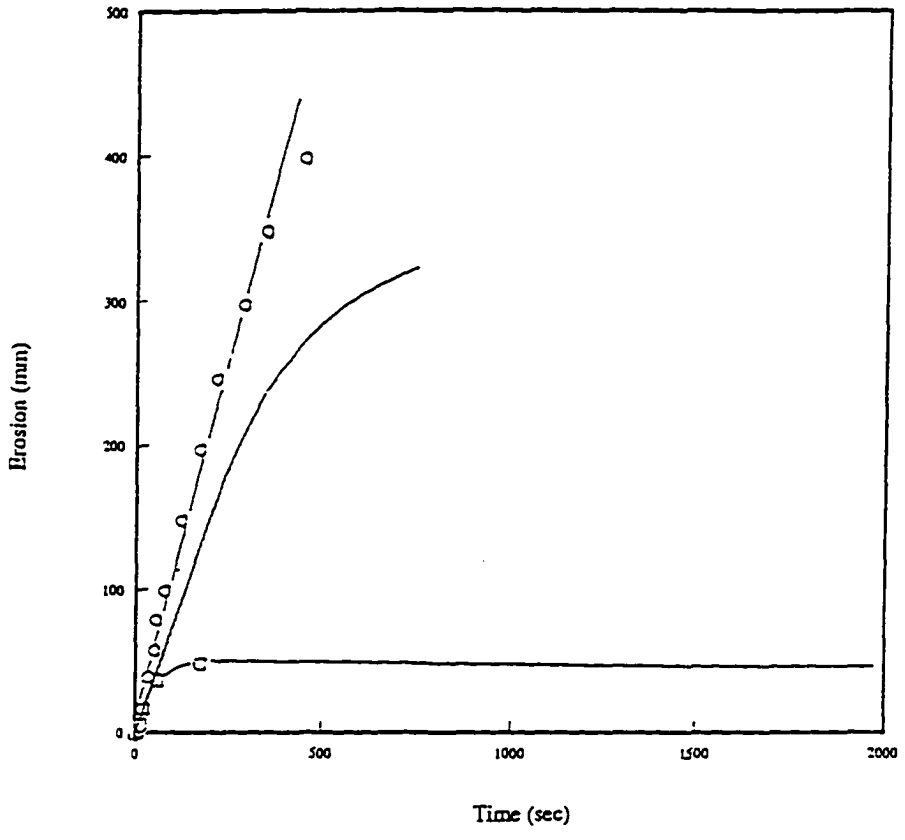

Figure 80: Predicted Erosion Depth by the Model for BETA V0.3 Test

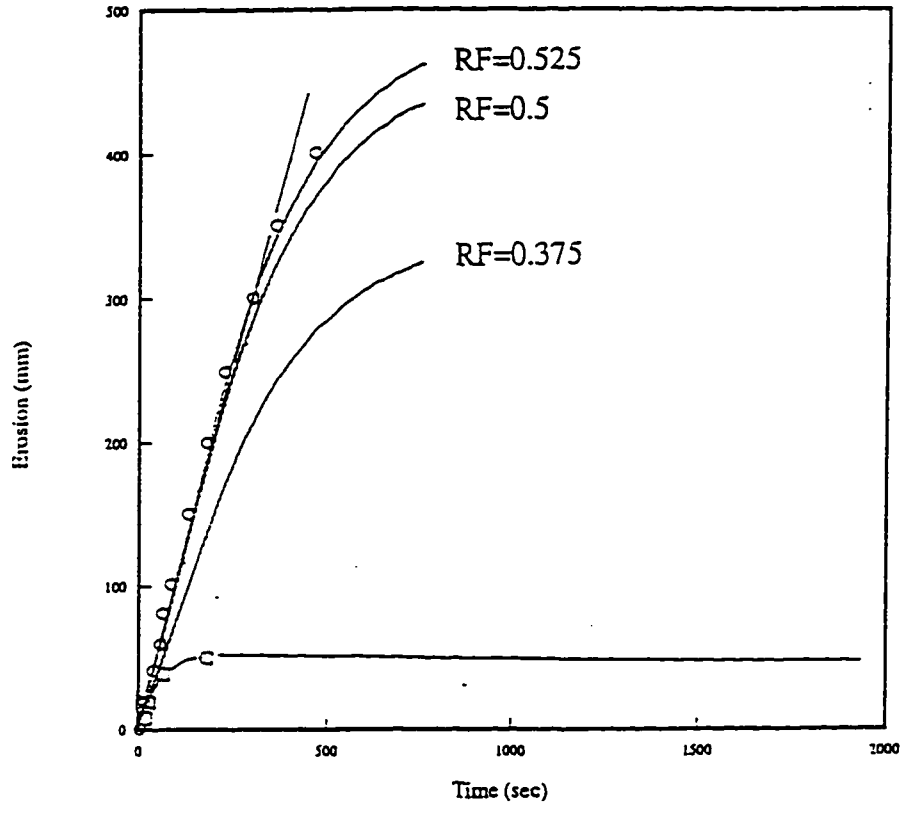

Figure 81: Predicted Erosion Depths for Various Surface to Incident Flux Ratios (RF) for BETA V 0.3 Test.

BETA V1.3 Experiment: This test was an experiment with intermediate input power where the effect of the existence of an initial oxidic melt in addition to the metallic melt was studied in more detail [60]. One melt behavior observed in this experiment was that power increase due to the coarse mixing in the beginning (from 1000 kW to almost 1400 kW), before fine dispersion of the metal reduced the power input. This is shown in Figure 82.

The power history in the modelling of this experiment is represented by assuming a constant surface heat flux of 1200 kW during coarse mixing (~first 200 sec) and an exponential decay from 1200 kW to 50 kW between 200 sec and 750 sec. A reduction factor of 52.5% is used for the incident surface heat flux based on the discussion given earlier. The experimental data is given in Figure 83 and the model results are presented in Figure 84. The model's prediction for the initial erosion rate of 0.7625 mm/sec agrees with the extrapolated initial rate of 0.76 mm/sec of the test. Again, the agreement between the test and the model results shows that the higher the incident heat flux, the more heat flux goes to the concrete erosion, and the correlation that was established for the reduction of the incident heat flux is a good assumption to reflect the actual phenomena.

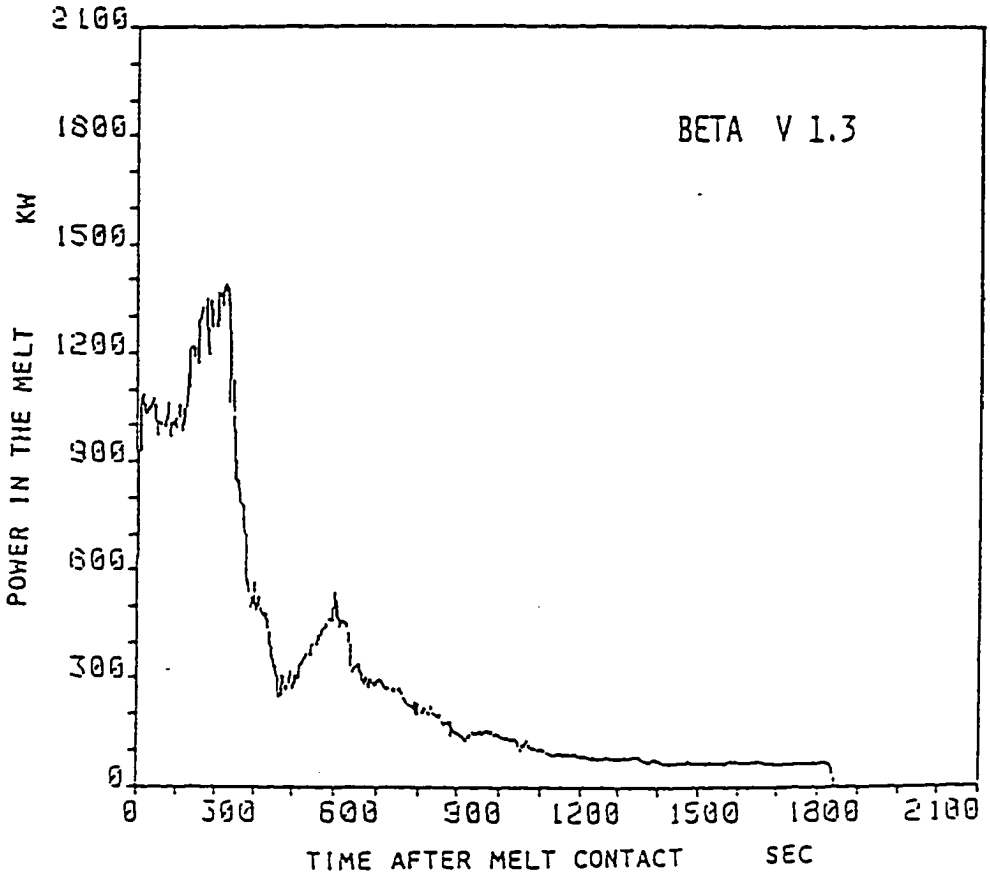

Figure 82: Melt Power for BETA V1.3 Test [60]

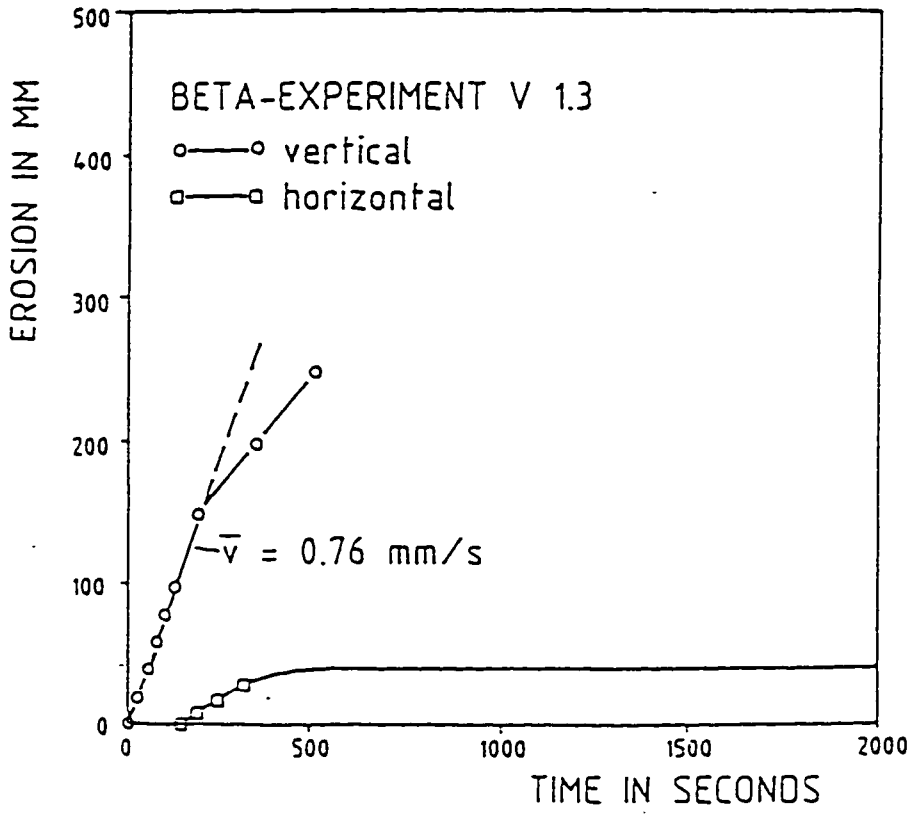

Figure 83: Observed Erosion Depth in BETA V1.3 Test

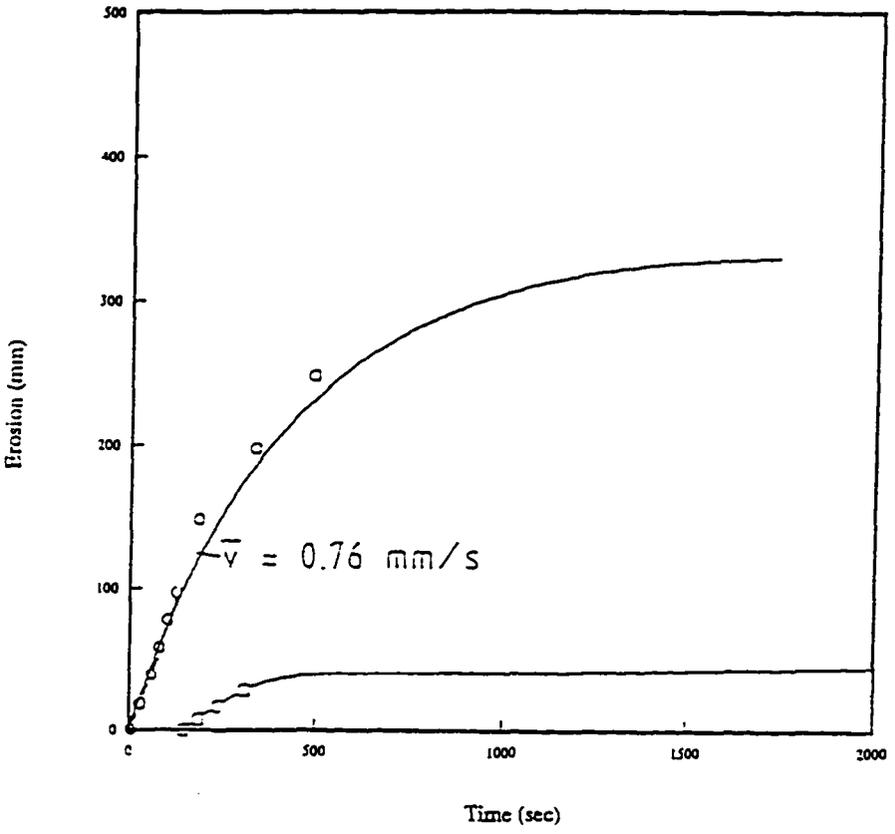

Figure 84: Predicted Erosion Depth by the Model

BETA V1.8 Experiment: This experiment involved the highest heating power achieved at 1900 kW, which corresponds to 10 times the power density expected in a meltdown accident in ex-vessel phase [84]. The melt consisted of 350 kg of steel with fractions of chromium and nickel, and 130 kg of an oxide. The aluminium oxide was added 30% of the burnt time, which reduced the melt viscosity, and thus provided a melt condition similar to the one in an actual core meltdown accident.

The power history in the modelling of this experiment is represented by assuming a constant surface heat flux of 1900 kW for the first 220 seconds, and an exponential decay from to 700 kW at 480 sec. A reduction factor of 52.5% is used for the incident surface heat flux based on the discussion given earlier.

The results of the model given in Figure 87 are compared with the experimental data, given in Figure 86. Again, the model agrees with the experiment well. The erosion rate derived from the experimental data is ~1 mm/sec, while the model predicted a rate of 1.15 mm/sec.

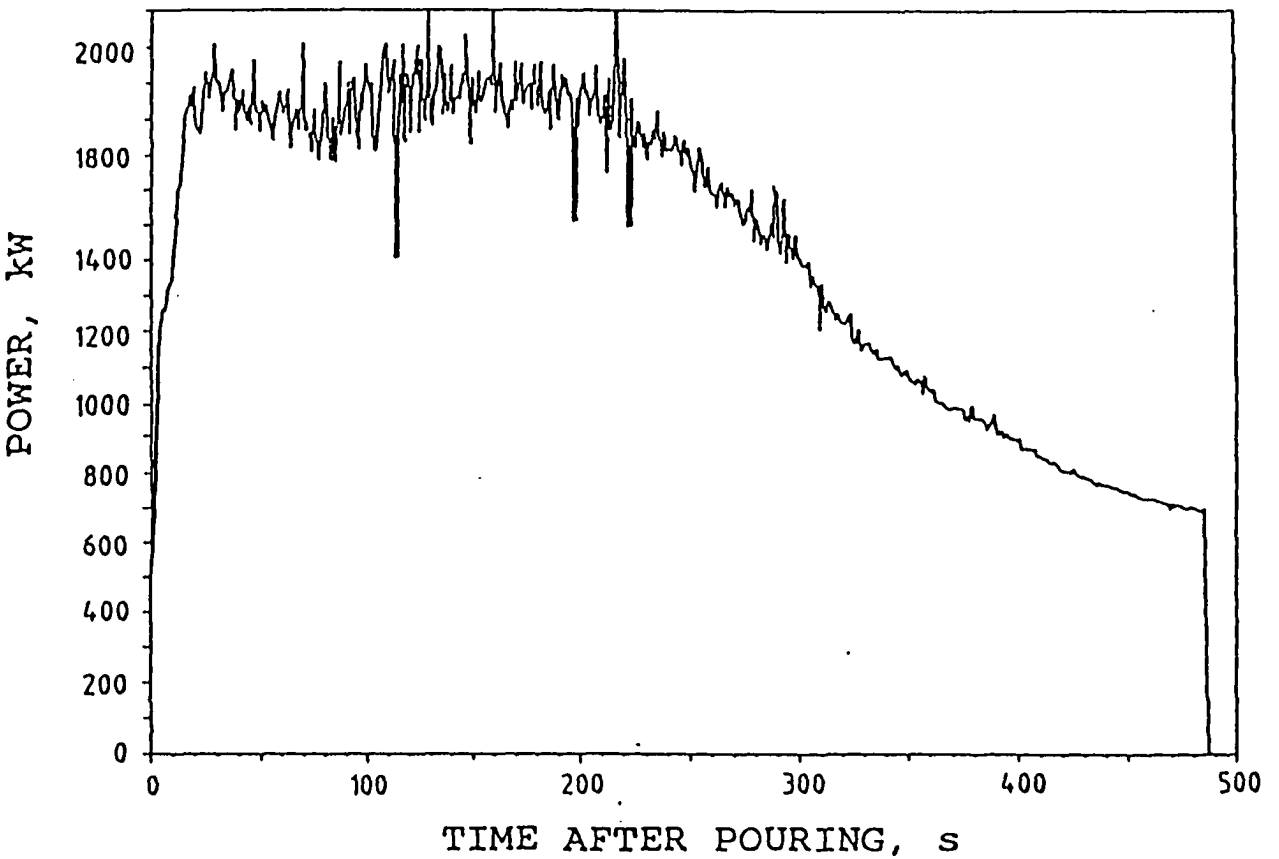

Figure 85: Melt Power for BETA V1.8 Test

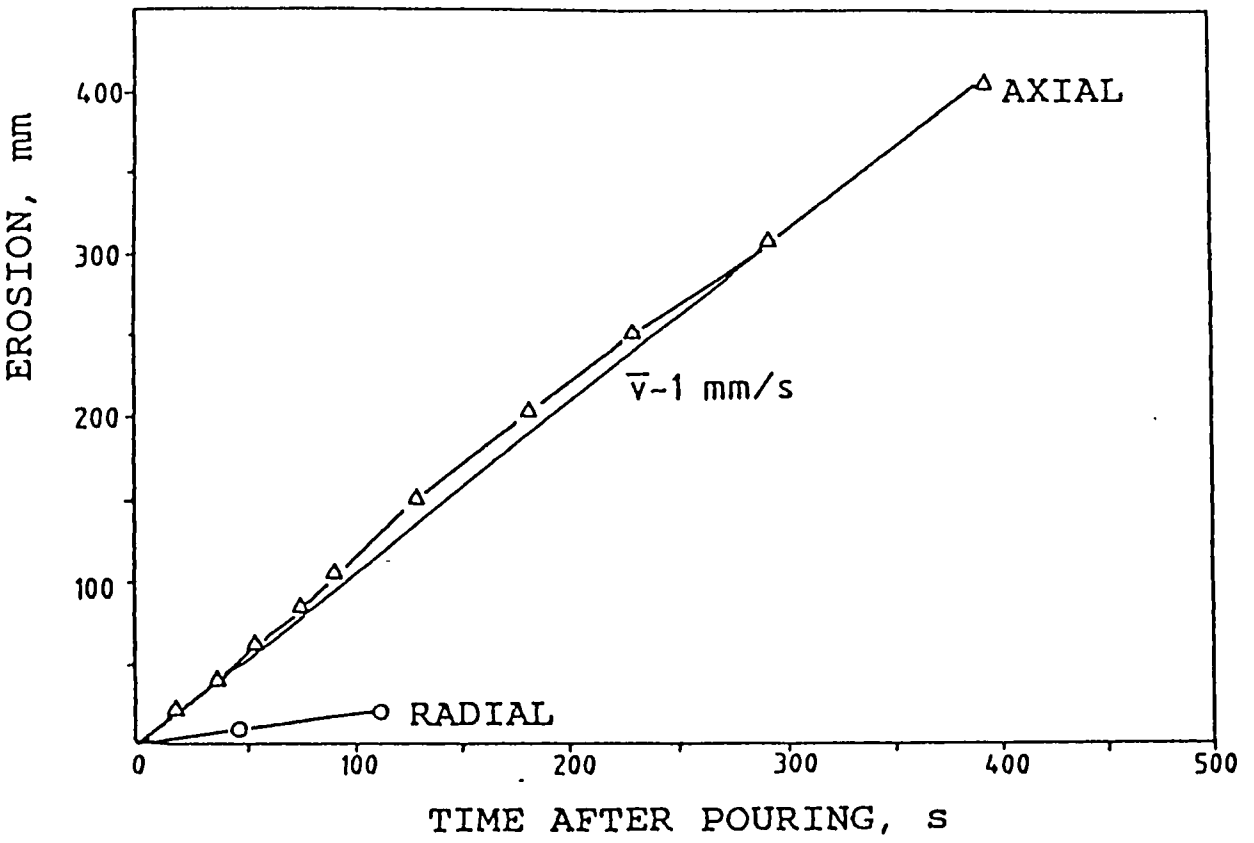

Figure 86: Observed Erosion Depth in BETA V1.8 Test

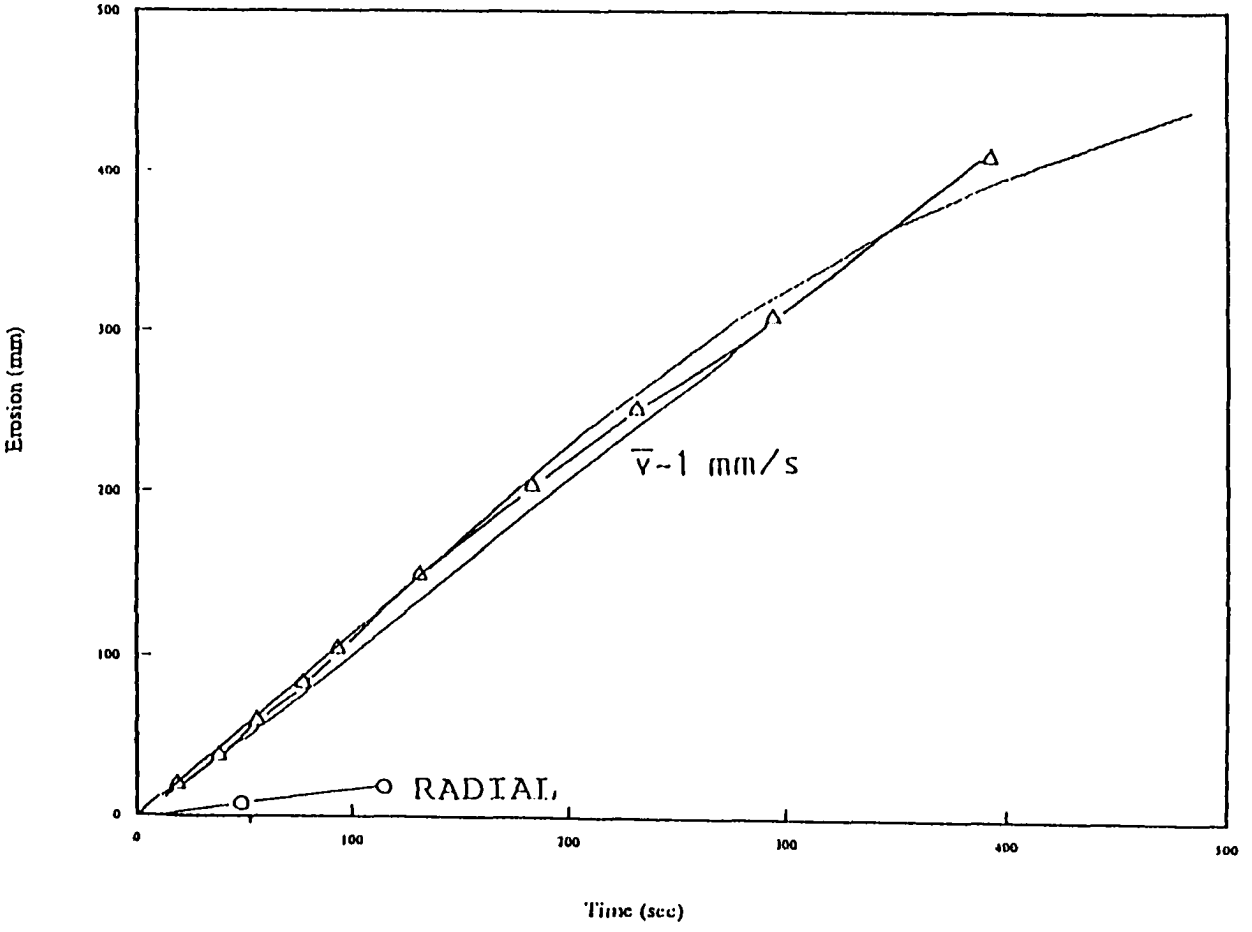

Figure 87: Predicted Erosion Depth by the Model for BETA V1.8 Test

4.3.3.2.2. TURC Experiments

TURC (Transient Uraina-Concrete) tests were performed at Sandia National Laboratories, and consisted of four large scale molten debris-concrete experiments [80]. In the reported first two tests, a melt (~100 kg thermite for the TURC1T and stainless steel for the TURC1SS) was teemed onto a limestone concrete crucible with a diameter of 41.6 cm and cylindrical MgO sidewalls. Then, the melt was allowed to cooldown naturally. The concrete erosion rate, composition of evolved gases, and aerosol data was evaluated for the interaction. The purpose of the first two experiments was to provide a comparison metallic database to minimize the geometry and test design conditions for the two later tests TURC2 (with UO_2/ZrO_2 melt) and TURC 3 (with $UO_2/ZrO_2/Zr$ melt). The TURC1SS and TURC1T tests are modelled for verification and validation of the model in this study.

Also, a new analysis model was derived and reported in Reference 80 to calculate the erosion and wet/dry interface of the concrete decomposition. That model was a heat balance model that was written primarily for analysis of TURC experiments of 1-D concrete ablation with refractory sidewalls. In this subsection, the results for erosion and wet/dry interface derived from the experimental data and calculated by the model used for TURC tests will be compared with the results of the multi-region transient erosion model of this dissertation. The power characteristics used in the model were based on the concrete surface heat flux calculated in Reference 80 which is presented in Figure 88. No reduction factor is used since the flux calculated took the heat losses into account and was given as the net heat flux. The limestone concrete properties are used in the model.

The erosion depth and wet/dry interface (423 K isotherm) data of the TURC1SS test is given in Figure 89. The same interfaces that are calculated by the model are presented in Figure 90. Comparing the model results with the TURC1SS results shows that the model prediction for the maximum eroded concrete depth of 4.25 cm was higher than the experimental data, which was derived from the thermocouple data for 1600 K isotherms, and TURC test heat balance model (3. 8 cm). On the other hand, post test results based on the X-rays of the crucible showed that the volume of concrete eroded was 7067 cm^3, resulting in an average erosion depth of 4.3 (+/- 0.5) cm. This agrees with the predicted erosion depth by the model derived in this study, and thus shows the accuracy of the model. Considering the thermocouple inaccuracy that was determined by the comparison of the isotherm results with post test X-ray observations, the model predicts the erosion front and wet/dry interface very accurately.

For the TURC1T results, a different approach is used to calculate the erosion depth to show the validity of the correlation given in Figure 16. In this case the erosion depth is derived by use of the results from the TURC1SS, and extrapolating the data given in Figure 16. This resulted in 7.6 cm erosion depth for the TURC1T test which is very close to 7.5 cm eroded concrete depth observed by the X-ray of the TURC1T crucible. Thus, the validity of the correlation given in Figure 16 is provided for use in future studies by extrapolating the results of this study.

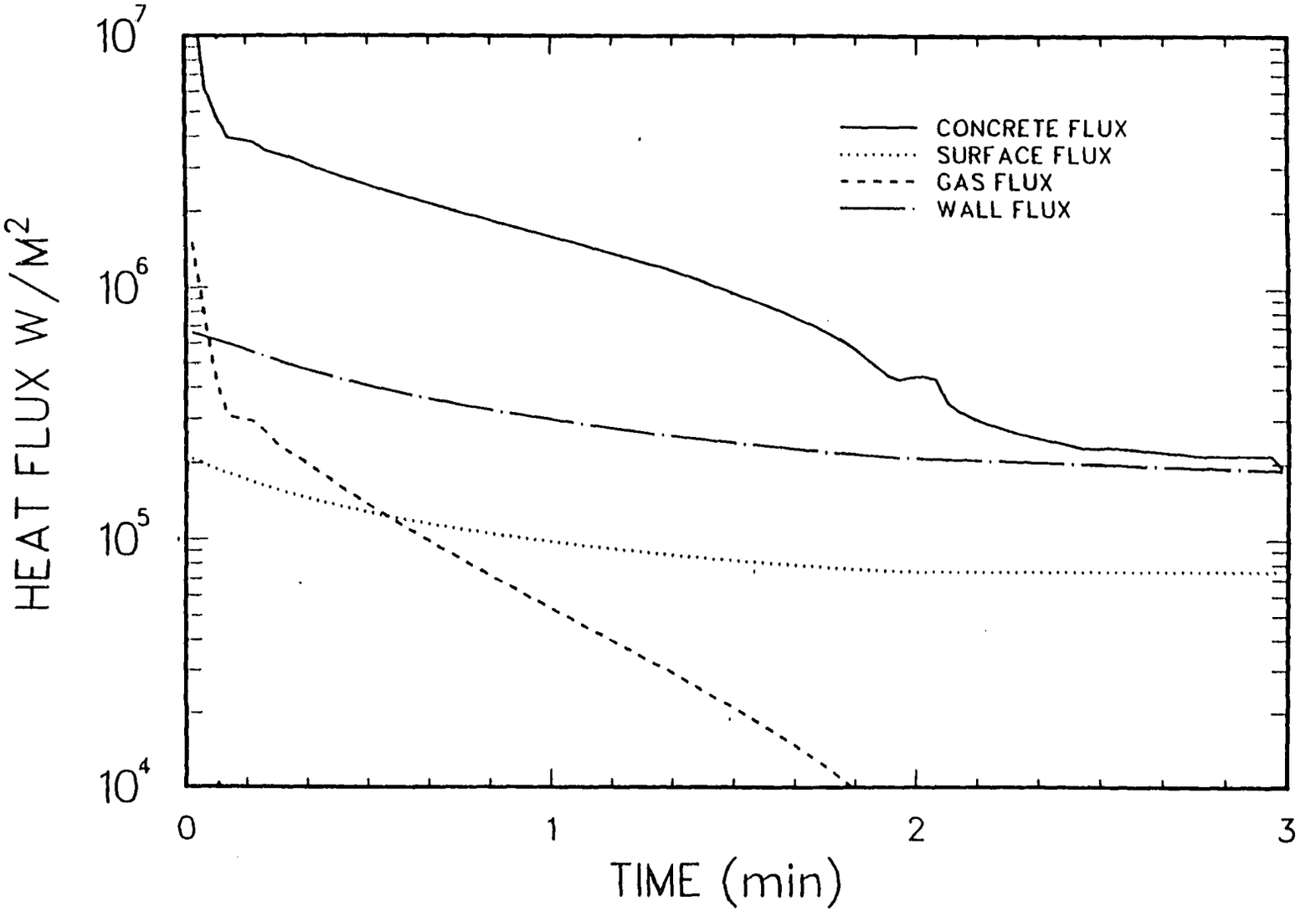

Figure 88: Calculated heat fluxes for TURCISS Test [80]

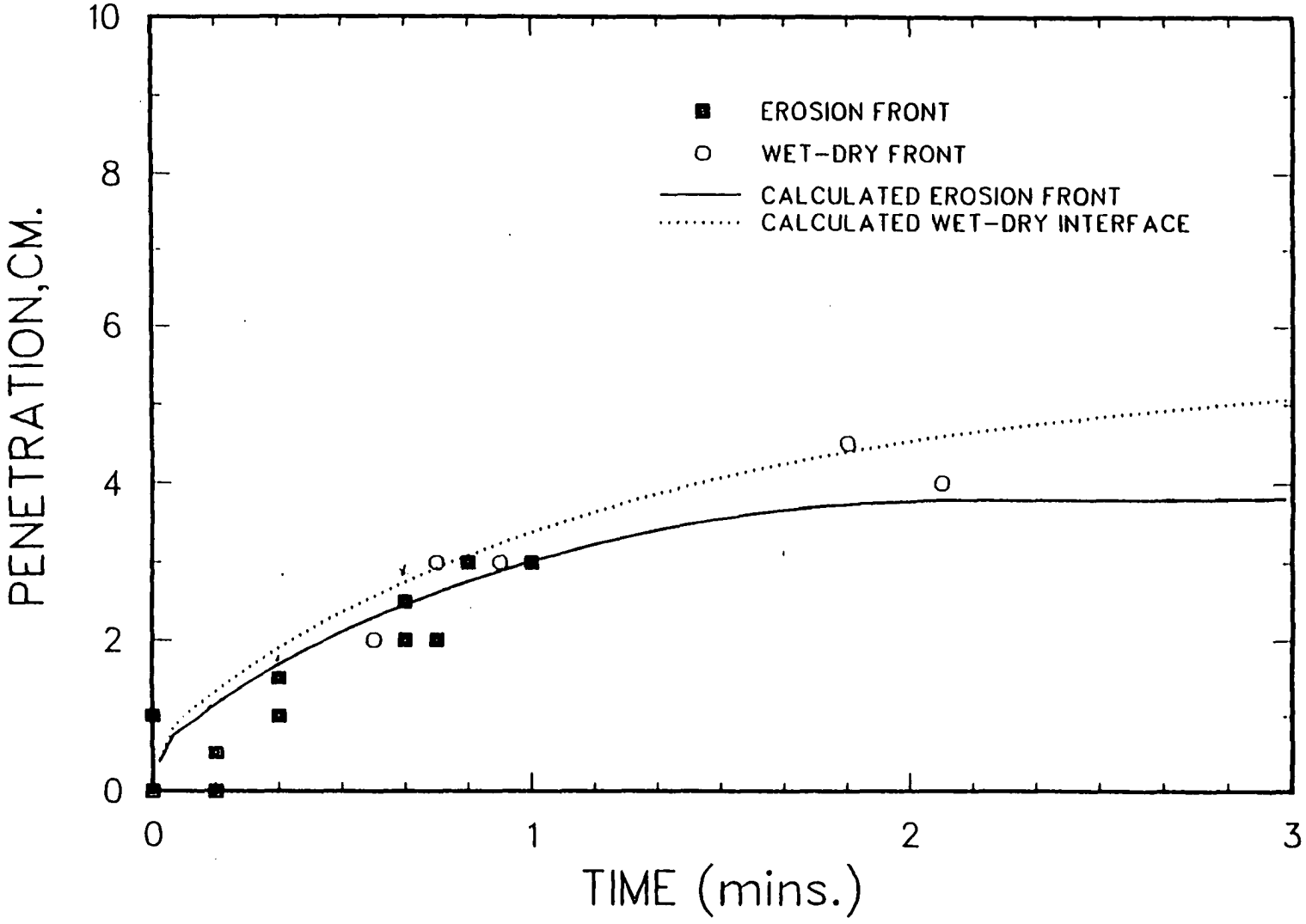

Figure 89: Predicted (by the TURC heat balance model) and experimental data for the TURC1SS

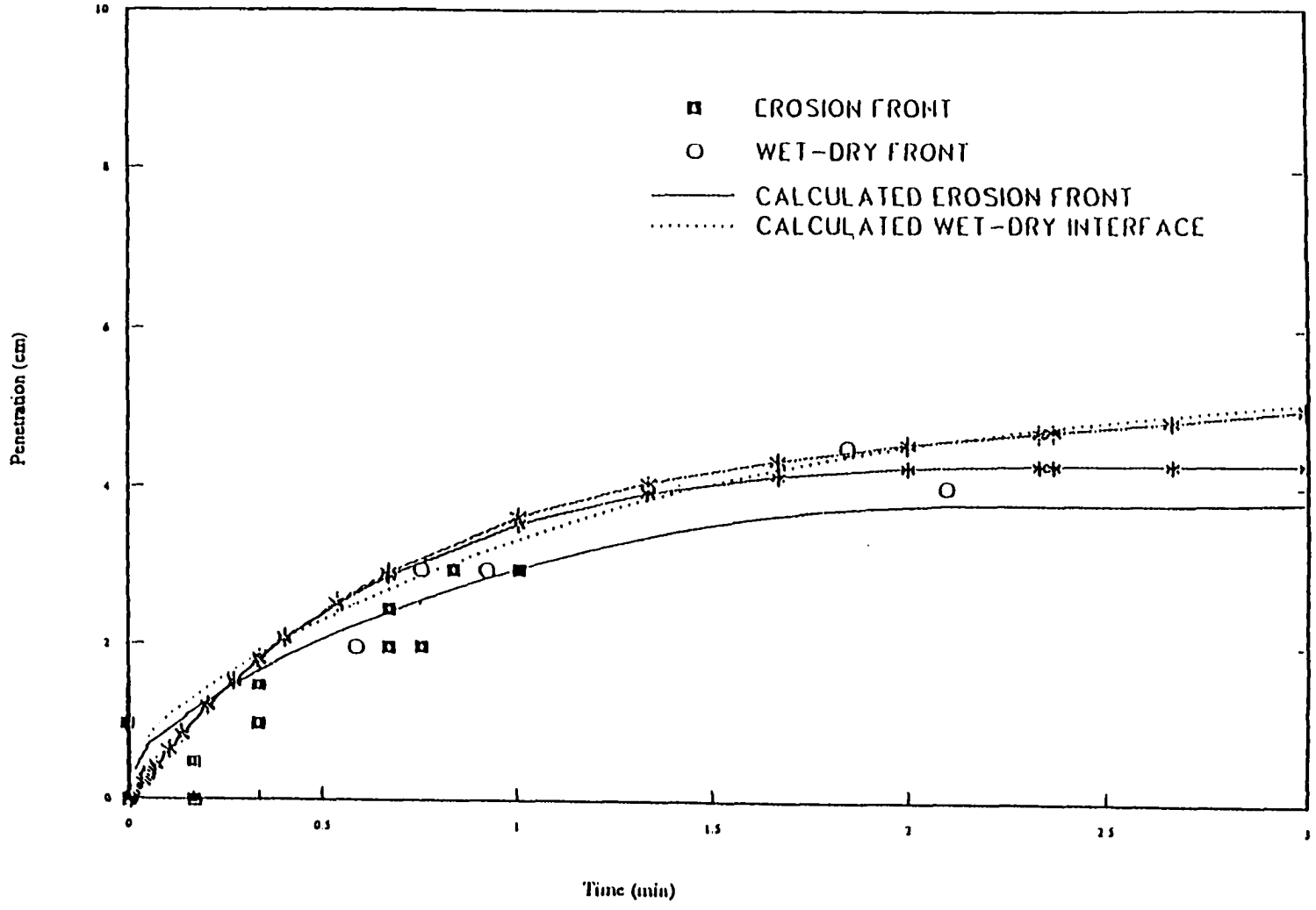

Figure 90: Predicted Erosion and Wet/dry Front by the Model for TURCISS Test

4.3.3.3. Conclusion for Comparison of the Model with Experiments

Based on the comparison with the experiments, the model is proven to be valid even if it is used as a stand alone code. Once the surface heat flux is known, by using the appropriate surface heat flux to incident heat flux ratios (~0.525 for high heat fluxes, and ~0.375 for the low heat fluxes), the erosion rates and depths can be predicted by the model in a short time without requiring larger computer codes. The accuracy and validity of the model for the different scenario of the melt/concrete inteaction, such as solidification, overlying water pool, viscous melt, and high heat fluxes shows that the model can also be used for actual molten core/concrete interaction predictions. The success of the code to calculate the other decomposed concret regions as shown in comparison with some of the experiments also enables the code to be used in prediction release of concrete ingredients to the melt and the containment atmosphere.

Overall, the code agrees with the experiments very well. The summary of the comparison of the model with experiments are given in Table 11.

Table 11: Summary of the Model's comparison with the Experimental Data

Experiment	Incident q" (MW/m^2)	Surface q" (MW/m^2)	$q_{surf}"/q_{inc}"$	Velocity Test (mm/sec)	Velocity Model (mm/sec)
BETA V0.2	3.53	1.32	0.375	0.18	0.18
BETA V0.3	15.0	5.61	0.375	1.0	0.76
BETA V0.3	15.0	7.88	0.525	1.0	1.08
BETA V1.3	10.6	3.96	0.375	0.76	0.54
BETA V1.3	10.6	5.62	0.525	0.76	0.76
BETA V1.8	16.8	6.26	0.375	1.0	0.85
BETA V1.8	16.8	8.88	0.525	1.0	1.15
BETA V2.1	1.24	0.46	0.375	0.06	0.06
SWISS1&2	1.91	0.72	0.375	0.083	0.08
TURC1SS	N/A	10.0	N/A	4.3 cm (erosion)	4.25 cm (erosion)
TURC1T	N/A	~10.0	N/A	7.5 cm (erosion)	7.6 cm (erosion)

4.4. Effect of the Thermal Parameters

Besides the surface heat flux that is provided by the molten debris, the other phenomena that greatly influence the concrete erosion process are the conduction of that heat into the concrete, and the heat sinks due to the decomposition reactions that occur at each front.

The conduction process is driven by the thermophysical parameters of the concrete. As was explained in the thermal parameters section of this chapter, these properties are hard to determine, and to generalize since the concrete is a heterogenous mixture of its constituents. In this study, the effects of the thermal parameters is examined based on the constant surface heat flux case, and by calculating the growth and growth rate of each region. The results of these calculations then can be extrapolated into actual concrete properties by using the curves that are determined for selected thermal properties.

4.4.1. Effect of the Thermal Diffusivity

Using the fact that thermal conductivity is the most temperature dependent thermal property, and specific heat and the density can be assumed constant, the effect of the thermal properties is examined by evaluating the effect of the thermal diffusivity, α. Also, non-dimensionalization is done by using the initial thermal diffusivity of the concrete. This provides a normalization for the growth rate and growth of each region. For this study, the thermal diffusivities are selected from the result of Reference 35 as presented in Figure 10. First the effect of the thermal diffusivity of the dehydrated region is investigated by using different ratios of dehydrated region thermal diffusivities to the initial thermal diffusivity of the con-

crete. Then for each case, the effect of the thermal diffusivity of the gas-free region is investigated by using various ratios of gas-free region thermal diffusivities to the initial concrete thermal diffusivity. The ratio of the thermal diffusivities is the significant parameter in the general solution, rather than the thermal diffusivity of the each region itself, as can be seen in the resulting equations in Chapter 3. Therefore, the cases were selected based on the ratios. Table 12 presents the cases used to perform this investigation. Figures 91 and 92 summarize the effect of the various thermal diffusivities on the erosion depth and rate, while Figures 93 through 98 illustrate the progress of the erosion front for those thermal diffusivities.

The lower ratio of the initial thermal concrete thermal diffusivity to the thermal diffusivity of the regions (e. g. higher thermal diffusivity of the regions) results in a higher erosion depth and a higher erosion rate since the higher diffusivity results in the faster propagation of heat in the gas-free and dehydrated region and thus causing the temperature in the medium to rise to the decomposition and melting temperatures faster. The higher erosion rate at the higher thermal diffusivities results in a larger heat loss to the melting front, and thus reduces the growth rate of the dehydrated and thermally affected regions. Since the incoming and outgoing heat flux is almost neutral for the gas-free region, the growth rate of this region is not significantly affected by the thermal diffusivities of the medium.

The results of evaluating the effect of the thermal diffusivity on other region growth and growth rates prior to and after the melting reaction are included in Appendix A. That information is to be used for calculation of the gas, and water release before the melting begins.

Table 12: Cases Used to Evaluate the Effect of Thermal Diffusivity

Case #	α_1	α_2	α_3	α_1/α_2	α_1/α_3
1	10	5	2.5	2	4
2	10	5	2.2	2	4.5
3	10	5	2	2	5
4	10	8	2.5	1.25	4
5	10	8	2.2	1.25	4.5
6	10	8	2	1.25	5
7	10	4	2.5	2.5	4
8	10	4	2.2	2.5	4.5
9	10	4	2	2.5	5

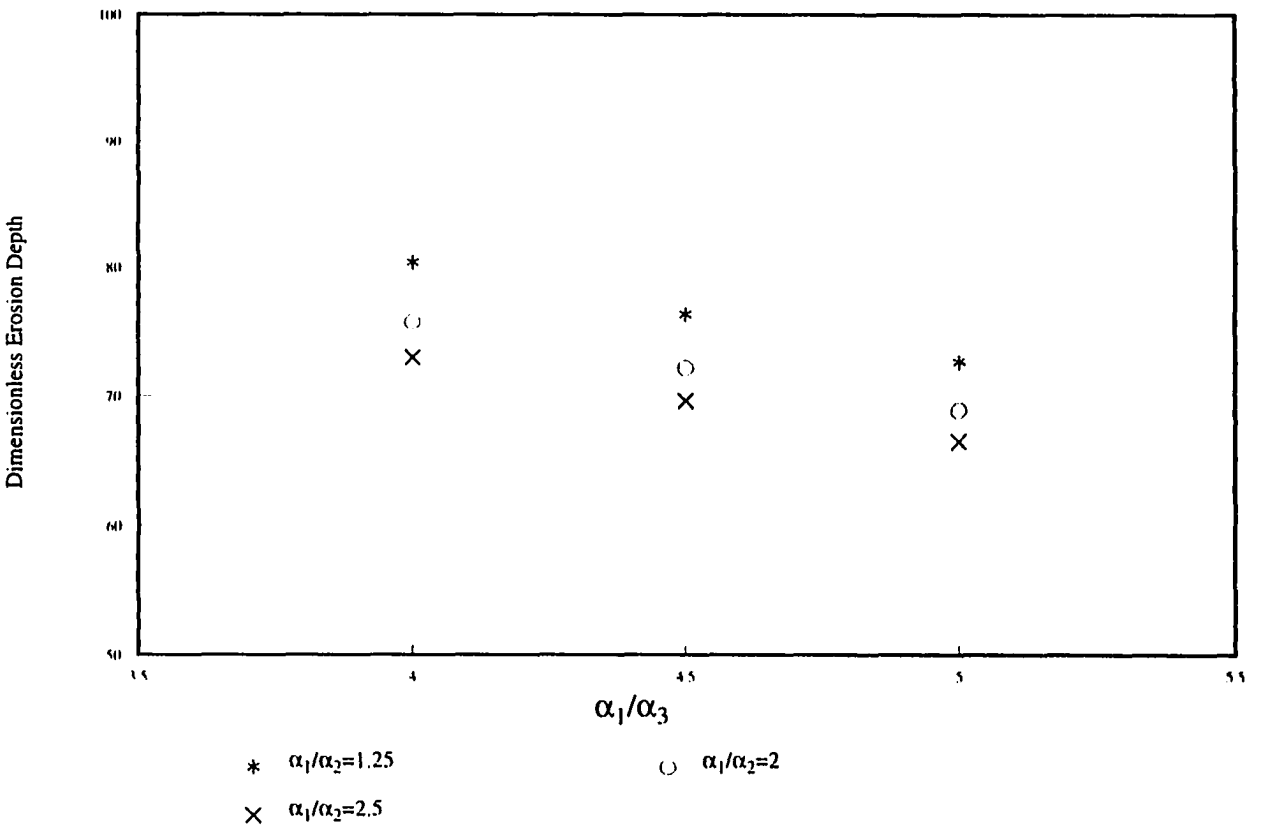

Figure 91: Effect of Thermal Diffusivity on the Erosion Depth (Depth @Fo=1000)

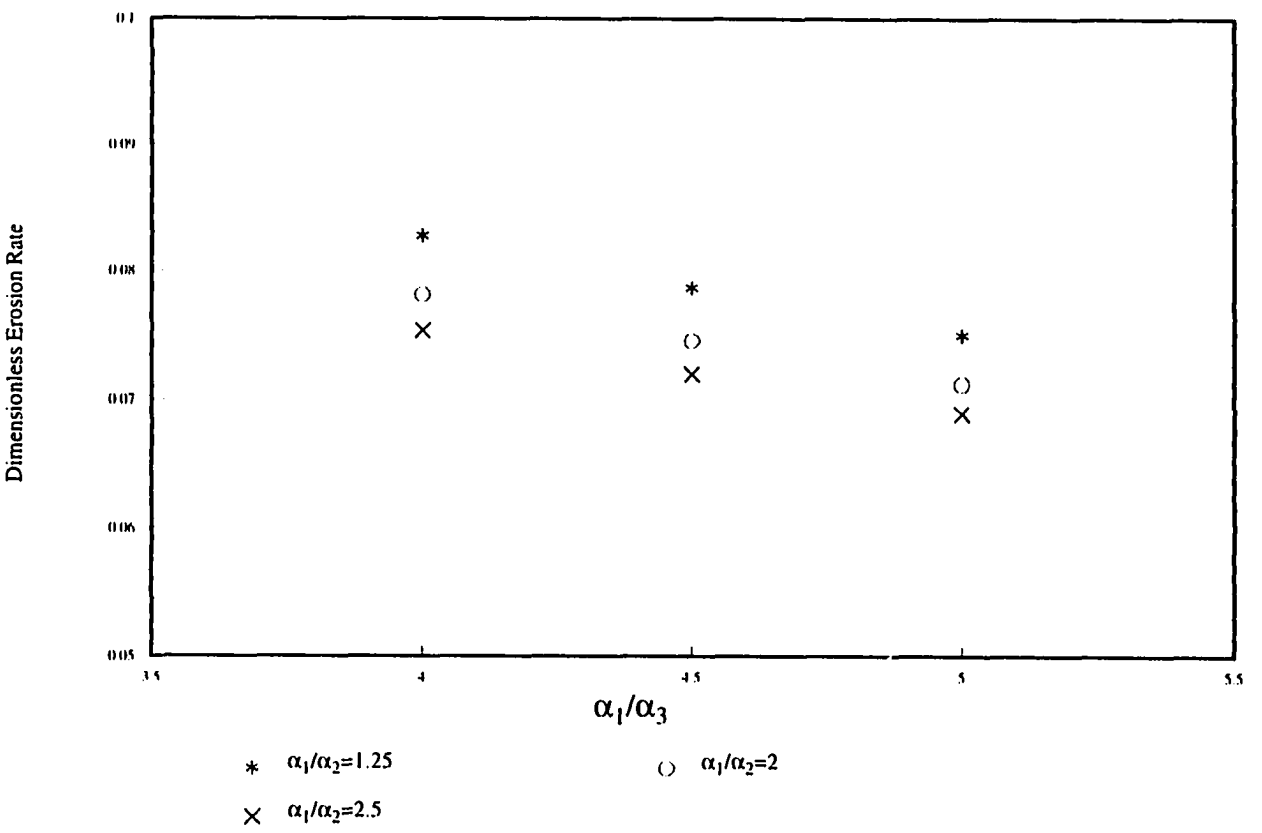

Figure 92: Effect of Thermal Diffusivity on Erosion Rate (Rate @ Fo=1000)

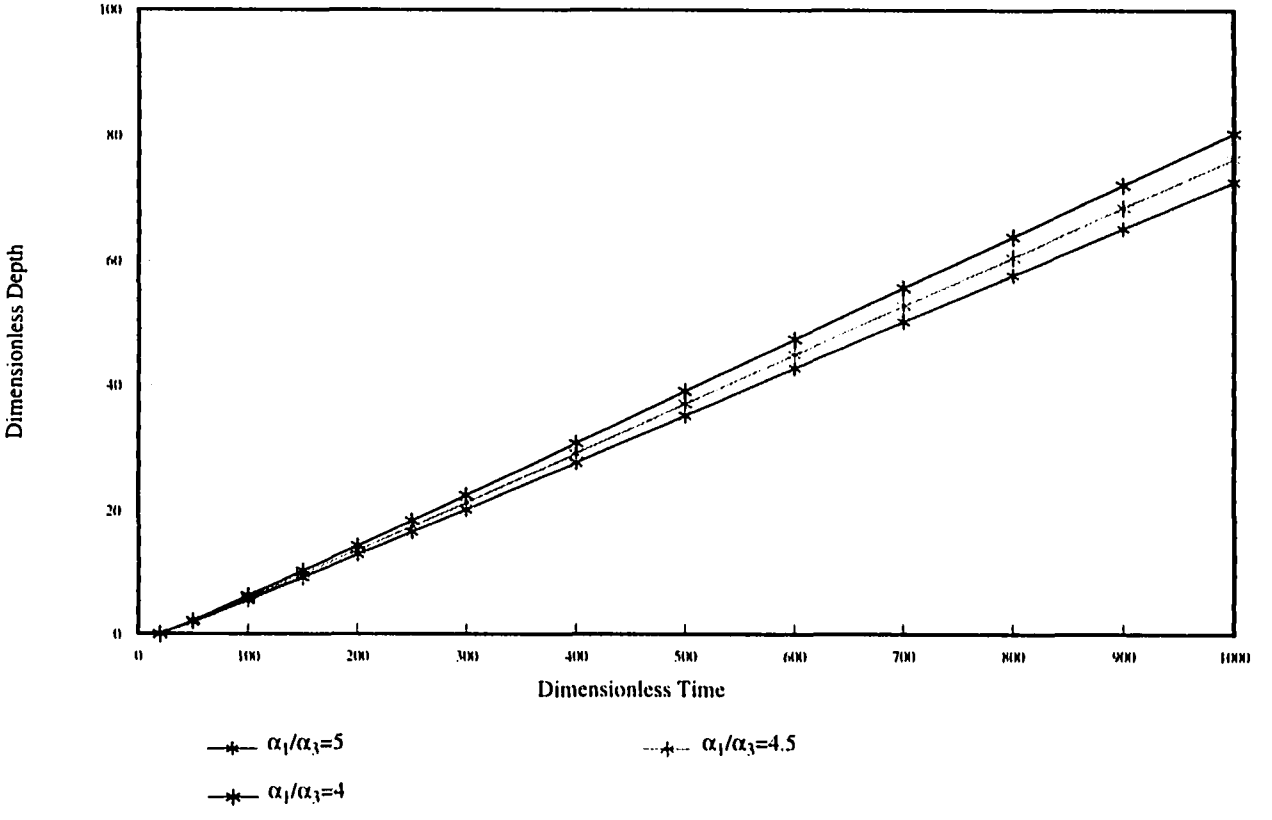

Figure 93: Erosion Growth for Various Thermal Diffusivities (α_1=1x10^{-7} m^2/sec; α_1/α_2=1.25)

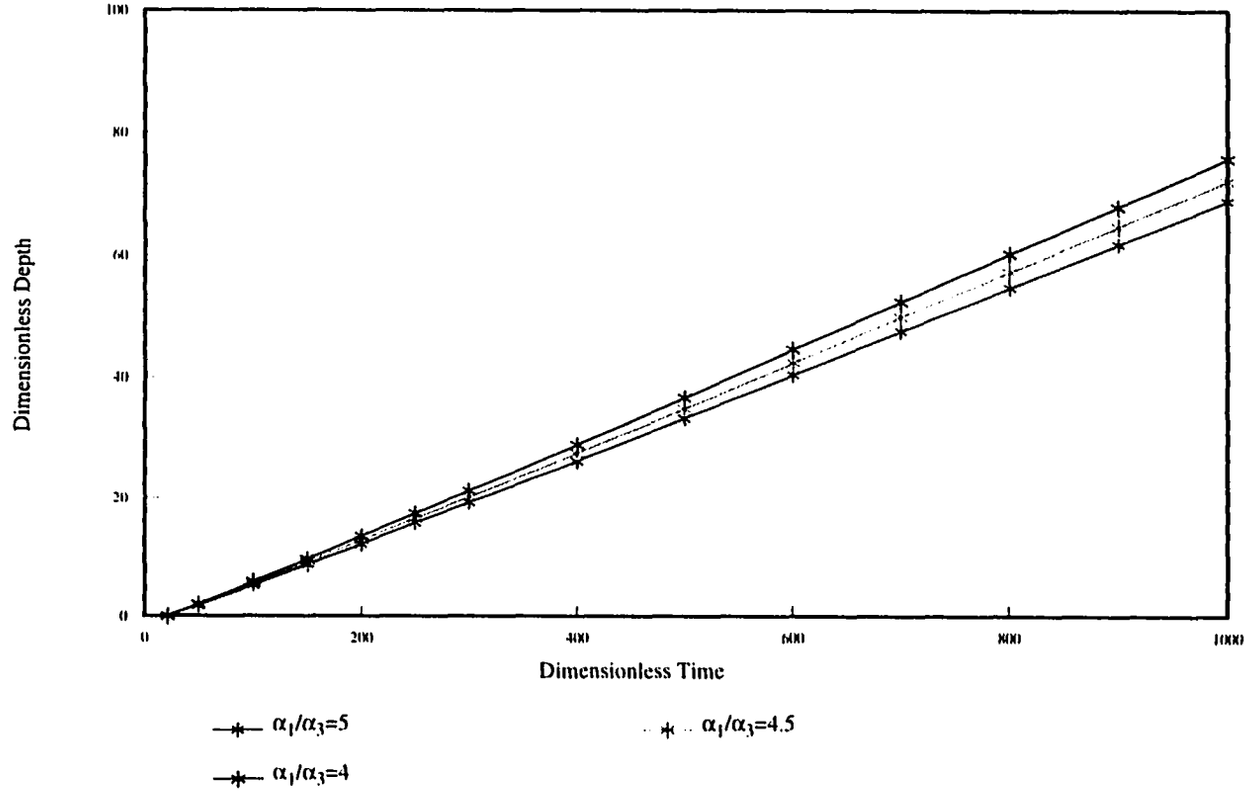

Figure 94: Erosion Growth for Various Thermal Diffusivities ($\alpha_1=1\times10^{-7}$ m^2/sec; $\alpha_1/\alpha_2=2$)

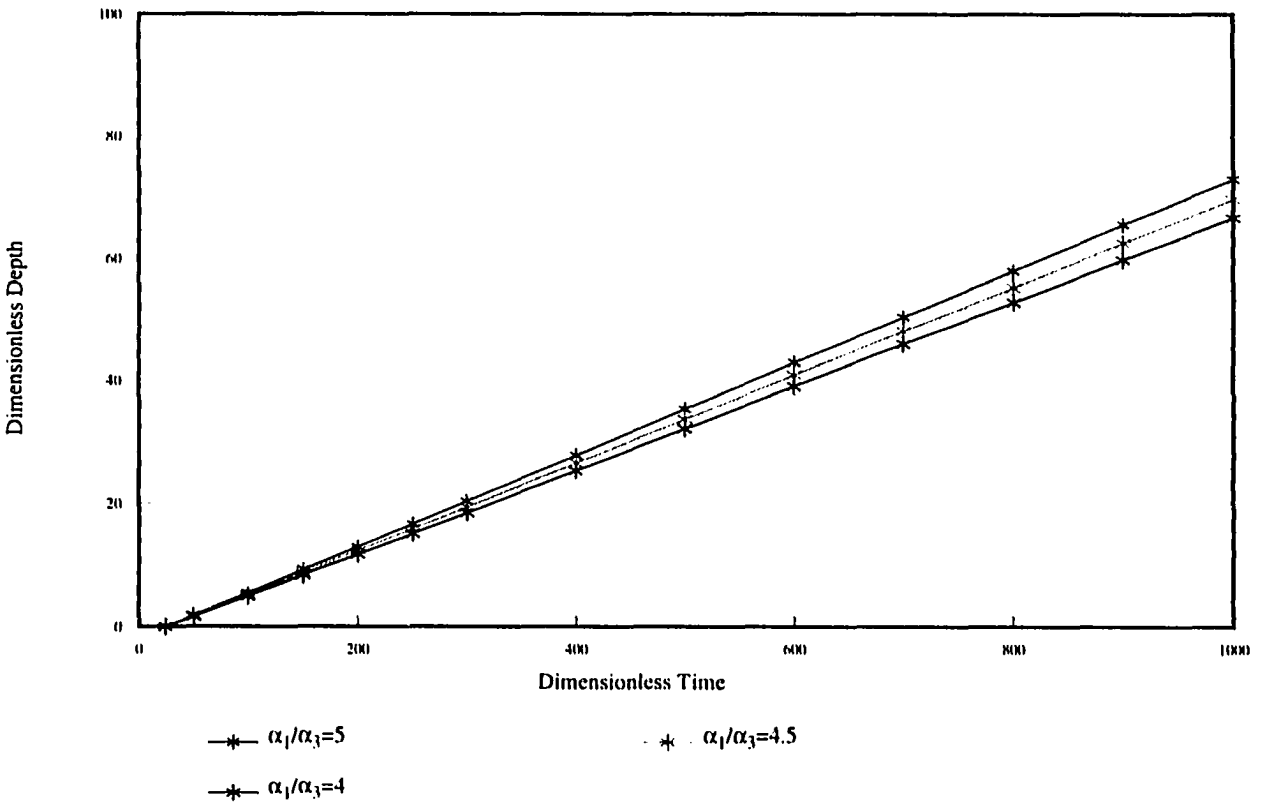

Figure 95: Erosion Growth for Various Thermal Diffusivities ($\alpha_1=1\times10^{-7}$ m^2/sec; $\alpha_1/\alpha_2=2.5$)

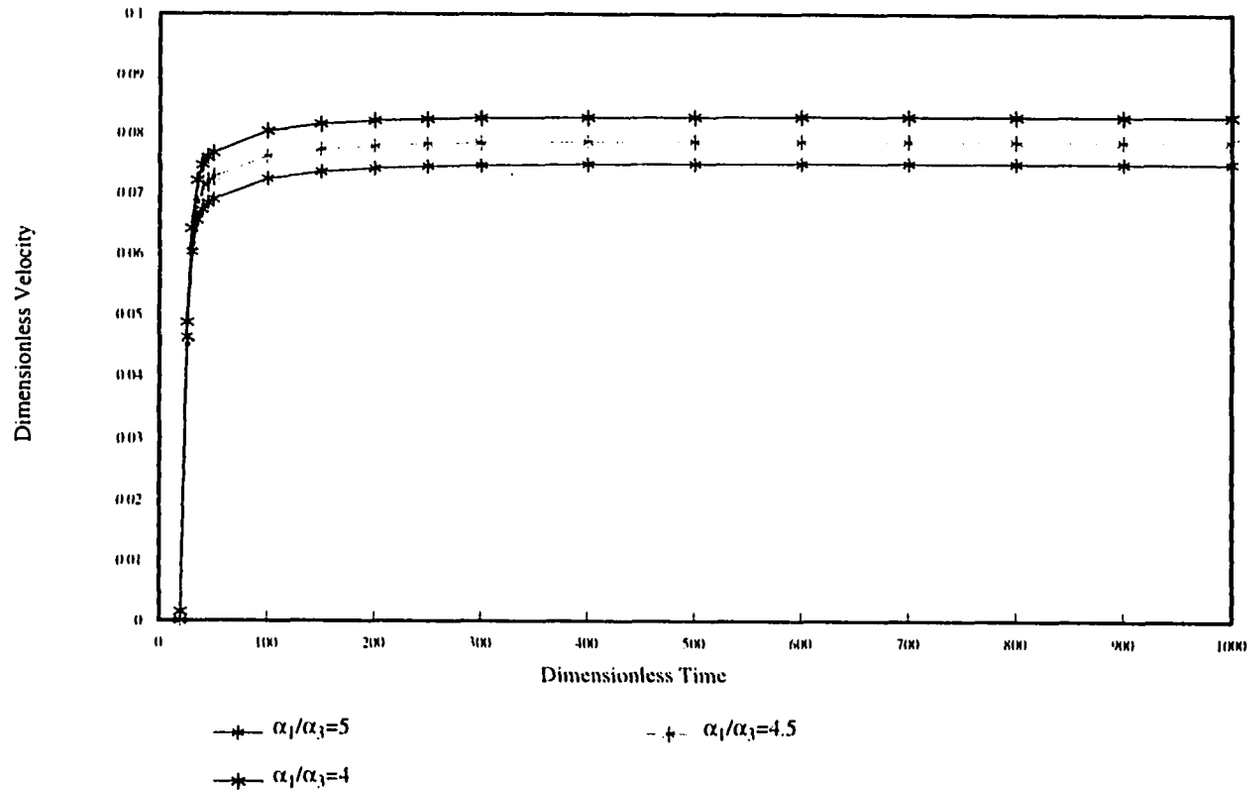

Figure 96: Erosion Growth Rate for Various Thermal Diffusivities ($\alpha_1=1\times10^{-7}$ m^2/sec; $\alpha_1/\alpha_2=1.25$)

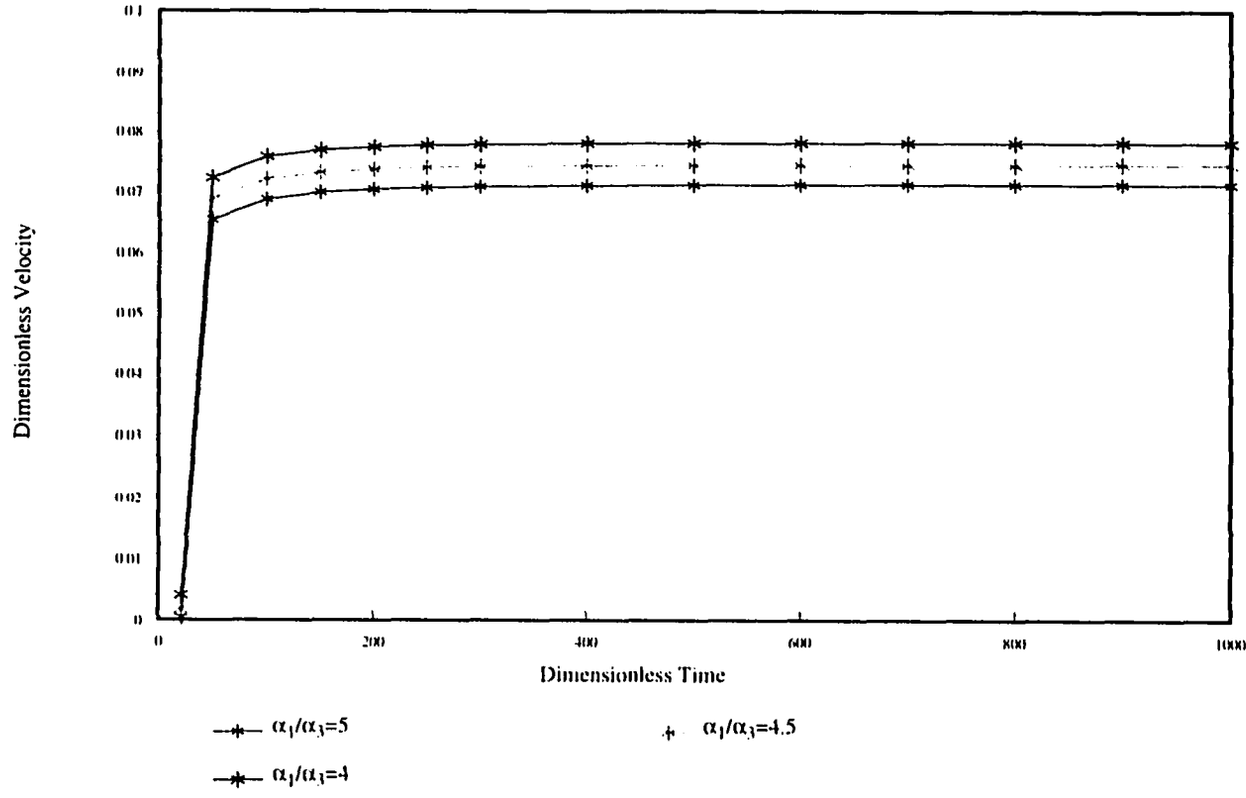

Figure 97: Erosion Growth Rate for Various Thermal Diffusivities ($\alpha_1=1\times10^{-7}$ m^2/sec; $\alpha_1/\alpha_2=2$)

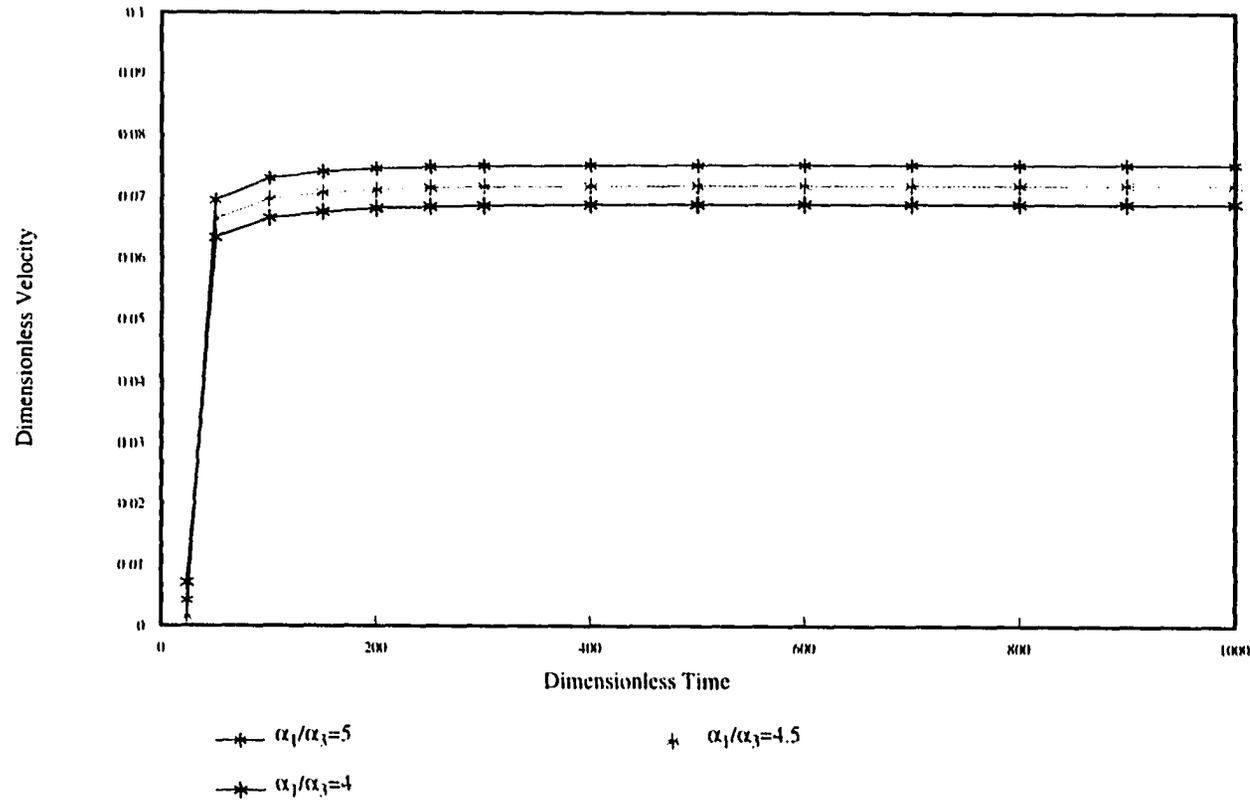

Figure 98: Erosion Growth Rate for Various Thermal Diffusivities ($\alpha_1=1x10^{-7}$ m^2/sec; $\alpha_1/\alpha_2=2.5$)

4.4.2. Effect of the Decomposition/Ablation Latent Heat

The endothermic reactions of decomposition and the melting of the concrete provide heat sinks at the reaction interface. This affects the amount of heat conducted to in-depth concrete and thus affects the growth and growth rates of each region. To evaluate this effect, one needs to consider the ablation and decomposition temperature of each reaction together with the density and the latent heat. The ablation and decomposition temperatures are not precisely defined because of several reasons: the decomposition does not take place at single front, the material does not completely decompose at that temperature, and the latent heats of decomposition and the ablation are not lumped together to that front. These parameters, in fact, are not totally independent since each reaction takes place at a temperature with the latent heat appropriate to that temperature. If all the latent heats are calculated with corresponding decomposition temperature, although it would differ at the different distances in the medium, it will not affect the overall energy balance.

The parameter that would be interesting to look at is the Stefan's number which represents the comparison of the volumetric heat loss (or the decomposition reaction range) with the latent heat of the reaction. Using the data presented in Figure 11 in the model, the growth rates and growth of each region can be calculated for various Stefan Numbers. Table 13 represents the selected Stefan Number with the corresponding decomposition temperatures and the latent heat. Again, the density and the specific heat of the concrete are assumed to be constant.

Table 14 lists the significant results from the model and the characteristic behaviors of the region growth and growth rates during melting for different Stefan Numbers, and are presented in Figures 101 through 106.

It is interesting to see that the Stefan Number is not the parameter that would help to see the affect of thermal parameters, but the decomposition temperatures have a direct effect on the erosion rate and depth. As was mentioned earlier, the Stefan Numbers can be translated into the relationship between the latent heat and the volumetric heat loss. Figures 99 and 100 show the effect of melting temperature on the erosion rate and depth.

As can be seen in Table 14, the melting temperature affects the erosion rate and the depth. The higher melting temperatures result in the lower erosion rate almost independent of the latent heat of melting. It is also interesting to see that the melting temperature is an effective parameter for the growth of the thermally affected region since the higher melting temperatures delay the melting reaction, and thus cause more heat to be transferred deep into the concrete. This results in the higher growth of the thermally affected region.

For the gas free region, the lower latent heat of melting results in more heat being transferred to the concrete and thus causing the dehydration to begin earlier which can be observed as a thinner gas-free region. For the dehydrated region, it is the combined effects of the melting temperature, decomposition temperature of the gas release, and the latent heats of those reactions.

The results of evaluating the effect of the decomposition temperature and enthalpy on other region growth and growth rates prior to and after the melting reaction are included in Appendix B. That information is to be used for the calculation of the gas, and water release before the melting begins.

Table 13: Thermal Parameters Used to Evaluate the Effects of Latent Heat

Case No.	T_w (K)	T_c (K)	T_m (K)	L_1 (kJ/kg)	L_2 (kJ/kg)	L_3 (kJ/kg)	St_1	St_2	St_3
1	450	850	1350	100	500	1100	2	0.98	0.56
2	600	850	1350	250	400	1100	1.5	0.77	0.56
3	750	850	1350	500	100	1100	1.125	1.23	0.56
4	450	1000	1350	100	750	800	2	0.90	0.54
5	600	1000	1350	250	600	800	1.5	0.82	0.54
6	750	1000	1350	500	400	800	1.125	0.77	0.54
7	450	1250	1350	100	1500	123	2	0.66	1.0
8	600	1250	1350	250	1250	123	1.5	0.64	1.0
9	750	1250	1350	500	1200	123	1.125	0.51	1.0
10	450	850	1500	100	500	1500	2	0.98	0.53
11	600	850	1500	250	400	1500	1.5	0.77	0.53
12	750	850	1500	500	100	1500	1.125	1.23	0.53
13	450	1000	1500	100	750	1250	2	0.90	0.49
14	600	1000	1500	250	600	1250	1.5	0.82	0.49
15	750	1000	1500	500	400	1250	1.125	0.77	0.49
16	450	1250	1500	100	1500	400	2	0.66	0.77
17	600	1250	1500	250	1250	400	1.5	0.64	0.77
18	750	1250	1500	500	1200	400	1.125	0.51	0.77
19	450	850	1650	100	500	1900	2	0.98	0.52
20	600	850	1650	250	400	1900	1.5	0.77	0.52
21	750	850	1650	500	100	1900	1.125	1.23	0.52
22	450	1000	1650	100	750	1650	2	0.90	0.48
23	600	1000	1650	250	600	1650	1.5	0.82	0.48
24	750	1000	1650	500	400	1650	1.125	0.77	0.48
25	450	1250	1650	100	1500	800	2	0.66	0.62
26	600	1250	1650	250	1250	800	1.5	0.64	0.62
27	750	1250	1650	500	1200	800	1.125	0.51	0.62

Table 14: Summary of Results for Latent Heat Case (Fo=1000)

Case No	ds/dt	s	s_3	s_2	s_1
1	0.114	111.75	1.64	5.24	17.63
2	0.113	111.01	1.63	2.39	17.72
3	0.118	115.99	1.69	0.66	16.95
4	0.115	113.61	0.94	5.98	17.34
5	0.116	114.11	0.95	3.24	17.24
6	0.116	113.67	0.95	1.52	17.29
7	0.114	112.75	0.18	7.05	17.41
8	0.118	116.66	0.18	4.34	16.77
9	0.111	109.63	0.18	2.75	17.78
10	0.095	93.16	2.37	6.26	21.04
11	0.095	92.72	2.37	2.84	21.10
12	0.099	96.57	2.47	0.79	20.24
13	0.095	93.04	1.54	7.26	21.06
14	0.096	93.48	1.55	3.94	20.92
15	0.096	93.36	1.55	1.84	20.92
16	0.098	95.92	0.54	8.16	20.43
17	0.100	98.43	0.54	5.03	19.89
18	0.095	93.22	0.53	3.15	20.95
19	0.082	79.72	3.19	7.27	24.44
20	0.082	79.43	3.19	3.30	24.47
21	0.085	82.51	3.35	0.92	23.52
22	0.082	79.53	2.21	8.45	24.49
23	0.082	79.91	2.22	4.57	24.32
24	0.082	79.95	2.23	2.13	24.28
25	0.084	81.41	0.96	9.56	23.93
26	0.086	83.31	0.97	5.91	23.35
27	0.082	79.52	0.96	3.67	24.39

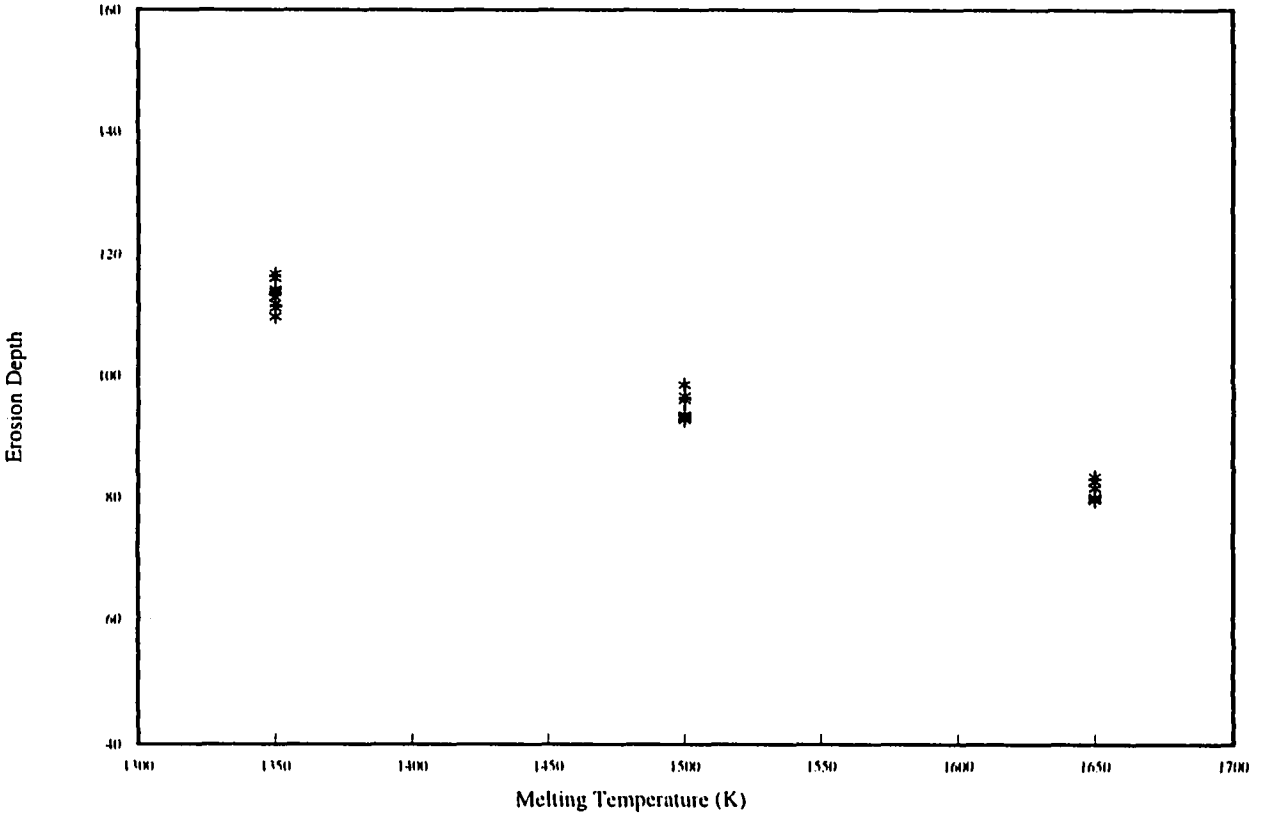

Figure 99: Effect of the Melting Temperature on Erosion Depth (Depth @ Fo=1000)

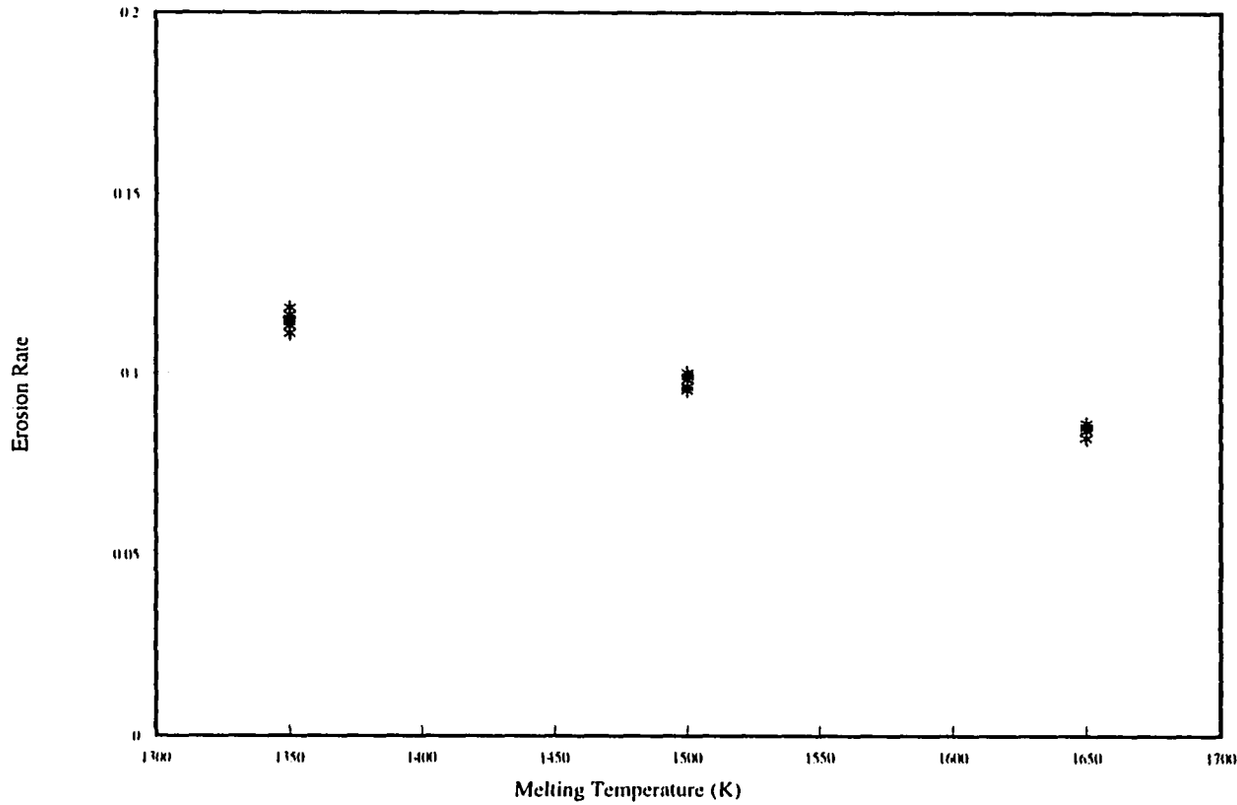

Figure 100: Effect of the Melting Temperature on Erosion Rate (Rate @ Fo=1000)

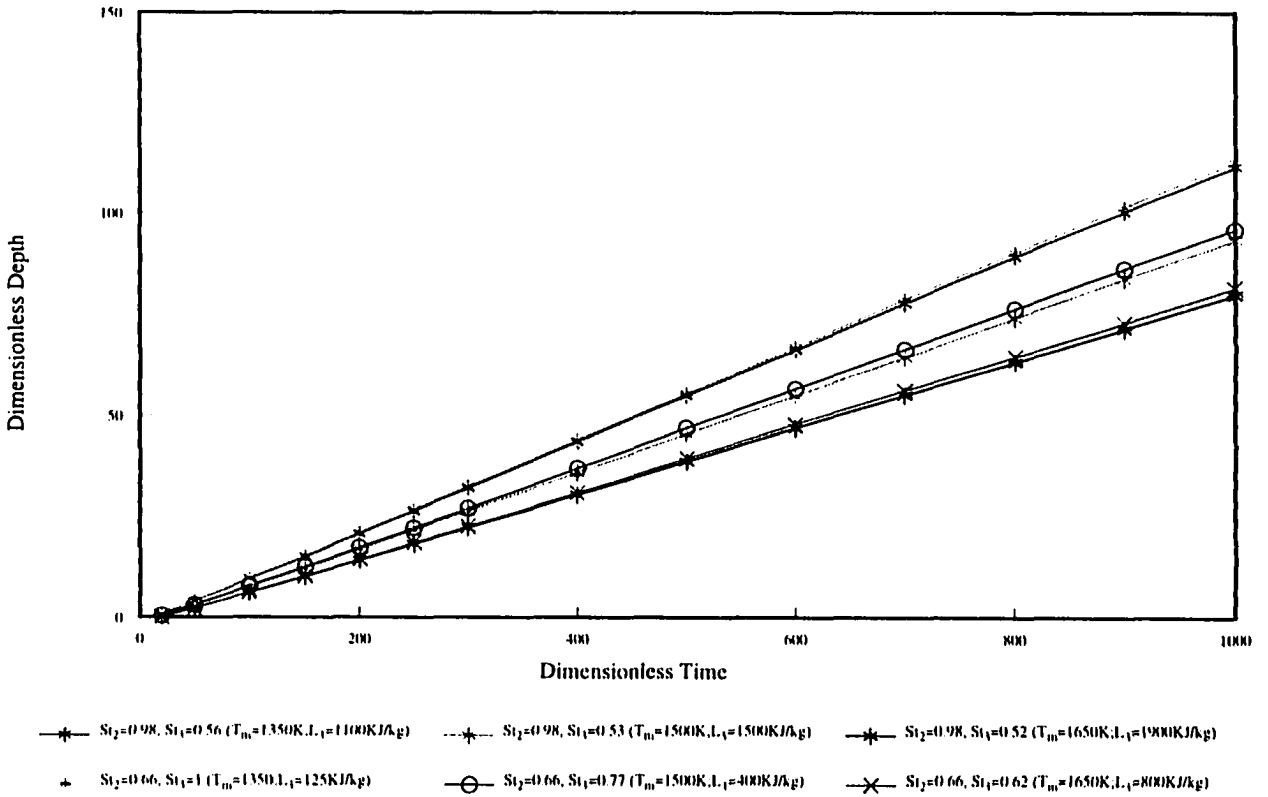

Figure 101: Erosion Growth for Various Stefan Numbers (St_1=2)

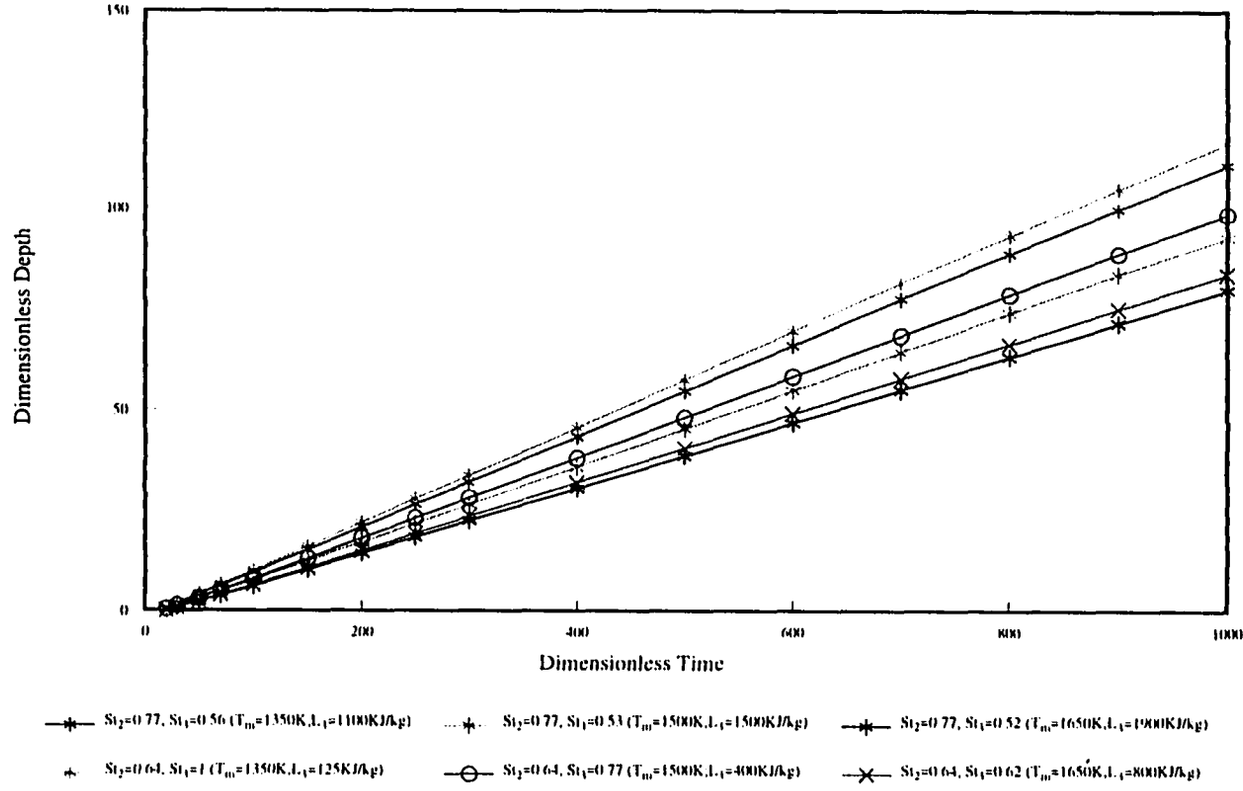

Figure 102: Erosion Growth for Various Stefan Numbers (St_1=1.5)

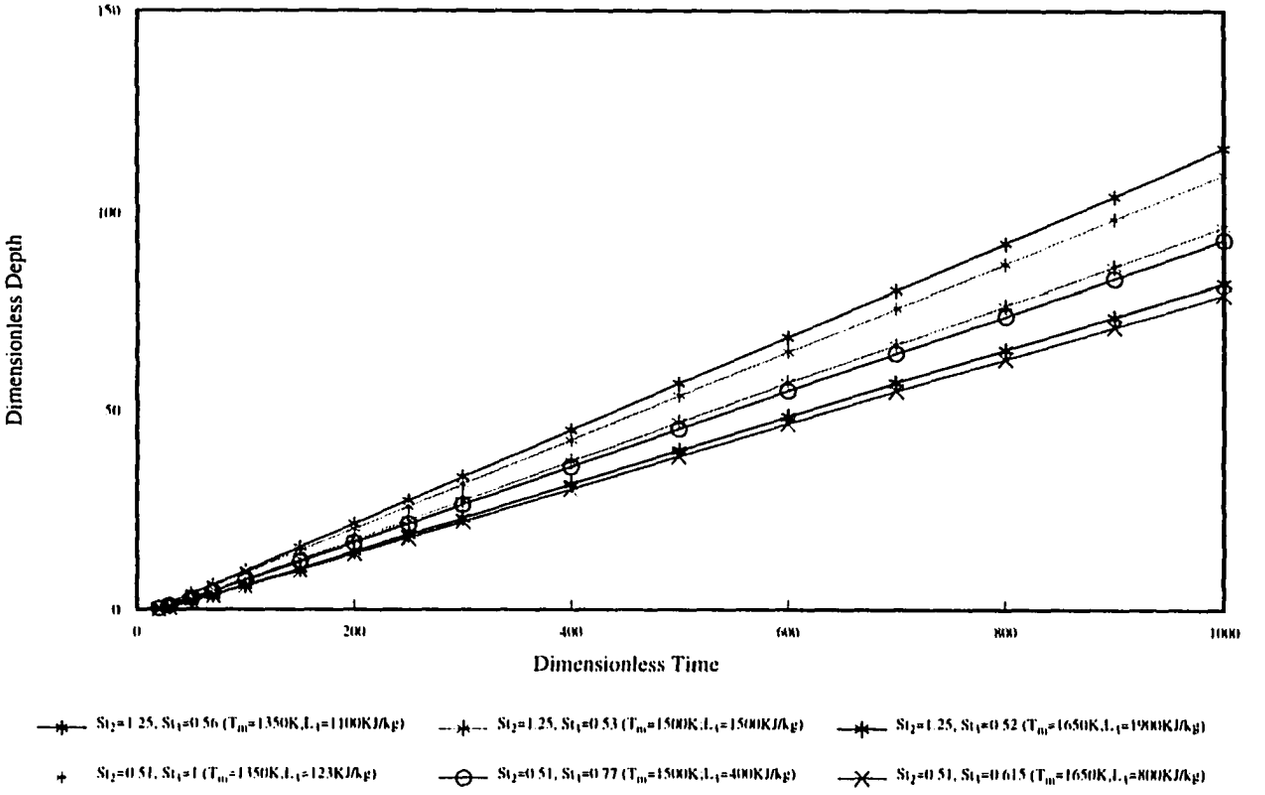

Figure 103: Erosion Growth for Various Stefan Numbers (St_1=1.125)

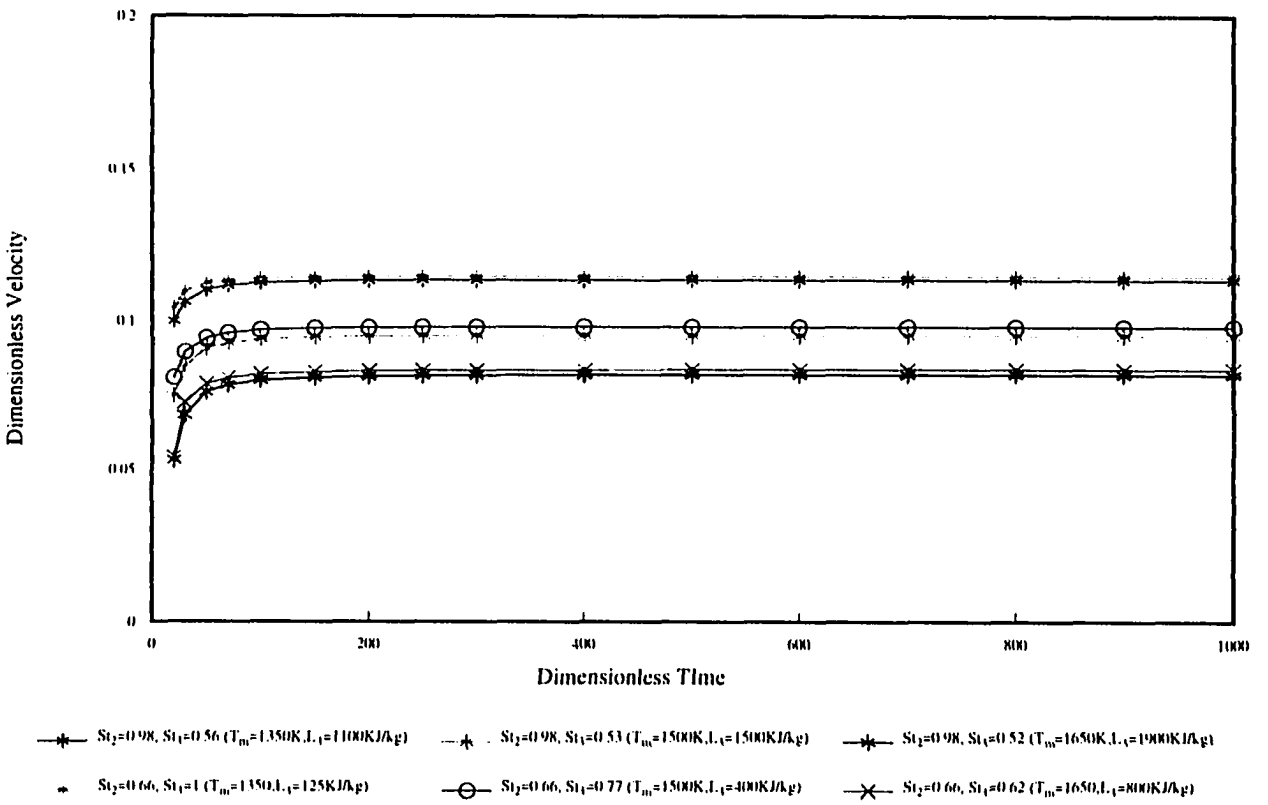

Figure 104: Erosion Growth Rate for Various Stefan Numbers (St_1=2)

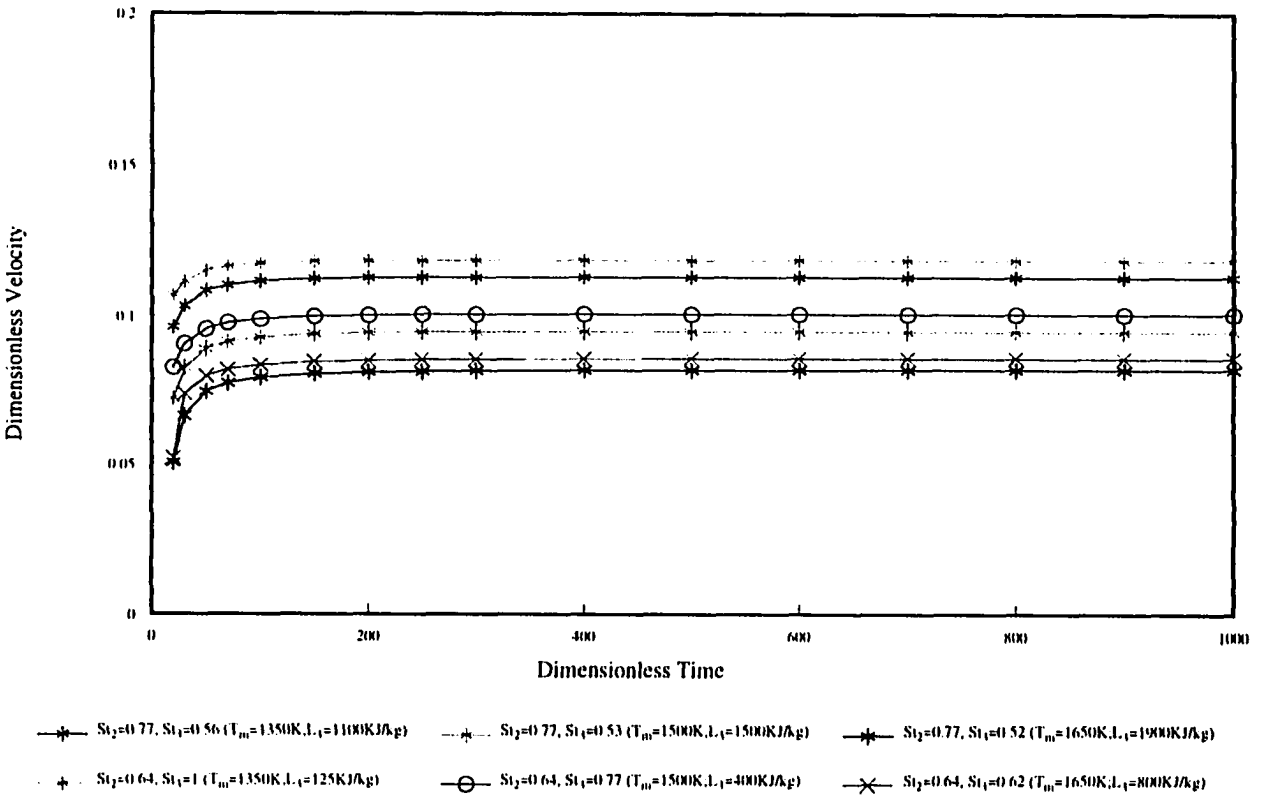

Figure 105: Erosion Growth Rate for Various Stefan Numbers (St_1=1.5)

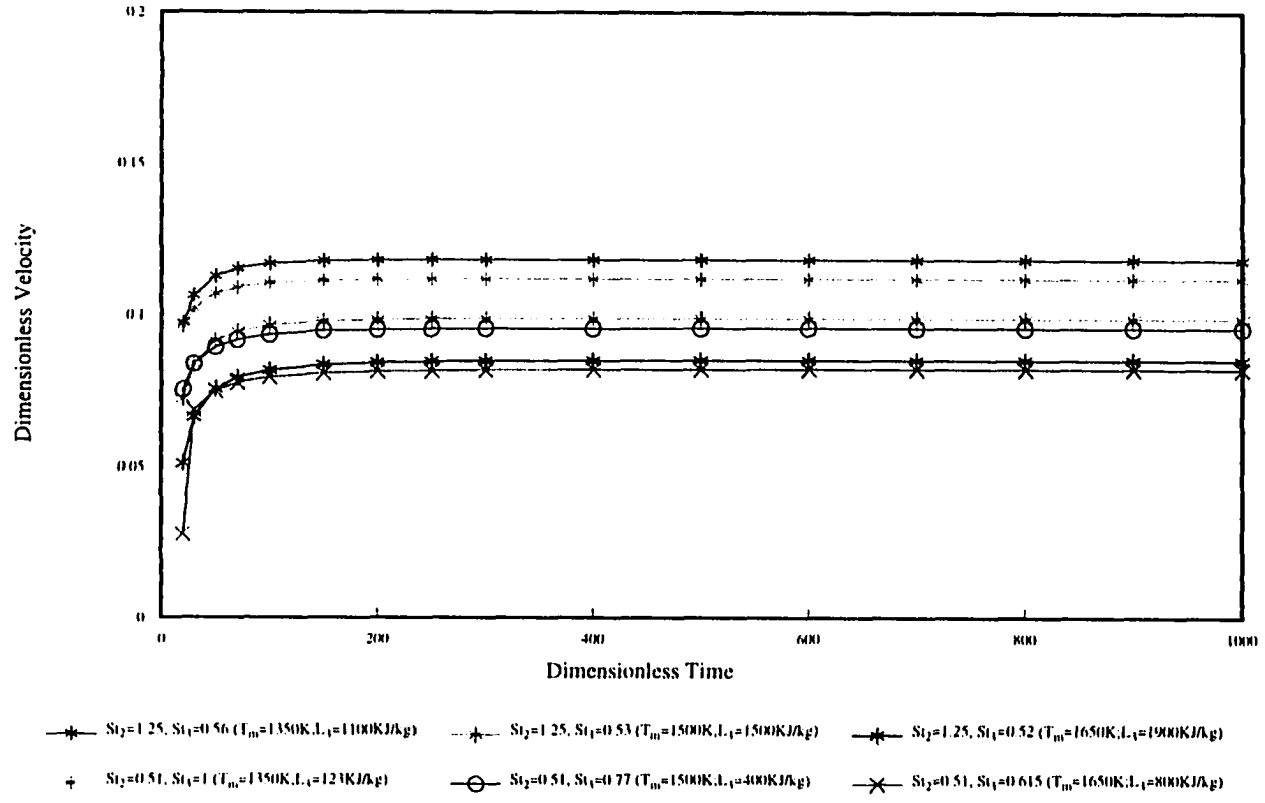

Figure 106: Erosion Growth Rate for Various Stefan Numbers (St_1=1.125)

CHAPTER 5

CONCLUSION

In this study, a multi-region, transient concrete ablation model is developed. The model consists of four regions of concrete containing a thermally affected region, a dry (evaporated and chemically dehydrated) region, and a gas-free region with ablated concrete at the melt/concrete interface. Each region has an interface where the latent heat of decomposition reactions is taken into account as heat sinks due to endothermic characteristics of the reaction. The time dependent temperature profiles in each region, and the time dependent depth and growth rate of the regions are evaluated by use of the heat balance integral method. Each region consists of a simultaneous solution to the conservation equation of energy. A set of constitutive relationships, that couple the equations and regions together, is included so that the closed form of solutions can be obtained. Of the various constitutive relationships, the surface and the heat fluxes, which were related by the incoming and lost energy due to the reactions, affect the depth and the growth rate of each region. This effect relates to the release of concrete ingredients that contribute to gas, water, and aerosol release from the concrete to the melt and eventually to the containment atmosphere. Of the thermophysical properties, the thermal conductivity has the greatest impact on the depth and growth rate of the erosion and other decomposition reactions in the concrete. The decomposition

temperatures and their corresponding latent heat (enthalpies) values have also substantial effect on the depth and the growth rate of the regions. The model is implemented to evaluate all these effects of the surface heat flux and the thermophysical parameters. The results are presented in a normalized form so that the actual phenomena can be extrapolated using the results of this study.

Based on the results of this study, the observations can be concluded as follows:

1. The erosion, and thermally affected, dehydrated, decarboxylated region depth and growth rate are proportional to the initial surface heat flux, and inversely proportional to the energy storage capacity of concrete, $(\rho c T_i)$, for all forms of surface heat flux.

2. For constant surface heat flux, the carboxylated, dehydrated, and thermally affected concrete regions reach a constant thickness almost immediately in case of high heat fluxes and in a very short time for the low heat fluxes, and the erosion becomes steady state with a constant growth rate.

The thermal front reaches its constant depth after the erosion front reaches its steady state velocity. This shows that the MCCI models that calculate the erosion rate based on the thermal front velocity overestimate the ablation of the concrete.

3. For the surface heat flux in forms of $e^{-\lambda t}$, erosion terminates in the event, while the depth of other regions continues to grow for a long period of time after the erosion stops. The time when the erosion stops and the maximum eroded con-

crete thickness are logaritmically proportional to the cooldown rate.

4. For the surface heat flux in forms of $t^{-\lambda}$, the erosion depth and the depth of the other regions approaches an asymptotic value. Erosion front reaches its asymptotic depth much earlier than the other regions. For practical purposes, the erosion terminates in this type of surface heat flux.

5. The higher thermal conductivity results in a higher erosion depth and rate due to the faster propagation of the heat into the gas-free concrete region, and thus increasing the temperature of that region to melting temperature faster.

6. The higher melting (ablation) temperature results in a lower erosion depths and rates since it causes the delay of melting reaction. This also translates into more time to propagate the heat into the concrete before the melting starts, and thus results in thicker and deeper thermally affected concrete region.

7. A reduction factor between 60 to 45 percent (model predicts 37.5 percent for heat fluxes <10 MW/m^2, and 52.5 percent for heat fluxes >10 MW/m^2) is applicable to the incident flux to approximate the surface heat flux. A further study is recommended to determine the ratio of net surface to incident heat fluxes by modelling the radiation and convection heat transfer mechanism.

The results of this study have been in very good agreement with the experimental data. It shows better agreement with the data than the previous steady state and single region transient ablation models. The results of the model are valid for the low heat fluxes and/or decreasing surface heat flux (due to cooling and crust formations that occur in the actual phenomena) cases where the steady state mod-

els fail.

The multi region approach to the problem is a more representative simulation of the concrete reaction in terms of modelling the individual decomposition reactions and their locations in the concrete. This provides not only the better prediction of the erosion rate and depth, but also the prediction of the thicknesses and growth rates of each decomposed concrete domain, thus locates and calculates the concrete degradation. This very useful information in order to calculate the amount of gas (CO, H_2, CO_2, etc.), water, and aerosol released to the melt and the containment atmosphere due to the concrete decomposition.

The study also presents the normalized results for the thermophysical properties of concrete which can be used to calculate the erosion depth and rates and degraded concrete region thicknesses and growth rates for any type of concrete used in an experiment or in an actual built-in concrete basemat of a containment building by extrapolating or interpolating the results to the actual thermophysical properties.

The model presented in this study is simple yet very detailed and accurate to simulate the actual MCCI phenomena, and investigates the concrete reaction to the molten core. It can be embodied into the MCCI codes currently being developed to determine the containment integrity, and the fission products release to the environment and to the public. It is also a valid and accurate code to be used alone for concrete erosion and decomposition calculations.

APPENDIX A:
MODEL RESULTS FOR REGION GROWTH AND GROWTH RATES FOR VARIOUS THERMAL DIFFUSIVITIES

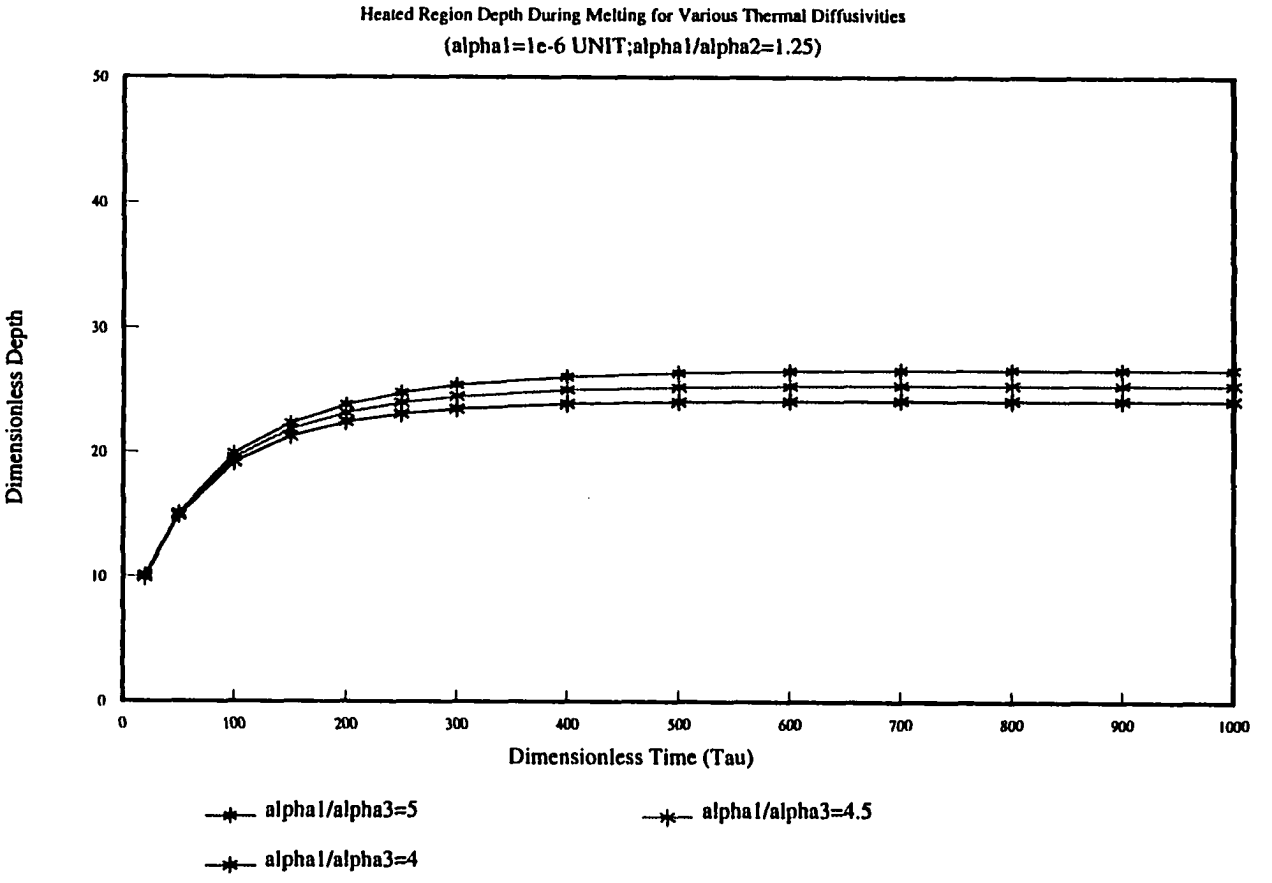

Figure 107: Heated Region Depth During Melting for Various Thermal Diffusivities (α_1=1x10^{-6} m^2/sec; α_1/α_2=1.25).

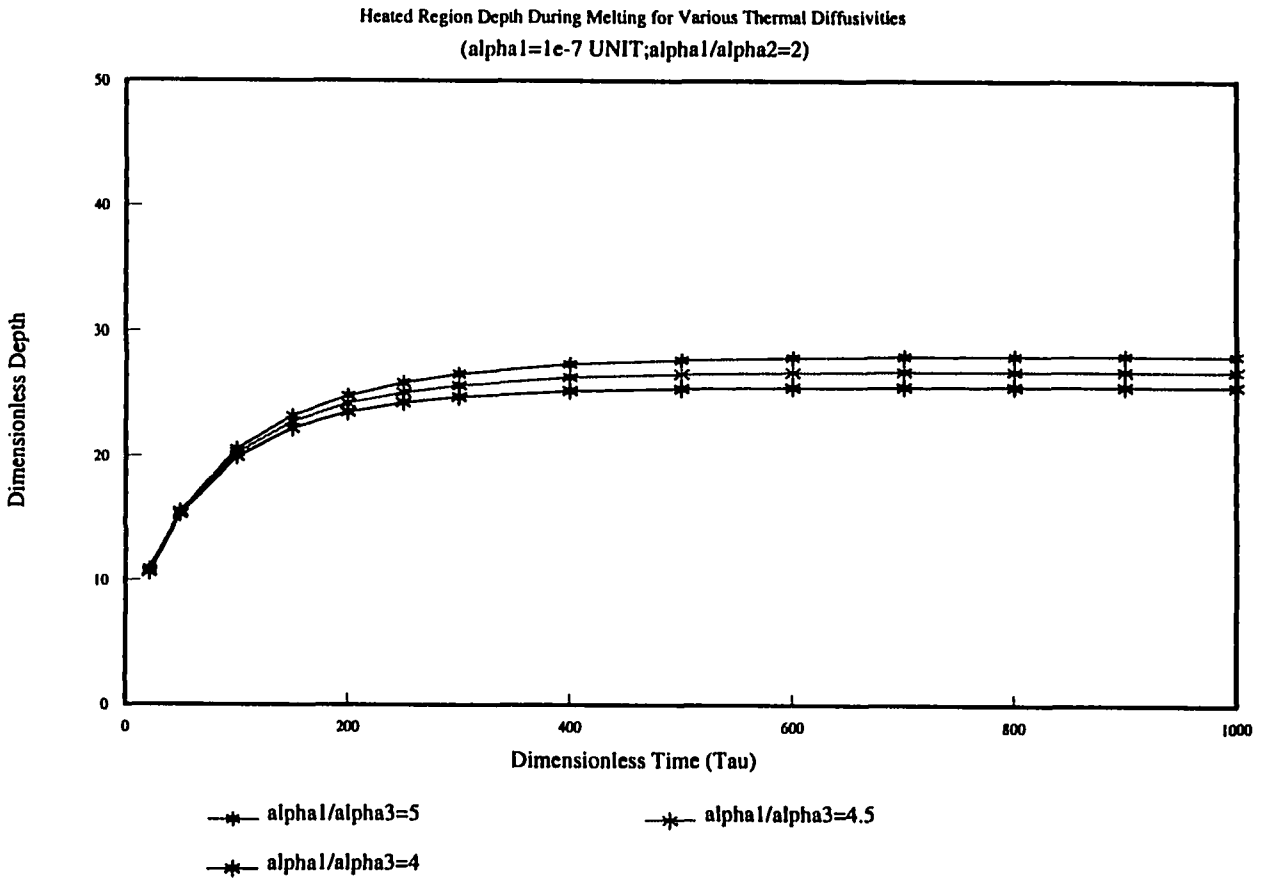

Figure 108: Heated Region Depth During Melting for Various Thermal Diffusivities (α_1=1x10^{-6} m^2/sec; α_1/α_2=2).

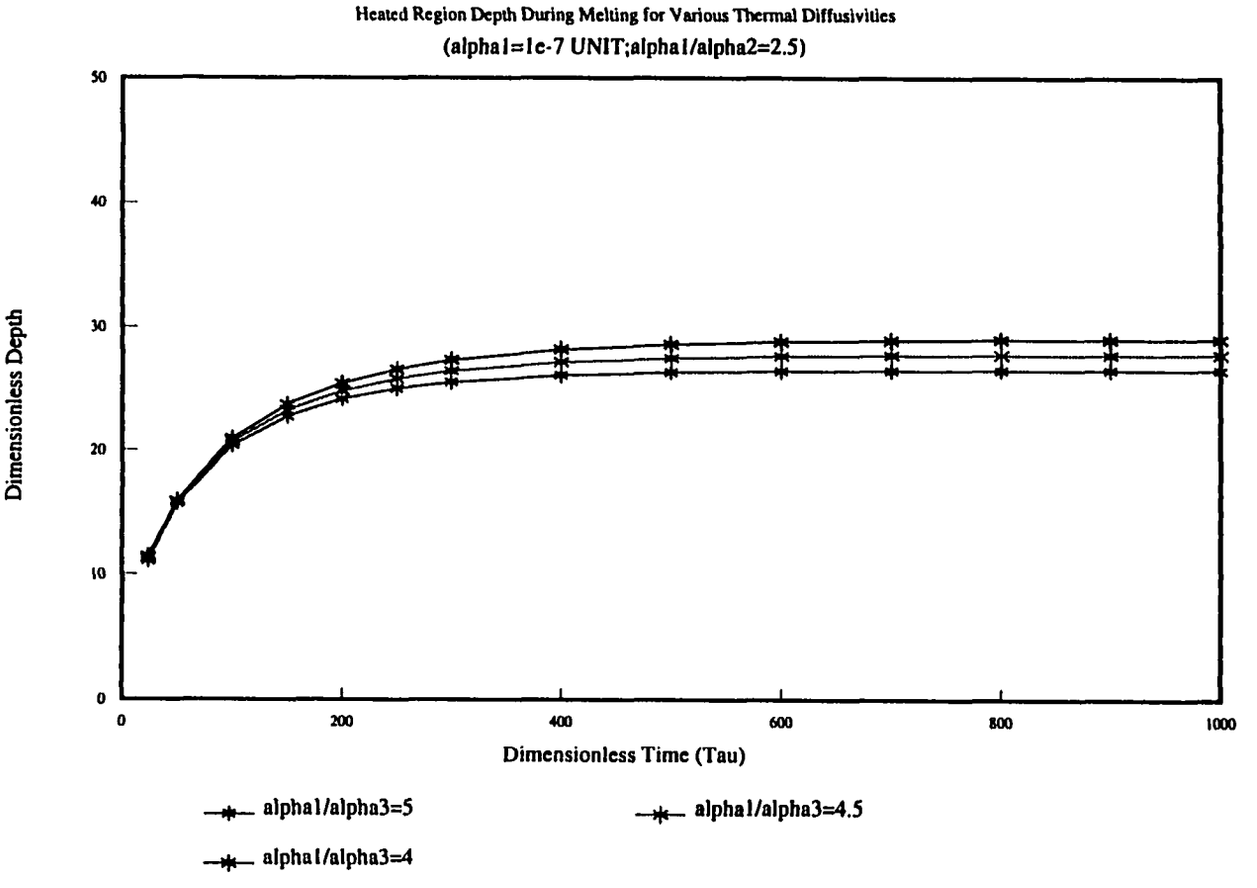

Figure 109: Heated Region Depth During Melting for Various Thermal Diffusivities ($\alpha_1=1x10^{-6}$ m^2/sec; $\alpha_1/\alpha_2=2.5$).

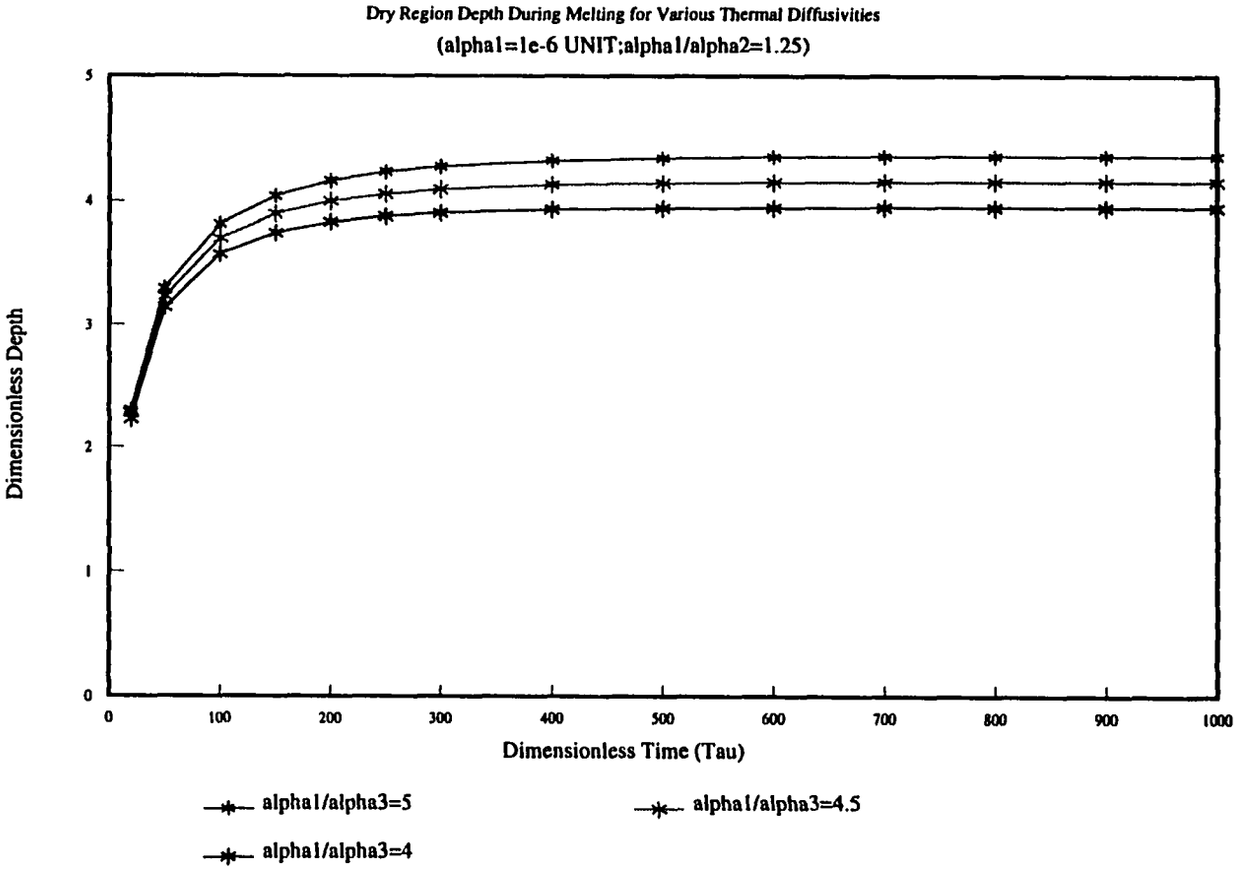

Figure 110: Dry Region Depth During Melting for Various Thermal Diffusivities (α_1=1x10^{-6} m^2/sec; α_1/α_2=1.25).

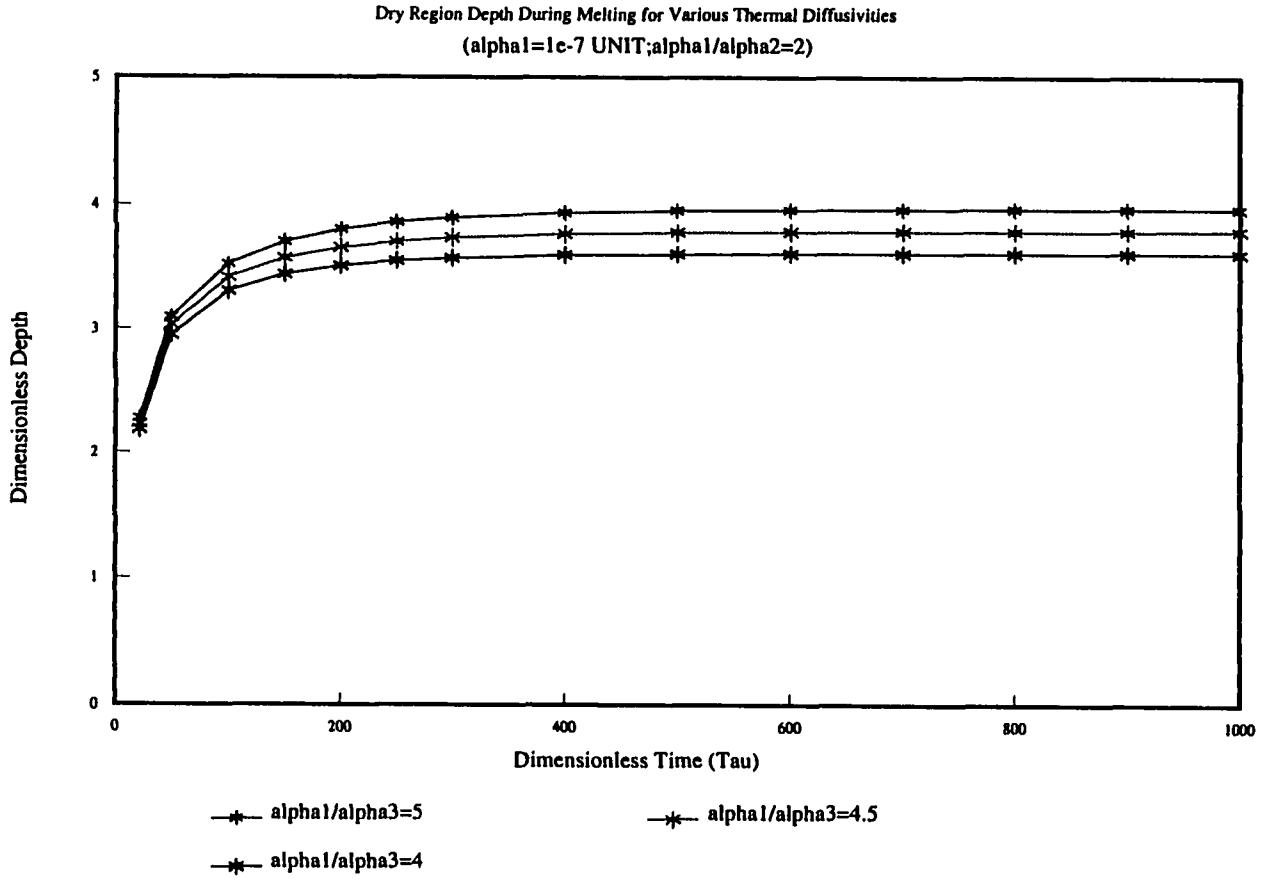

Figure 111: Dry Region Depth During Melting for Various Thermal Diffusivities (α_1=1x10^{-6} m^2/sec; α_1/α_2=2).

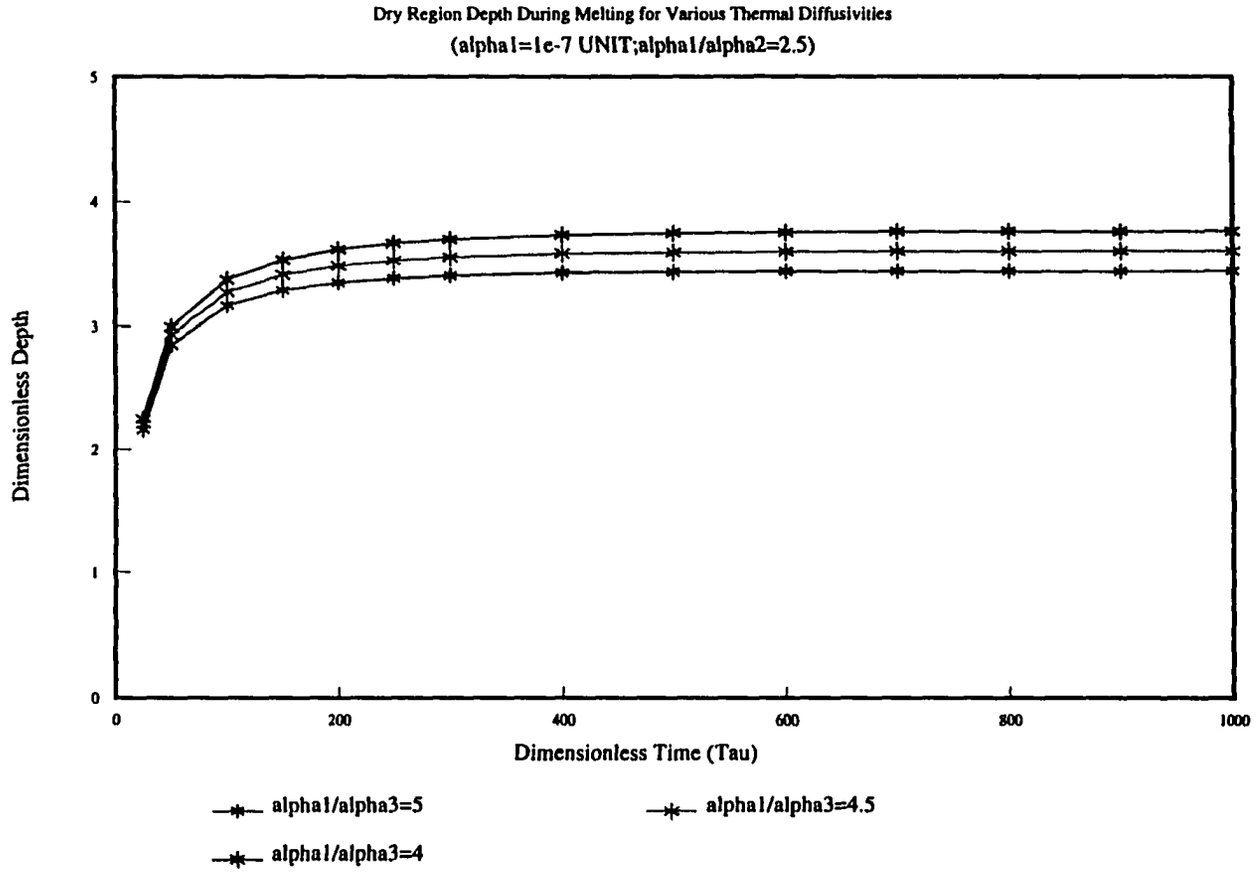

Figure 112: Dry Region Depth During Melting for Various Thermal Diffusivities (α_1=1x10^{-6} m^2/sec; α_1/α_2=2.5).

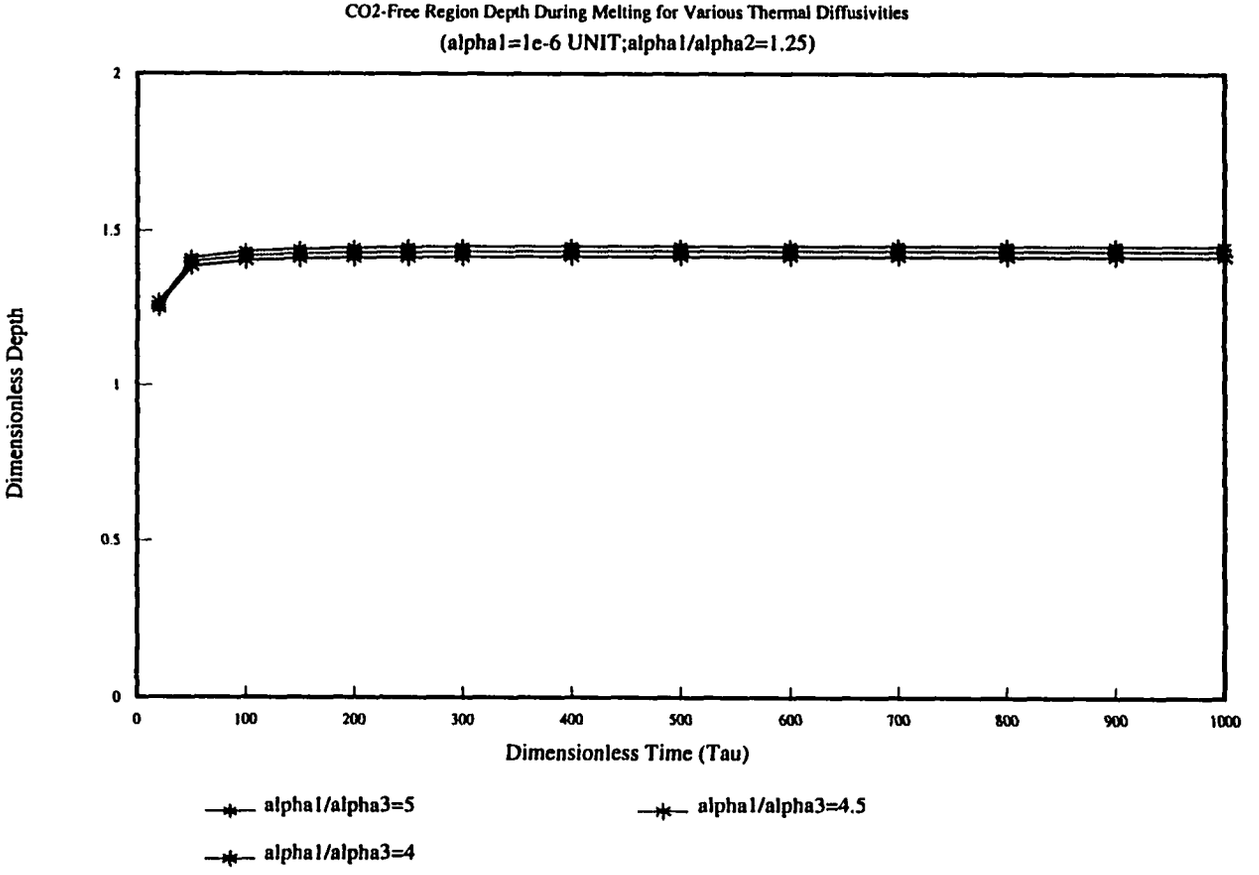

Figure 113: CO_2-Free Region Depth During Melting for Various Thermal Diffusivities ($\alpha_1=1x10^{-6}$ m^2/sec; $\alpha_1/\alpha_2=1.25$).

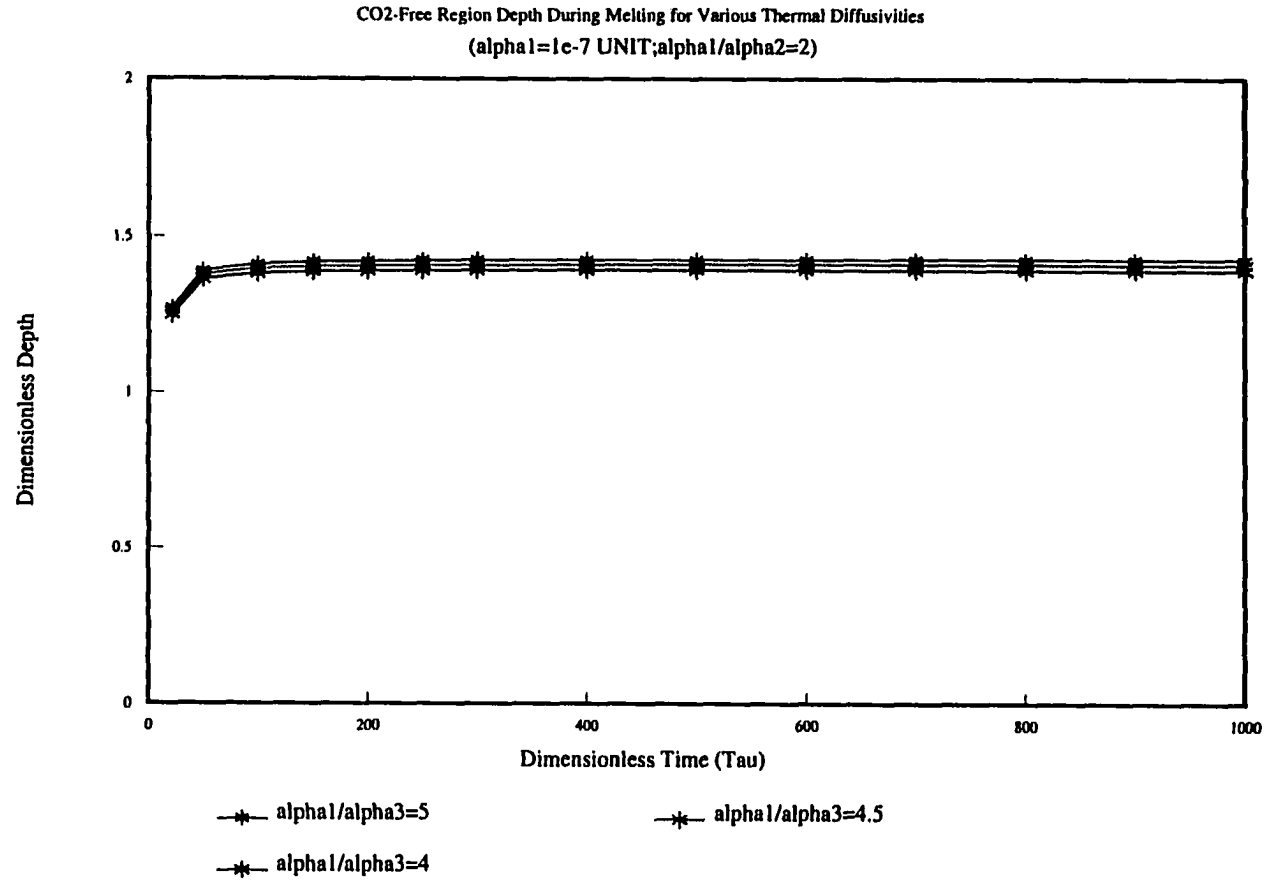

Figure 114: CO_2-Free Region Depth During Melting for Various Thermal Diffusivities ($\alpha_1=1\times10^{-6}$ m^2/sec; $\alpha_1/\alpha_2=2$).

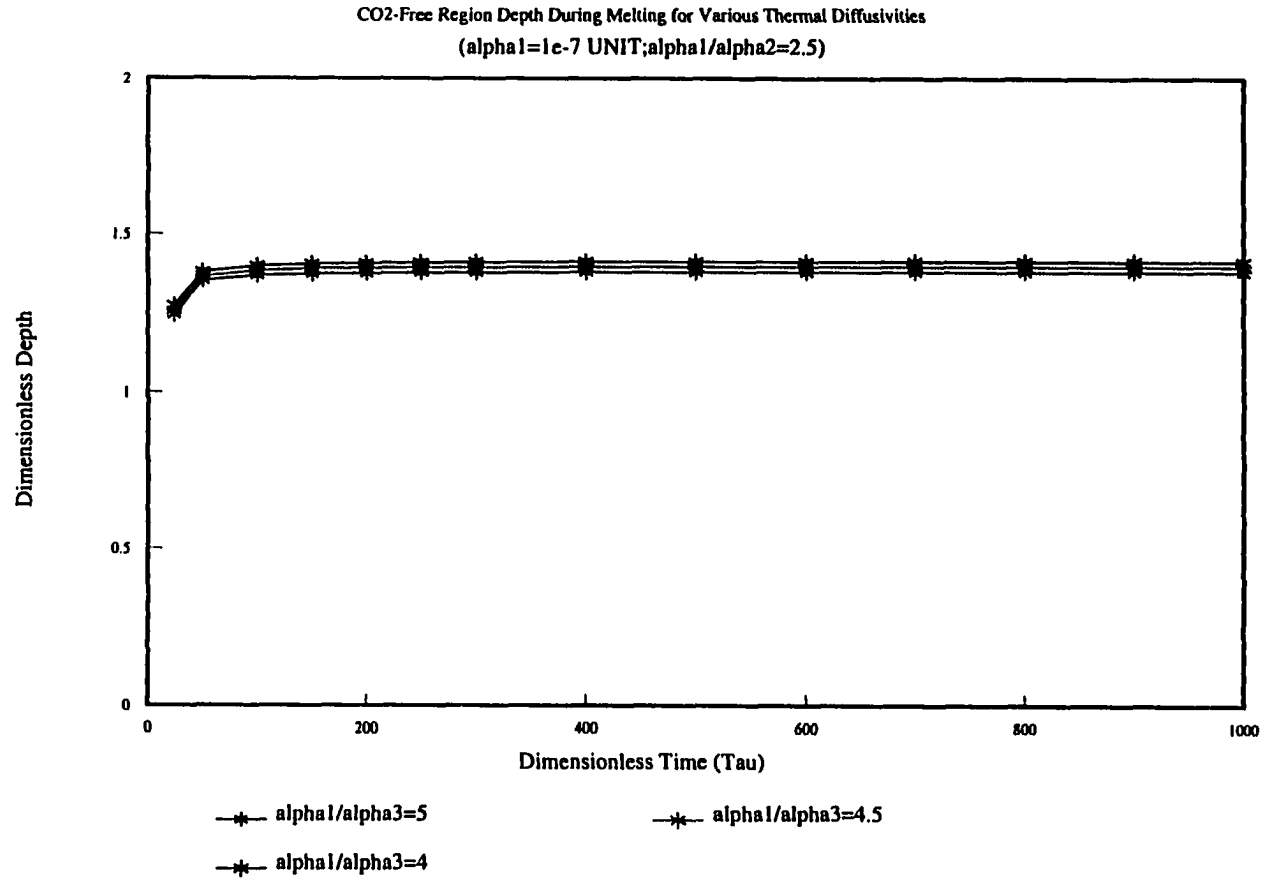

Figure 115: $C0_2$-Free Region Depth During Melting for Various Thermal Diffusivities ($\alpha_1=1x10^{-6}$ m^2/sec; $\alpha_1/\alpha_2=2.5$).

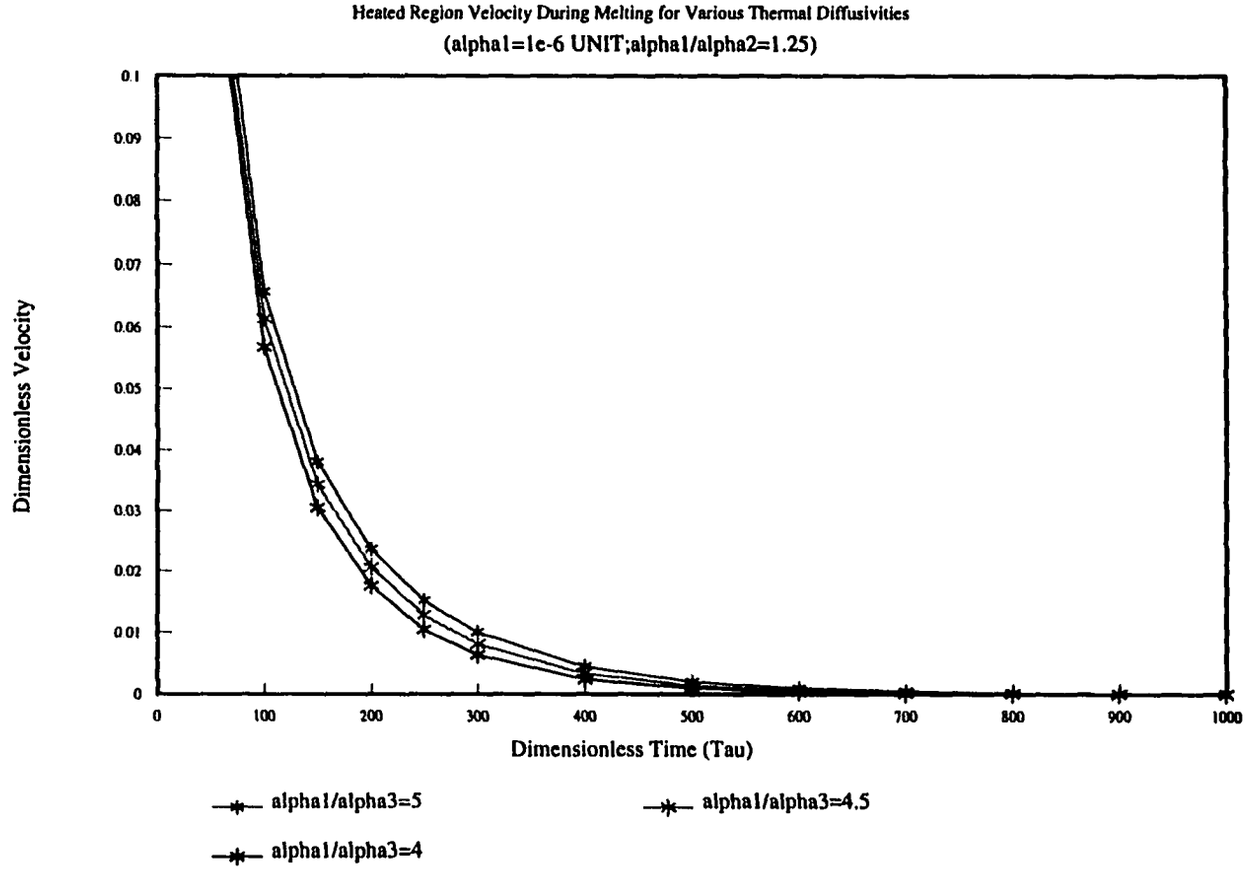

Figure 116: Heated Region Velocity During Melting for Various Thermal Diffusivities ($\alpha_1=1x10^{-6}$ m^2/sec; $\alpha_1/\alpha_2=1.25$).

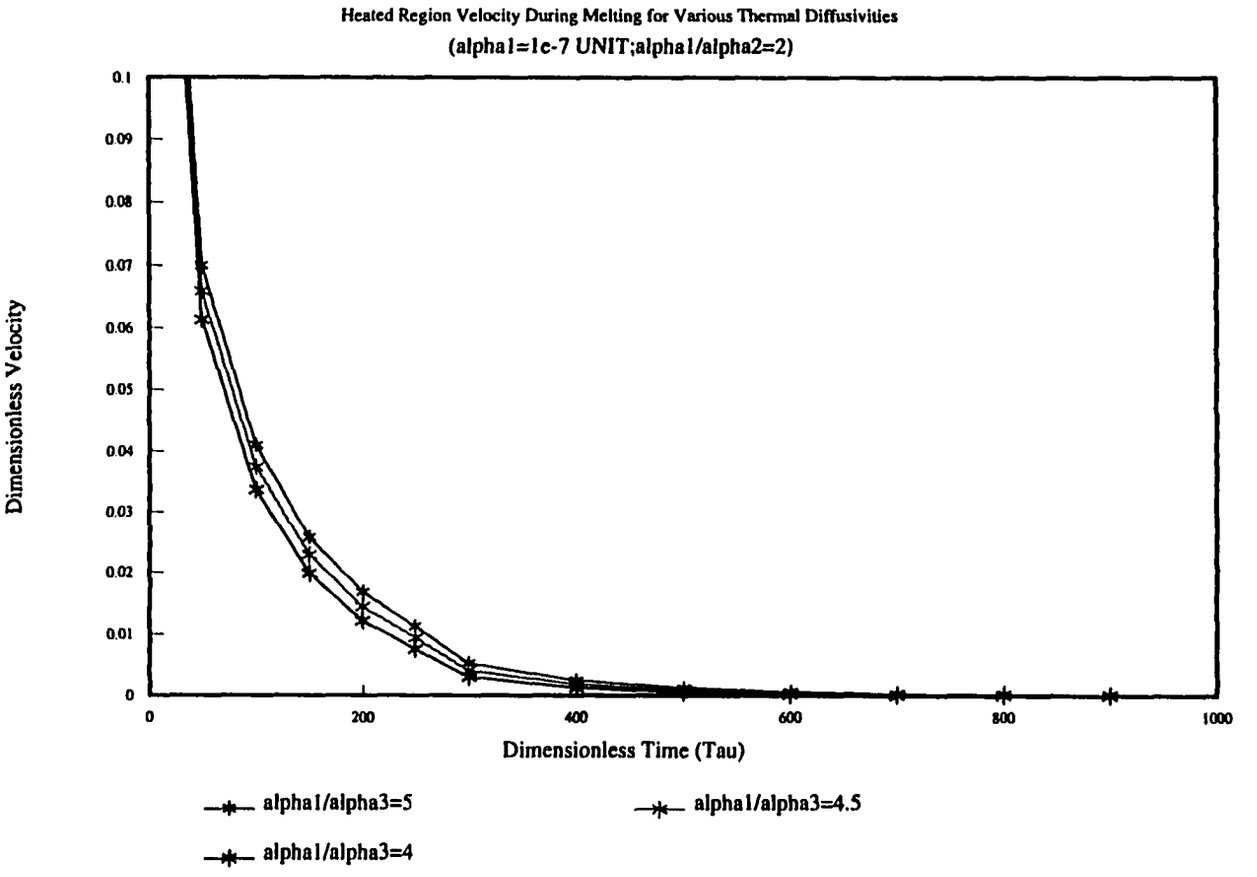

Figure 117: Heated Region Velocity During Melting for Various Thermal Diffusivities (α_1=1x10^{-6} m^2/sec; α_1/α_2=2).

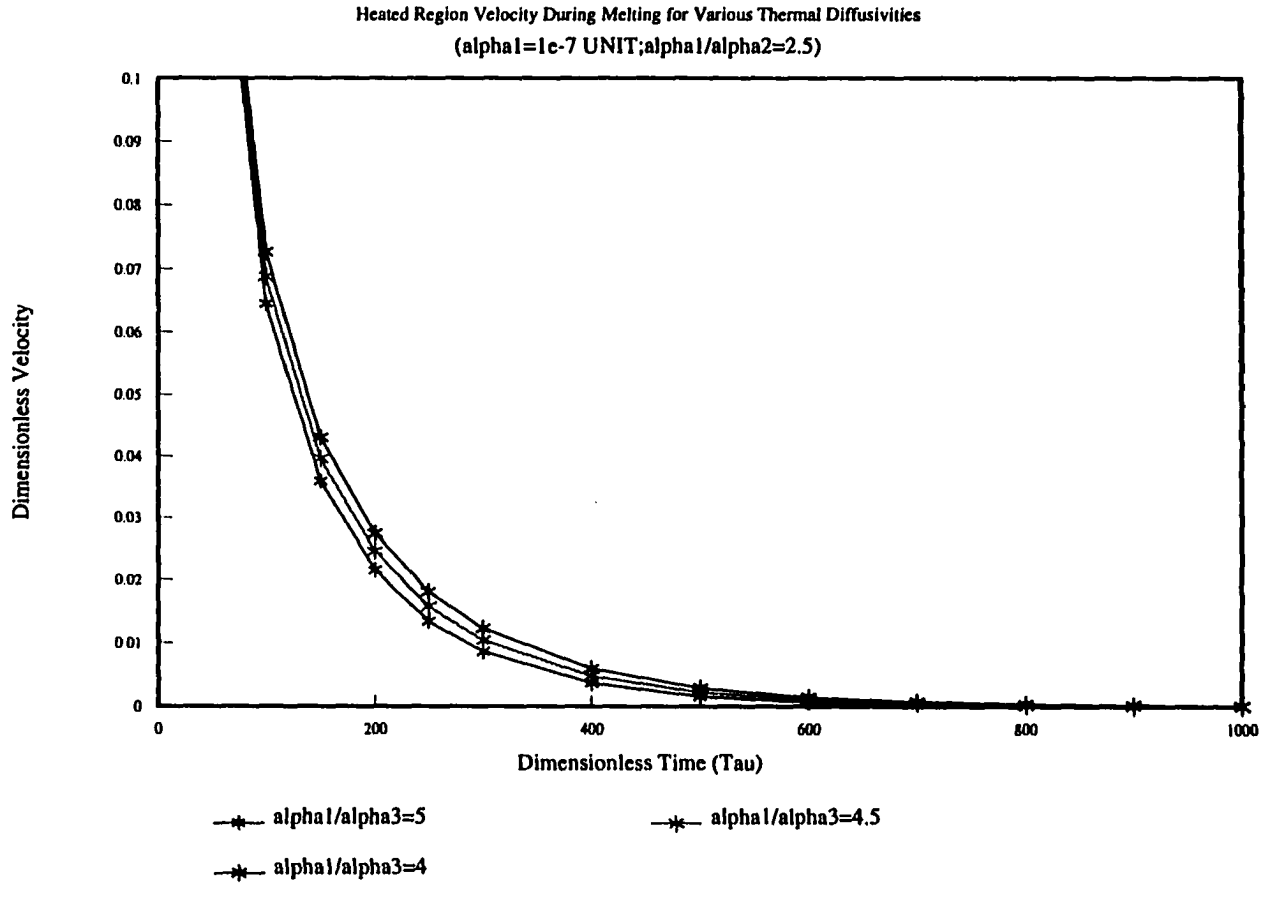

Figure 118: Heated Region Velocity During Melting for Various Thermal Diffusivities (α_1=1x10^{-6} m^2/sec; α_1/α_2=2.5).

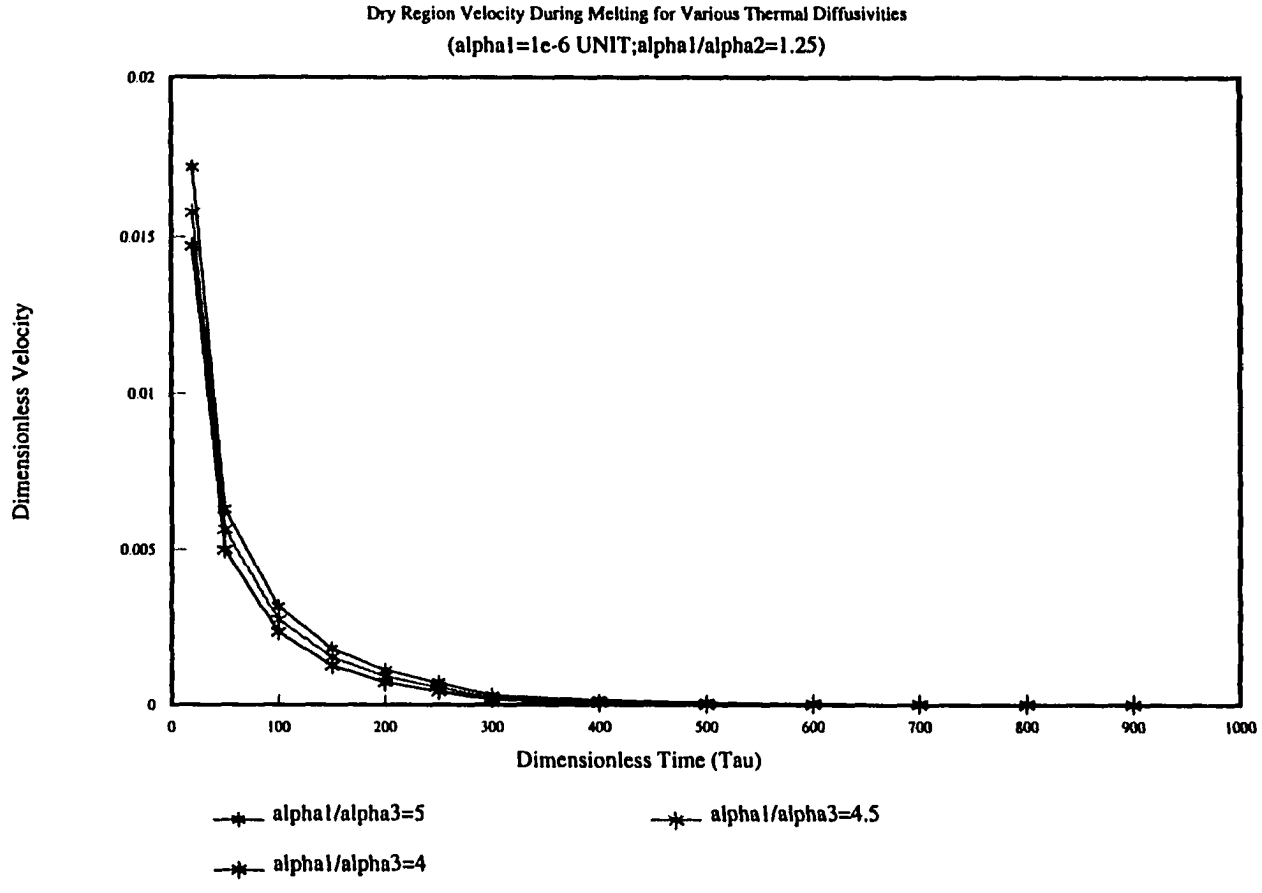

Figure 119: Dry Region Velocity During Melting for Various Thermal Diffusivities (α_1=1x10^{-6} m^2/sec; α_1/α_2=1.25).

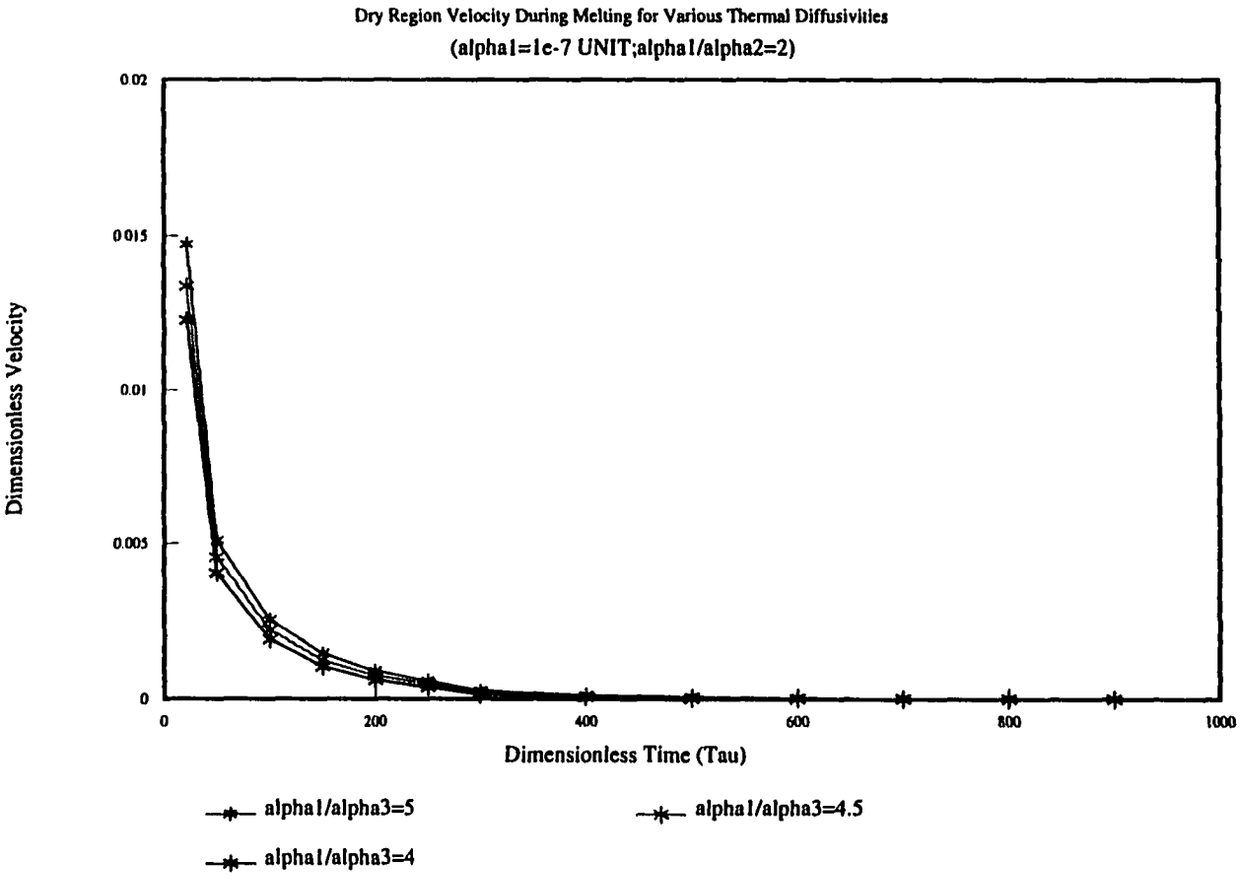

Figure 120: Dry Region Velocity During Melting for Various Thermal Diffusivities (α_1=1x10^{-6} m^2/sec; α_1/α_2=2).

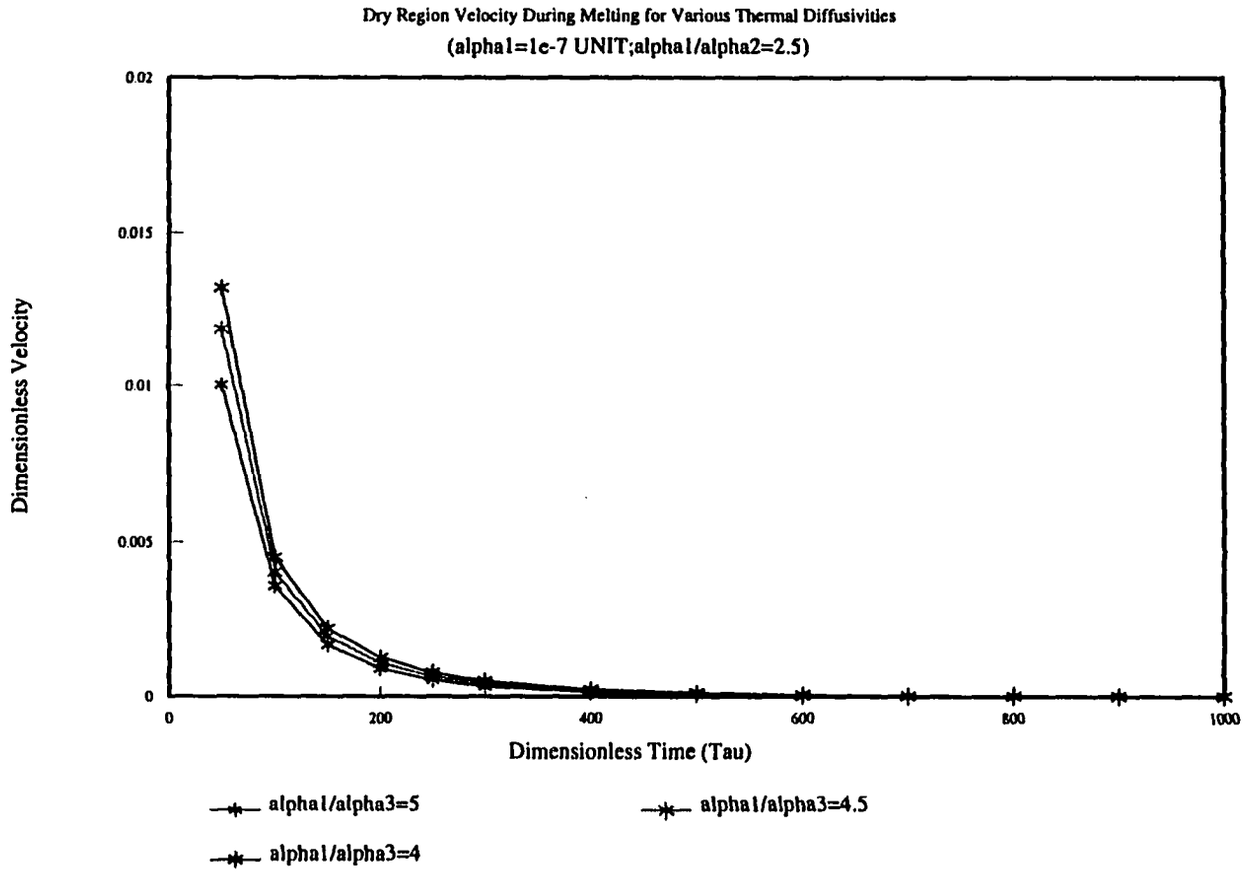

Figure 121: Dry Region Velocity During Melting for Various Thermal Diffusivities (α_1=1x10^{-6} m^2/sec; α_1/α_2=2.5).

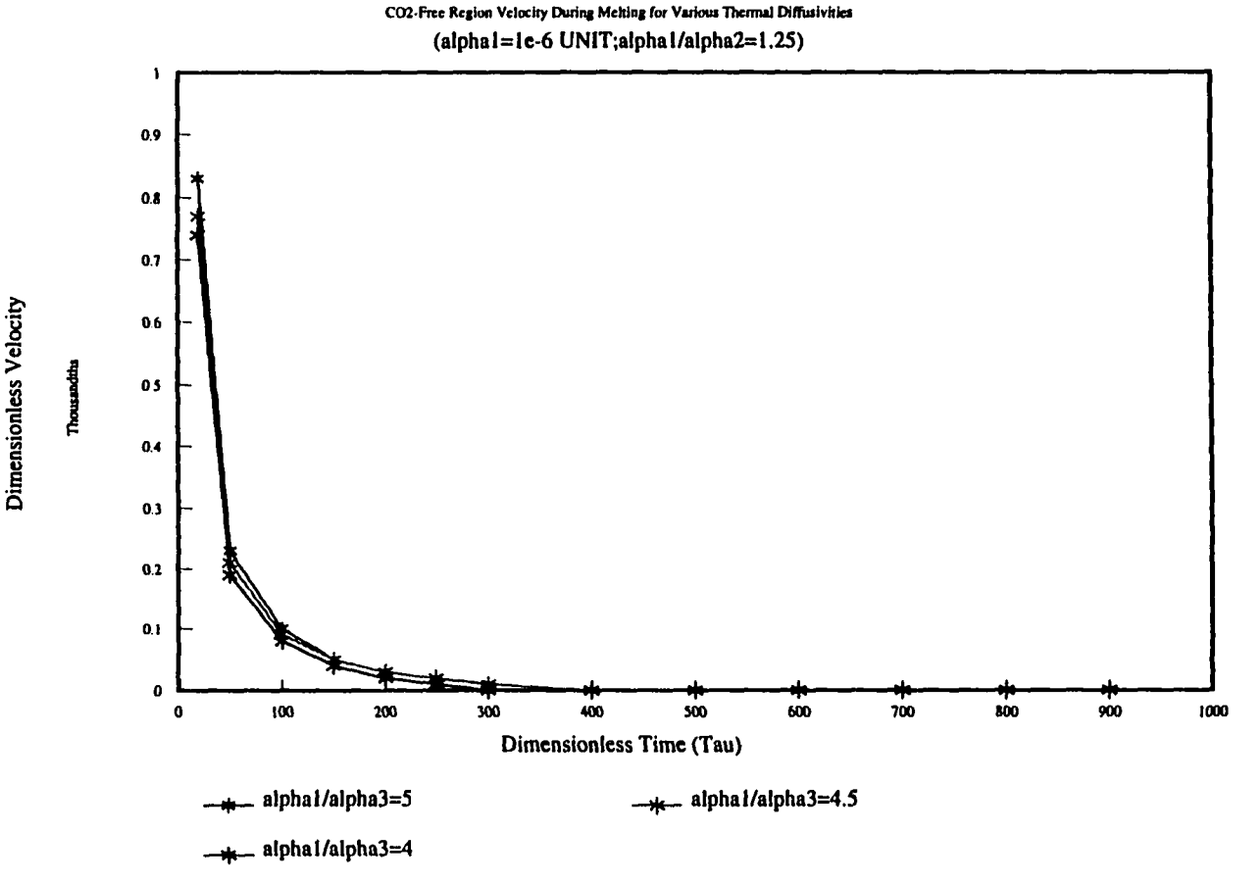

Figure 122: CO_2-Free Region Velocity During Melting for Various Thermal Diffusivities (α_1=1x10^{-6} m^2/sec; α_1/α_2=1.25).

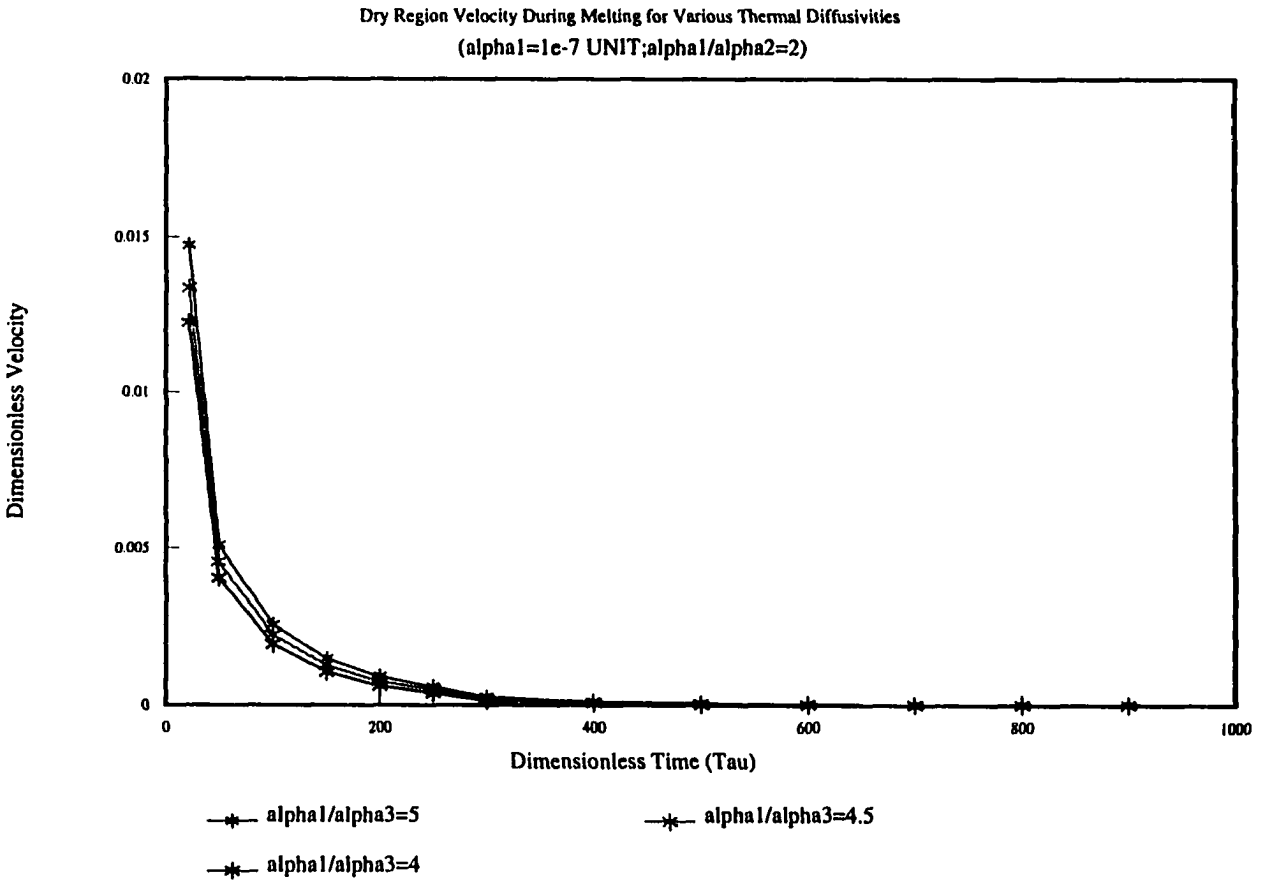

Figure 123: CO_2-Free Region Velocity During Melting for Various Thermal Diffusivities (α_1=1x10^{-6} m^2/sec; α_1/α_2=2).

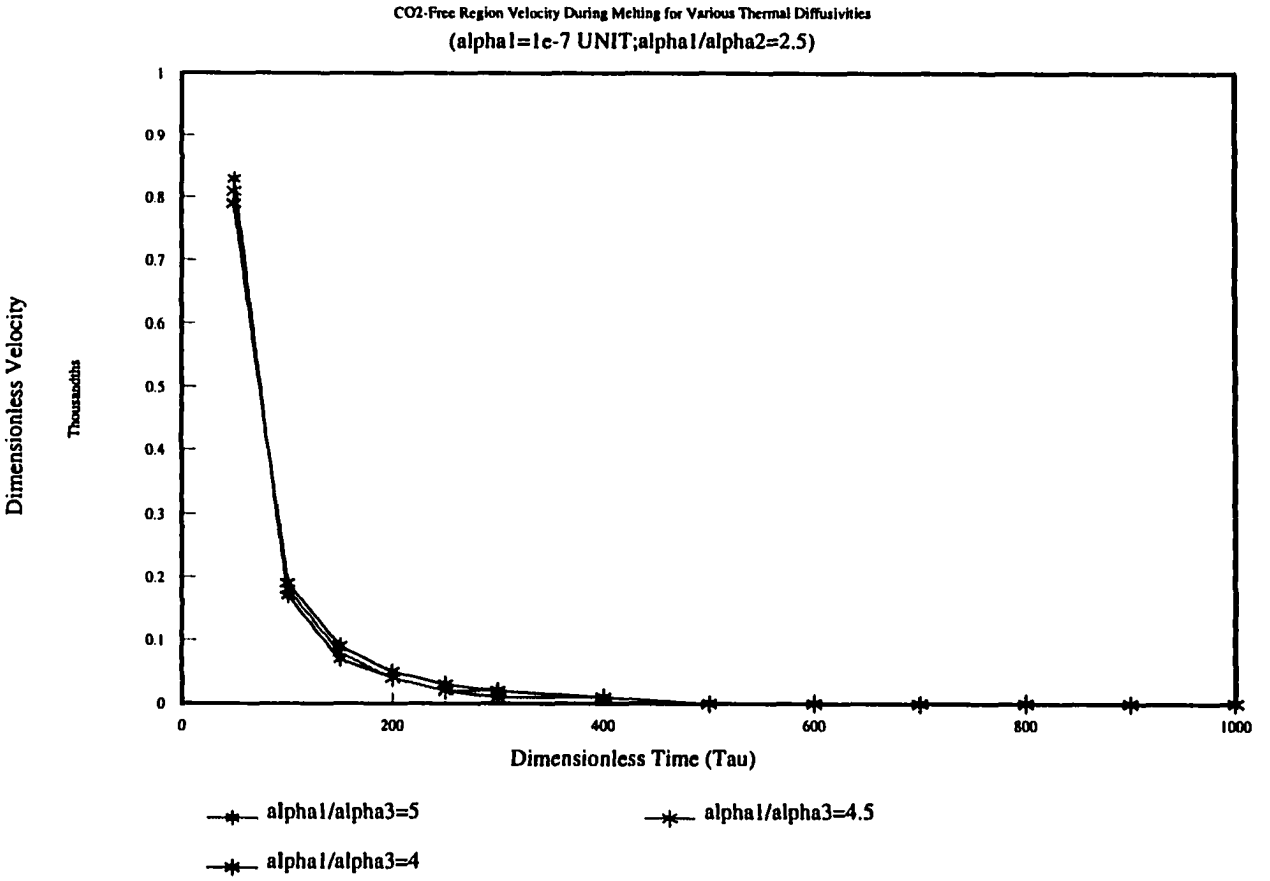

Figure 124: CO_2-Free Region Velocity During Melting for Various Thermal Diffusivities (α_1=1x10^{-6} m^2/sec; α_1/α_2=2.5).

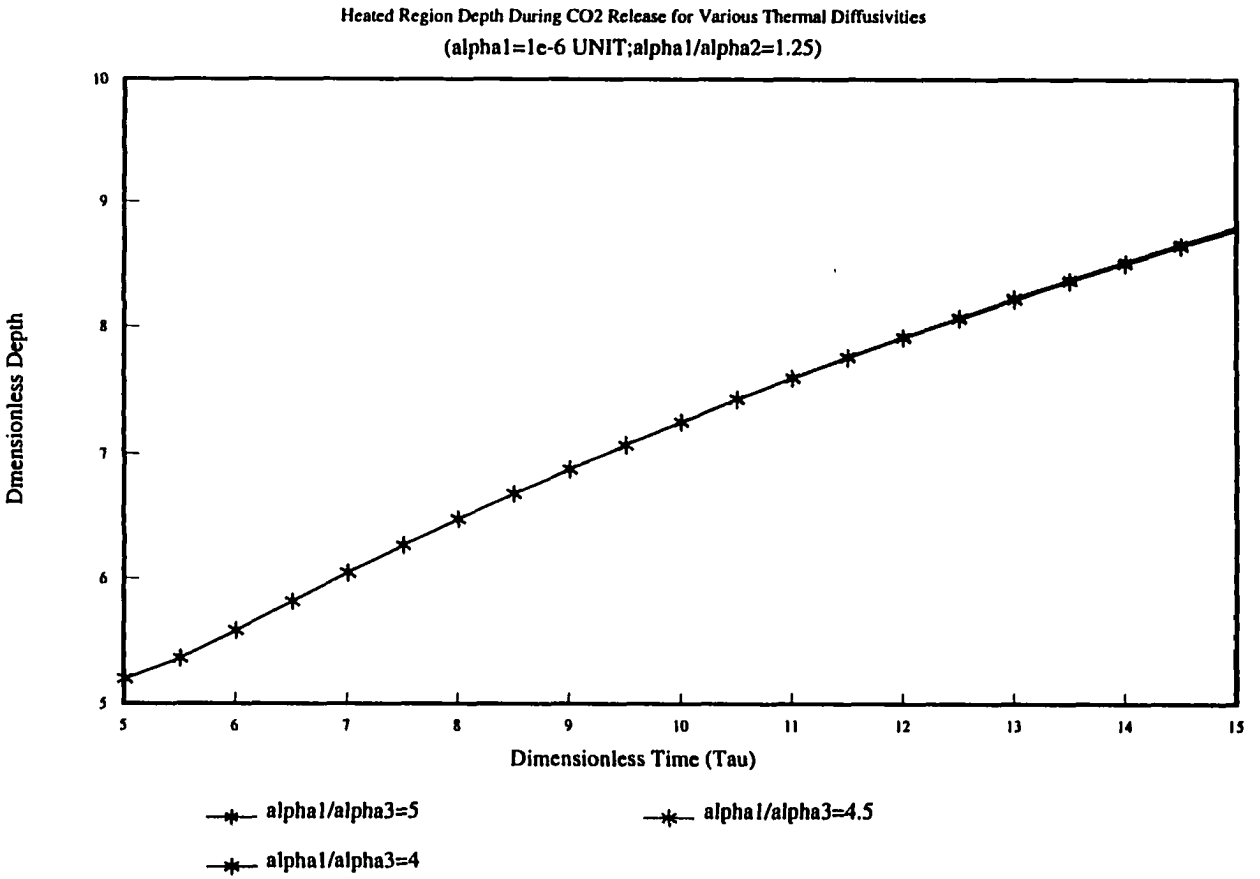

Figure 125: Heated Region Depth During CO_2 Release for Various Thermal Diffusivities (α_1=1x10^{-6} m^2/sec; α_1/α_2=1.25).

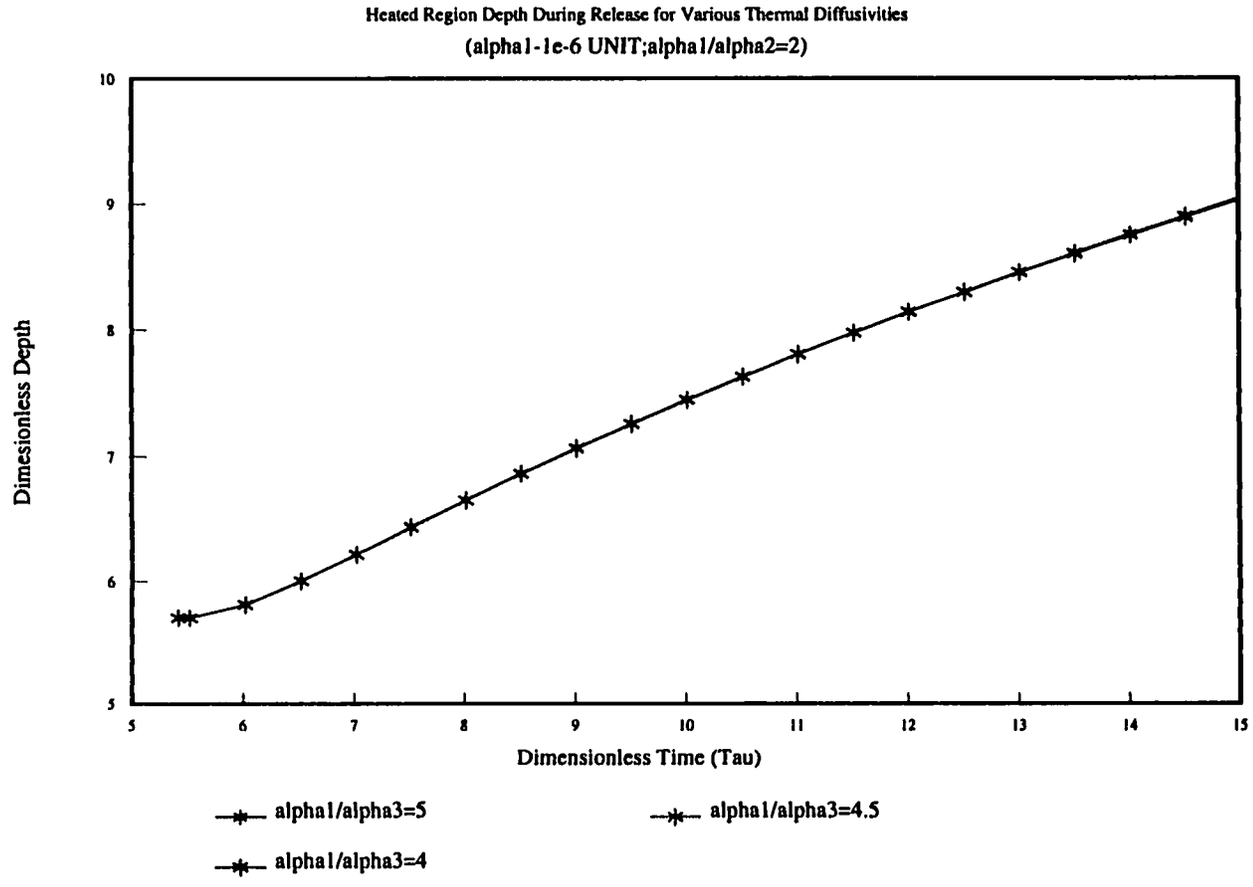

Figure 126: Heated Region Depth During CO_2 Release for Various Thermal Diffusivities (α_1=1x10^{-6} m^2/sec; α_1/α_2=2).

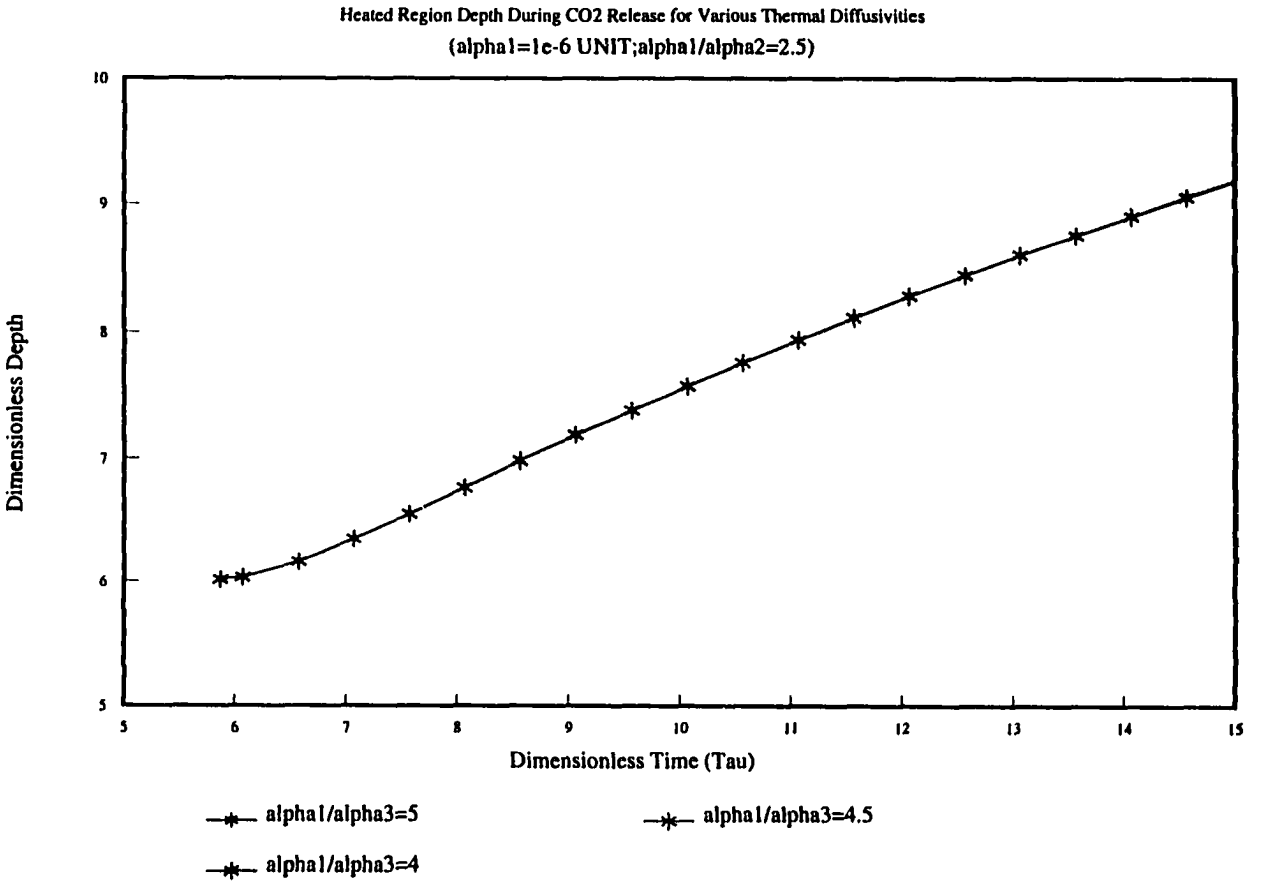

Figure 127: Heated Region Depth During CO_2 Release for Various Thermal Diffusivities ($\alpha_1=1x10^{-6}$ m^2/sec; $\alpha_1/\alpha_2=2.5$).

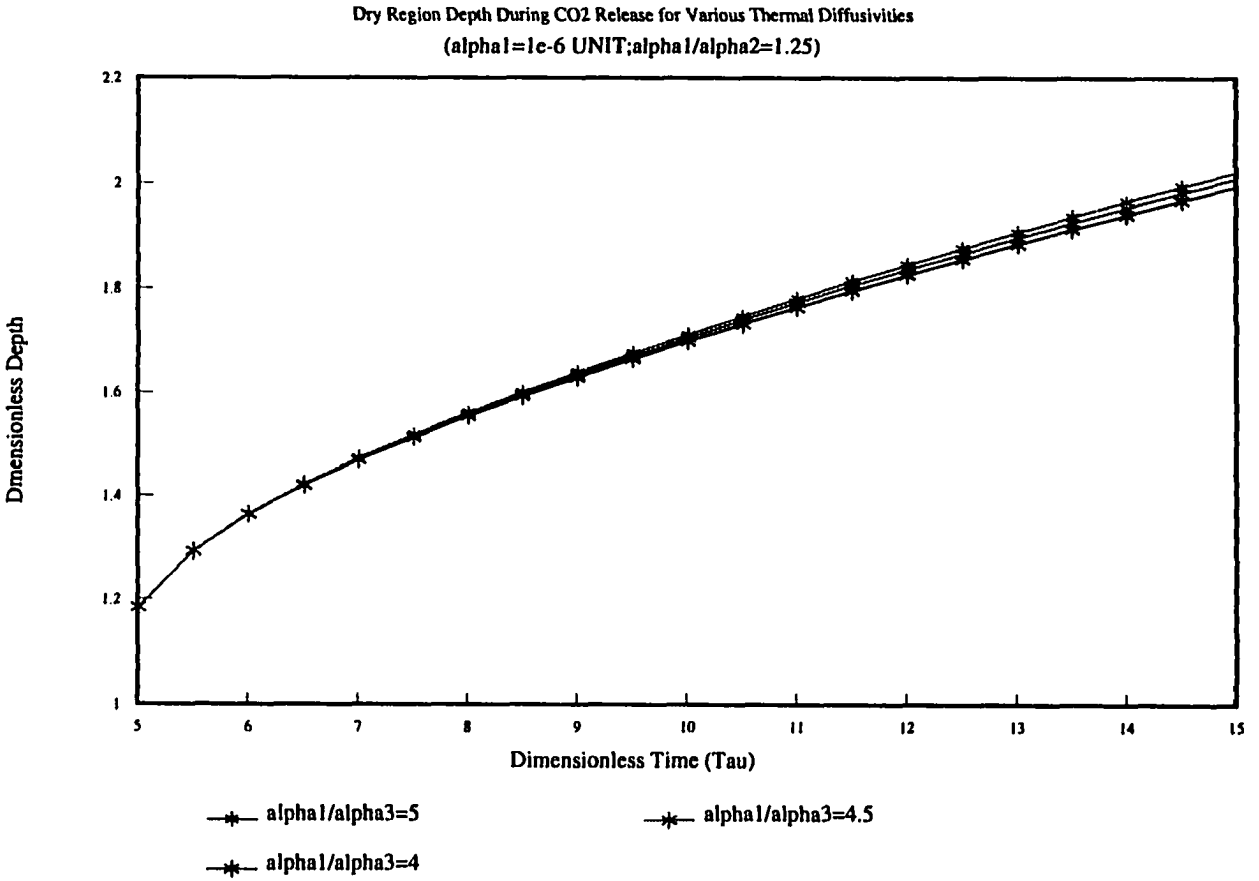

Figure 128: Dry Region Depth During CO_2 Release for Various Thermal Diffusivities (α_1=1x10^{-6} m^2/sec; α_1/α_2=1.25).

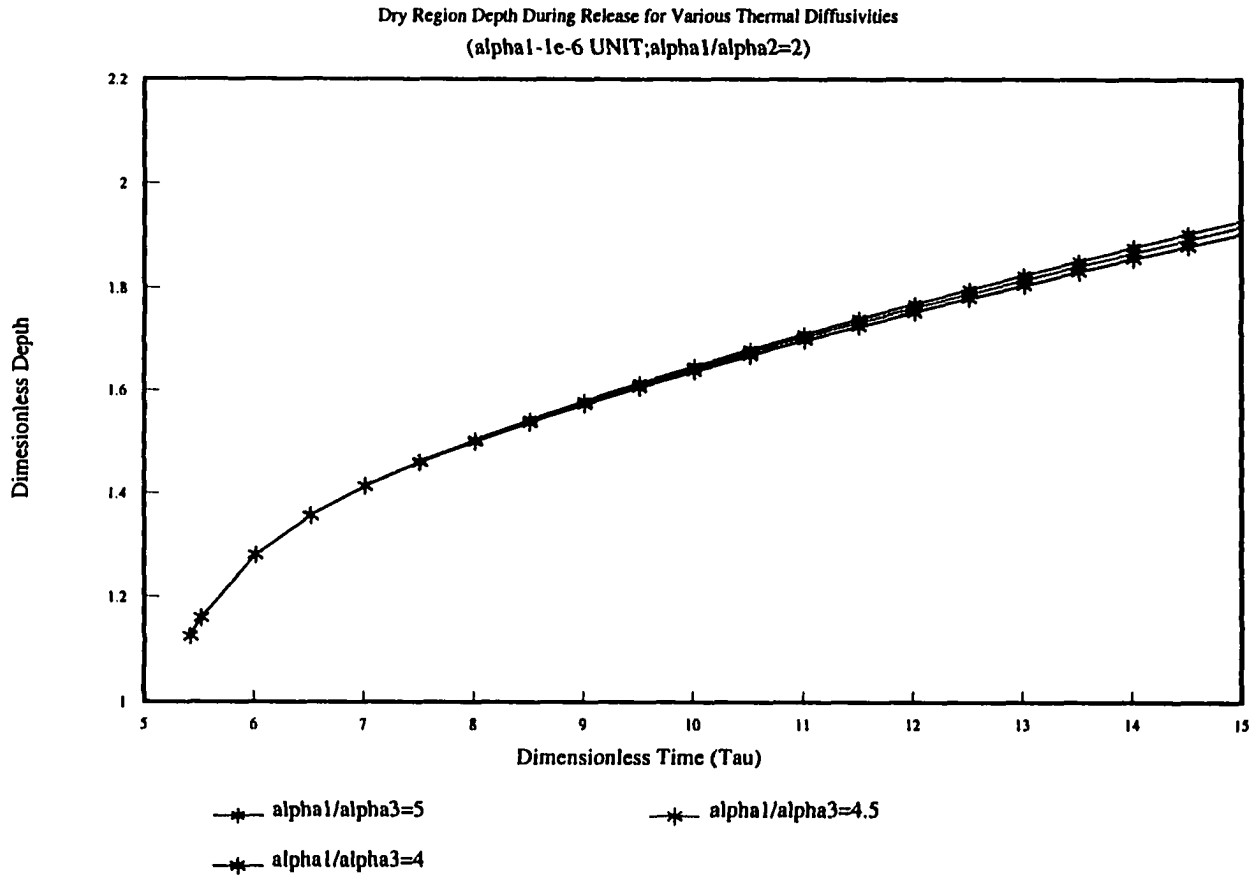

Figure 129: Dry Region Depth During CO_2 Release for Various Thermal Diffusivities (α_1=1x10^{-6} m^2/sec; α_1/α_2=2).

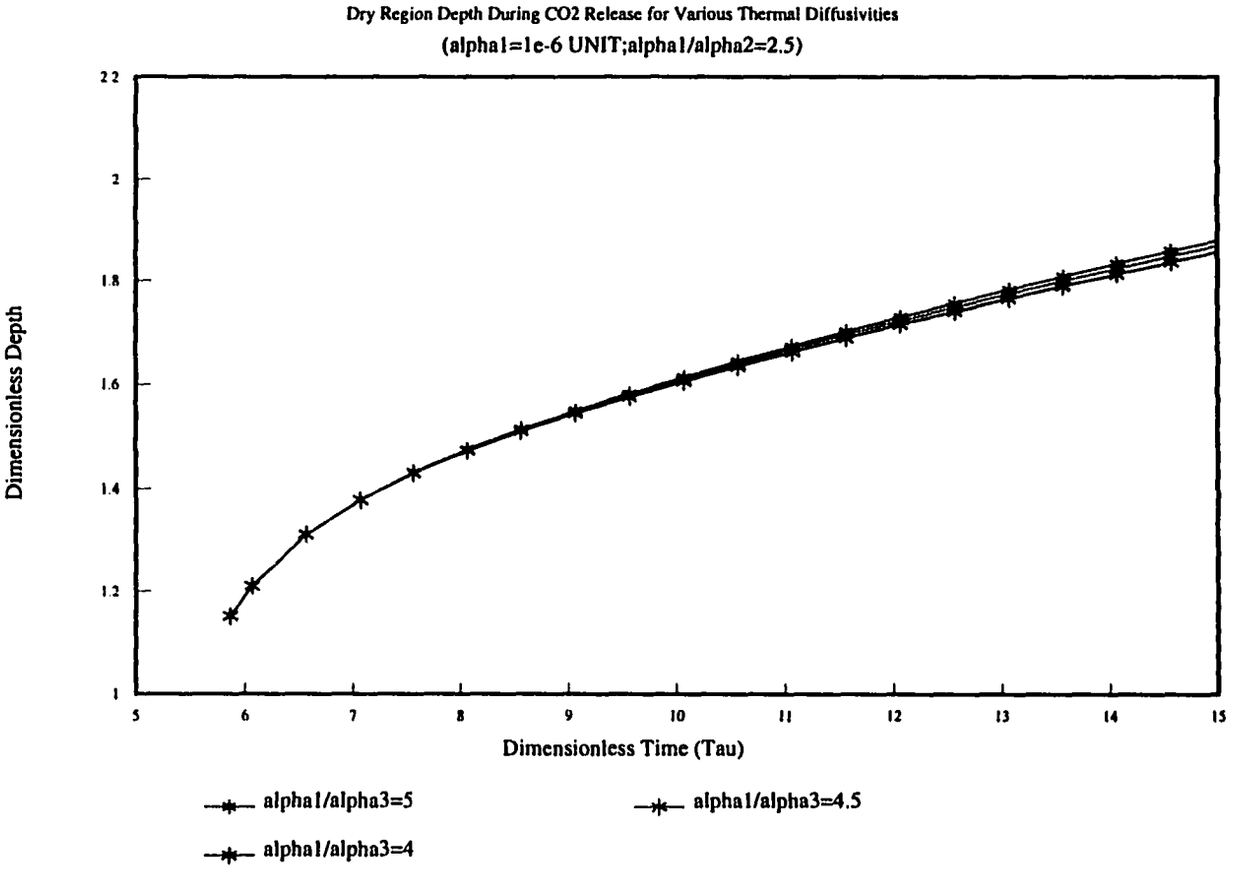

Figure 130: Dry Region Depth During CO_2 Release for Various Thermal Diffusivities ($\alpha_1=1x10^{-6}$ m^2/sec; $\alpha_1/\alpha_2=2.5$).

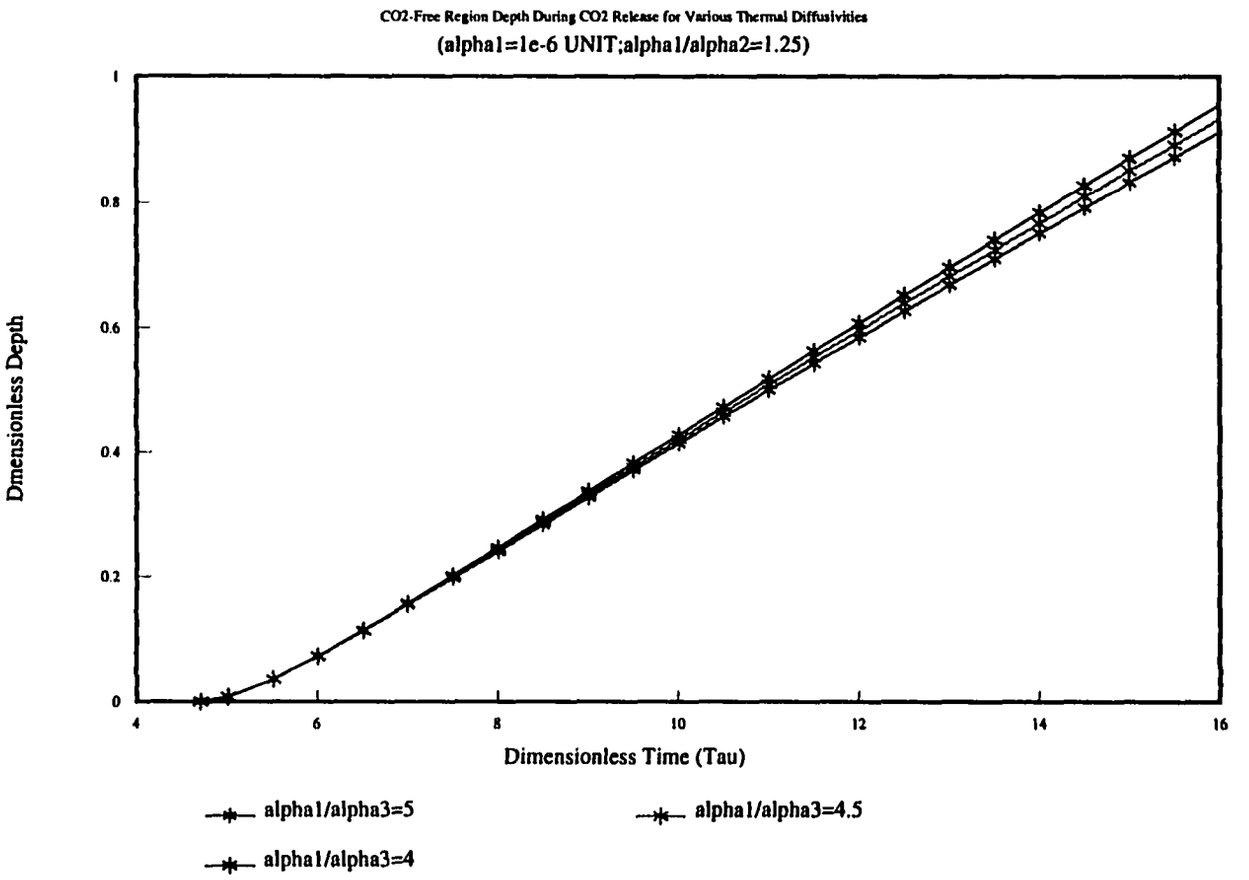

Figure 131: CO_2-Free Region Depth During CO_2 Release for Various Thermal Diffusivities ($\alpha_1=1x10^{-6}$ m^2/sec; $\alpha_1/\alpha_2=1.25$).

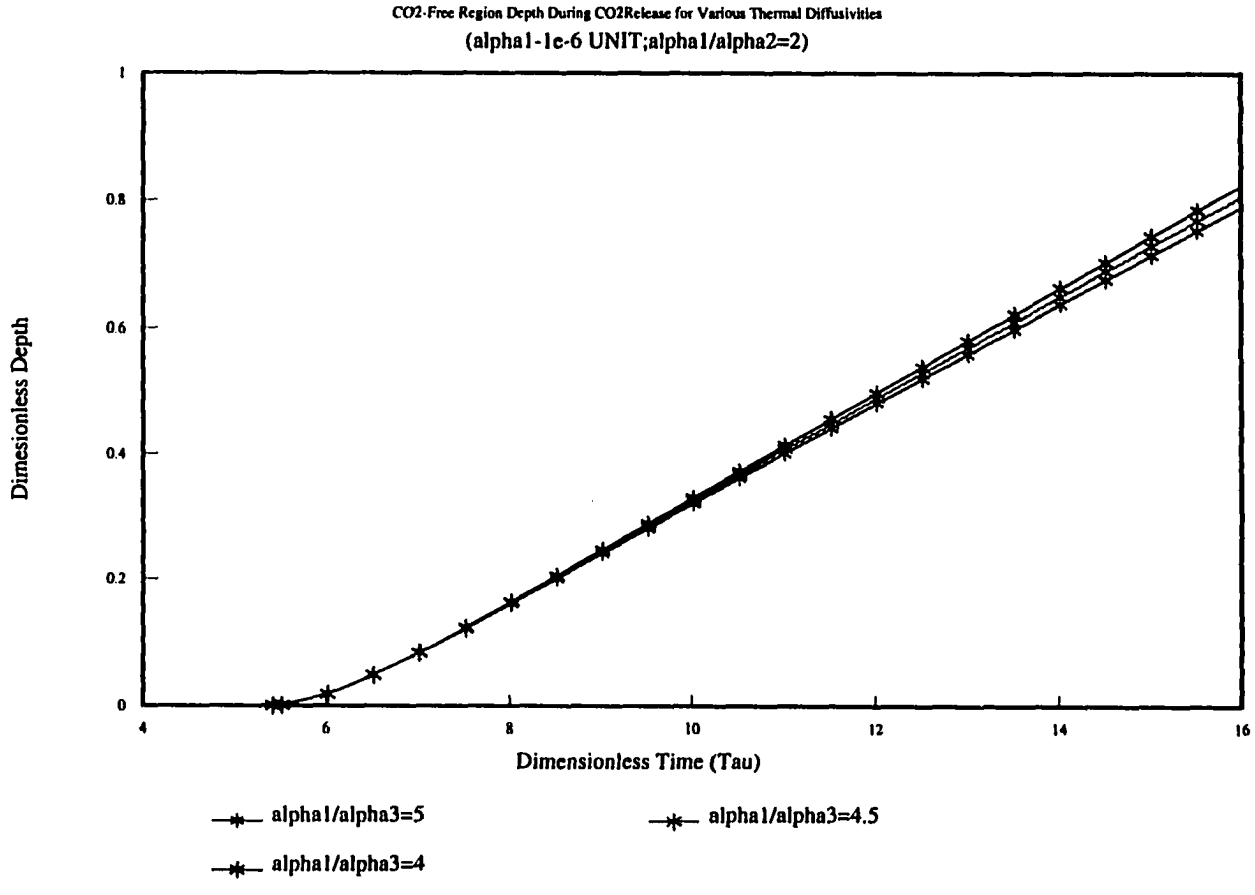

Figure 132: CO_2-Free Region Depth During CO_2 Release for Various Thermal Diffusivities (α_1=1x10^{-6} m^2/sec; α_1/α_2=2).

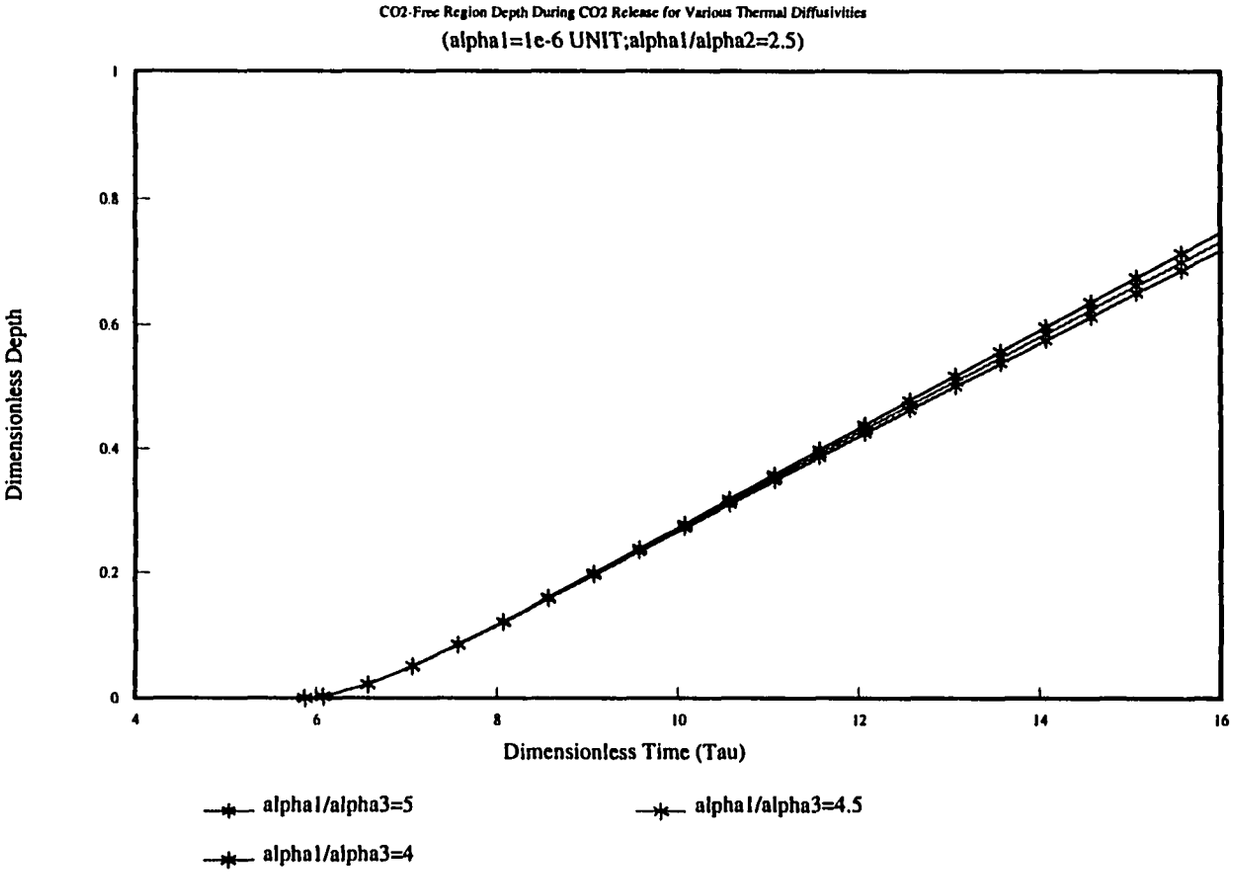

Figure 133: CO_2-Free Region Depth During CO_2 Release for Various Thermal Diffusivities ($\alpha_1=1\times10^{-6}$ m^2/sec; $\alpha_1/\alpha_2=2.5$).

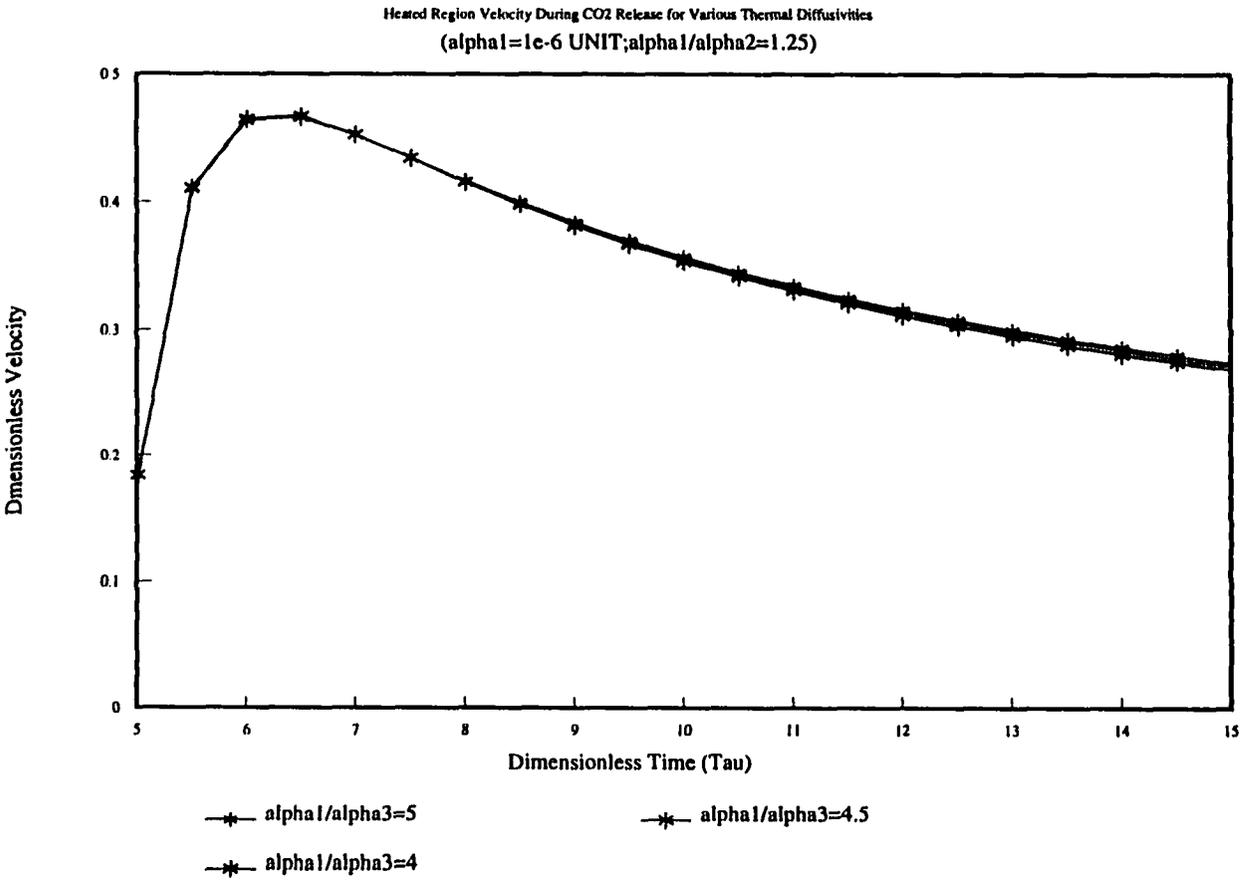

Figure 134: Heated Region Velocity During CO_2 Release for Various Thermal Diffusivities (α_1=1x10^{-6} m^2/sec; α_1/α_2=1.25).

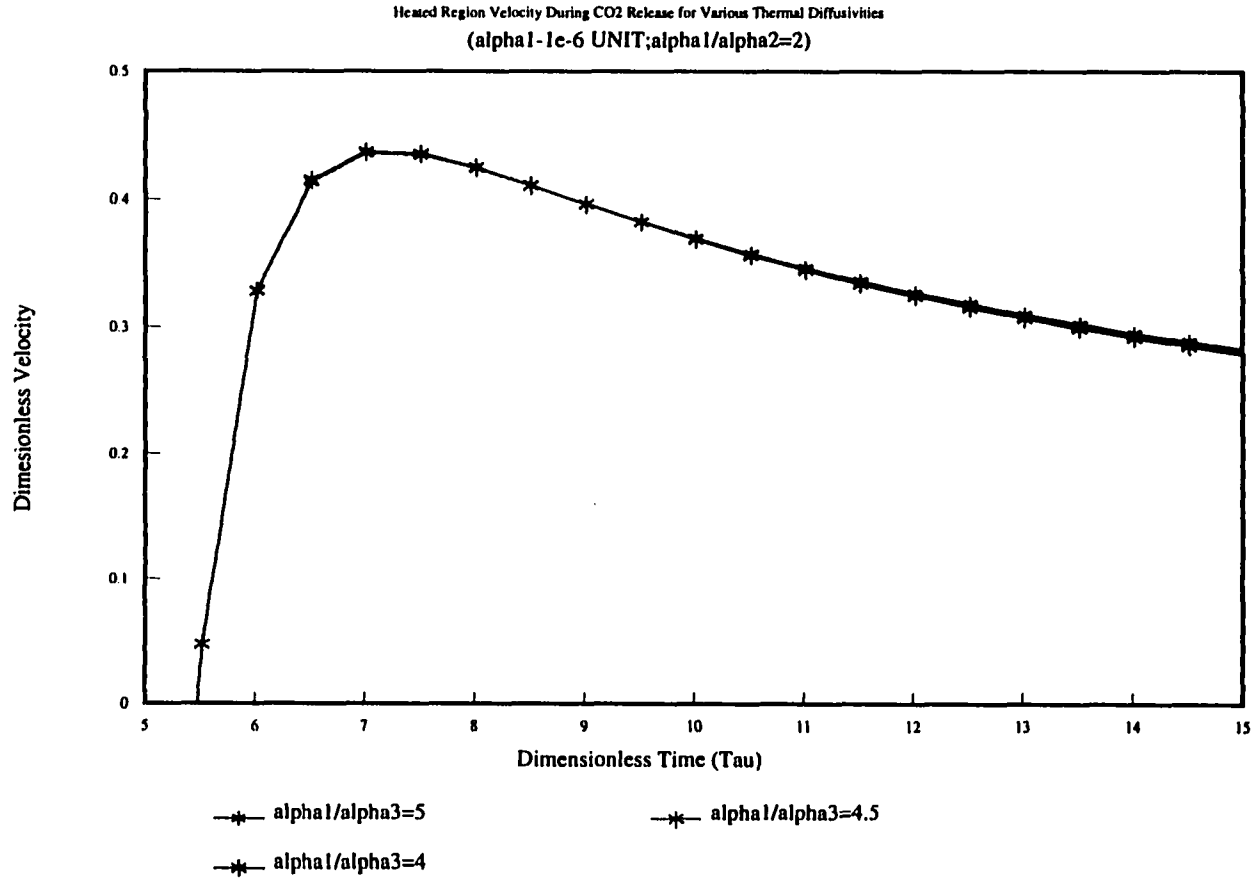

Figure 135: Heated Region Velocity During CO_2 Release for Various Thermal Diffusivities (α_1=1x10^{-6} m^2/sec; α_1/α_2=2).

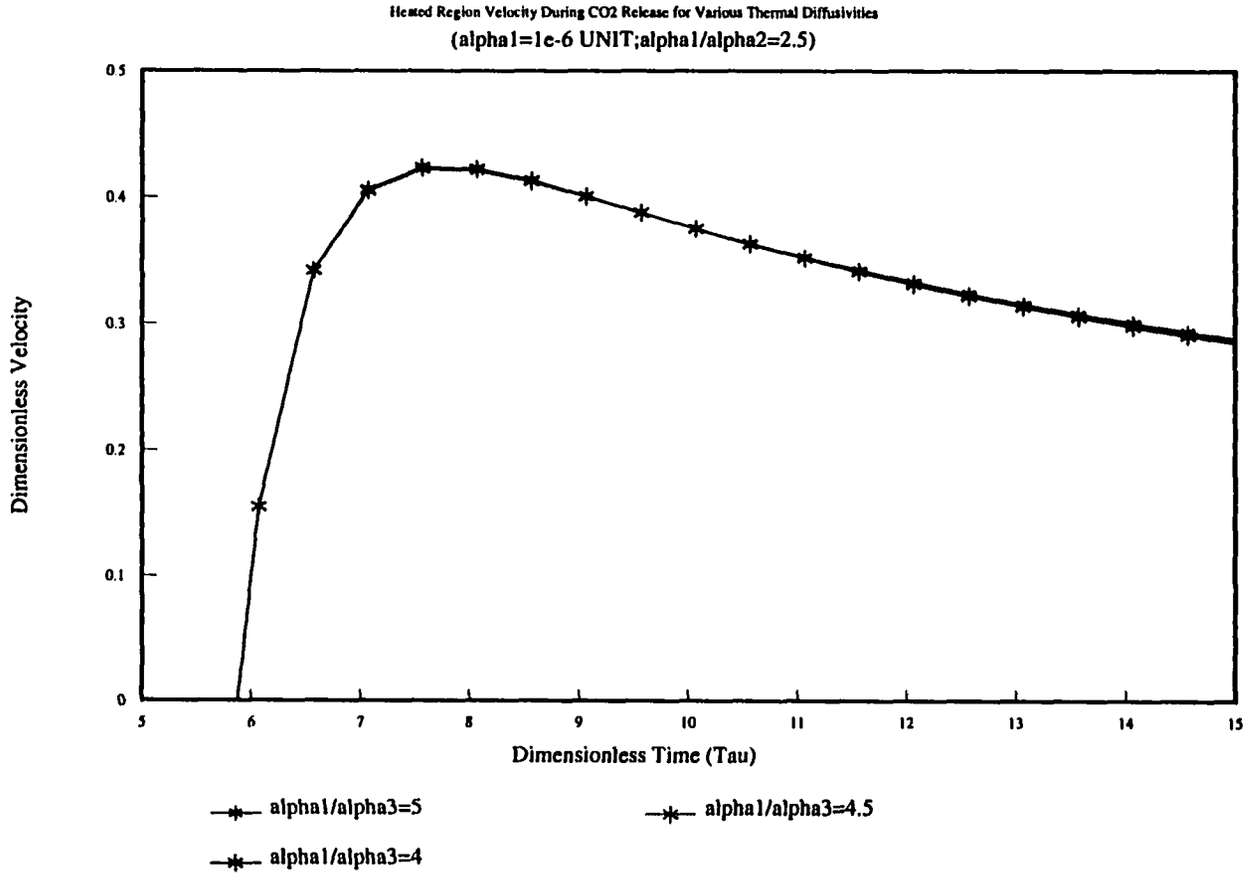

Figure 136: Heated Region Velocity During CO_2 Release for Various Thermal Diffusivities ($\alpha_1=1\times10^{-6}$ m^2/sec; $\alpha_1/\alpha_2=2.5$).

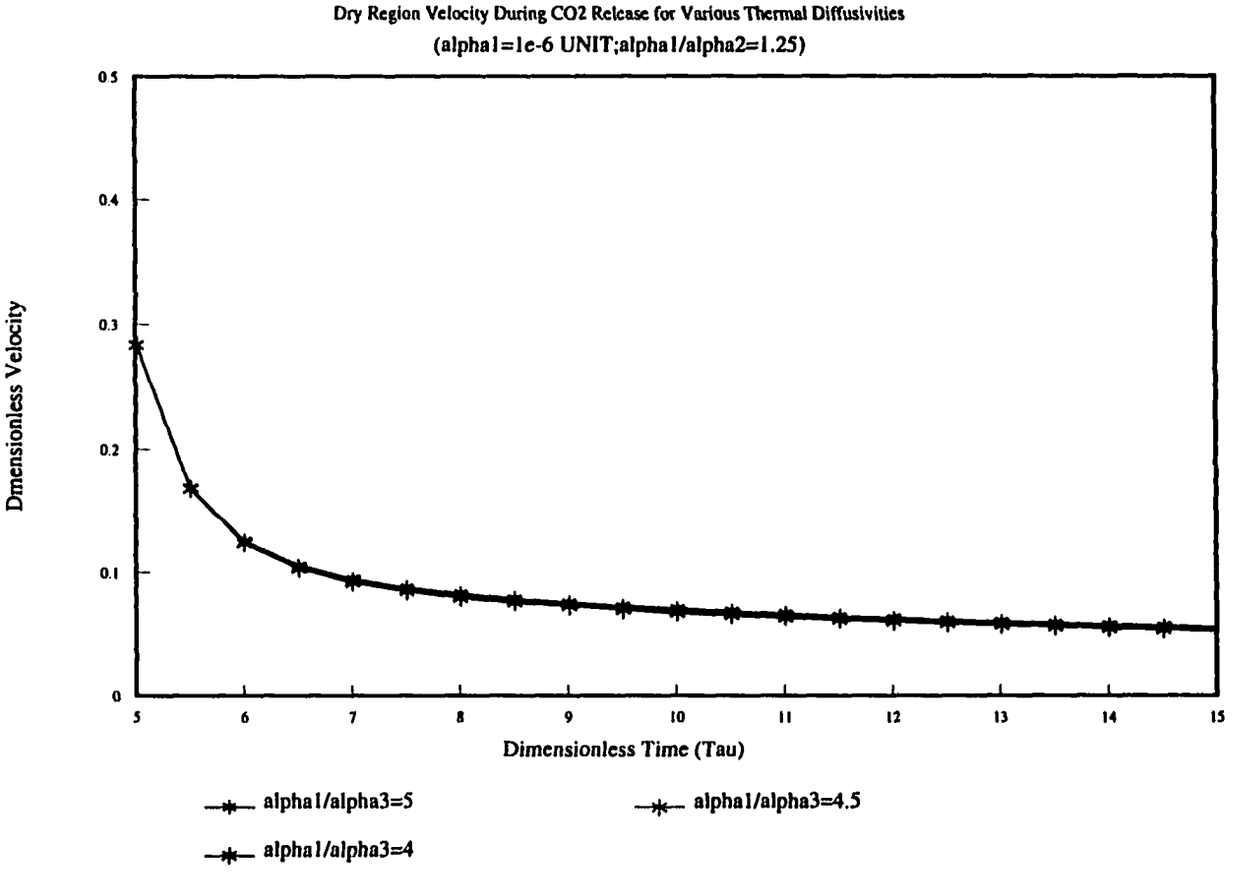

Figure 137: Dry Region Velocity During CO_2 Release for Various Thermal Diffusivities ($\alpha_1=1x10^{-6}$ m^2/sec; $\alpha_1/\alpha_2=1.25$).

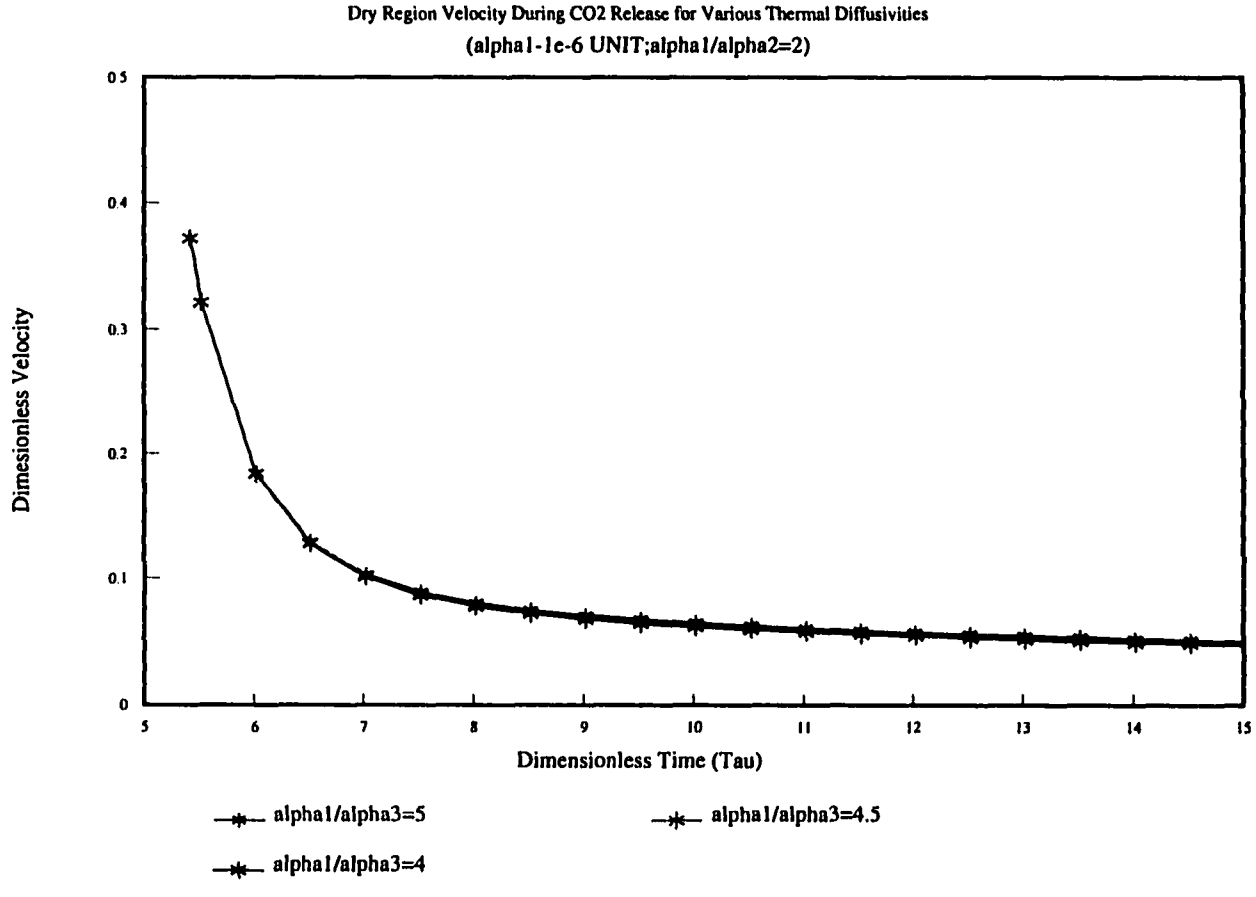

Figure 138: Dry Region Velocity During CO_2 Release for Various Thermal Diffusivities ($\alpha_1=1x10^{-6}$ m^2/sec; $\alpha_1/\alpha_2=2$).

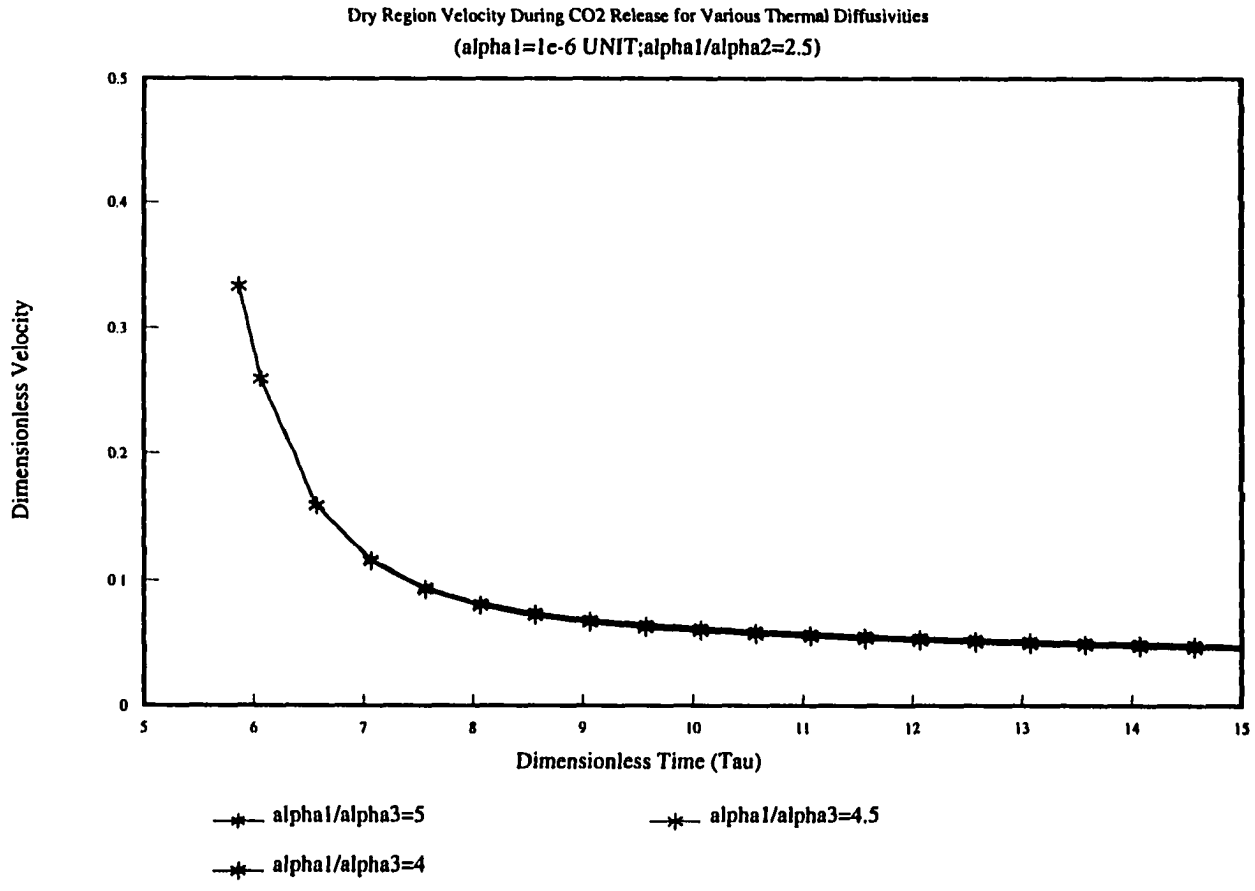

Figure 139: Dry Region Velocity During CO_2 Release for Various Thermal Diffusivities (α_1=1x10^{-6} m^2/sec; α_1/α_2=2.5).

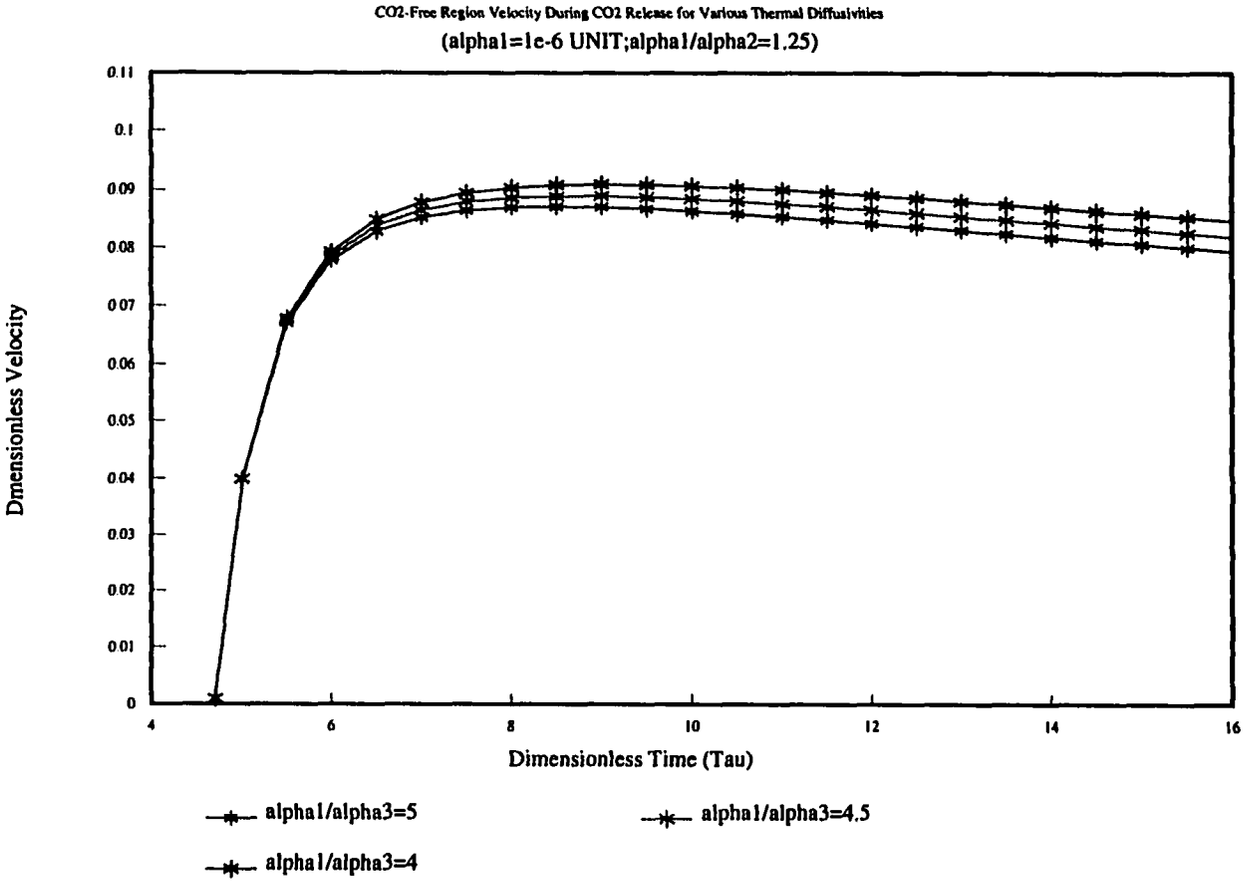

Figure 140: CO_2-Free Region Velocity During CO_2 Release for Various Thermal Diffusivities ($\alpha_1=1x10^{-6}$ m^2/s; $\alpha_1/\alpha_2=1.25$)

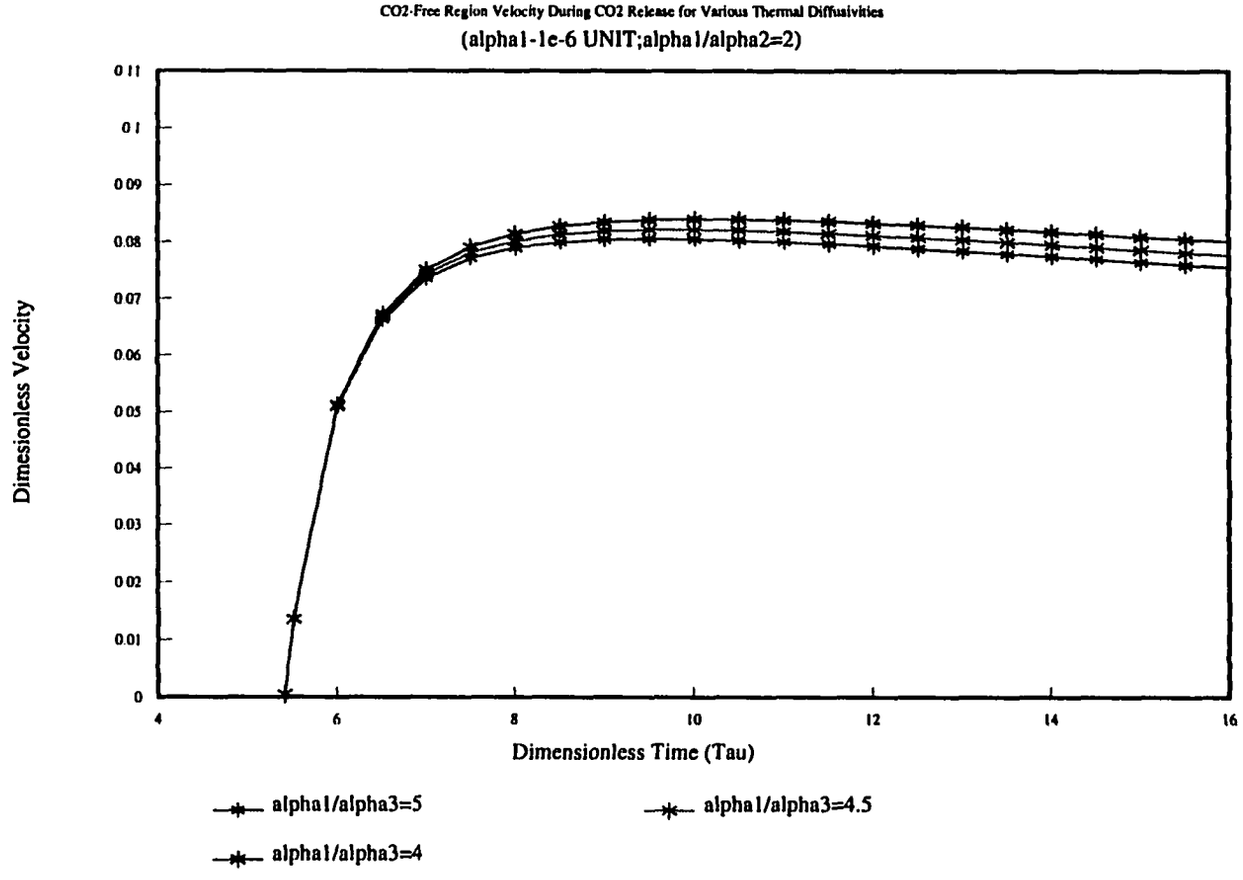

Figure 141: CO_2-Free Region Velocity During CO_2 Release for Various Thermal Diffusivities (α_1=1x10^{-6} m^2/sec; α_1/α_2=2)

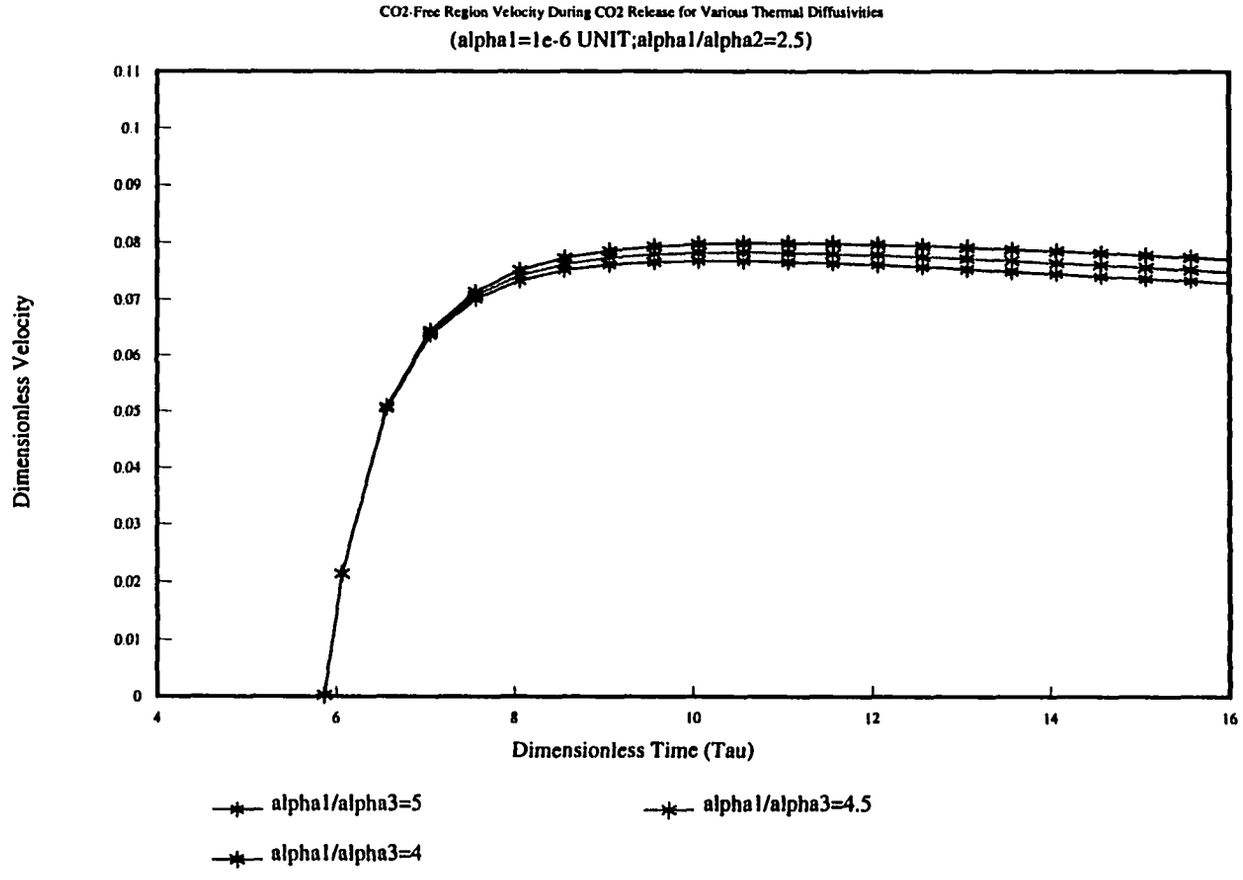

Figure 142: CO_2-Free Region Velocity During CO_2 Release for Various Thermal Diffusivities ($\alpha_1=1x10^{-6}$ m^2/sec; $\alpha_1/\alpha_2=2.5$)

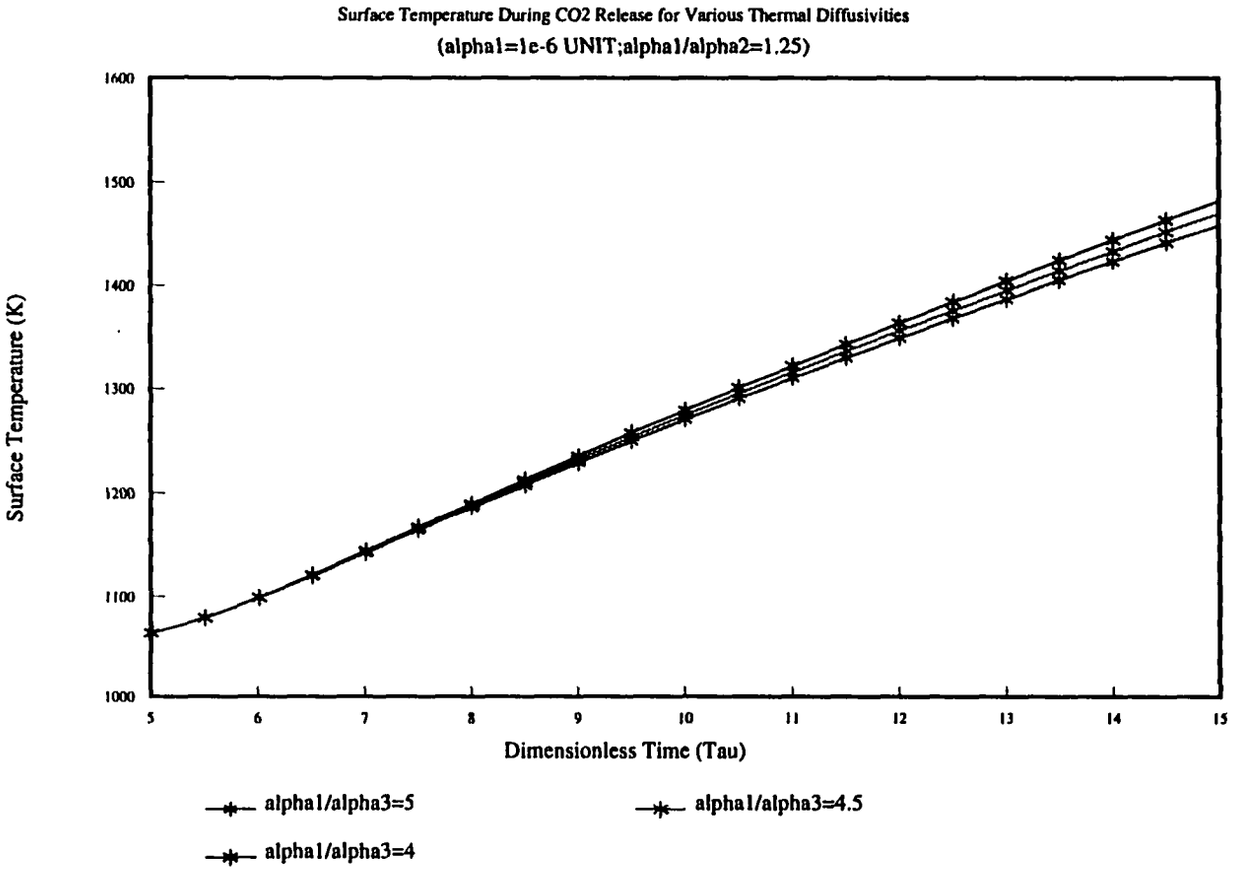

Figure 143: Surface Temperature During CO_2 Release for Various Thermal Diffusivities (α_1=1x10^{-6} m^2/sec; α_1/α_2=1.25)

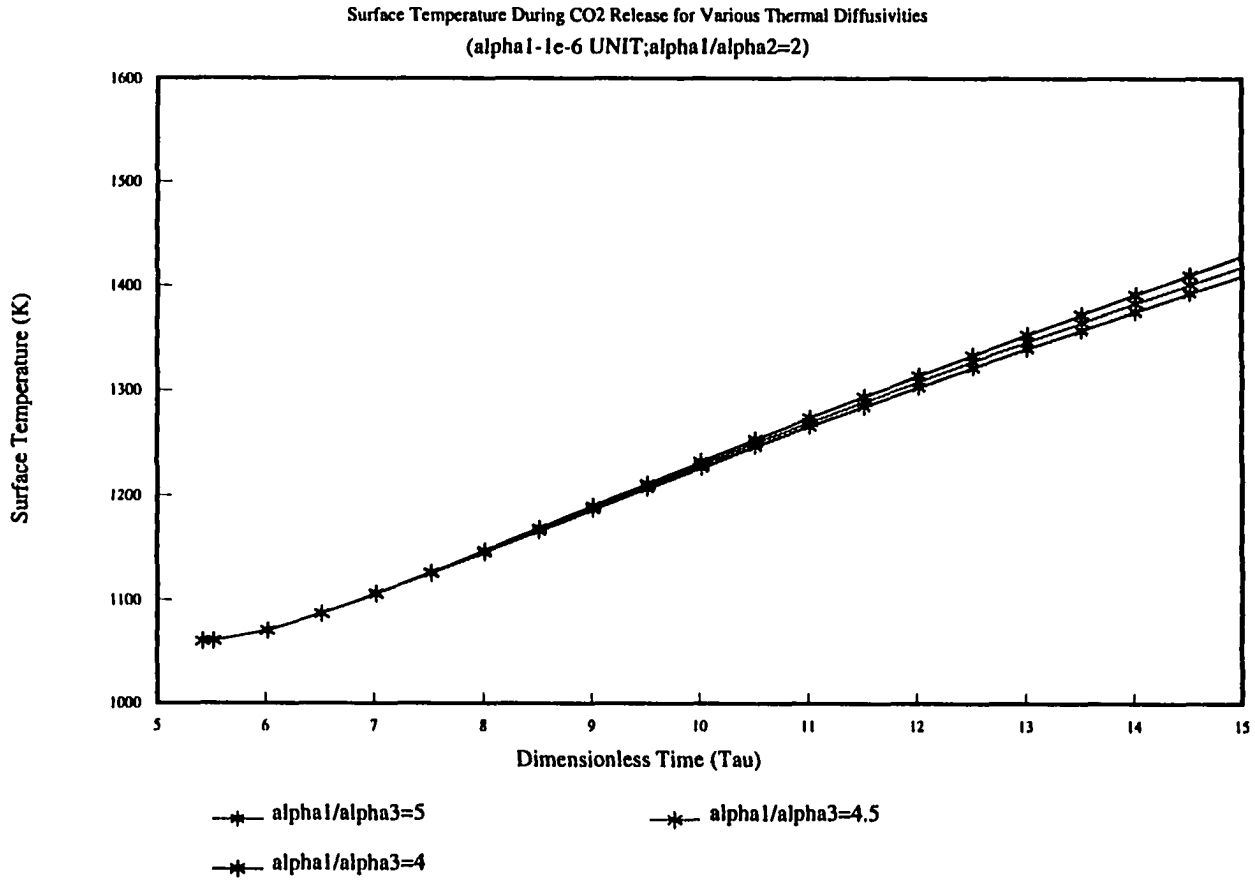

Figure 144: Surface Temperature During CO_2 Release for Various Thermal Diffusivities ($\alpha_1=1x10^{-6}$ m^2/sec; $\alpha_1/\alpha_2=2$)

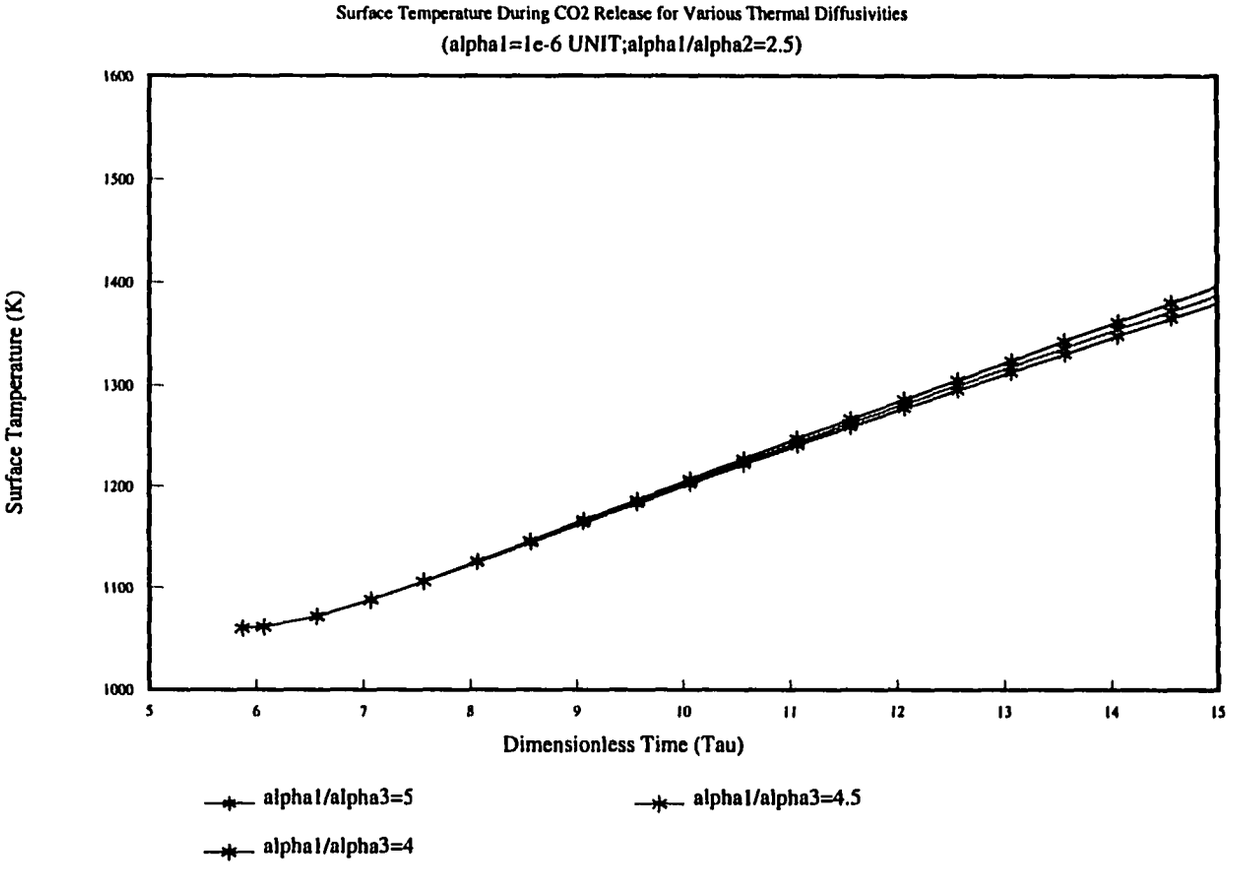

Figure 145: Surface Temperature During CO_2 Release for Various Thermal Diffusivities ($\alpha_1=1\times10^{-6}$ m^2/sec; $\alpha_1/\alpha_2=2.5$)

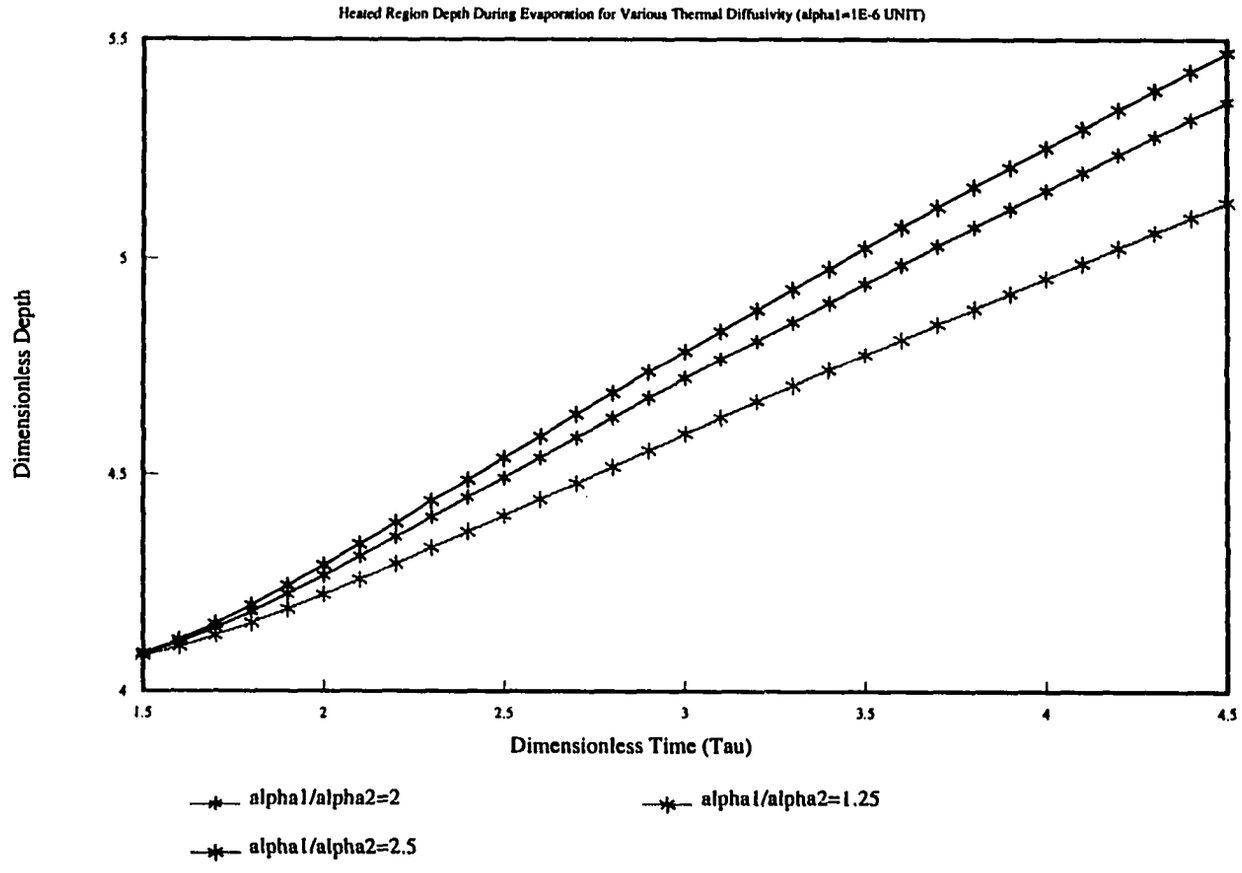

Figure 146: Heated Region Depth During Evaporation for Various Thermal Diffusivities (α_1=1x10^{-6} m^2/sec)

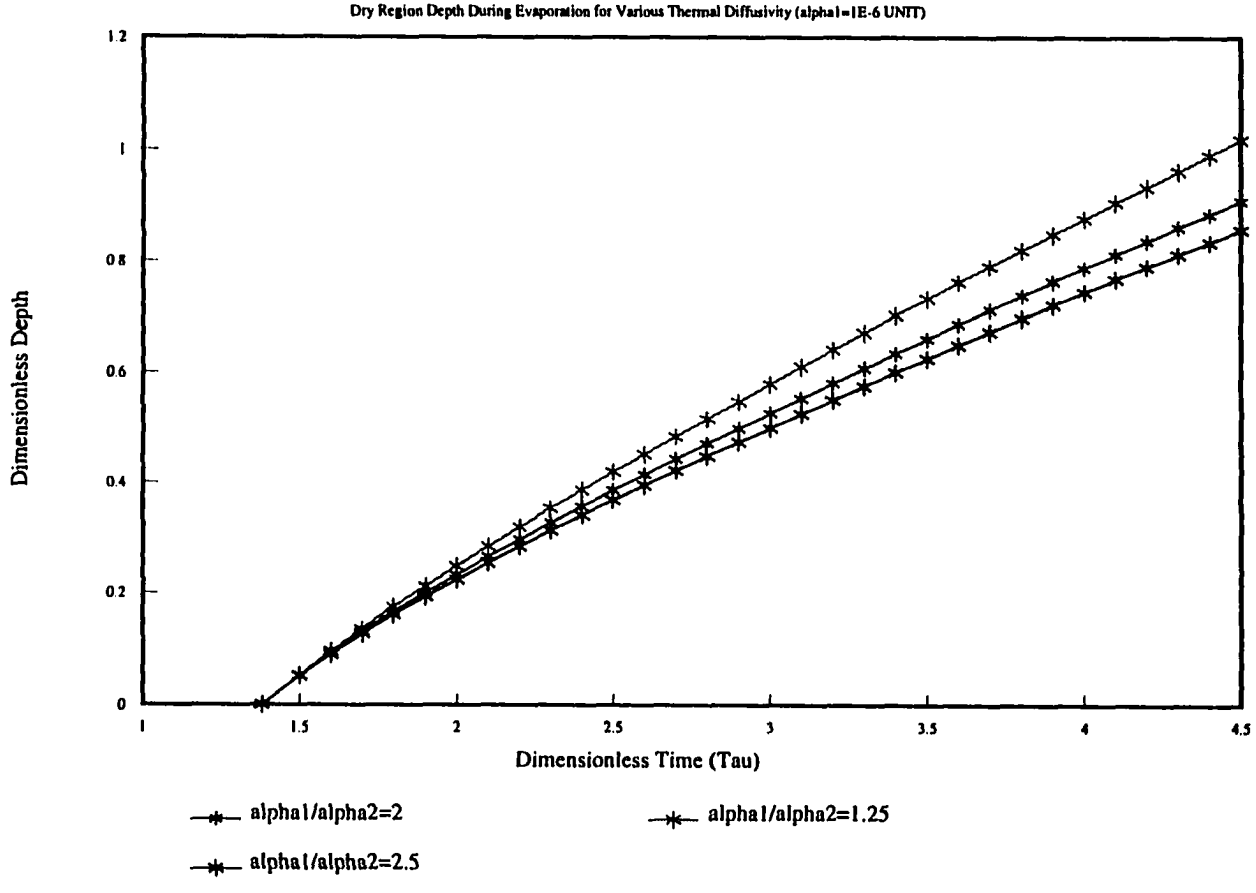

Figure 147: Dry Region Depth During Evaporation for Various Thermal Diffusivities (α_l=1x10^{-6} m^2/sec)

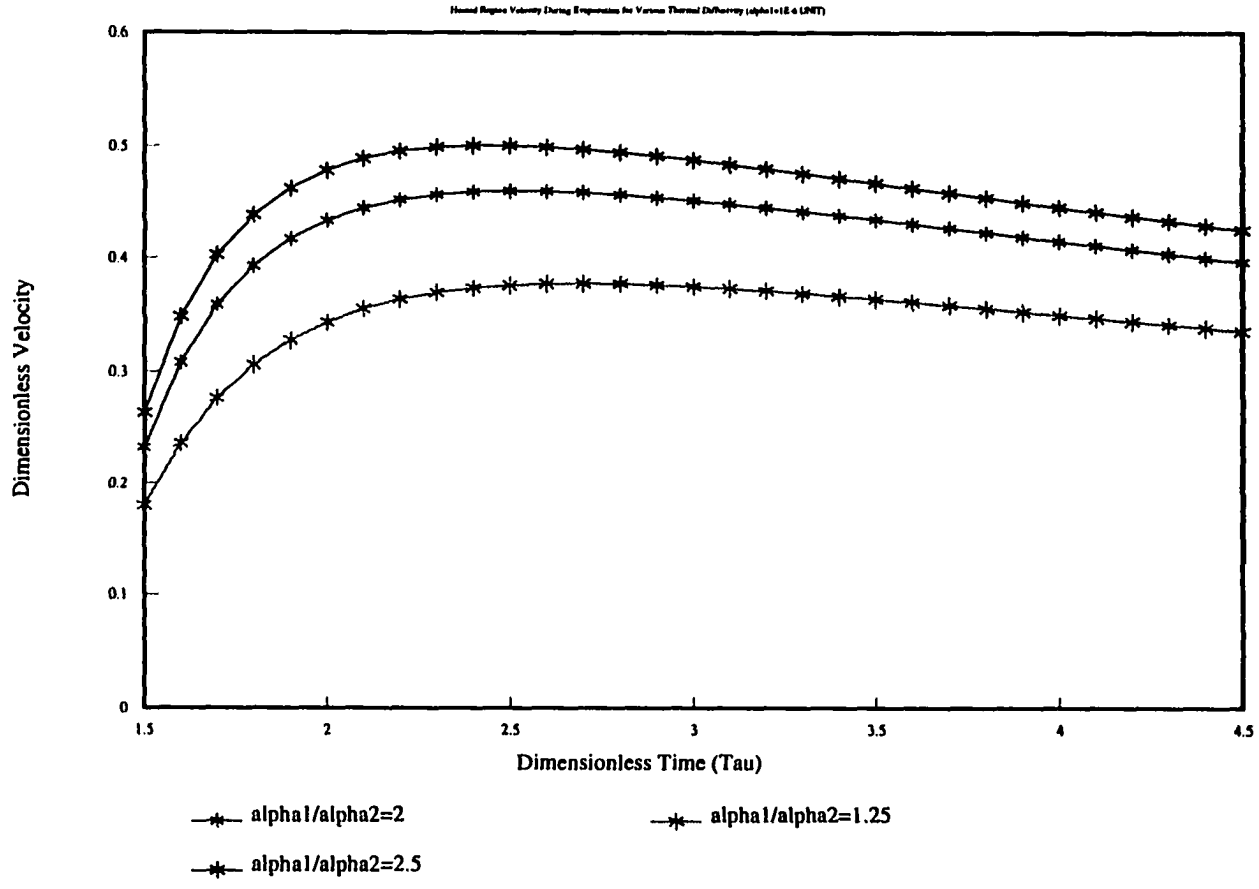

Figure 148: Heated Region Velocity During Evaporation for Various Thermal Diffusivities (α_l=1x10^{-6} m^2/sec)

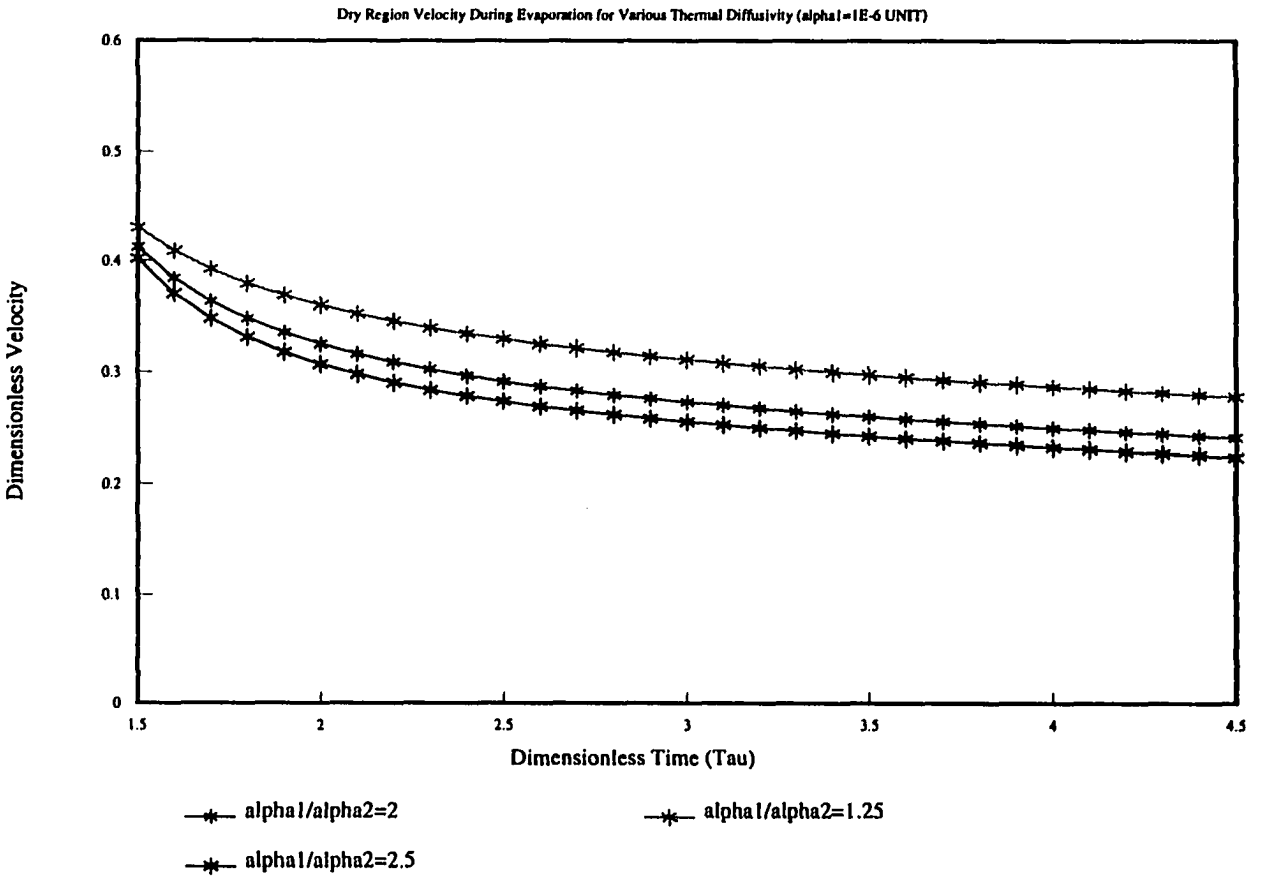

Figure 149: Dry Region Velocity During Evaporation for Various Thermal Diffusivities (α_l=1x10^{-6} m^2/sec)

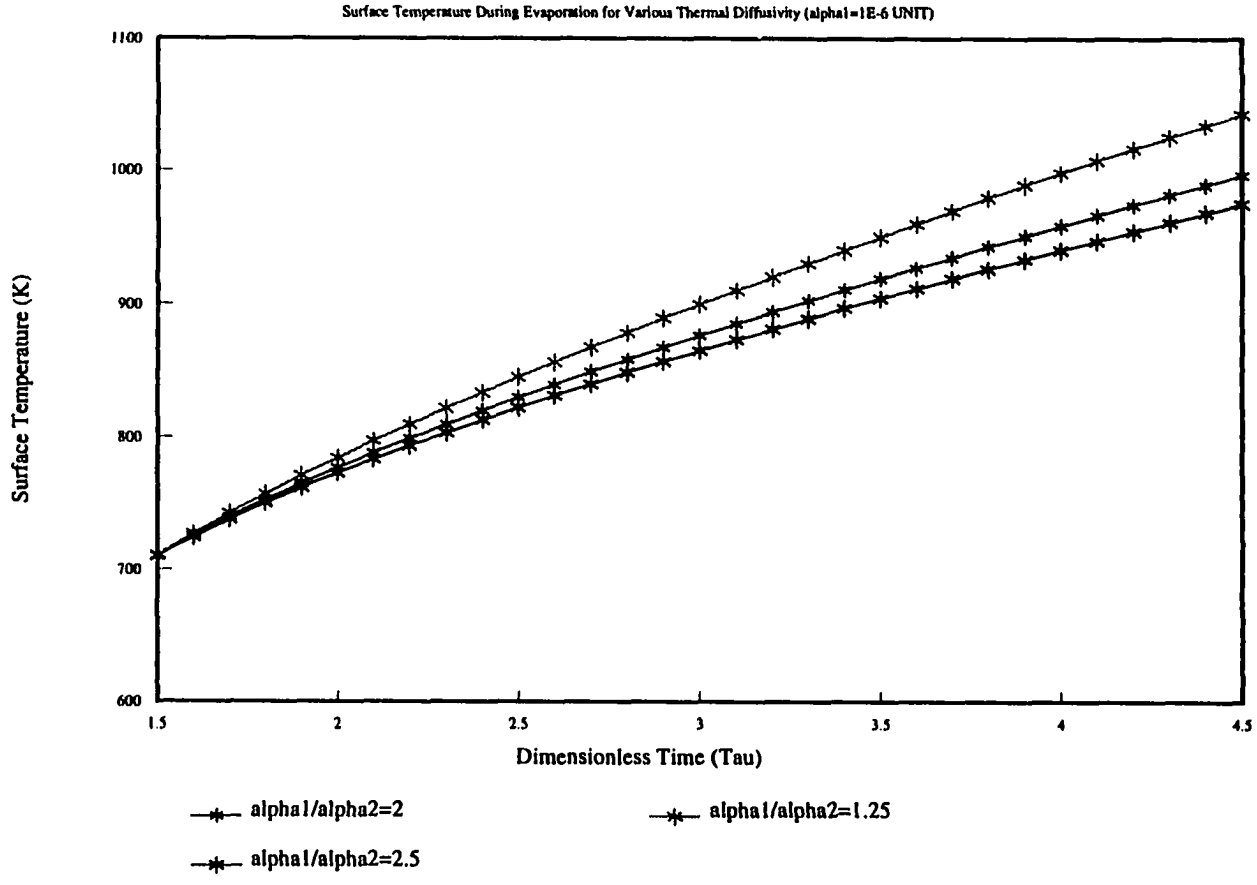

Figure 150: Surface Temperature During Evaporation for Various Thermal Diffusivities (α_l=1x10^{-6} m^2/sec)

APPENDIX B:
MODEL RESULTS FOR REGION GROWTH AND GROWTH RATES FOR VARIOUS STEFAN NUMBERS

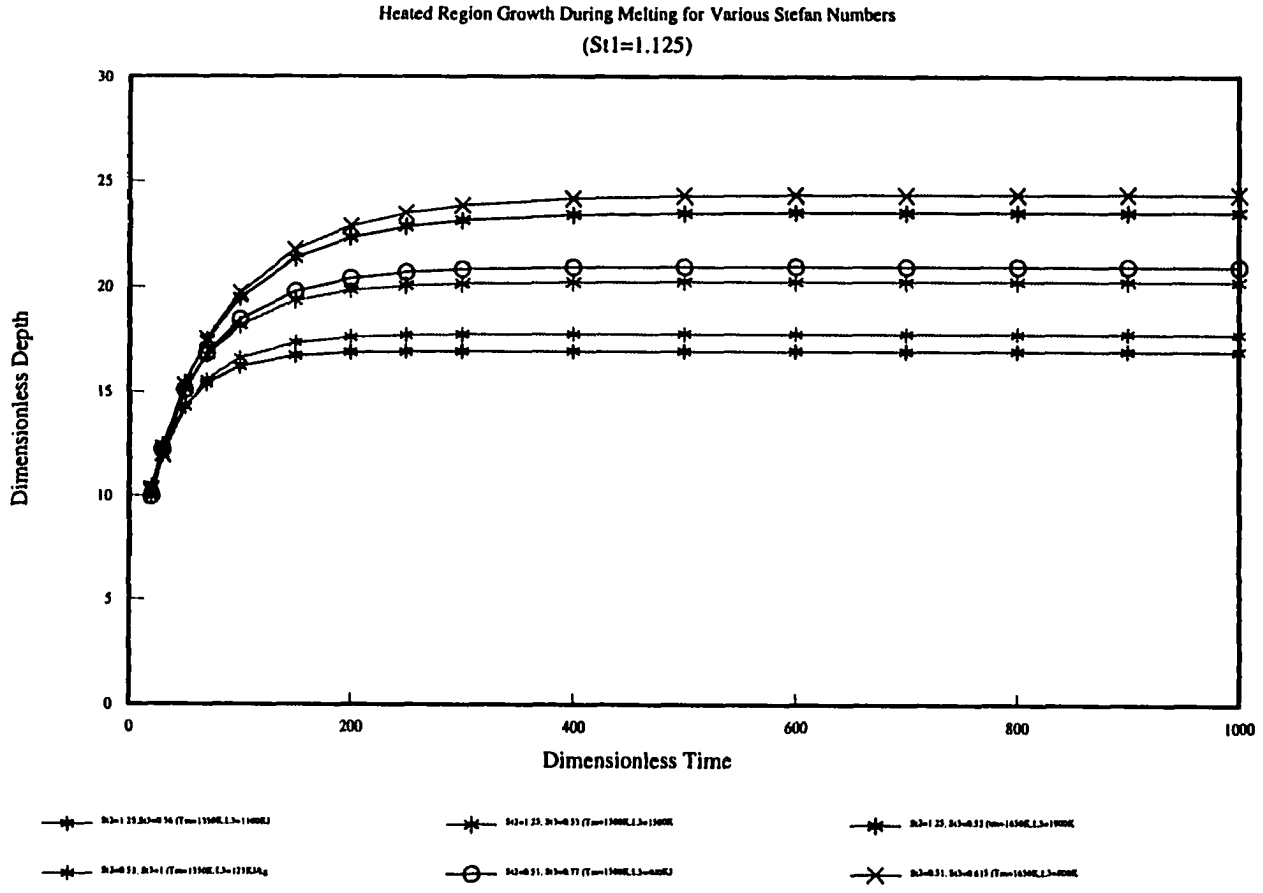

Figure 151: Heated Region Growth During Melting for Various Stefan Numbers (St_1=1.125).

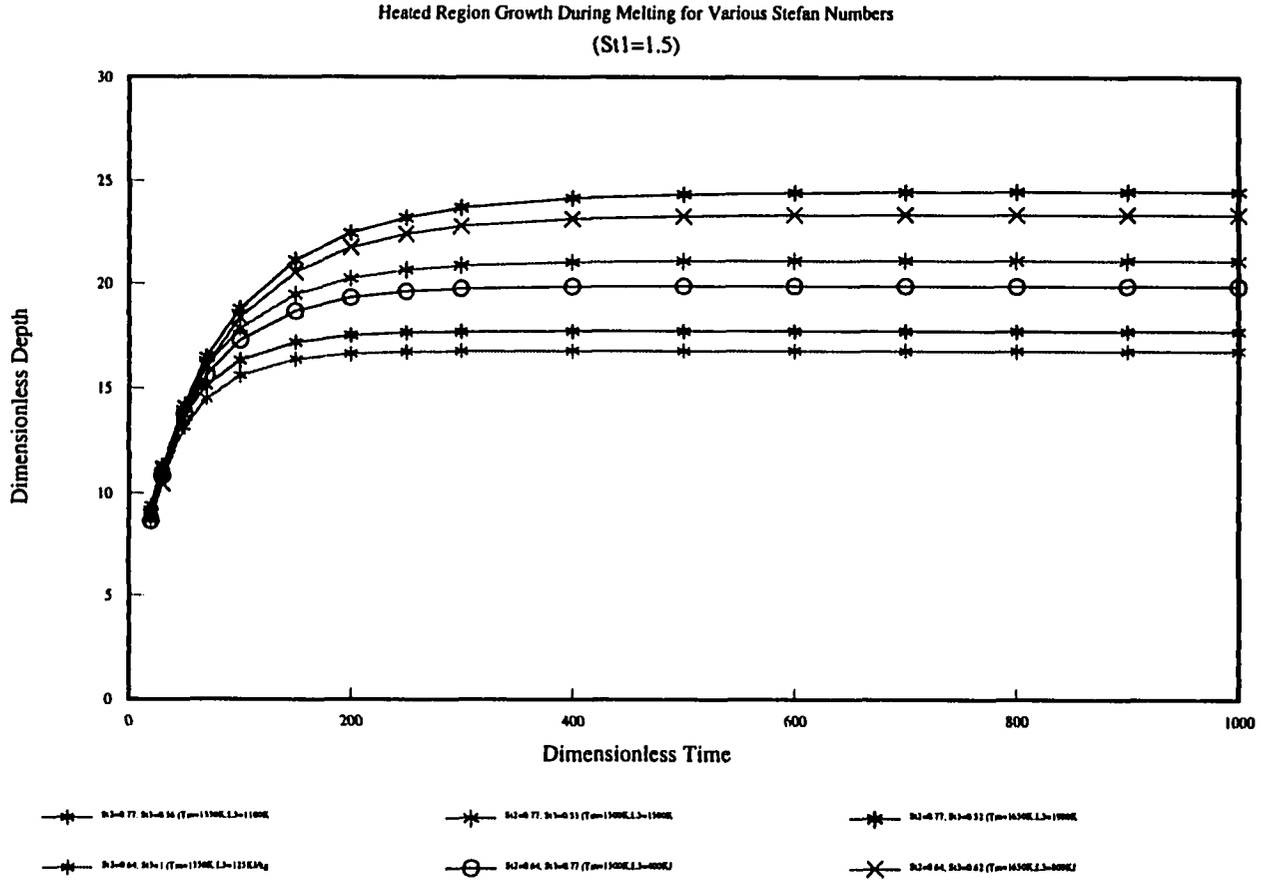

Figure 152: Heated Region Growth During Melting for Various Stefan Numbers (St_1=1.5).

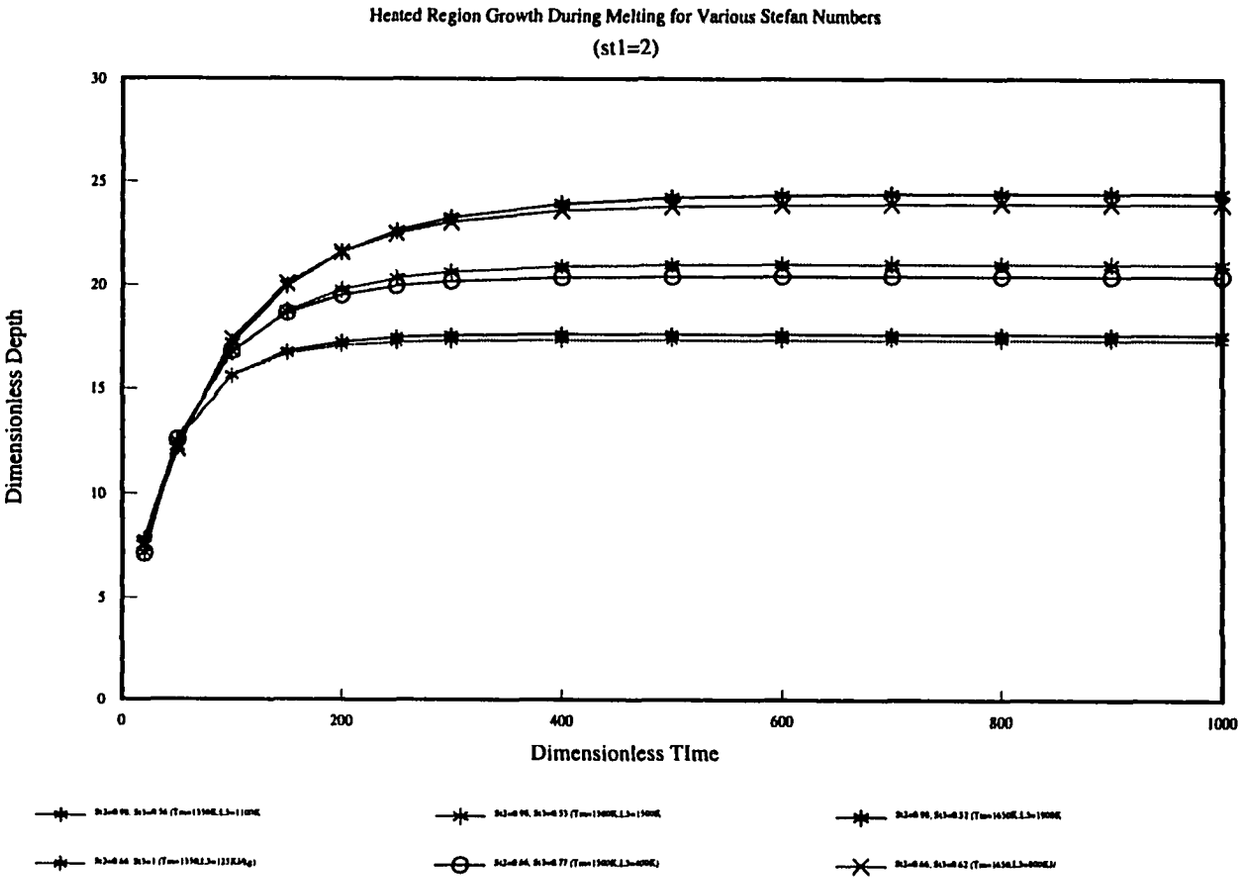

Figure 153: Heated Region Growth During Melting for Various Stefan Numbers (St_1=2).

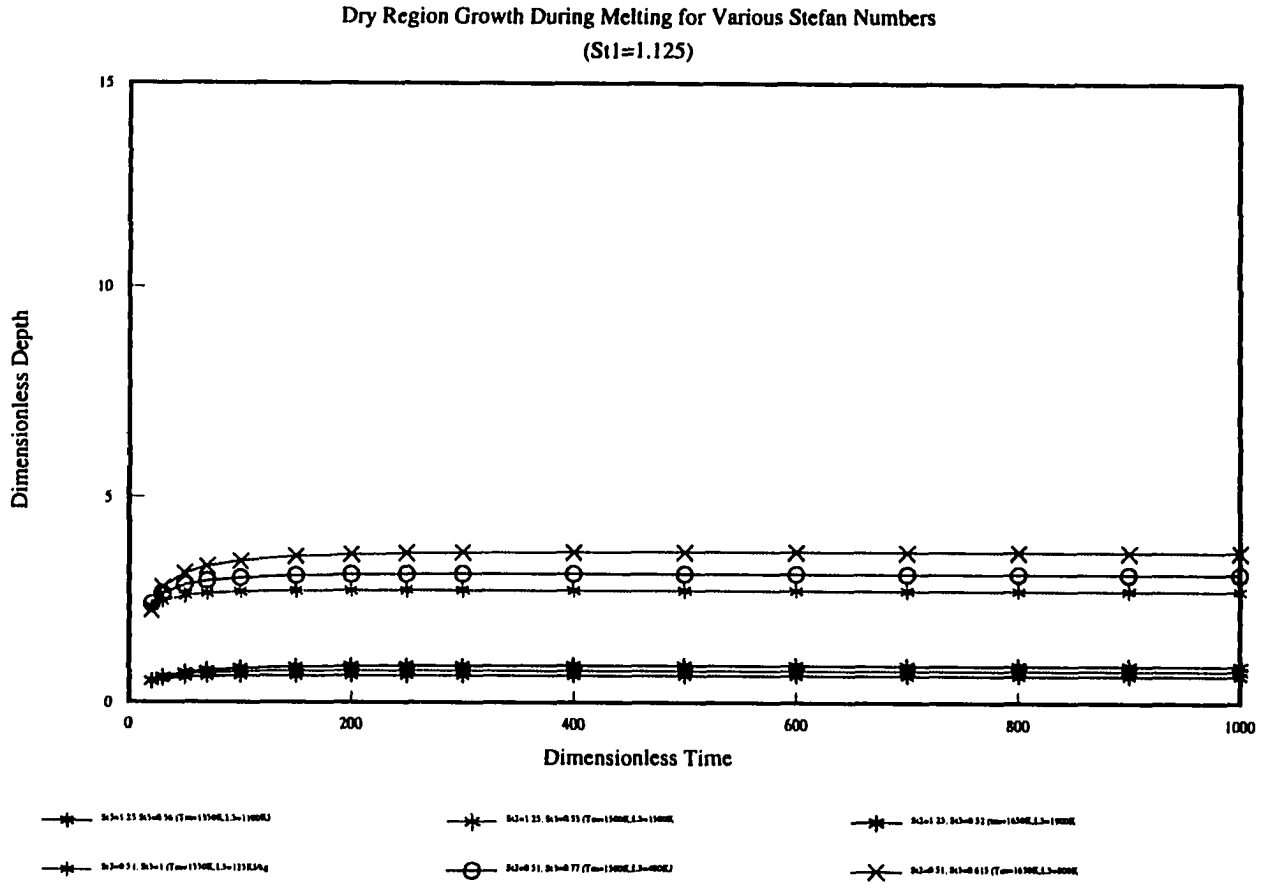

Figure 154: Dry Region Growth During Melting for Various Stefan Numbers (St_l=1.125).

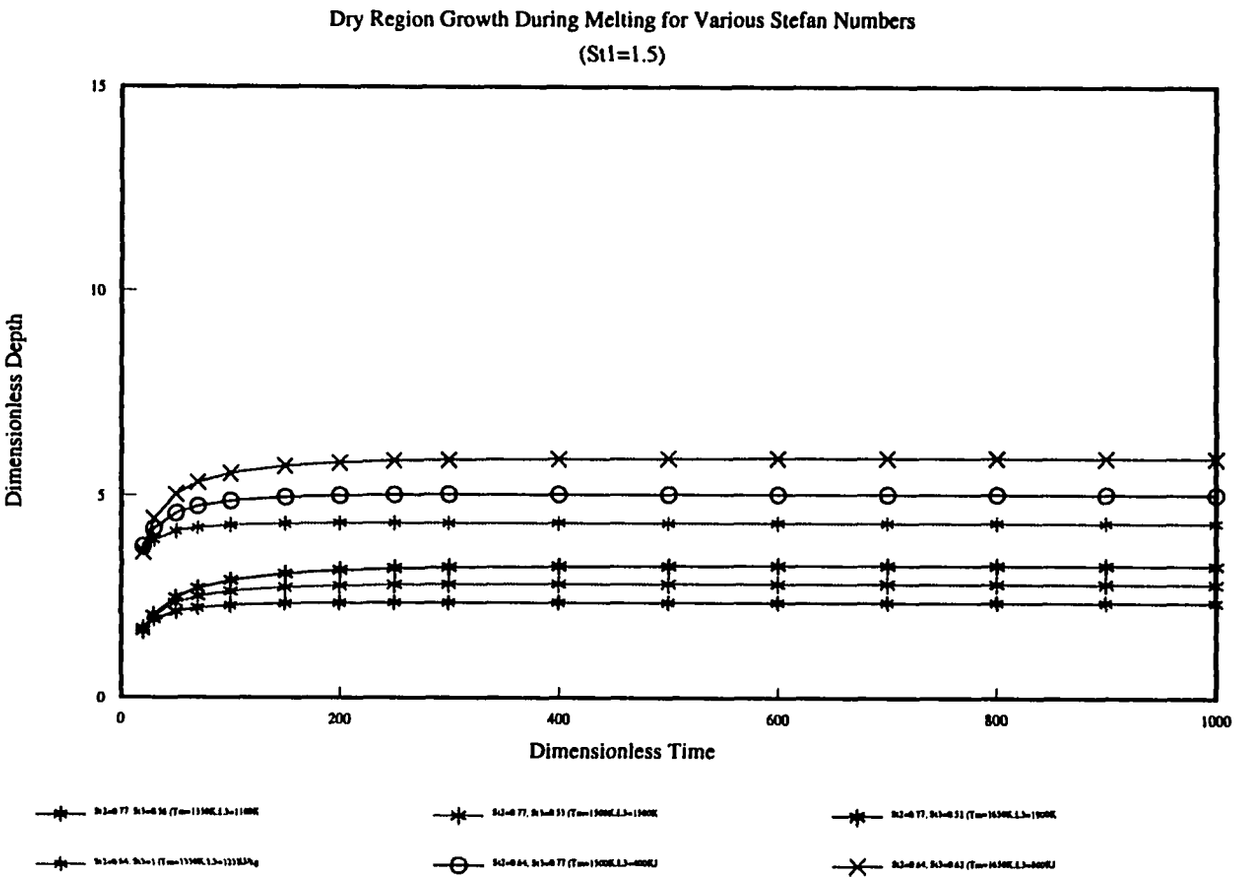

Figure 155: Dry Region Growth During Melting for Various Stefan Numbers (St_1=1.5).

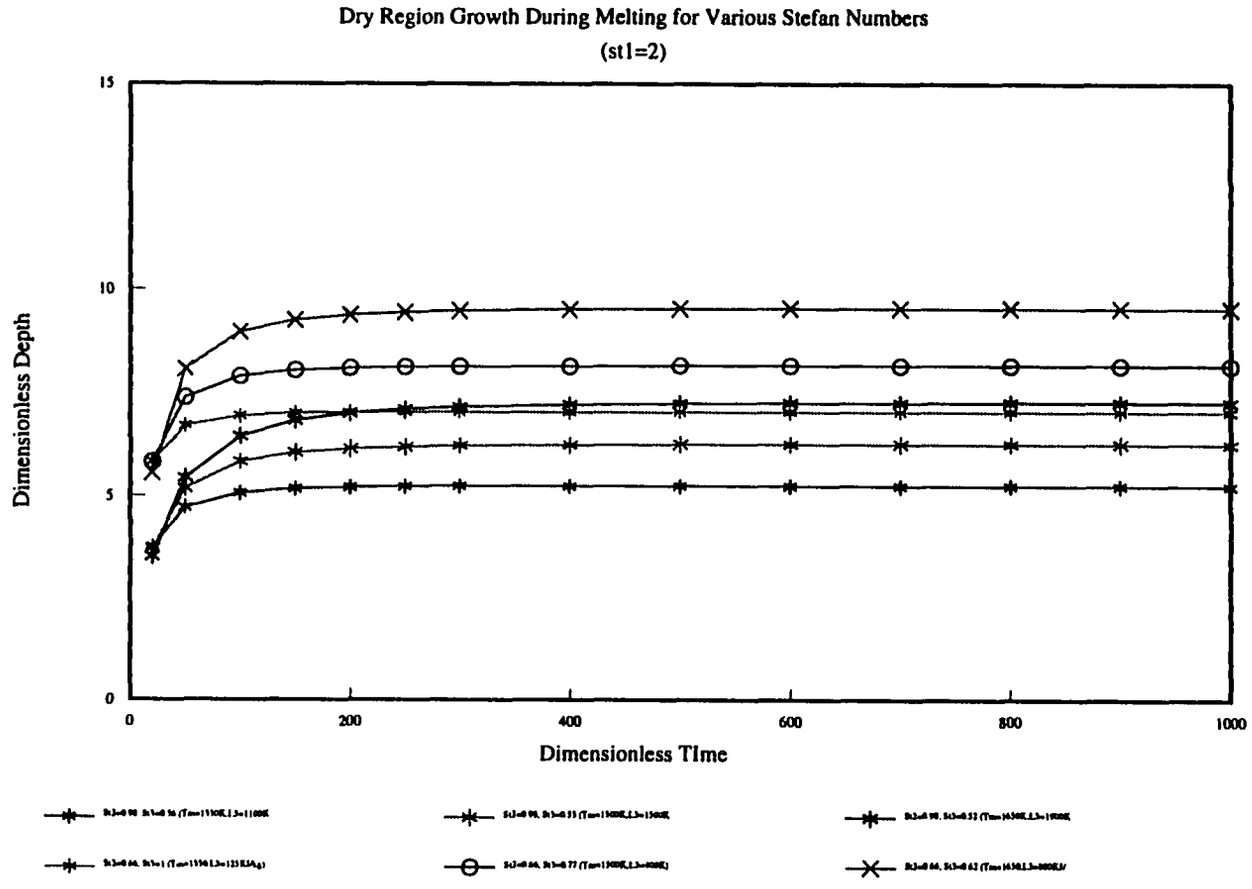

Figure 156: Dry Region Growth During Melting for Various Stefan Numbers (St_1=2).

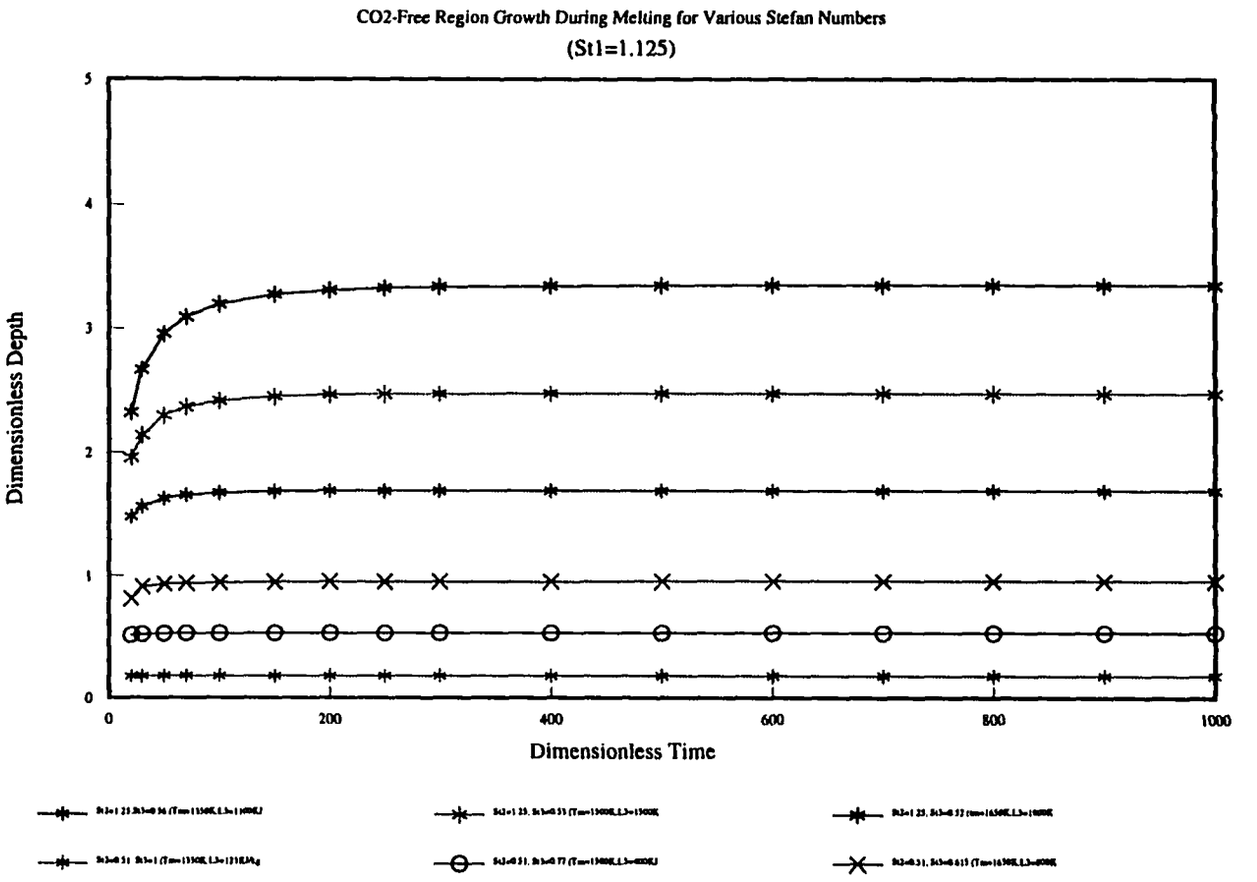

Figure 157: CO_2-Free Region Growth During Melting for Various Stefan Numbers (St_1=1.125).

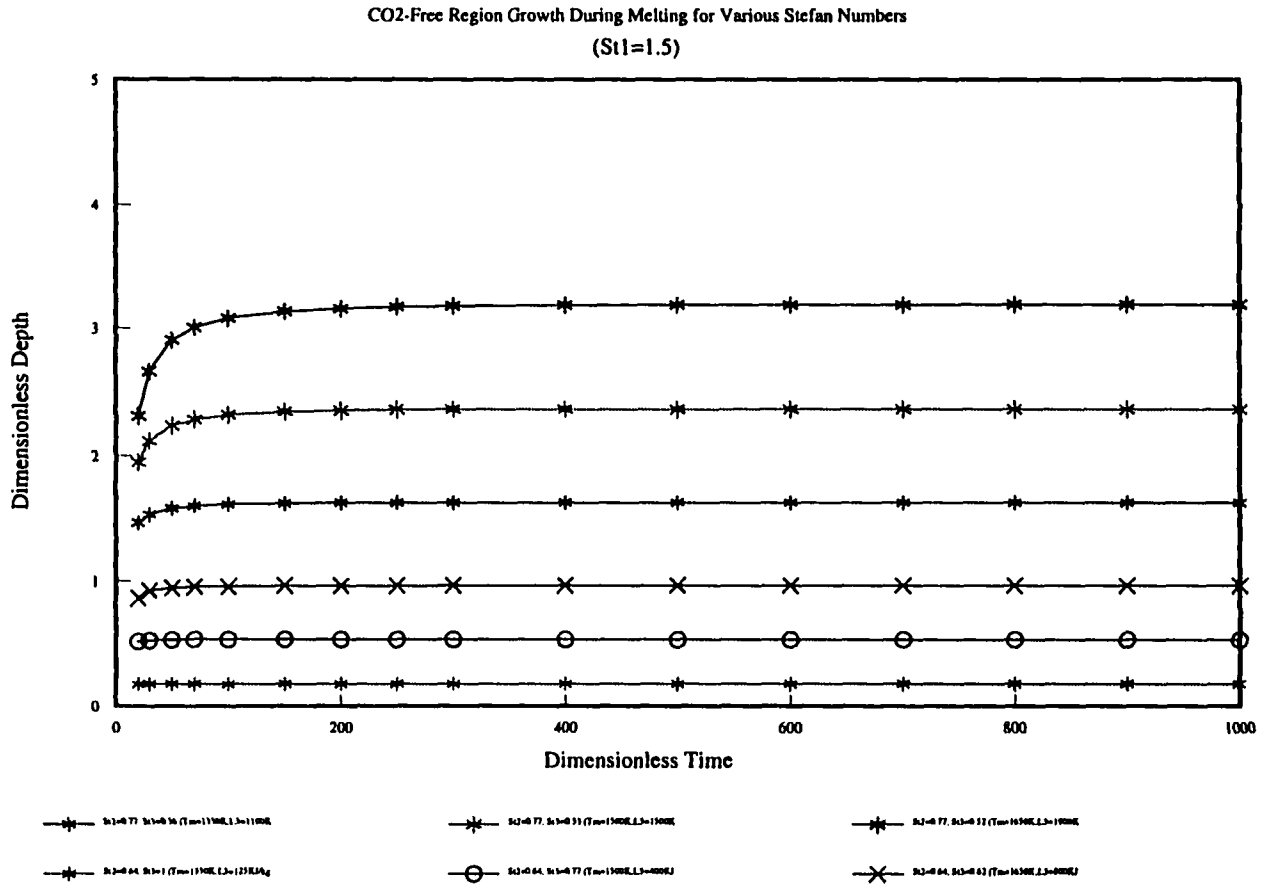

Figure 158: CO_2-Free Region Growth During Melting for Various Stefan Numbers (St_1=1.5).

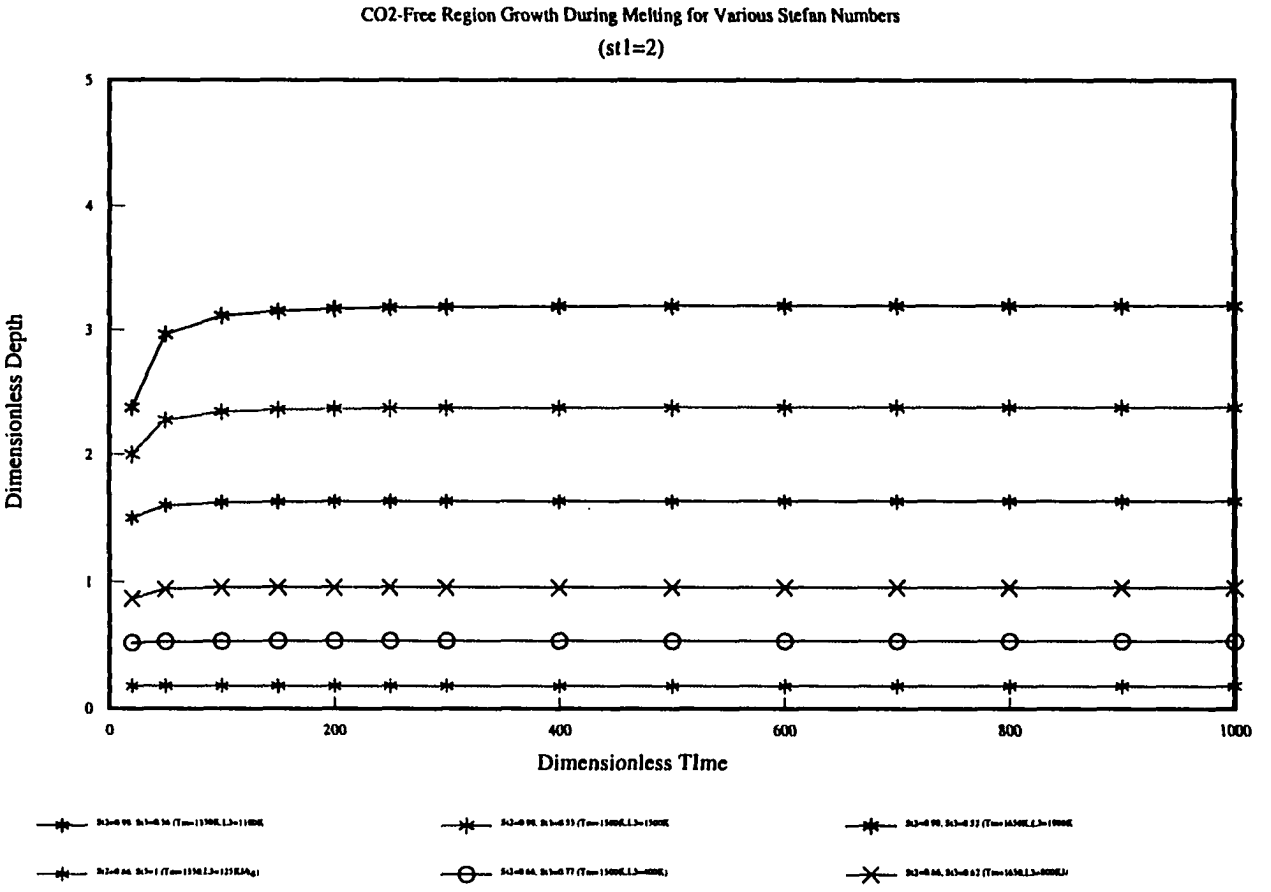

Figure 159: CO_2-Free Region Growth During Melting for Various Stefan Numbers (St_1=2).

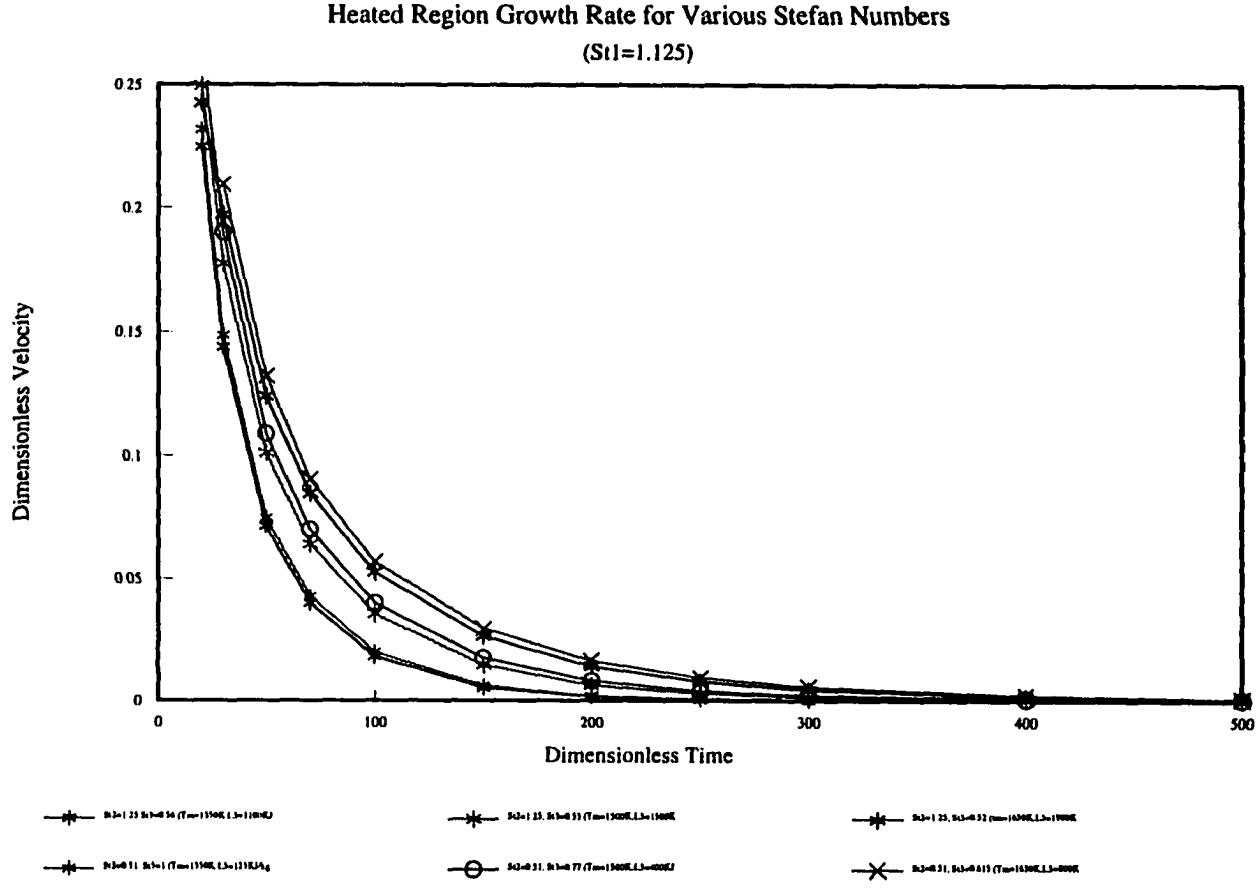

Figure 160: Heated Region Growth Rate During Melting for Various Stefan Numbers (St_1=1.125).

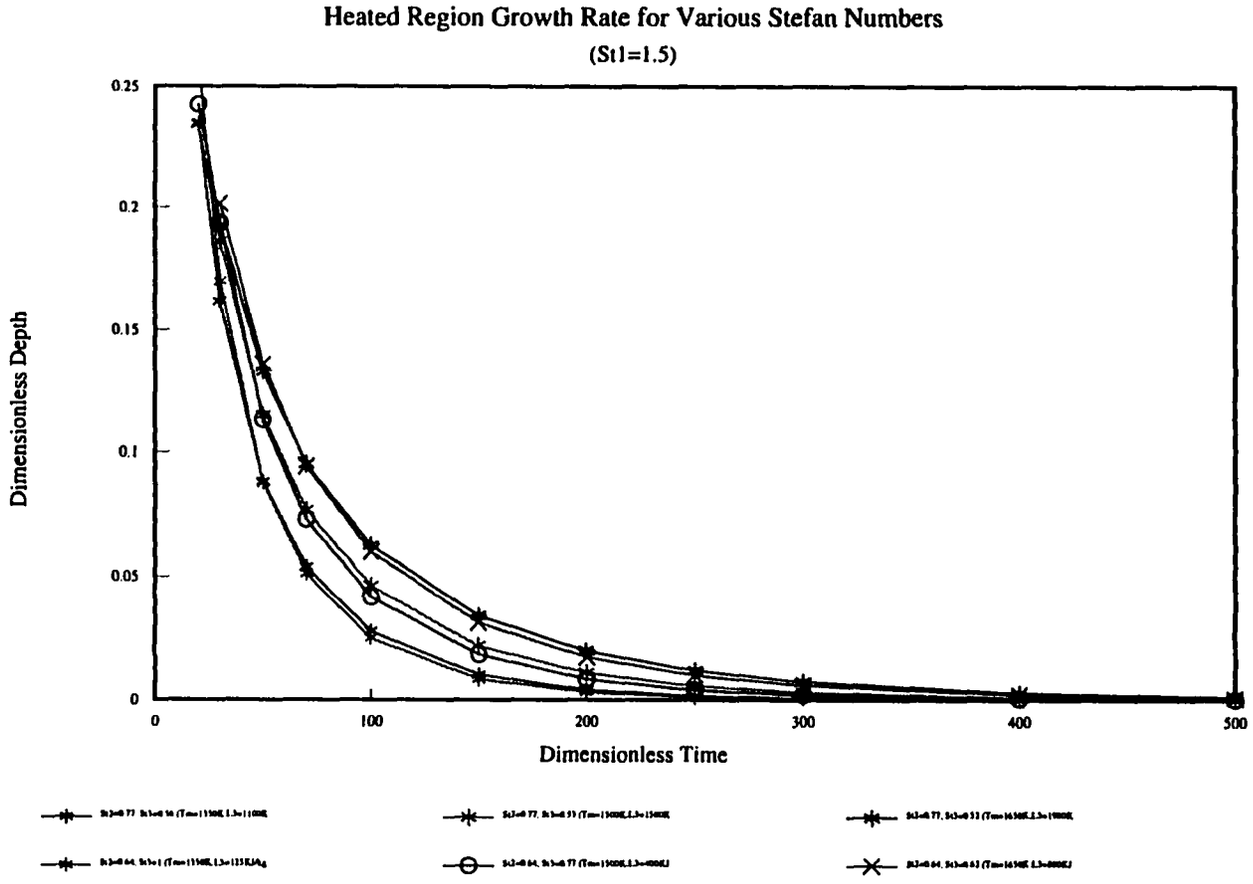

Figure 161: Heated Region Growth Rate During Melting for Various Stefan Numbers (St_l=1.5).

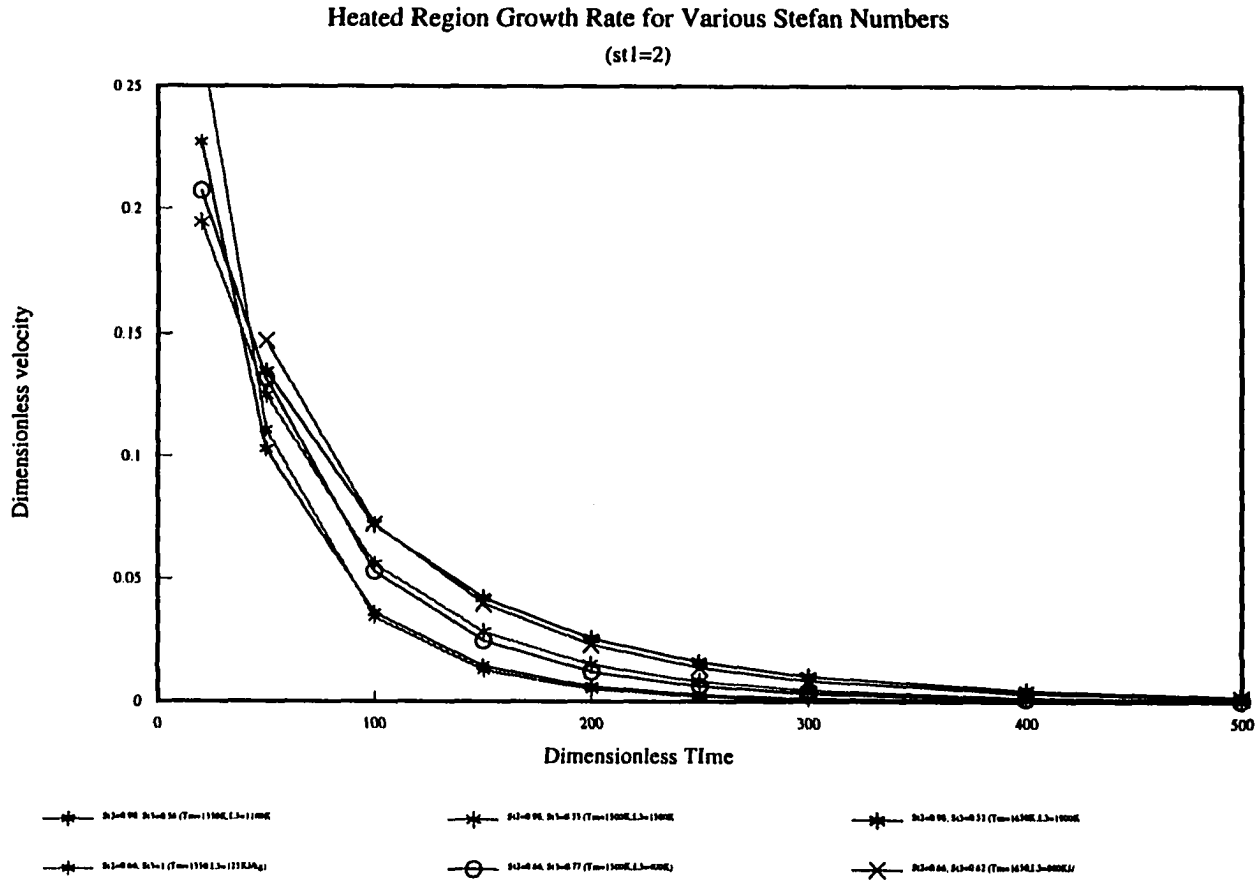

Figure 162: Heated Region Growth Rate During Melting for Various Stefan Numbers (St_1=2).

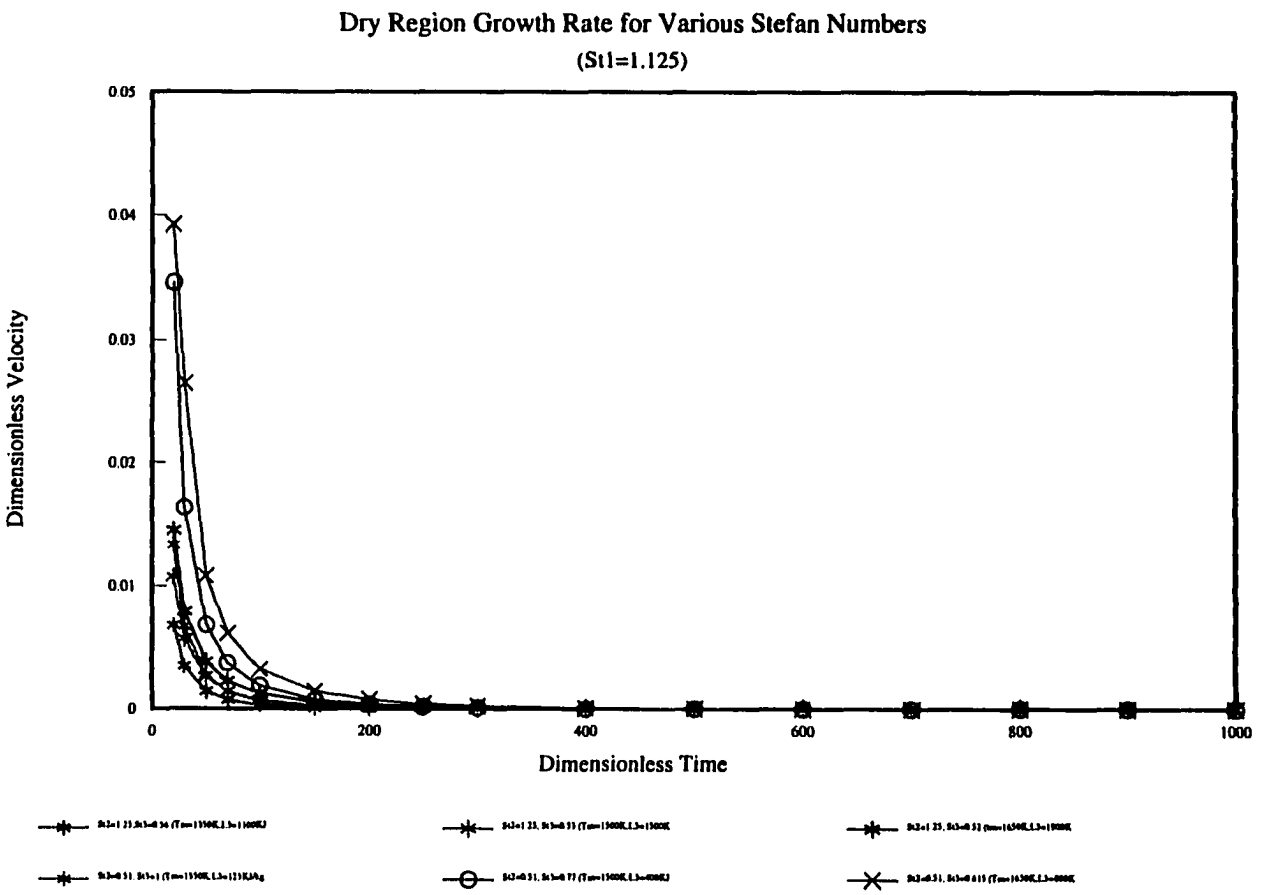

Figure 163: Dry Region Growth Rate During Melting for Various Stefan Numbers (St_1=1.125).

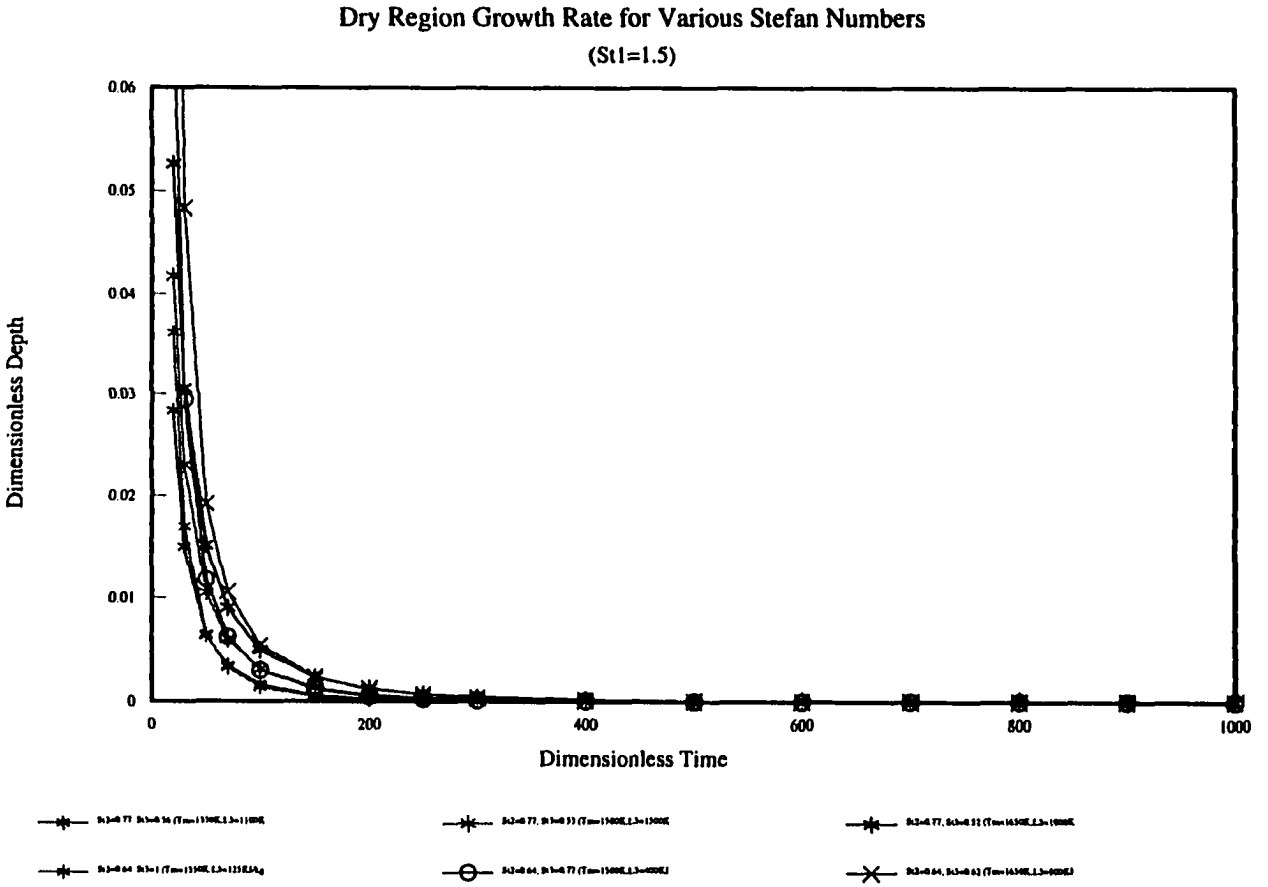

Figure 164: Dry Region Growth Rate During Melting for Various Stefan Numbers (St_l=1.5).

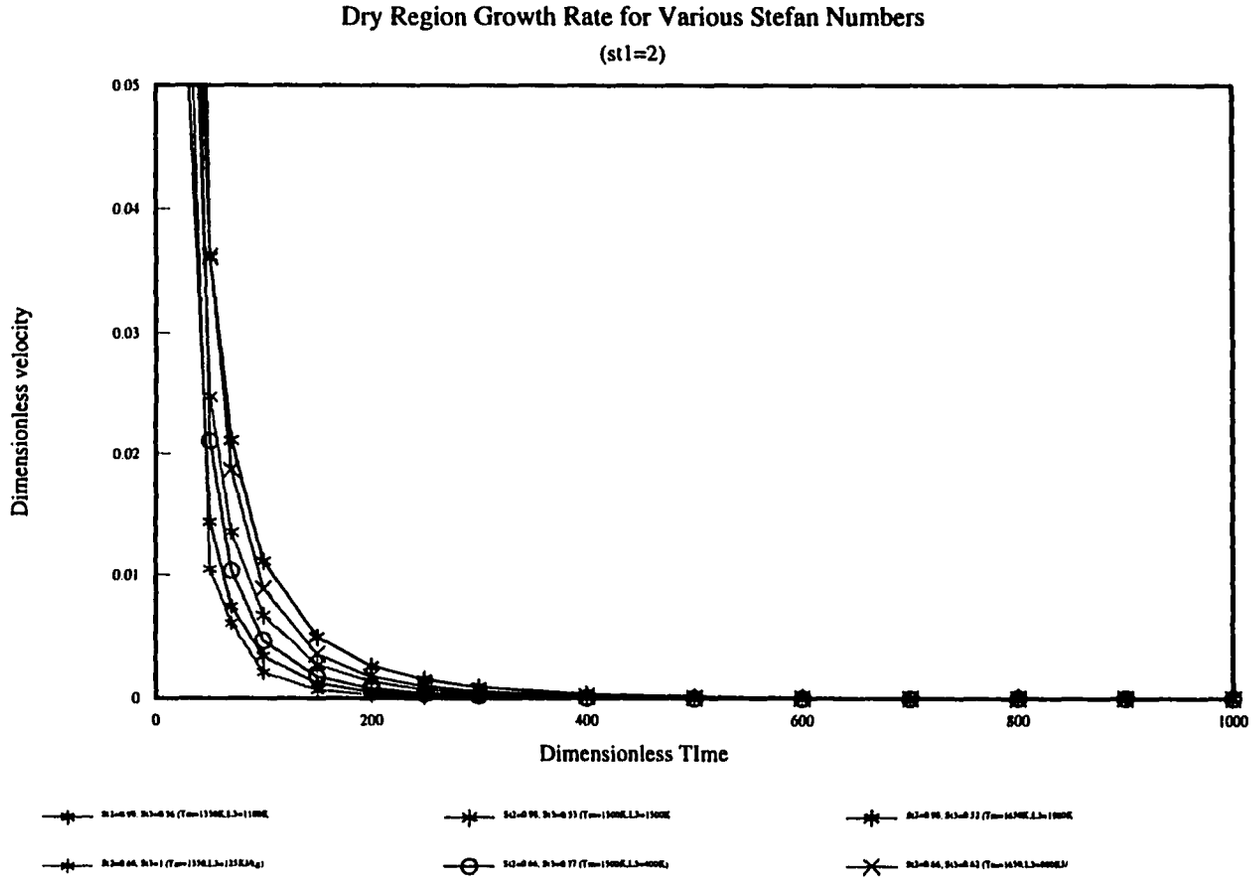

Figure 165: Dry Region Growth Rate During Melting for Various Stefan Numbers (St_1=2).

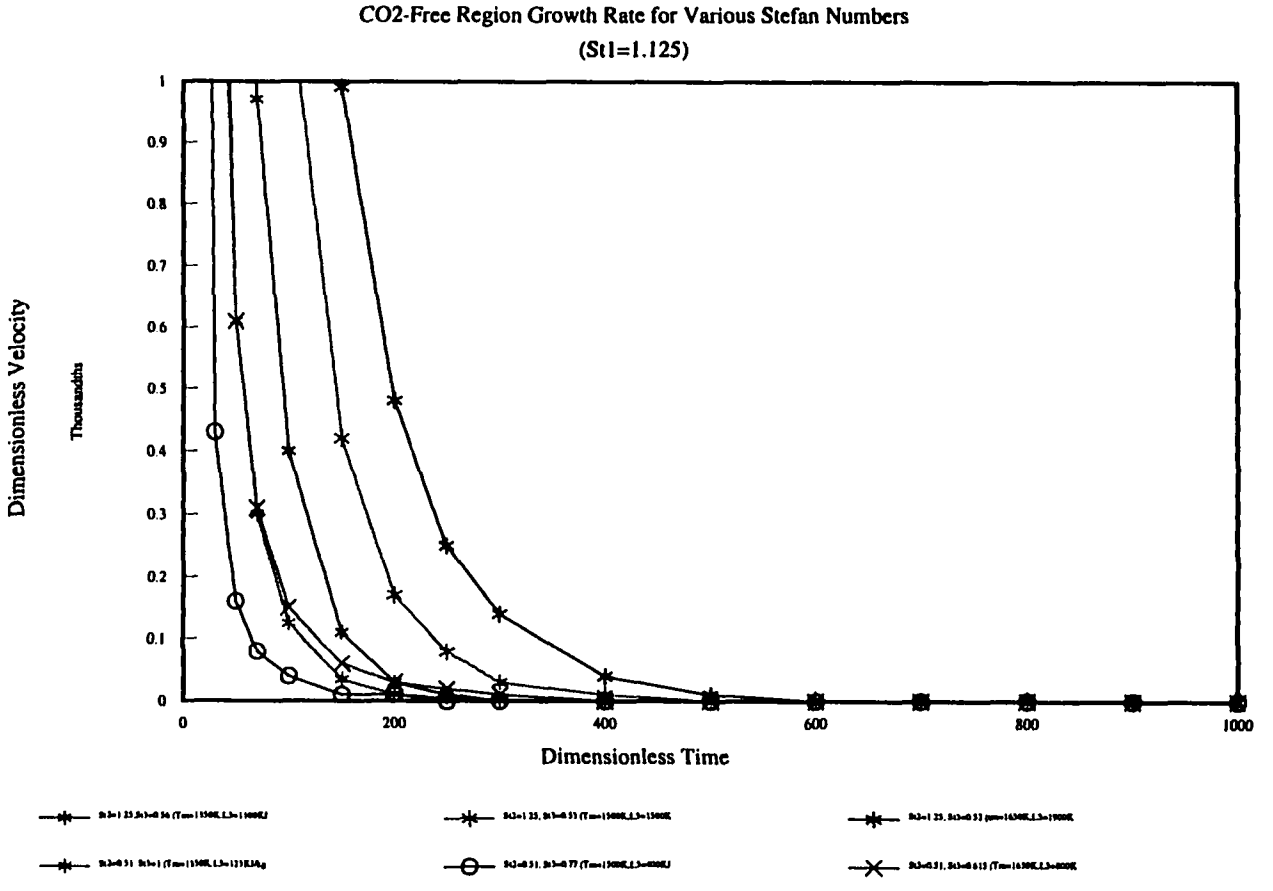

Figure 166: CO_2-Free Region Growth Rate During Melting for Various Stefan Numbers (St_l=1.125).

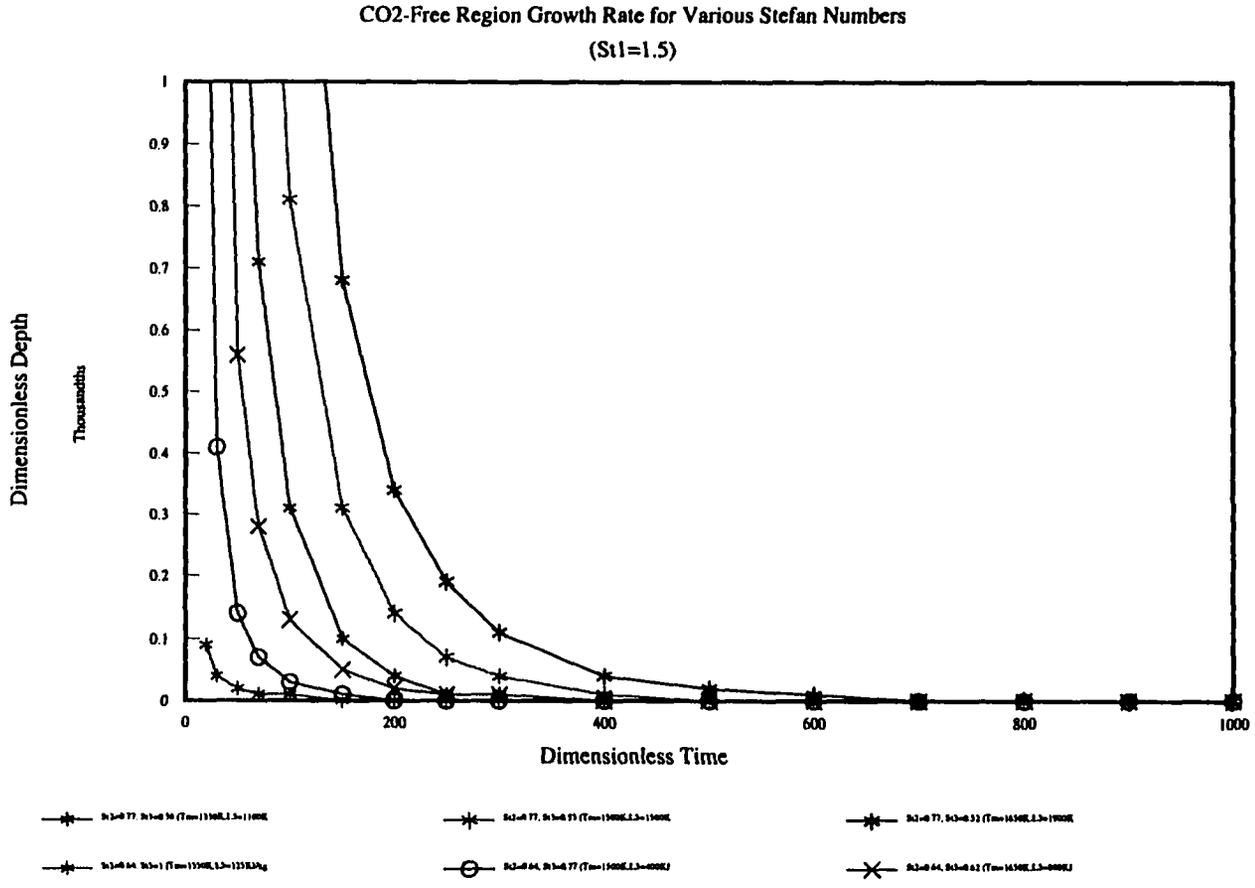

Figure 167: CO_2-Free Region Growth Rate During Melting for Various Stefan Numbers (St_1=1.5).

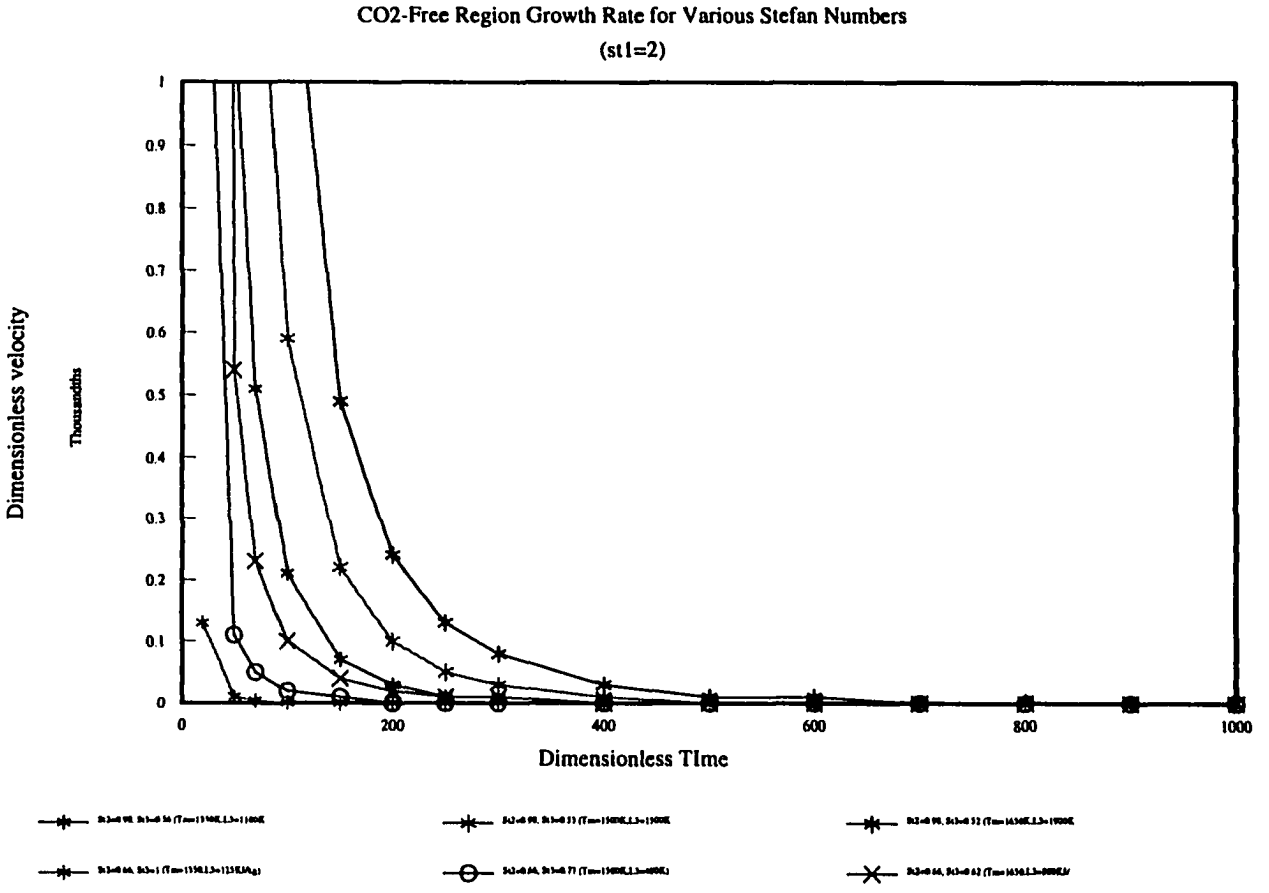

Figure 168: CO_2-Free Region Growth Rate During Melting for Various Stefan Numbers (St_1=2).

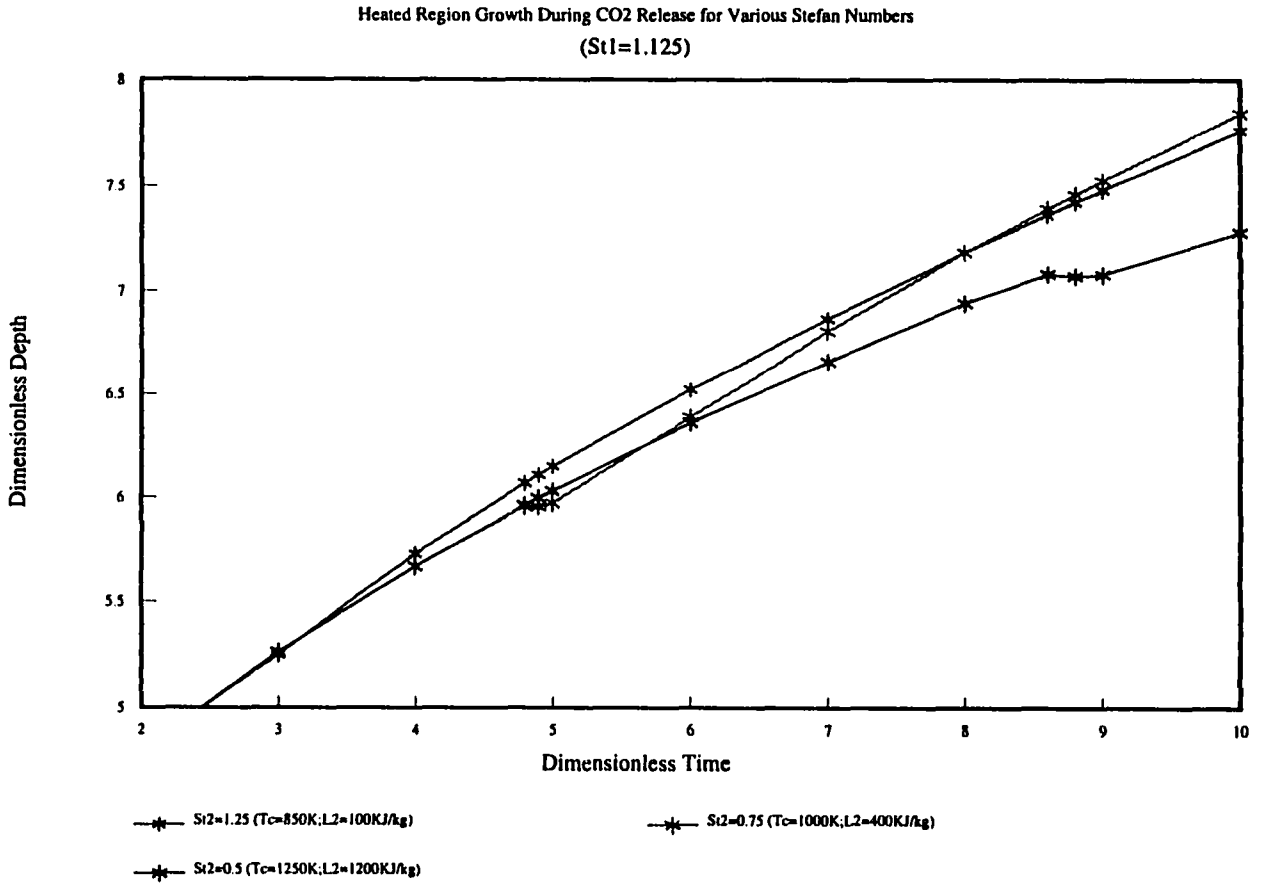

Figure 169: Heated Region Growth During CO_2 Release for Various Stefan Numbers (St_1=1.125).

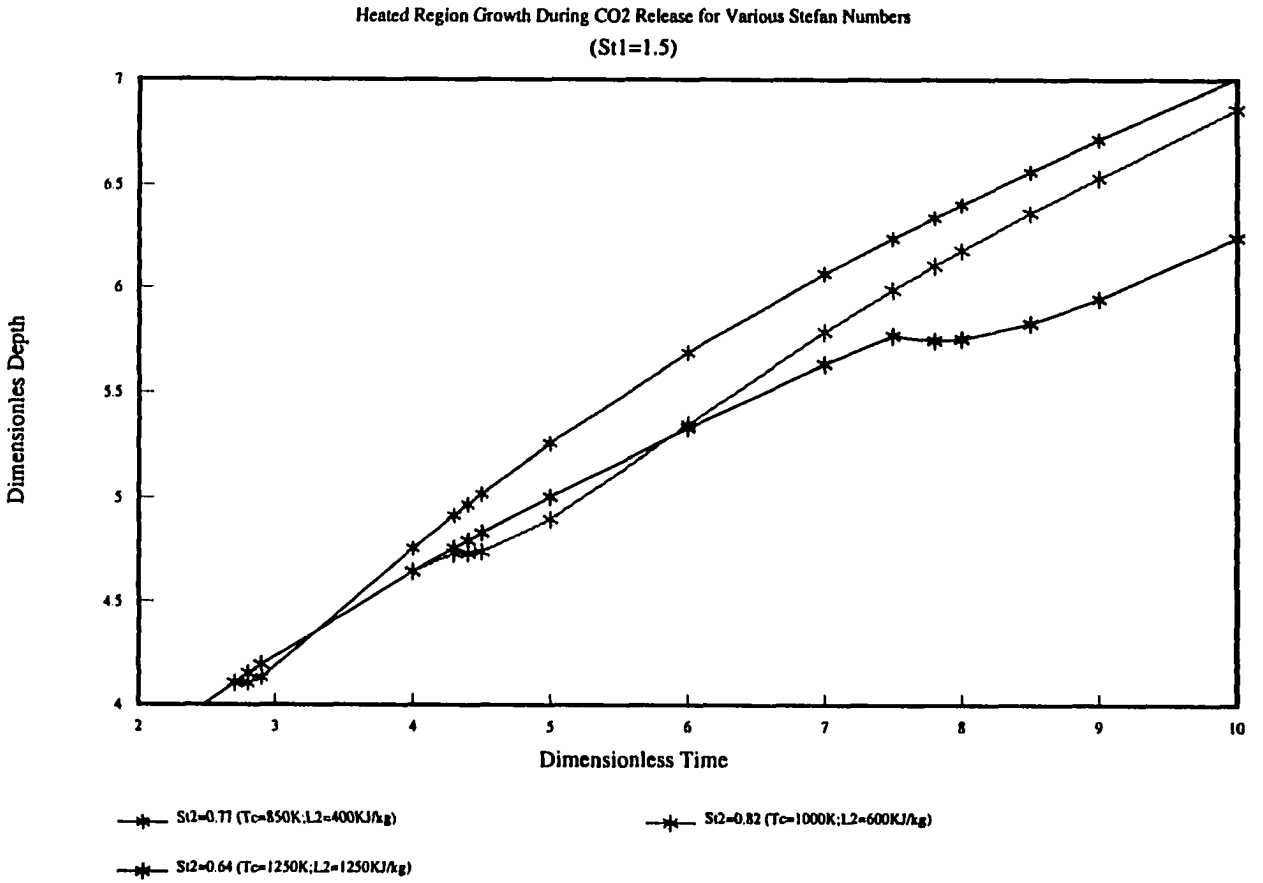

Figure 170: Heated Region Growth During CO_2 Release for Various Stefan Numbers (St_1=1.5).

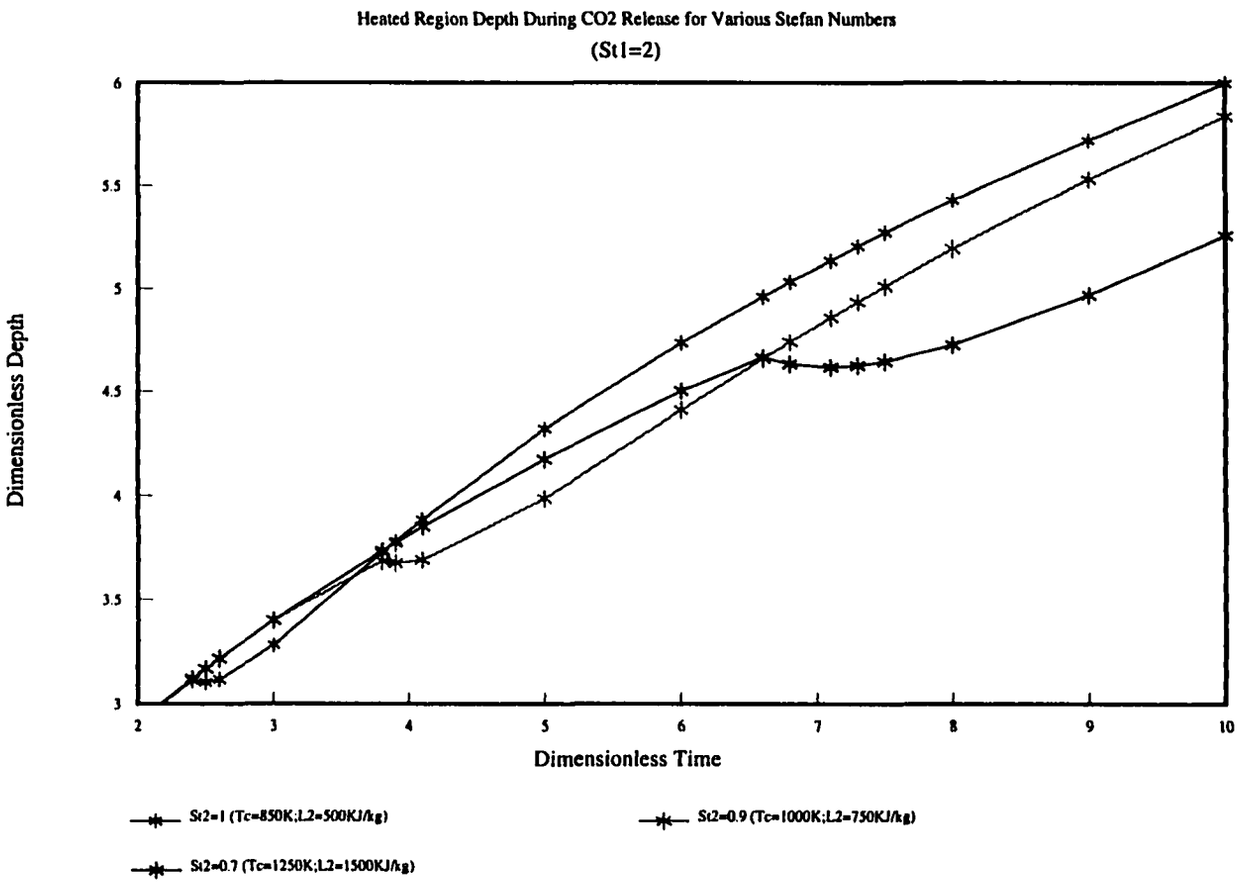

Figure 171: Heated Region Growth During CO_2 Release for Various Stefan Numbers (St_1=2).

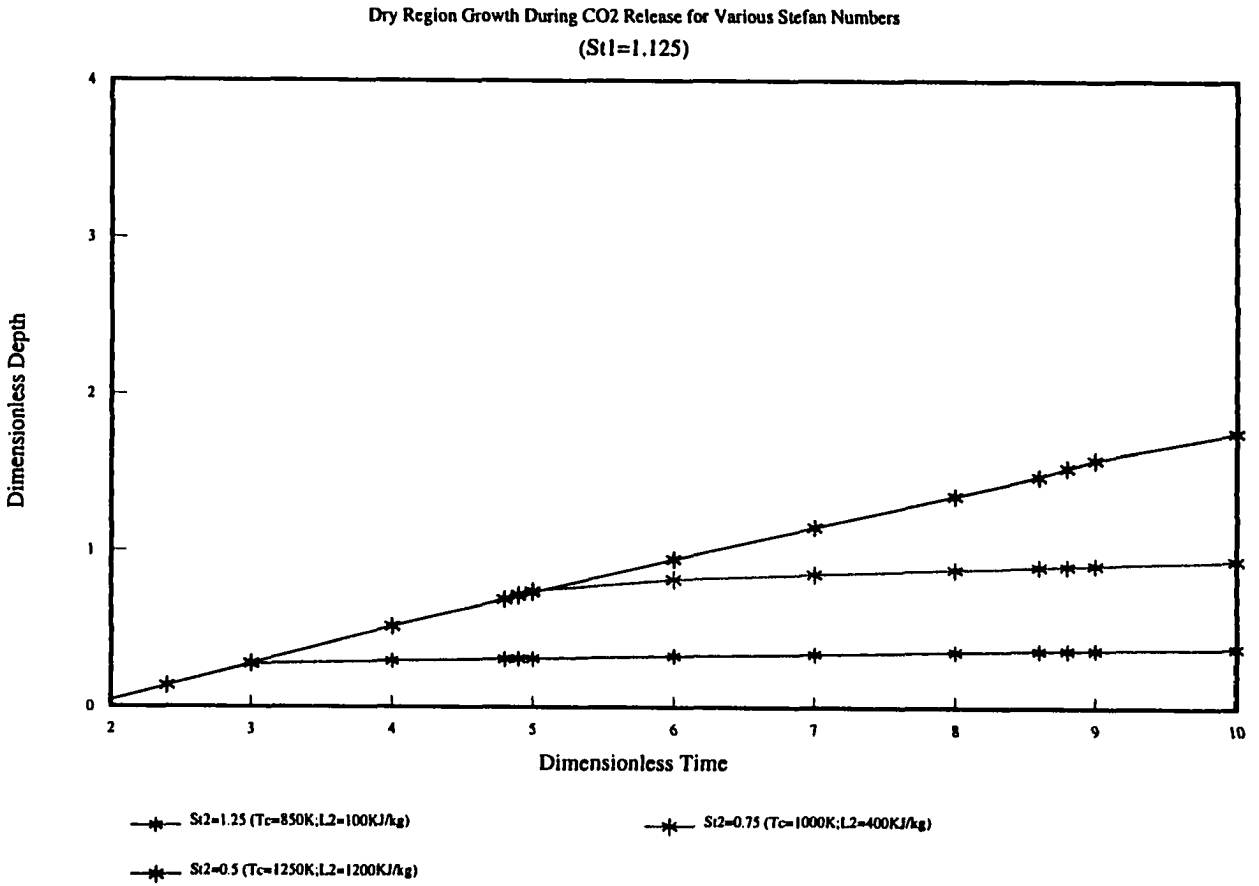

Figure 172: Dry Region Growth During CO_2 Release for Various Stefan Numbers (St_1=1.125).

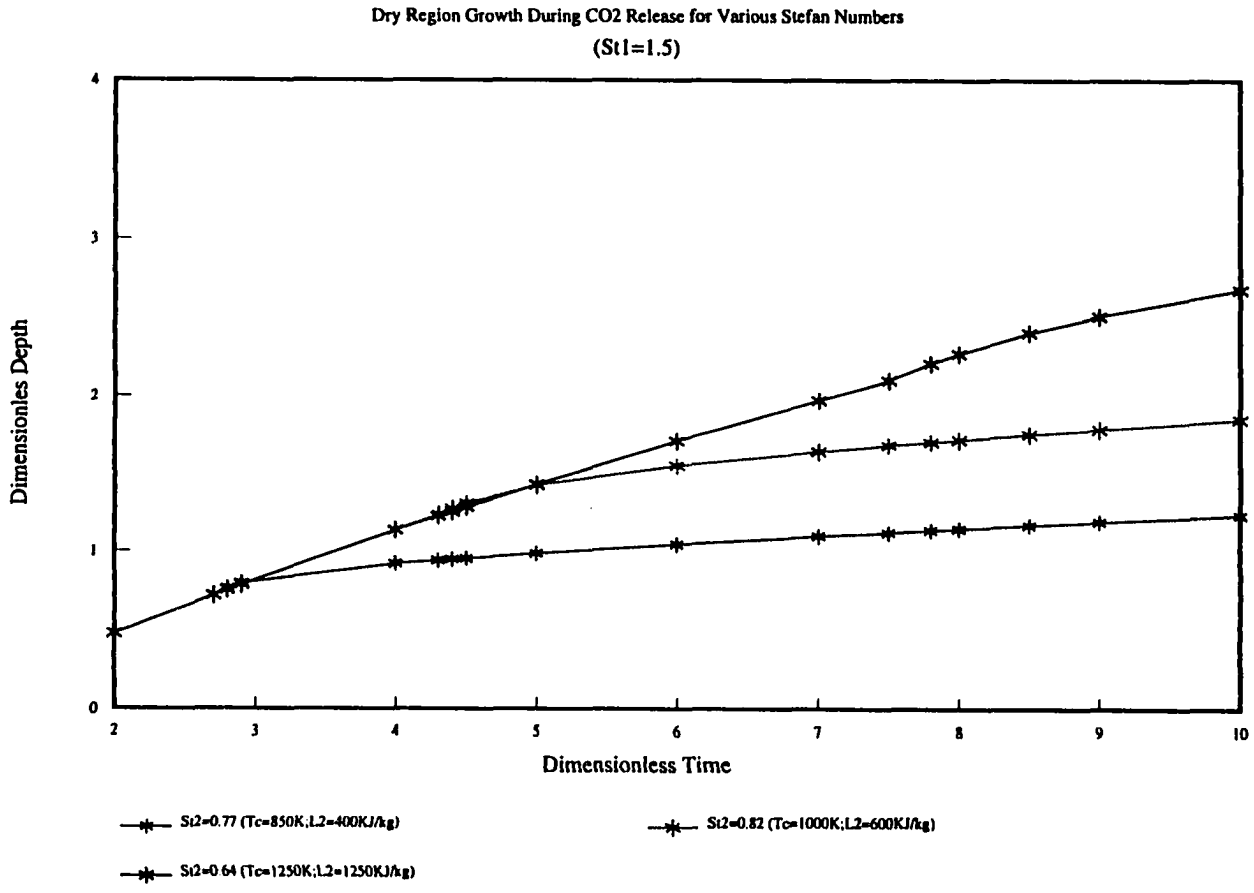

Figure 173: Dry Region Growth During CO_2 Release for Various Stefan Numbers (St_1=1.5).

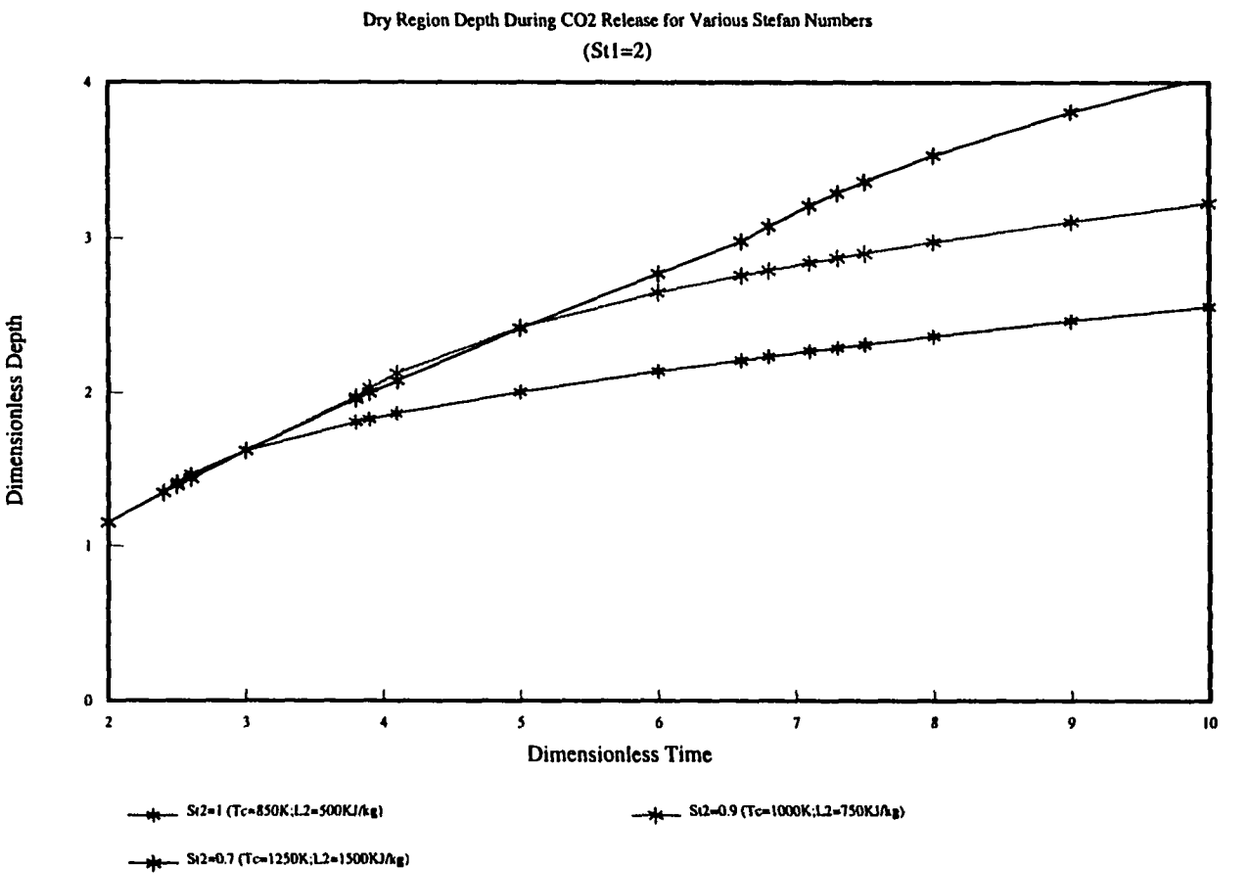

Figure 174: Dry Region Growth During CO_2 Release for Various Stefan Numbers (St_1=2).

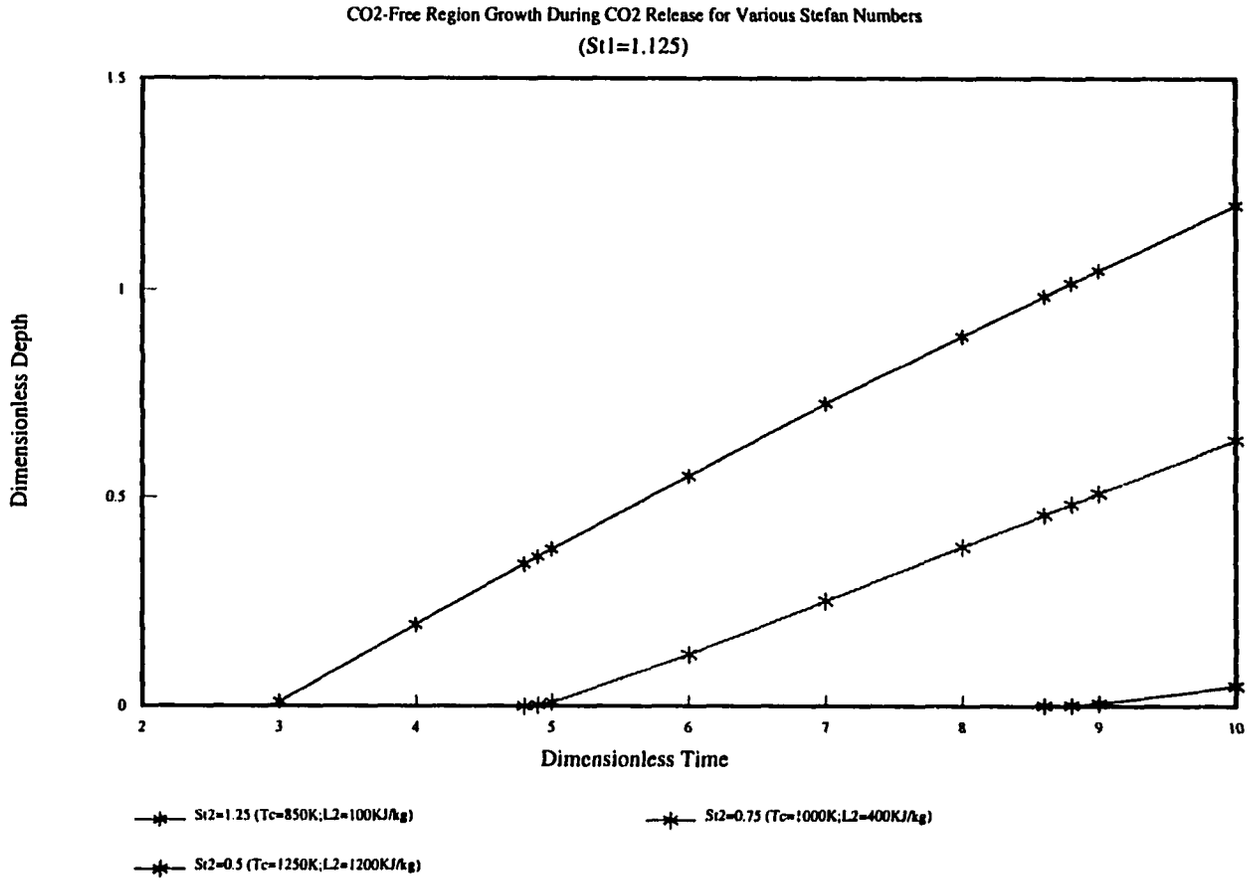

Figure 175: CO_2-Free Region Growth During CO_2 Release for Various Stefan Numbers (St_1=1.125).

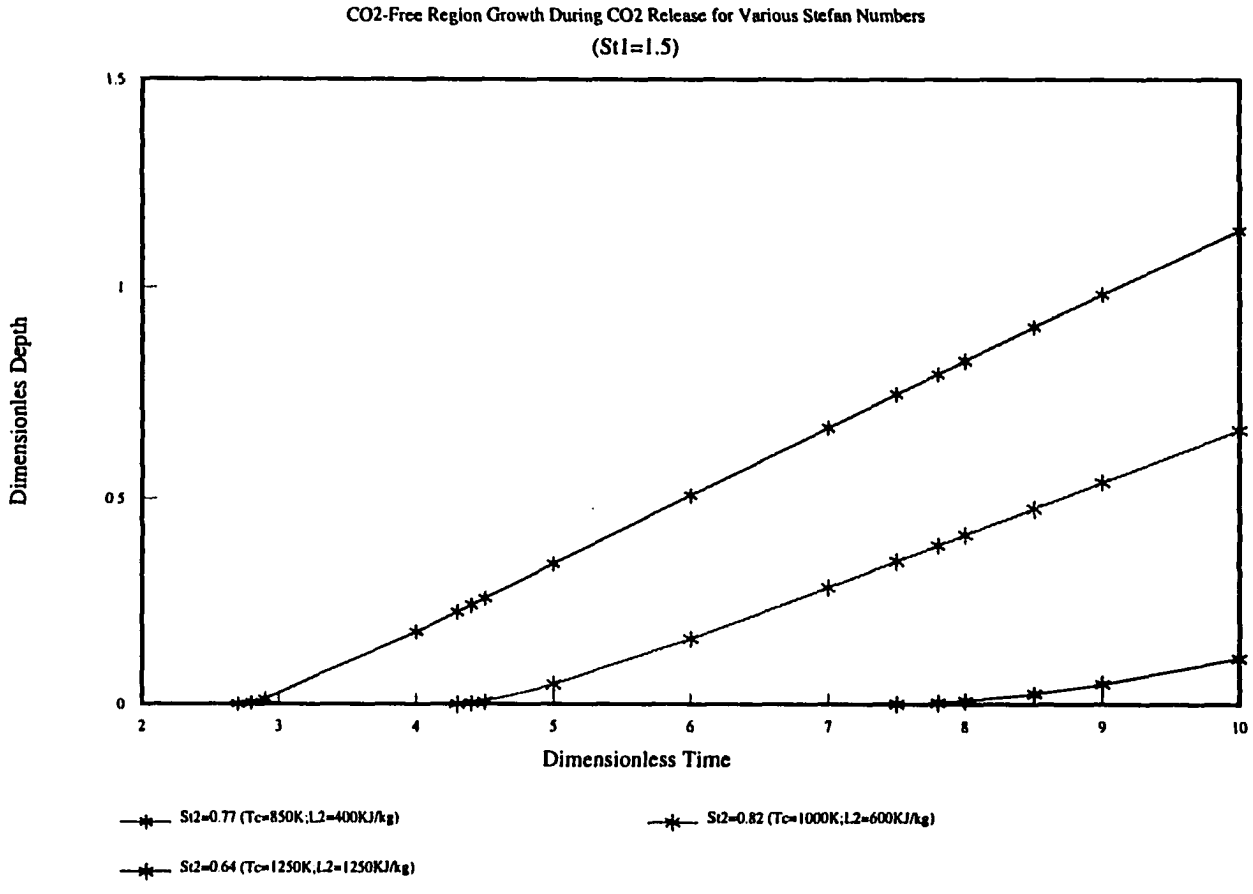

Figure 176: CO_2-Free Region Growth During CO_2 Release for Various Stefan Numbers (St_1=1.5).

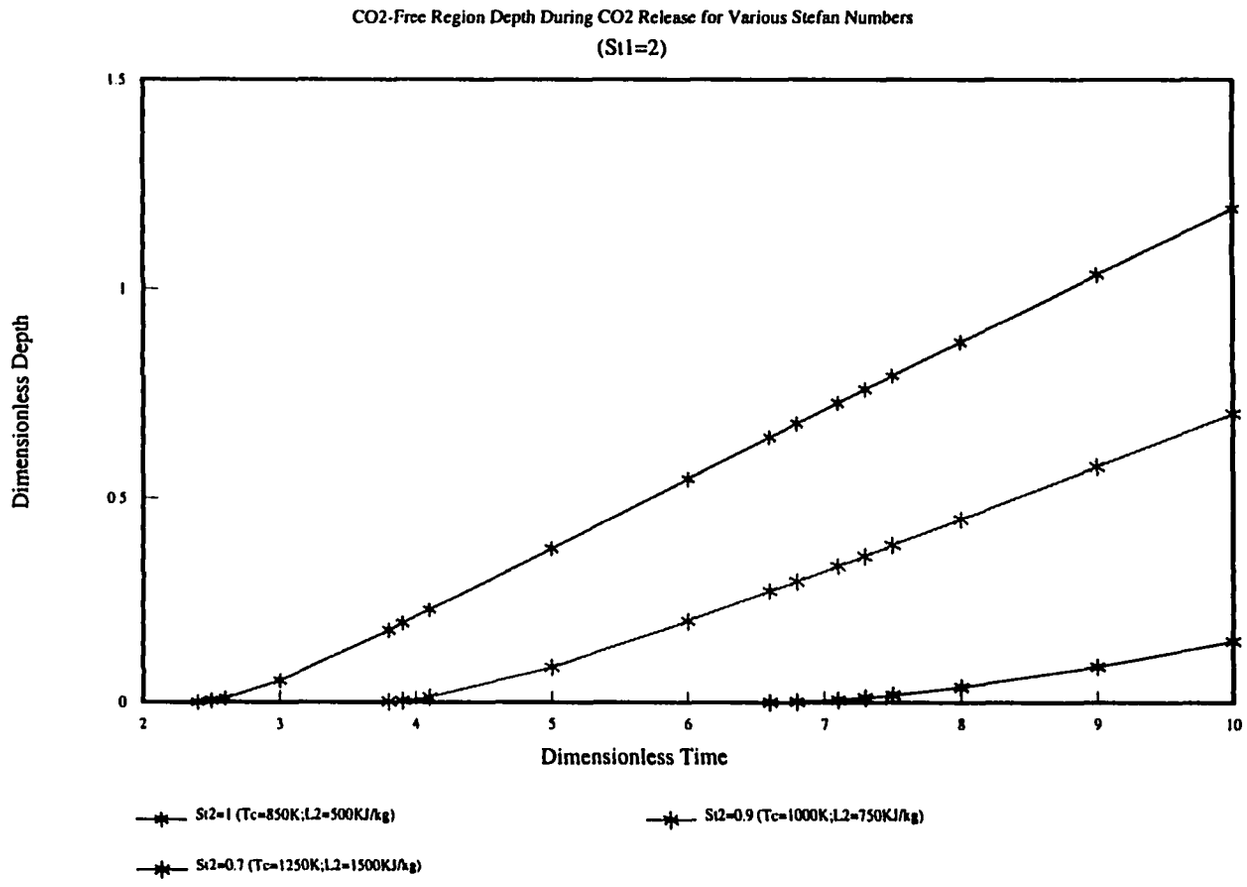

Figure 177: CO_2-Free Region Growth During CO_2 Release for Various Stefan Numbers (St_1=2).

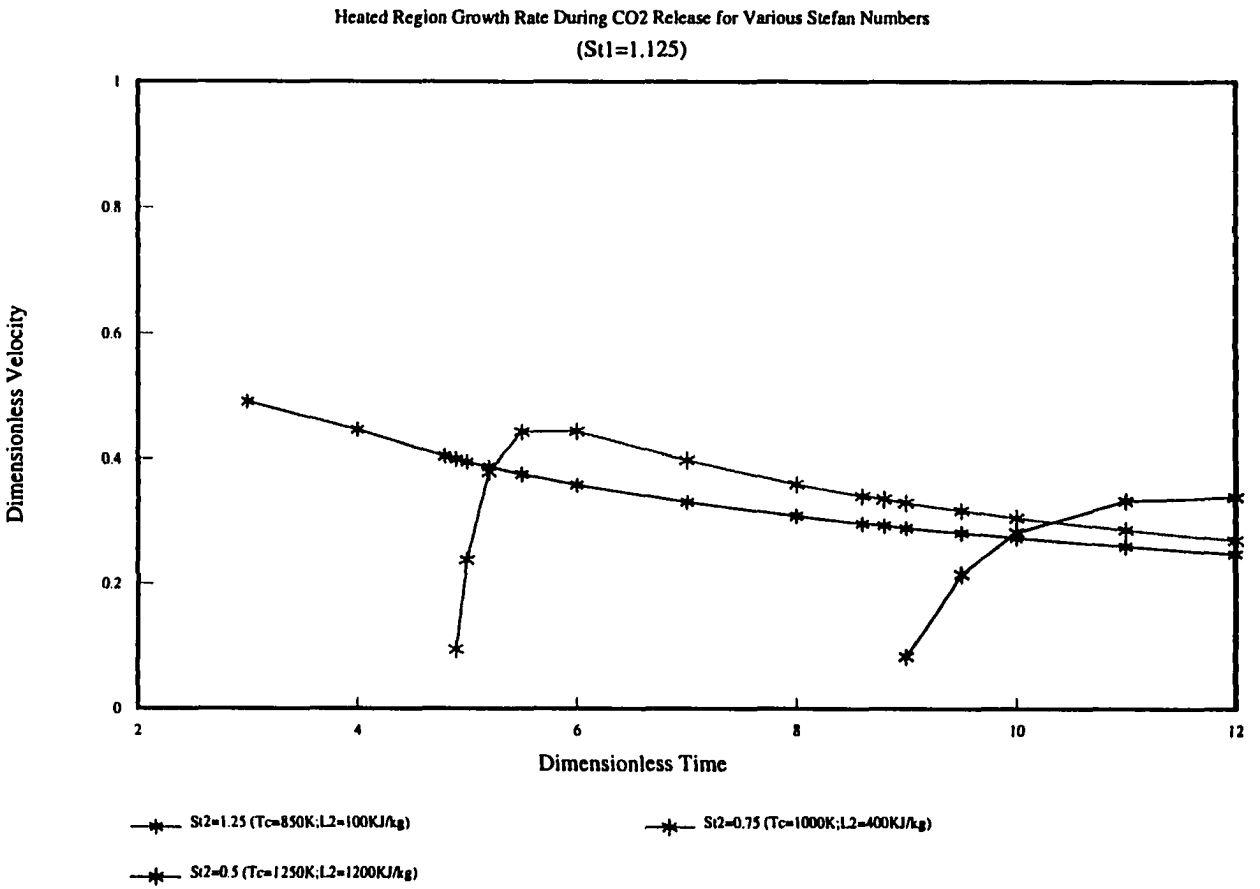

Figure 178: Heated Region Growth Rate During CO_2 Release for Various Stefan Numbers (St_1=1.125).

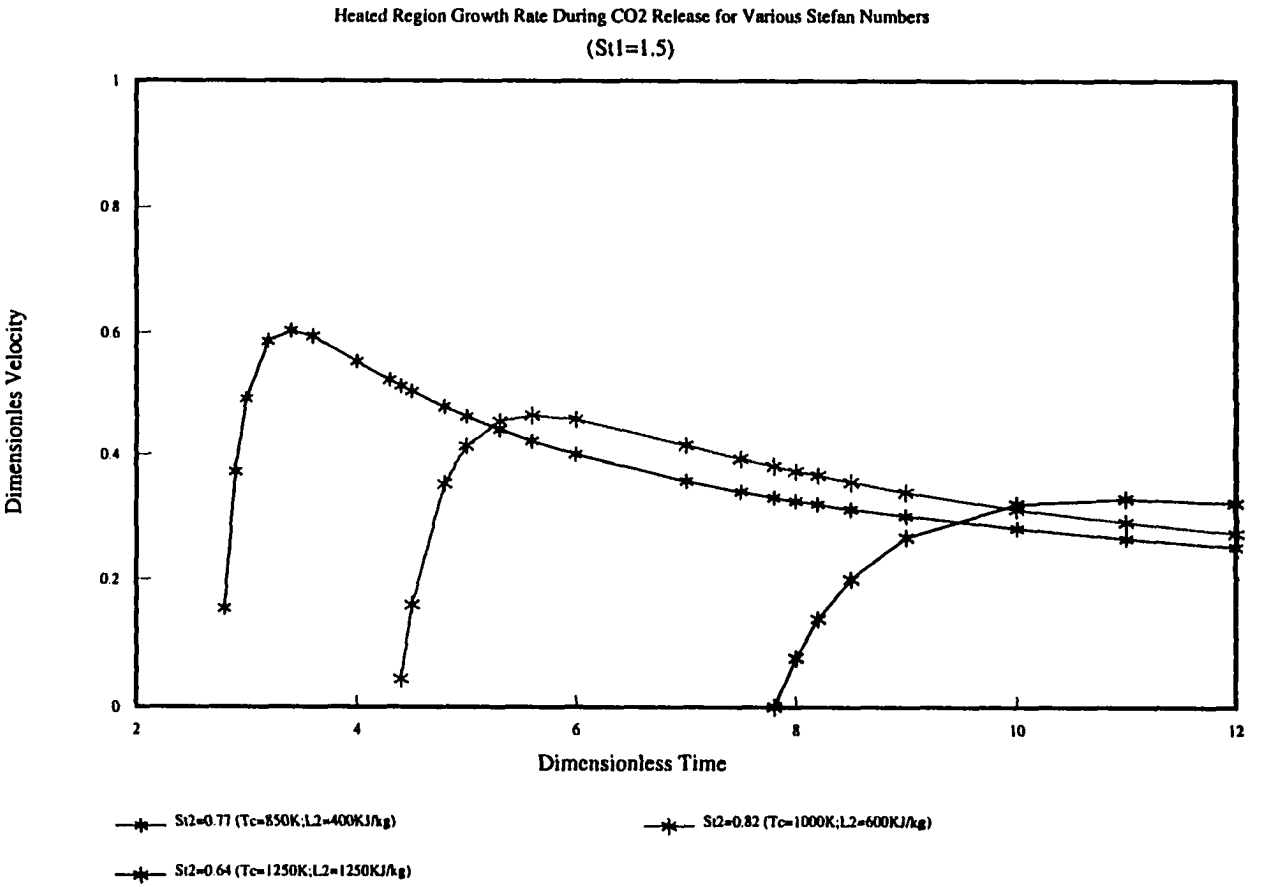

Figure 179: Heated Region Growth Rate During CO_2 Release for Various Stefan Numbers (St_1=1.5).

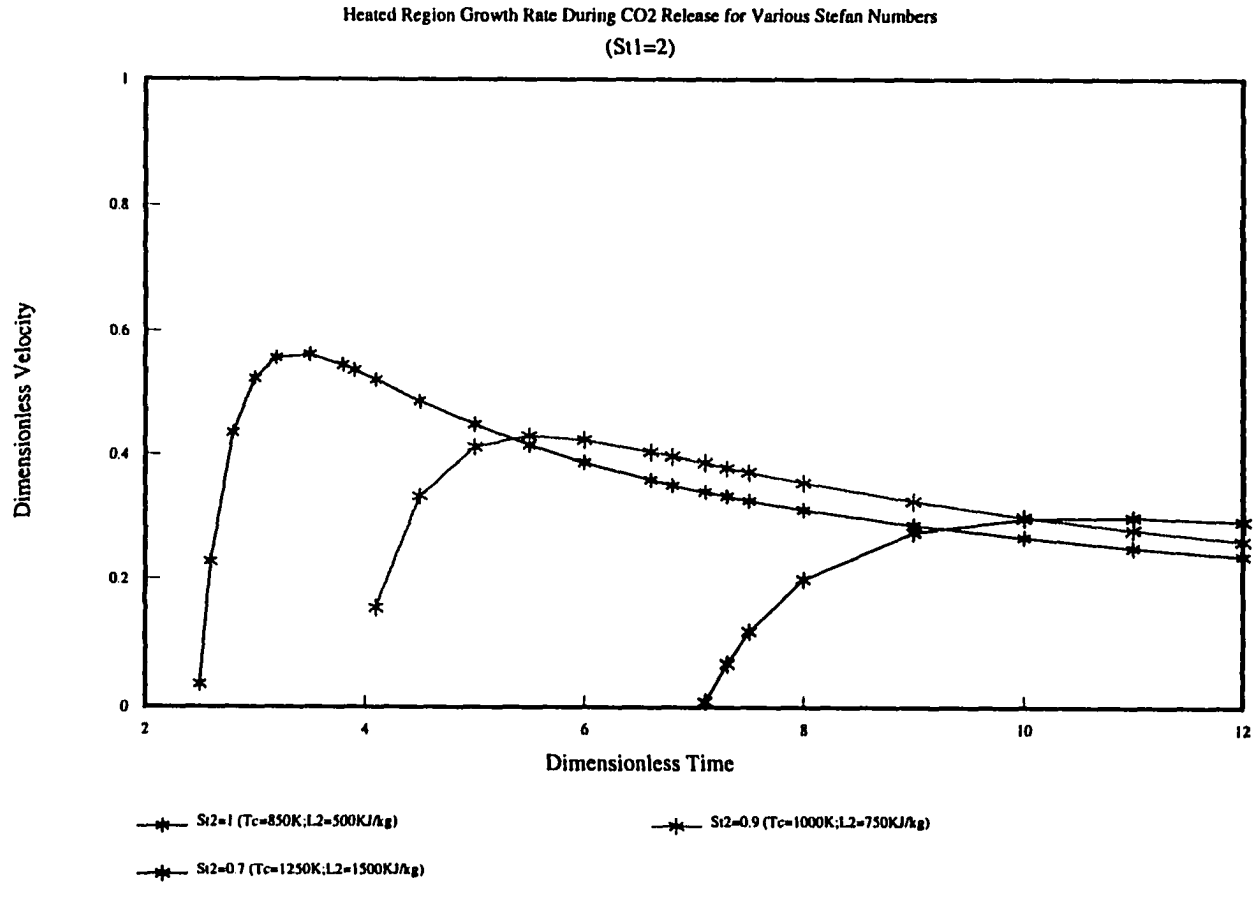

Figure 180: Heated Region Growth Rate During CO_2 Release for Various Stefan Numbers (St_1=2).

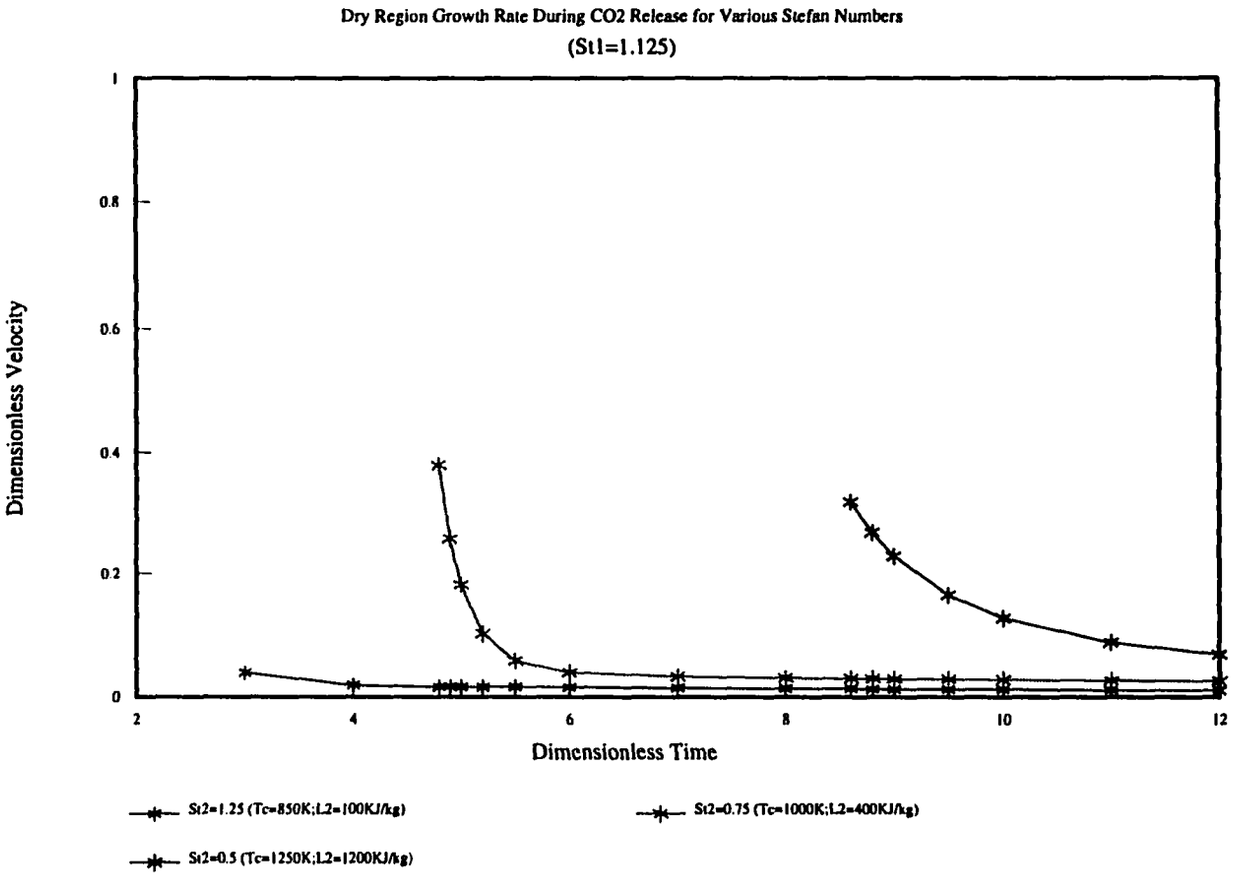

Figure 181: Dry Region Growth Rate During CO_2 Release for Various Stefan Numbers (St_1=1.125).

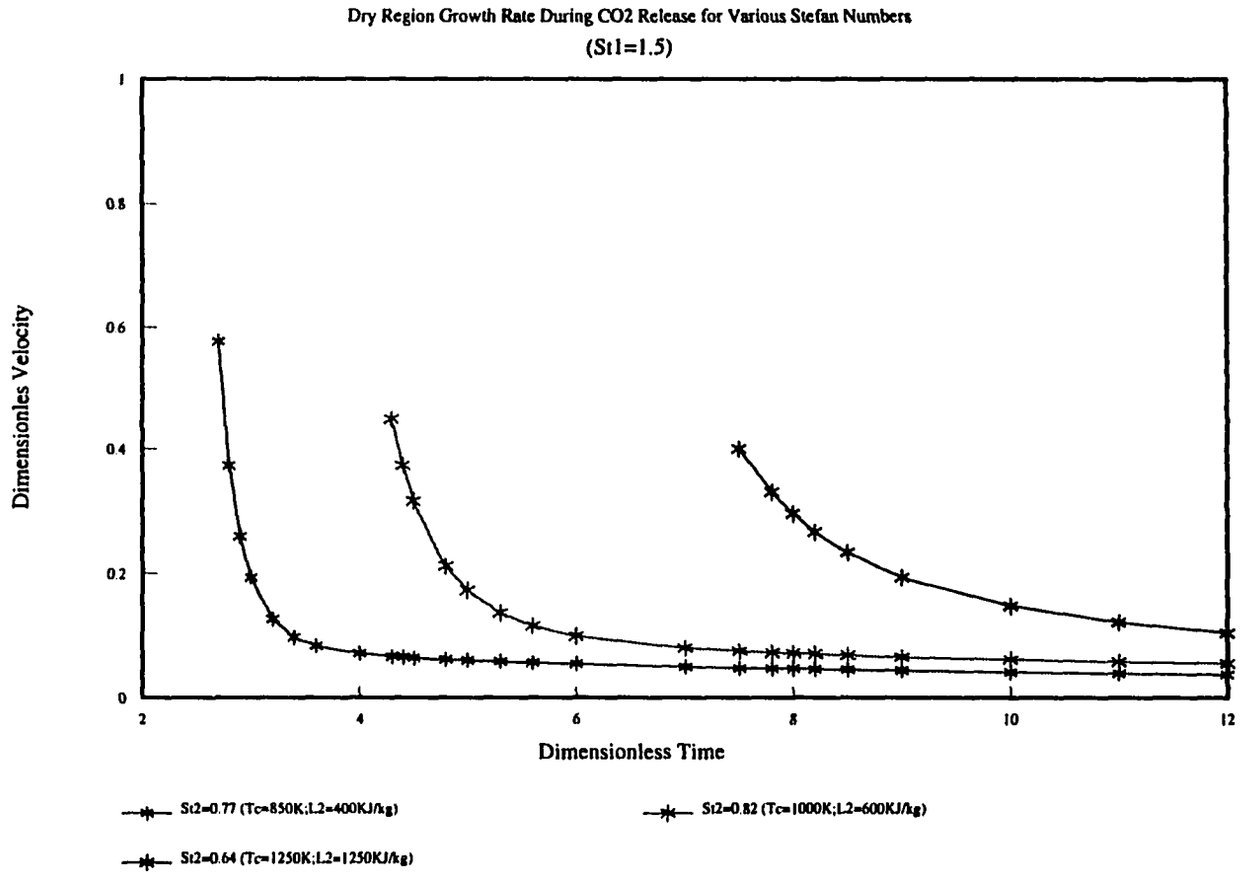

Figure 182: Dry Region Growth Rate During CO_2 Release for Various Stefan Numbers (St_1=1.5).

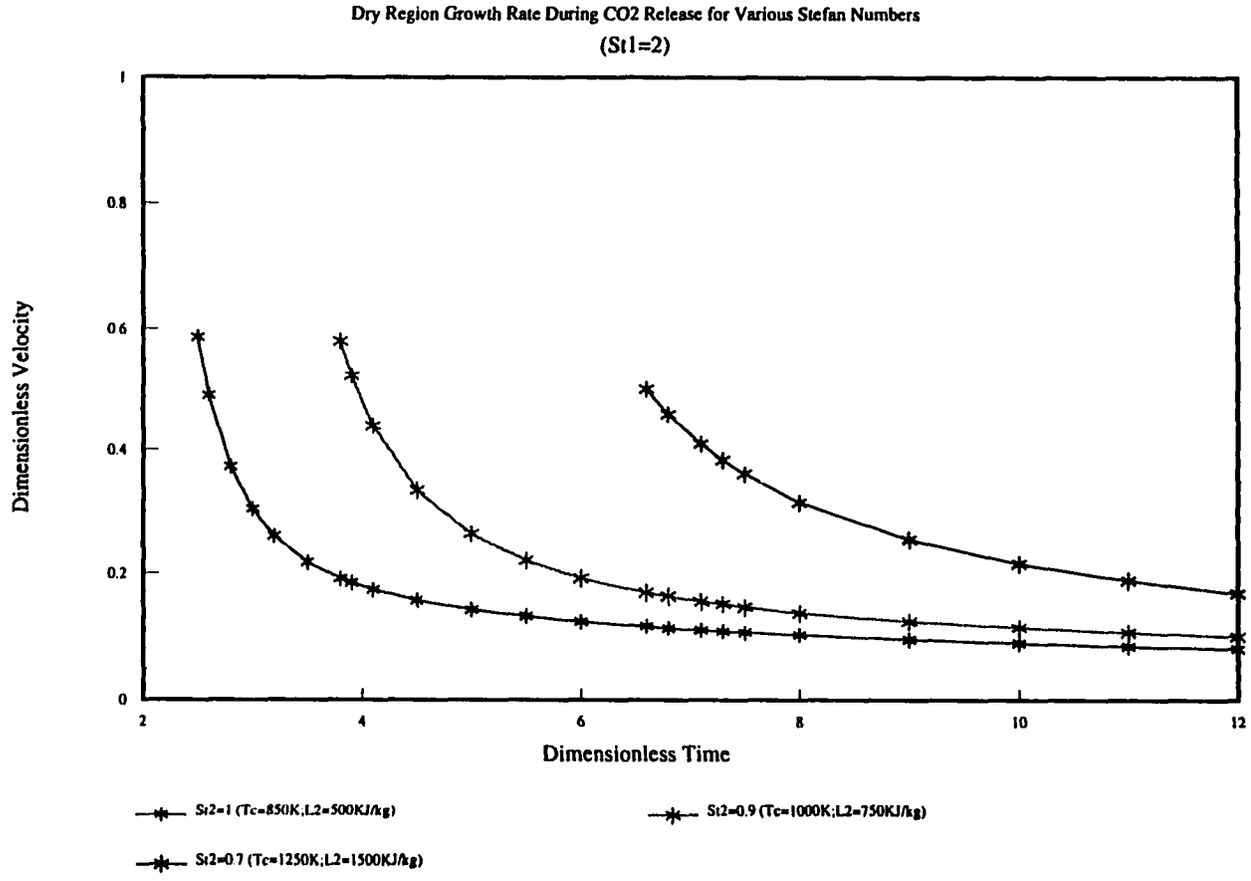

Figure 183: Dry Region Growth Rate During CO_2 Release for Various Stefan Numbers (St_1=2).

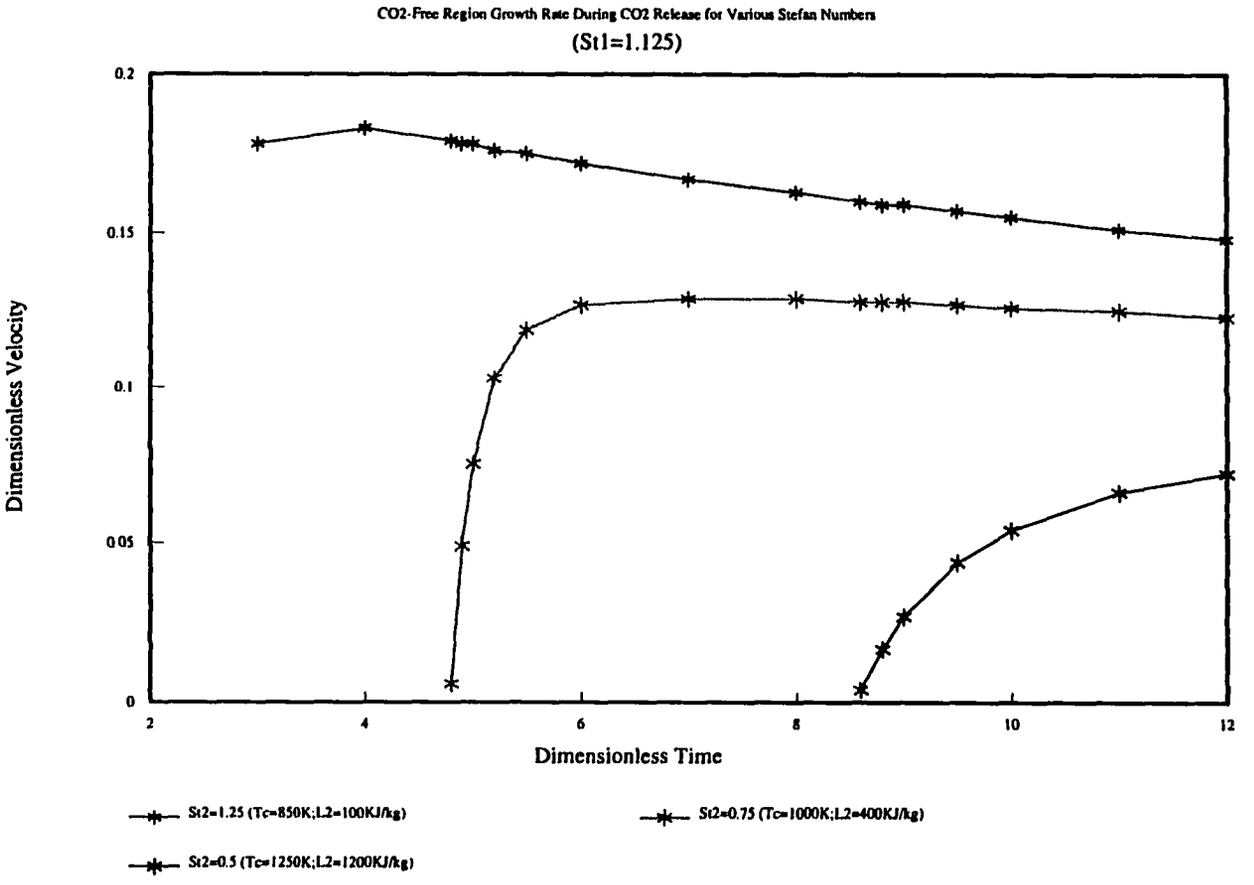

Figure 184: CO_2-Free Region Growth Rate During CO_2 Release for Various Stefan Numbers (St_1=1.125).

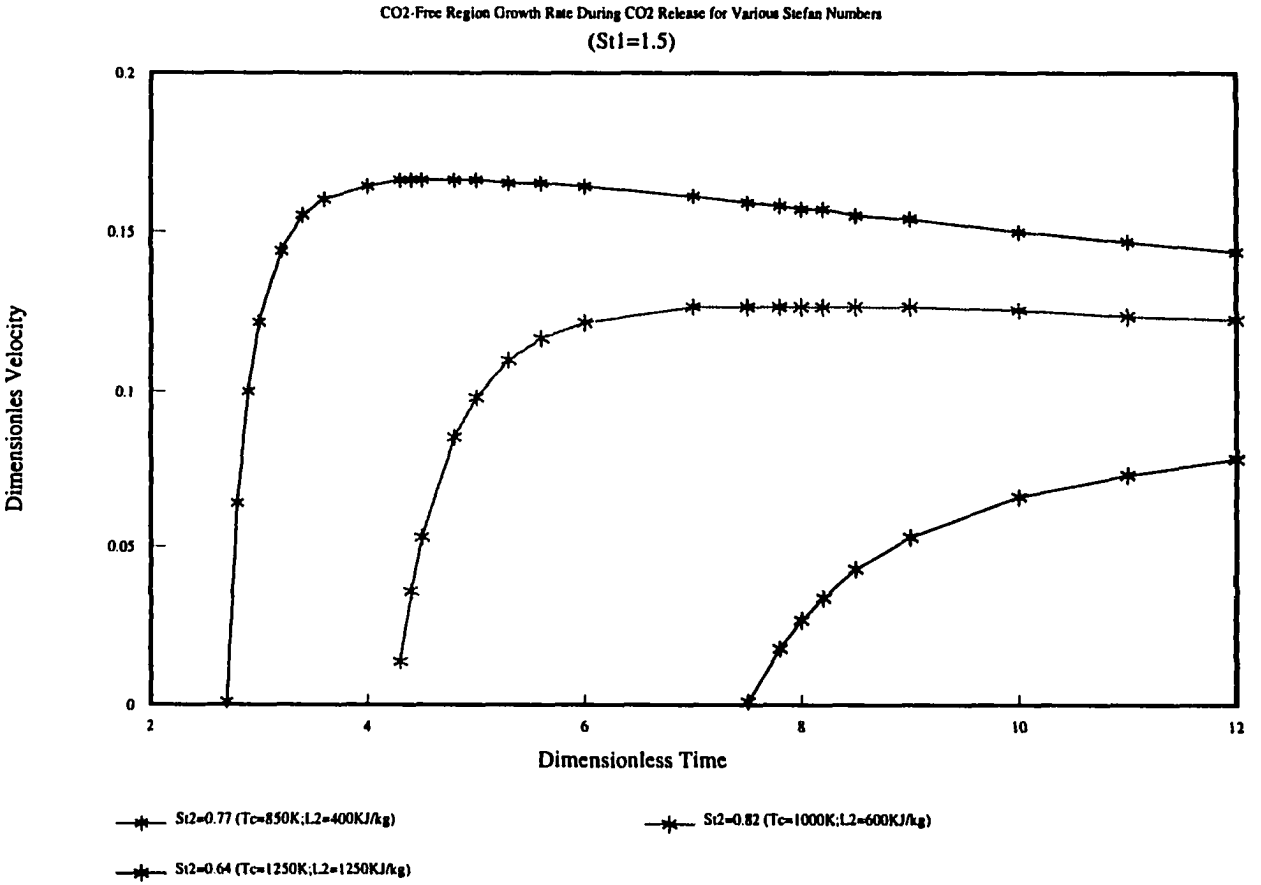

Figure 185: CO_2-Free Region Growth Rate During CO_2 Release for Various Stefan Numbers (St_1=1.5).

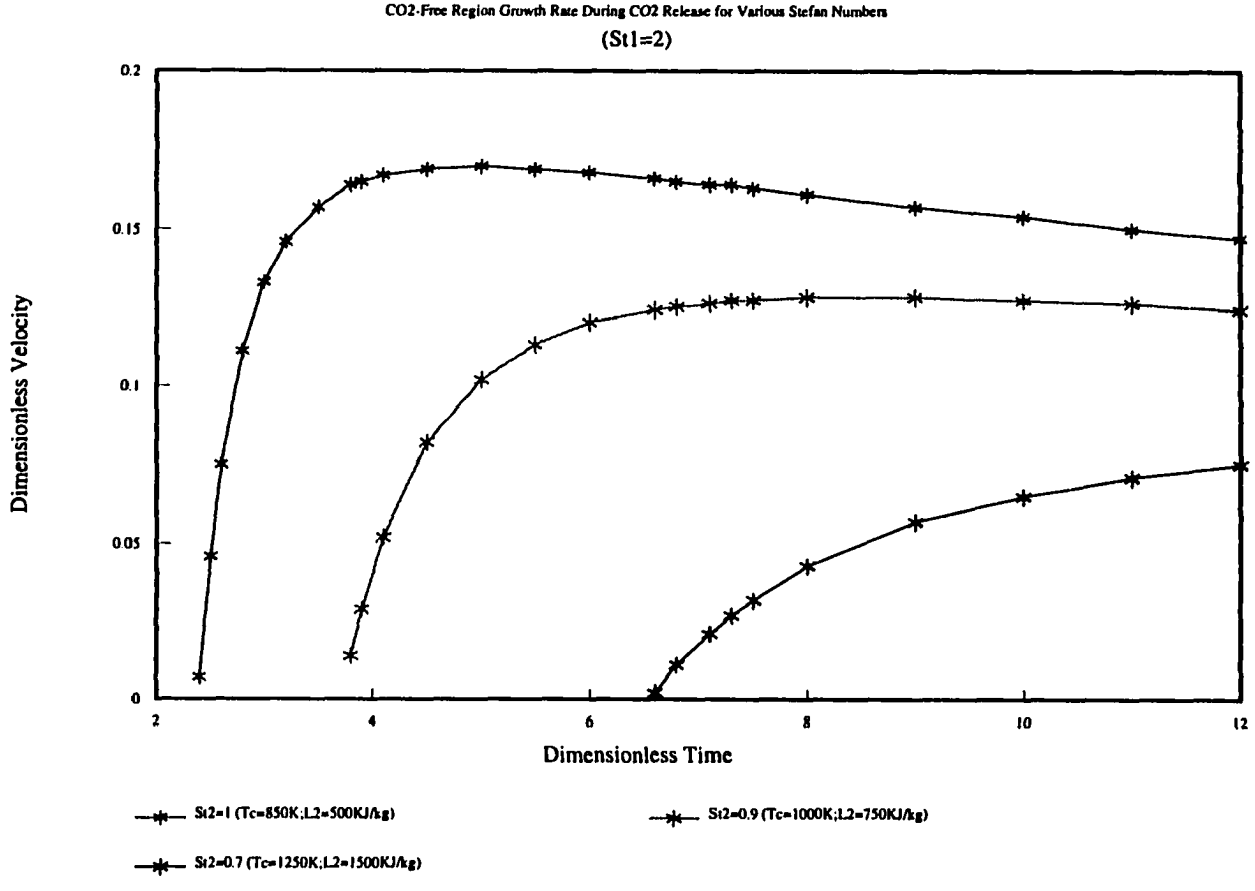

Figure 186: CO_2-Free Region Growth Rate During CO_2 Release for Various Stefan Numbers (St_1=2).

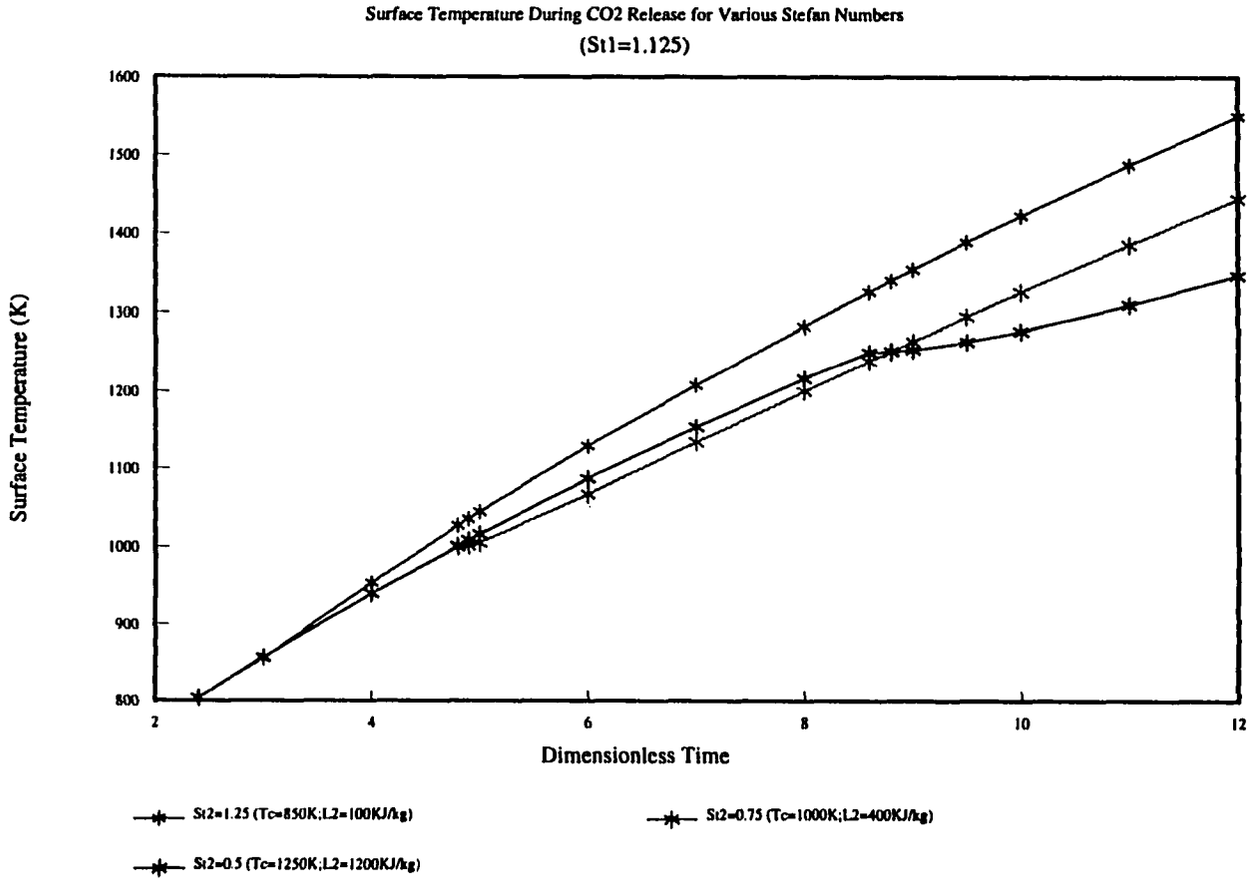

Figure 187: Surface Temperature During CO_2 Release for Various Stefan Numbers (St_1=1.125).

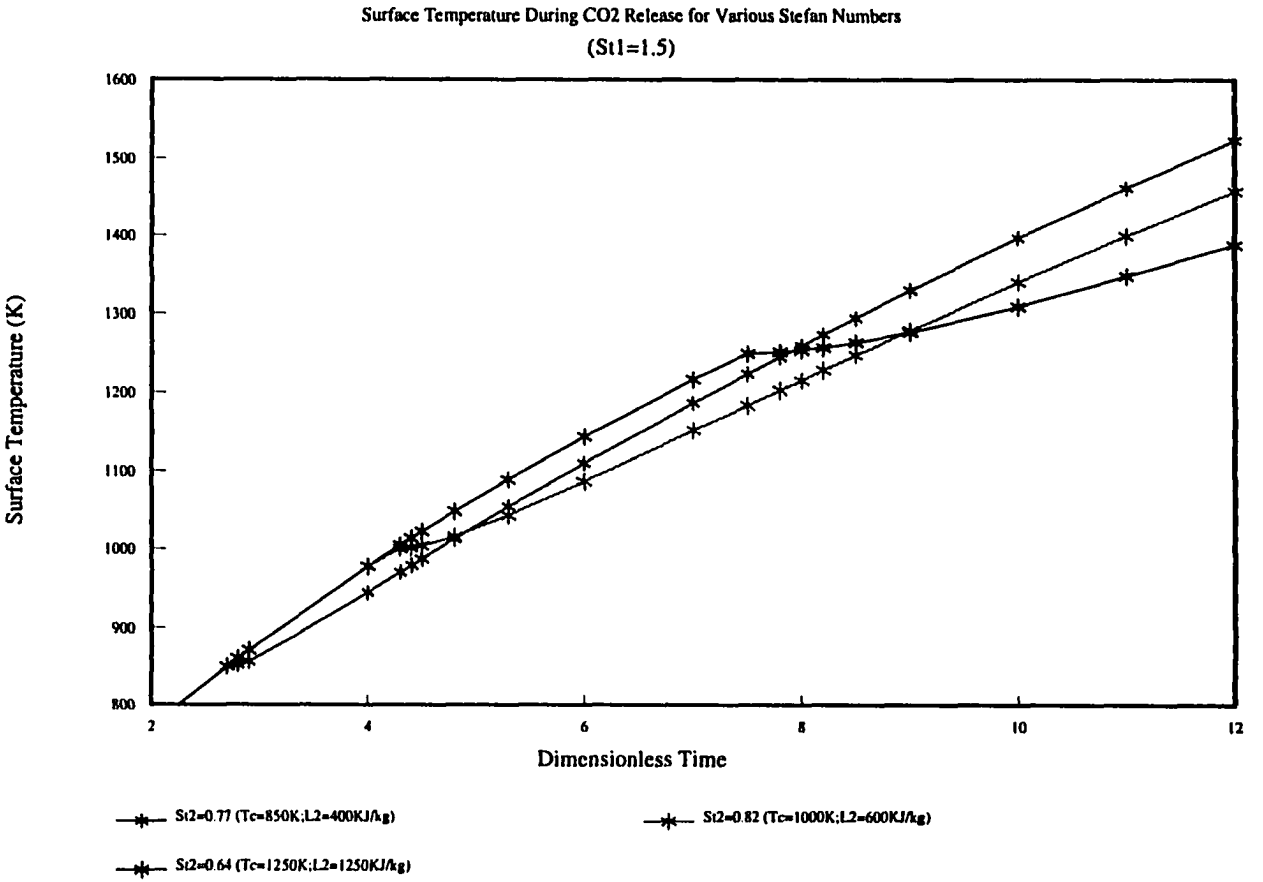

Figure 188: Surface Temperature During CO_2 Release for Various Stefan Numbers (St_1=1.5).

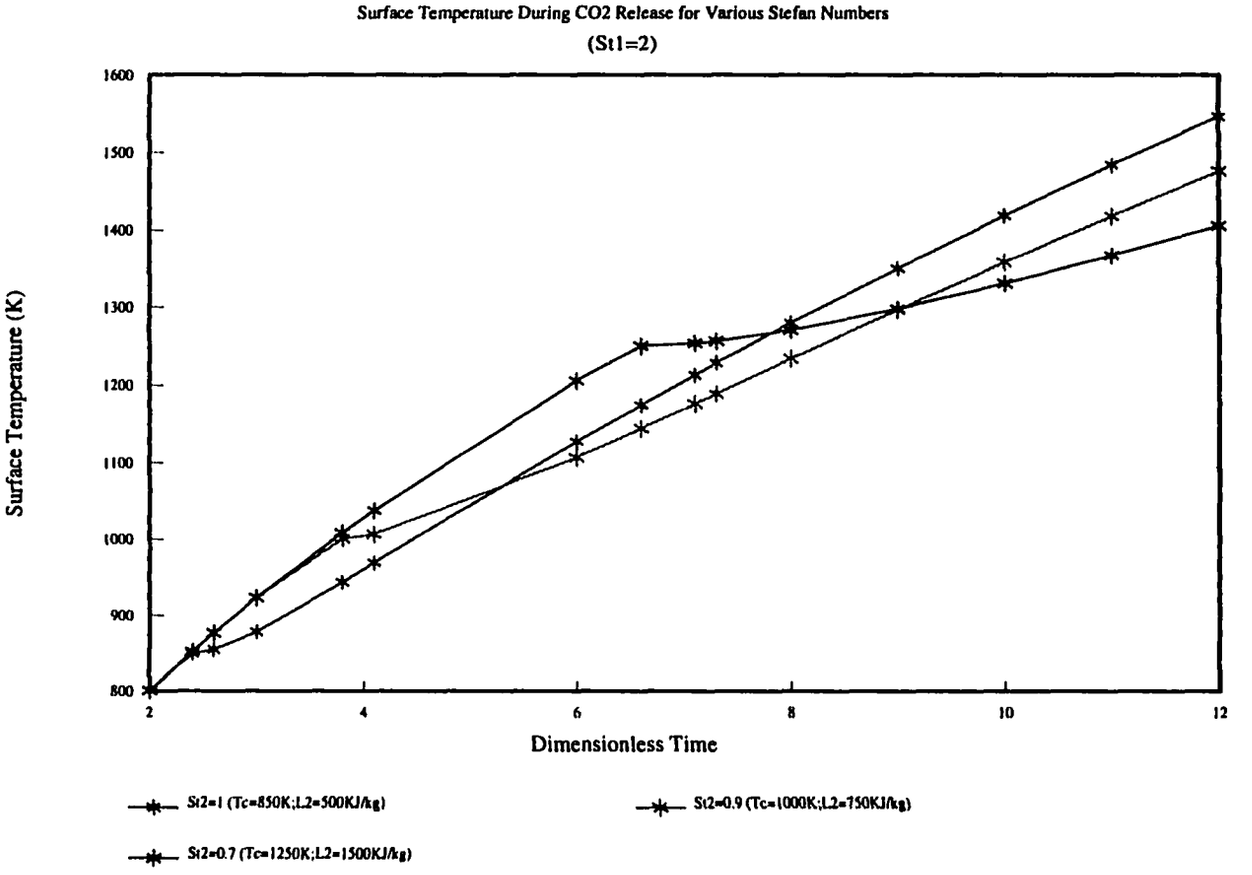

Figure 189: Surface Temperature During CO_2 Release for Various Stefan Numbers (St_1=2).

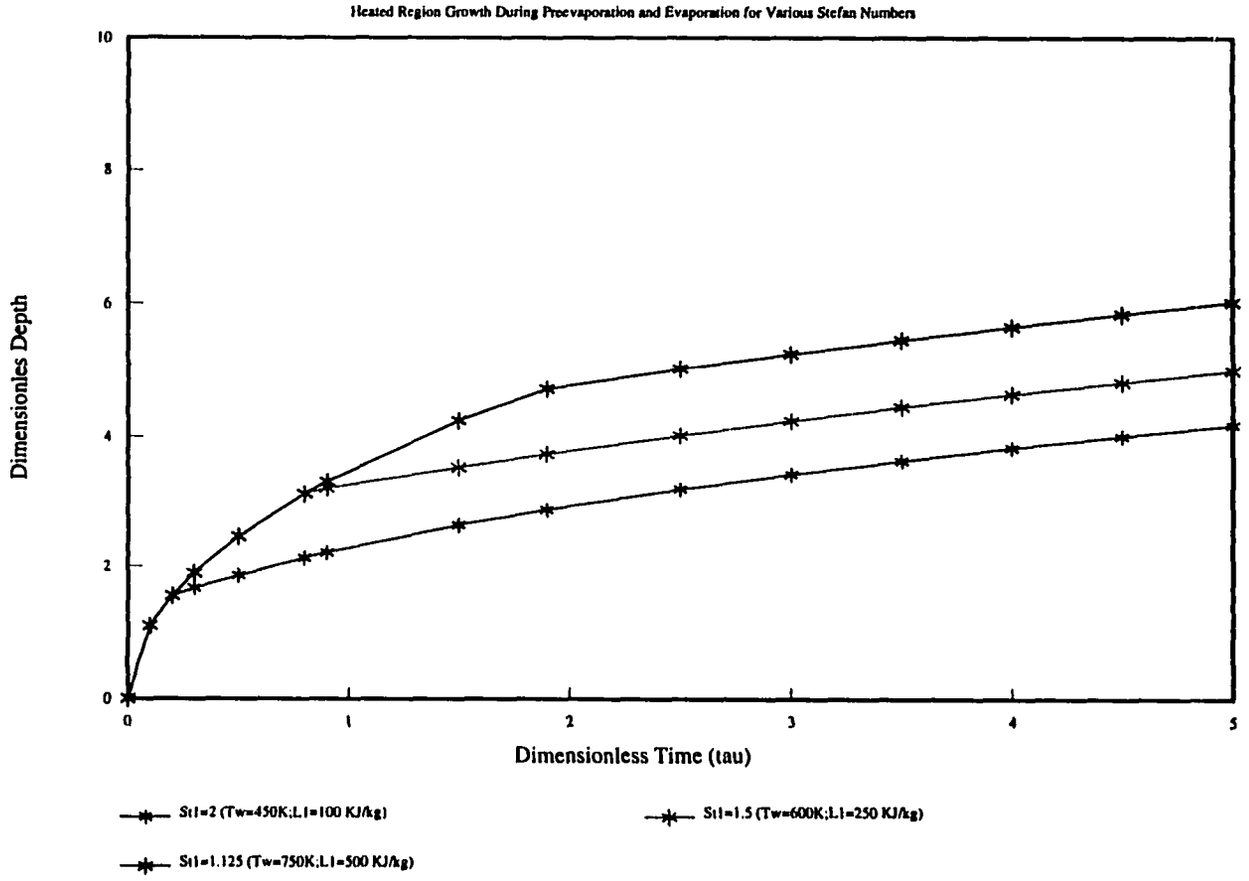

Figure 190: Heated Region Growth Before CO_2 Release for Various Stefan Numbers.

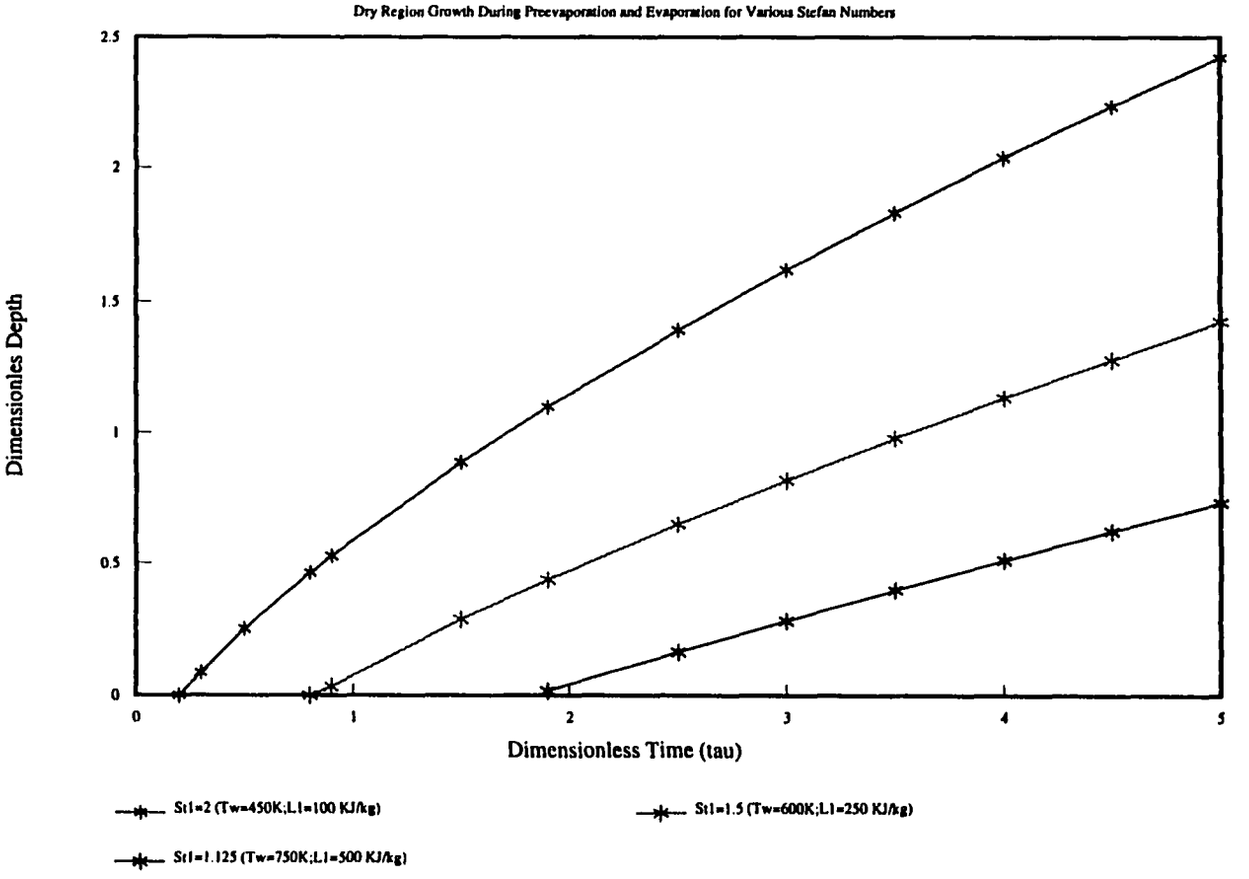

Figure 191: Dry Region Growth Before CO_2 Release for Various Stefan Numbers.

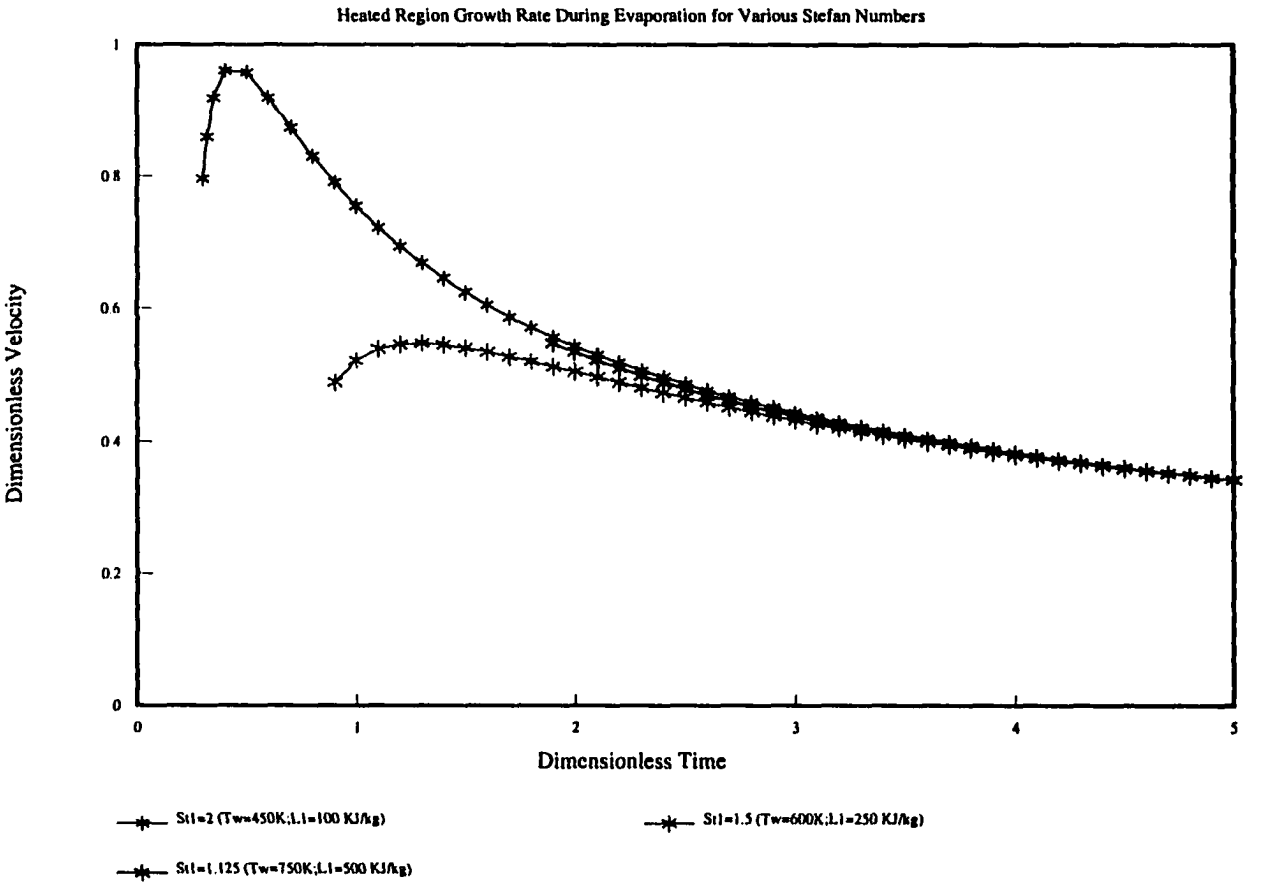

Figure 192: Heated Region Growth Rate Before CO_2 Release for Various Stefan Numbers.

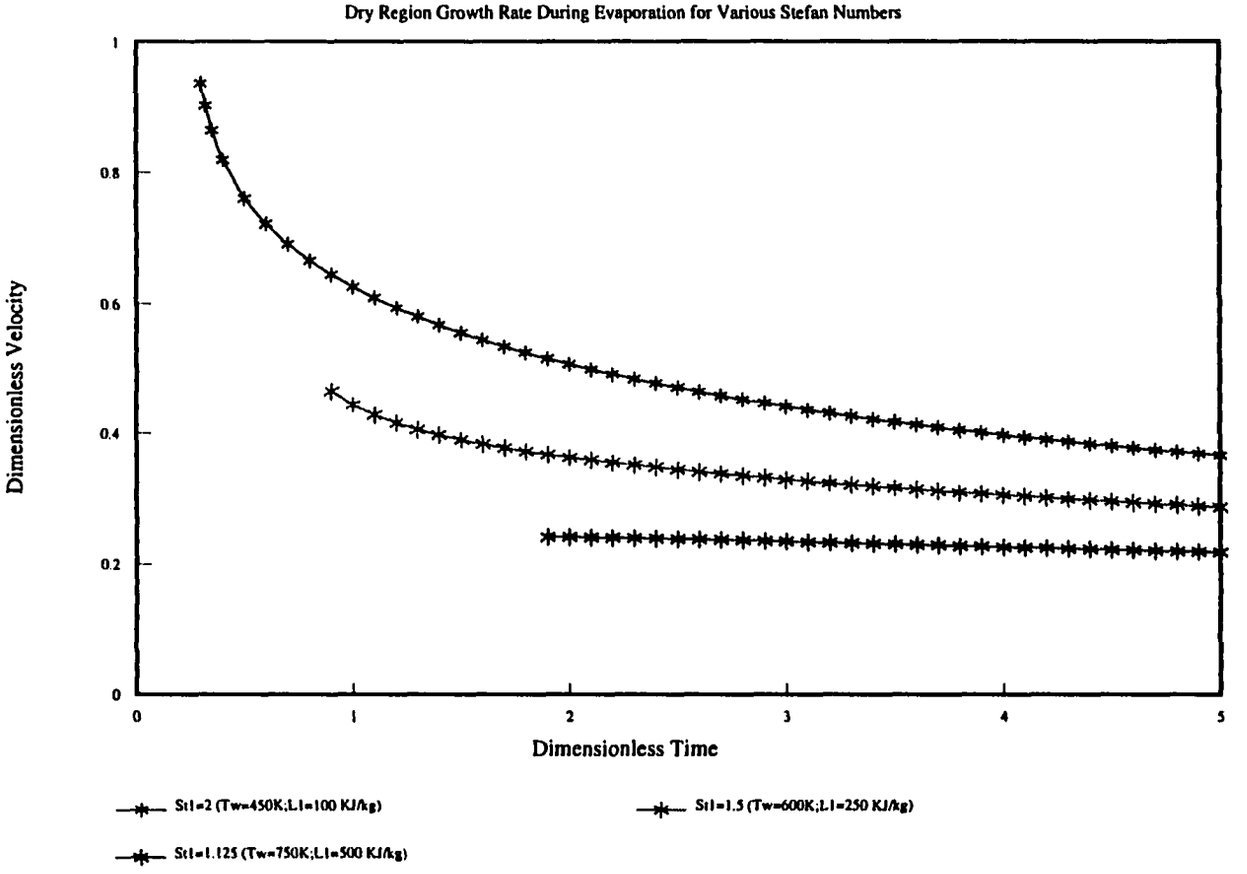

Figure 193: Dry Region Growth Rate Before CO_2 Release for Various Stefan Numbers.

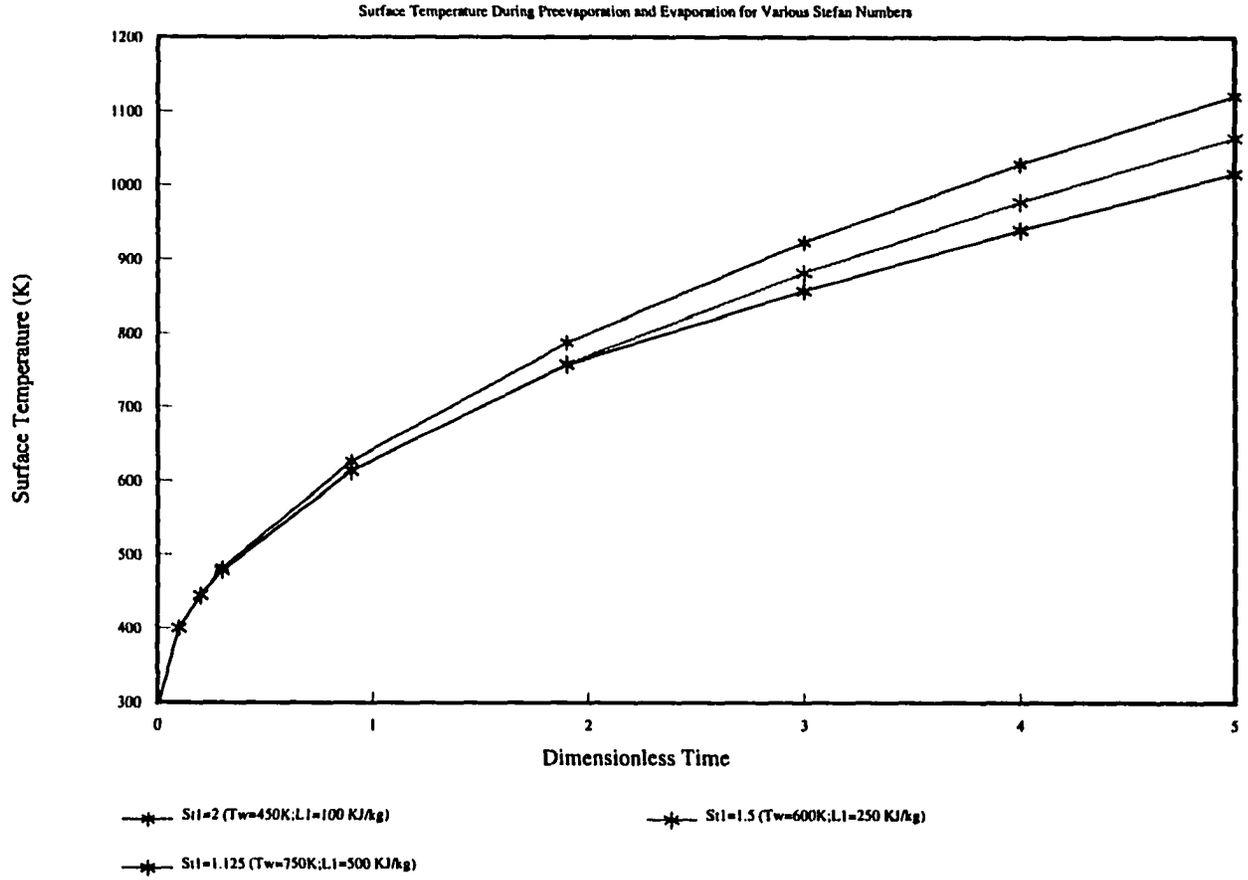

Figure 194: Surface Temperature Before CO_2 Release for Various Stefan Numbers.

REFERENCES

[1] W. A. Carbinier, "Physical Process in Reactor Meltdown Accidents", *Reactor Safety Study*, NUREG-75/014, WASH-1400, U.S. Nuclear Regulatory Commission, 1975.

[2] J. P. Hosemann, H. H. Hennies and K. Hassman, "German Results on Consequences of LWR Severe Accidents", Status of Light Water Reactor Safety Research, *Proceedings of the International Conference*, pp. 41-59, 1984.

[3] NUREG-0800, USNRC Standard Review Plan, Revision 2, Section 4.2, "Fuel System Design", July 1981.

[4] L. Baker, R. C. Liimatainen, The Technology of Nuclear Reactor Safety, vol. 2, Chapter 17, "Chemical Reactions", edited by T.J. Thompson and J.G. Beckerly, MIT Press, 1973.

[5] A. Skokan and H. Holleck, "The Significance of Chemical Reactions Between Reactor Materials Under Core Melting Conditions", *Nuclear Engineering and Design*, vol. 103, pp. 107-113, 1987.

[6] R. S. Peckover, "Outline of Post Accident Heat Removal Programs Related to Licenings", Post Accident Debris Cooling, *Proceedings of the Fifth Information Exchange Meeting*, edited by U. Müller and C. Günther, Karlsruhe, Germany, 1982.

[7] R. K. Cole, D. P. Kelly and M. A. Ellis, "CORCON MOD-1: An Improved Model for Molten Core/Concrete Interactions", SAND80-2415, Sandia National Laboratories, 1981.

[8] R. K. Cole, D. P. Kelly and M. A. Ellis, "CORCON MOD-2: A Computer Program for Analysis of Molten Core/Concrete Interactions", NUREG/CR-3920, August 1984.

[9] D. A. Powers, J. E. Brockmann and A. W. Shiver, "VANESA: A Mechanistic Model of Radionuclide Release and Aerosol Generation During Core Debris Interaction with Concrete", NUREG/CR-4308, SAND85-1370, Sandia National Laboratories, 1985.

[10] M. Reimann and W. B. Murfin, "The WECHSL Code: A Computer Program for the Interaction of Core Melt with Concrete", KfK 2890, 1981.

[11] H. G. Landau, "Heat Conduction in a Melting Solid", *Quarterly of Applied Mathematics*, vol. 8, pp. 81, 1950.

[12] R. E. Henry, "A Model for Core-Concrete Interaction", *Proceedings of the ANS/ENS International Meeting on LWR Severe Accident Evaluation*, Cambridge, Mass., August 8-September 1, 1983.

[13] M. L. Corradini, "A Transient Model for the Ablation and Decomposition of Concrete", *Nuclear Technology*, vol. 62, pp. 263, 1983.

[14] Z. F. Bažant, "Review of Literature on High Temperature Behaviour of Concrete", ORNL-TM-5145, Oak Ridge National Laboratories, 1976.

[15] L. A. Kent, "Water Release from Heated Concrete", NUREG/CR-2279, SAND81-1732, Sandia National Laboratories, 1982.

[16] J. F. Muir, "Response of Concrete Exposed to a High Heat Flux on One Surface", SAND77-1467, Sandia National Laboratories, 1977.

[17] E. R. Copus, D. R. Bradley, "Interaction of Hot Solid Core Debris with Concrete", NUREG/CR-4558, SAND85-1739, Sandia National Laboratories,

1986.

[18] L. S. Kao, M. Lee and M. S. Kazimi, "Assessment of Heat Transfer Models for Corium Concrete Interaction", *Proceedings of the Third International Topical Meeting on Reactor Thermal Hydraulics*, Newport, Rhode Island, October 15-18, 1985.

[19] H. Alsmeyer et al., "A Model Describing the Interaction of a Core Melt with Concrete", NUREG/TR-0039, 1978.

[20] H. Rininsland, "German Research Program on Severe Fuel Damage, Core Melt and Source Term", personal correspondence.

[21] T. R. Goodman, "The Heat-Balance Integral and Its Applications to Problems Involving a Change of Phase", *Journal of Heat Transfer, Transactions of ASME*, vol. 80, pp. 335, 1958.

[22] T. R. Goodman, "Application of Integral Methods to Transient Nonlinear Heat Transfer", in *Advances in Heat Transfer*, edited by T.F. Irvine and J.T. Harnett, vol. 1, pp. 51-122, Academic Press, New York, 1964.

[23] H. Schlichting, Boundary Layer Theory, 6th edition, Chapter 13, McGraw-Hill Book Co., Inc., New York, 1968.

[24] G. E. Bell, "A Refinement of the Heat Balance Integral Method Applied to a Melting Problem", *Journal of Heat and Mass Transfer*, vol. 21, pp. 1357-1362, 1978.

[25] R. H. Tien and G. E. Geiger, "The Unidimensional Solidification of a Binary Eutectic System with a Time-Dependent Surface Temperature", *Journal of Heat Transfer, Transactions of ASME*, vol. 90, pp. 27, 1968.

[26] R. H. Tien and G. E. Geiger, "A Heat Transfer Analysis of the Solidification

of a Binary Eutectic System", *Journal of Heat Transfer, Transactions of ASME*, vol. 89, pp. 230, 1967.

[27] J. C. Muehlbauer and J. E. Sunderland, "Heat Conduction with Freezing or Melting", *Applied Mechanics Review*, vol. 18, No. 2, pp. 951, 1965.

[28] S. H. Cho and J. E. Sunderland, "Heat Conduction Problems with Melting or Freezing", *Journal of Heat Transfer, Transactions of ASME*, vol. 91, pp. 421, 1969.

[29] H. S. Carlslaw and J. C. Jaeger, Conduction of Heat in Solids, 2nd Edition, Clanderon Press, Oxford, 1959.

[30] M. N. Özisik, Heat Conduction, John Wiley & Sons, Inc., New York, 1980.

[31] T. Z. Harmathy, "Thermal Properties of Concrete at Elevated Temperatures", *Journal of Materials, JMLSA*, vol. 5, pp. 47-74, No. 1, 1970.

[32] A. Petzhold and M. Röhrs, Concrete for High Temperatures, translated by A.B. Phillips and F.H. Turner, Maclaren and Sons Inc., London, 1970.

[33] T. Z. Harmathy, "Design of Concrete Masonary Walls for Fire Endurance", Behavior of Concrete Under Temperature Extremes, *American Concrete Institute Publication* SP-39, pp. 179-203, 1973.

[34] E. Crispino, "Studies on the Technology of Concretes Under Thermal Conditions", Concrete for Nuclear Reactors, *American Concrete Institute Publication* SP-34, pp. 443-480, 1972.

[35] T. Harada, J. Takeda, S. Yamane and F. Furumura, "Strength, Elasticity and Thermal Properties of Concretes Subjected to Elevated Temperatures", Concrete for Nuclear Reactors, *American Concrete Institute Publication* SP-34, pp. 377-406, 1972.

[36] L J. Mitchell, "Thermal Properties", *ASTM Special Technical Publications*, No. 169, pp. 129-135, 1959.

[37] J. A. Rhodes, "Thermal Properties", *ASTM Special Technical Publications*, No. 169B, pp. 242-261, 1978.

[38] R. Philleo , "Some Physical Properties of Concrete at High Temperatures", *Journal of American Concrete Institute*, vol. 54, pp. 857-864, 1958.

[39] D. Whiting, A. Litvin and S. E. Goodini , "Specific Heat of Selected Concretes", *Journal of American Concrete Institute*, vol. 75, pp. 299-305, 1978.

[40] A. M. Neville, Properties of Concrete, Pitnam Publishing, London, 1981.

[41] D. A. Powers, D.A. Dahlgreen, J.F. Muir and W.D. Murfin, "Explatory Study of Molten Core Material/Concrete Interactions, July 1975-March 1977", SAND77-2042, Sandia National Laboratories, 1977.

[42] M. Abramowitz, I.A. Stegun, Handbook of Mathematical Functions, Dover Publications, Inc., New York, 1972.

[43] E. P. HuangFu, B. T. Chung, "Transient Heat Transfer in Alloys Solodification Subject to a Prescribed Surface Heat Flux", *Numerical Methods in Heat Transfer, Proceedings to the Winter Annual Meeting of the ASME*, HTD-vol. 88, edited by A. F. Emery, Boston, Mass., December 13-18, 1987.

[44] E. E. Lewis, Nuclear Power Reactor Safety, John Wiley & Sons Inc., New York, 1977.

[45] S. D. Conte, C. deBoor, Elementary Numerical Analysis, McGraw-Hill Book Co., New York, 1980.

[46] D. R. Bradley, D. R. Gardner, J. E. Brockman, R. O. Griffith, "CORCON MOD-3: An Integrated Computer Model for Analysis of Molten Core/Con-

crete Interactions", NUREG/CR-5843, 1993.

[47] A. N. Kilic, "A Transient Model for Decomposition and Ablation of Concrete During Molten Core/Concrete Interactions", M. S. Thesis, University of Arizona, Department of Nuclear and Energy Engineering, Tucson, 1991.

[48] D. A. Powers, F. E. Arellano, "Large Scale Transient Tests of the Interaction of Molten Steel with Concrete", NUREG/CR-2282, SAND81-1753, Sandia National Laboratories, January 1982.

[49] A. N. Kilic, "A Transient Analysis of Decomposition and Erosion of Concrete Exposed to a Surface Heat Flux", *Nuclear Technology*, vol. 108, pp. 413, December 1994.

[50] N. Rasmussen, "Reactor Safety Study: An Assessment of Accident Risks in U. S. Commercial Nuclear Power Plants", WASH-1700, NUREG/CR-75/014, U. S. Nuclear Regulatory Commission, 1975.

[51] J. Crank, Free and Moving Boundary Problems, Clarendon Press, Oxford, 1984.

[52] R. Viskanta, "Phase Change Heat Transfer", in Solar Heat Storage: Latent Heat Materials, Chapter 5, edited by G. A. Lane, CRC Press, Boca Raton, FL, 1985.

[53] J. Crank, Mathematics of Diffusion, Oxford University Press, 1975.

[54] Deutche Risikostudie, Band 6, Gesellschaft für Reactorsicherheit (GRS), 1980.

[55] J. V. Beck, "Sensitivity Analysis for USINT-A Program for Calculating Heat and Mass Transfer in Concrete Subjected to High Heat Fluxes", NUREG/CR-2180, October 1981.

[56] A. L'Homme, J. Duco, D. Manesse, J. M. Evrard, "Training Session on Severe PWR Accidents", SASC Technical Report 86/513, French Atomic Energy Commission, Institute for Nuclear Protection and Safety, Safety Analysis Department, Site, Accidents and Containment Analysis Service, April 1986.

[57] A. Suo-Anttilla, "Sodium Concrete Ablation Model", NUREG/CR-2029, October 1981.

[58] K. D. Marx, "A Model for the Transport and Chemical Reaction of Molten Debris in Direct Containment Heating Experiments", NUREG/CR-5120, SAND88-8213, May 1988.

[59] A. J. Suo-Anttilla, "SLAM-A Sodium-Limestone Concrete Ablation Model", NUREG/CR-3379, SAND83-7114, December 1983.

[60] H. Alsmeyer, M. Reimann, J. P. Hosemann, "Preliminary Results of the KfK Molten Core/Concrete Experimental Beta Facility", Kernforschungszentrum Karlsruhe, FDR.

[61] L. Kao, M. S. Kazimi, "The Impact of Heat Transfer Models on Core/Concrete Interaction", *Nuclear Technology*, vol. 78, pp. 170, August 1987.

[62] M. Reimann, "Verification of the WECHSL Code on Melt-Concrete Interaction and Application to the Core Melt Accident", *Nuclear Engineering and Design*, vol. 103, pp. 127-137, 1987.

[63] D. A. Powers, D. A. Dahlgren, J. F. Muir, W. D. Murfin, "Exploratory Study of Molten Core Material/Concrete Interactions July 1975-March 1977", SAND77-2042. Sandia National Laboratories, Albequerque, 1977.

[64] G. W. Evans II, E. Isaacson, J. K. L. MacDonald, "Stefan-Like Problems",

vol.8, No. 3, 1950.

[65] L. N. Gupta, "An Approximate Solution of the Generalized Stefan's Problem in a Porous Medium", *International Journal of Heat Mass Transfer*, vol. 17, pp. 313-321, 1974.

[66] R. Viskanta, "Heat Transfer During Melting and Solidification of Metals", *Journal of Heat Transfer*, vol. 110, pp. 1205, November 1988.

[67] C. K. Hsieh, C. Y. Choi, "Solution of One- and Two-Phase Melting and Solidification Problems Imposed with Constant or Time-Variant Temperature and flux Boundary Conditions", *Transactions of the ASME*, vol. 114, pp. 524, May 1992.

[68] F. A. Mohamed, "The Energy-Integral Method: Application to One-Phase Hyperbolic Stefan Problems", *International Journal of Heat Mass Transfer*, vol. 33, pp. 409-416, 1990.

[69] H. T. Chen, J. Y. Lin, "Hybrid Laplace Transform Technique for Stefan Problems with Radiation-Convection Boundary Condition", *International Journal of Heat Mass Transfer*, vol. 35, pp. 3345-3351, 1992.

[70] V. R. Voller, "Development and Application of a Heat Balance Integral Method for Analysis of Metallurgical Solidification", *Applied Mathematical Modelling*, vol. 13, pp. 3, January 1989.

[71] G. C. J. Bart, C. J. Hoogendoorn, "A Model for the Extracted Heat and the Phase Front Position in Solidification with Boundary Condition of the Third Kind", *International Journal of Heat Mass Transfer*, vol. 35, pp. 375-382, 1992.

[72] T. F. Zien, "Approximate Solutions of Transient Heat Conduction in a Finite

Slab", *AIAA Journal*, vol. 16, pp. 229.

[73] B. T. F. Chung, J. S. Hsiao, "Heat Transfer with Ablation in a Finite Slab Subjected to Time-Variant Heat Fluxes", *AIAA Journal*, vol. 23, No. 1, pp. 145, January 1985.

[74] T. F. Zien, "Integral Solution of Ablation Problems with Time-Dependent Heat Flux", *AIAA Journal*, vol. 16, No. 12, pp. 1287, December 1978.

[75] D. A. Powers, E. R. Copus, D. R. Bradley, "Results of Recent Investigations at SANDIA National Laboratories on Core Debris Interactions with Concrete", *Nuclear Technology*, vol. 101, pp. 255, March 1993.

[76] W. H. Amarasooriya, H. Yan, U. Ratnam, T. G. Theofanous, "The Probability of Linear Failure in a MARK-1 Containment, Part III: Corium/Concrete Interactions and Linear Attack Phenomena", *Nuclear Technology*, vol. 101, pp.355, March 1993.

[77] W. W. Tarbell, D. R. Bradley, R. E. Blose, J. W. Ross, D. W. Gilbert, "Sustained Concrete Attack by Low-Temperature, Fragmented Core Debris", NUREG/CR-3024, SAND82-2476, Sandia National Laboratories, July 1987.

[78] M. F. Roche, L. Leibowitz, J. K. Fink, L. Baker, Jr, "Solidus and Liquidus Temperatures of Core-Concrete Mixtures", NUREG/CR-6032, ANL-93/9, Argonne National Laboratory, June 1993.

[79] D. A. Powers, F. E. Arellano, "Direct Observation of Melt Behavior During High Temperature Melt/Concrete Interactions", NUREG/CR-2283, SAND81-1754, Sandia National Laboratories, January 1982.

[80] J. E. Gronager, A. J. Suo-Anttila, D. R. Bradley, J. E. Brockmann, "TURC1: Large Scale Metallic Melt-Concrete Interaction Experiments and Analysis",

NUREG/CR-4420, SAND85-0707, Sandia National Laboratories, January 1986.

[81] H. J. Sutherland, S. Hagen, "Acoustically Measured Penetration Profiles for a Molten Metallic Pool Into River-Stone Concrete", NUREG/CR-2634, SAND82-0676, Sandia National Laboratories, November 1982.

[82] E. R. Copus, R. E. Blose, J. E. Brockmann, R. D. Gomez, D. A. Lucero, "Core-Concrete Interactions Using Molten Steel with Zirconium on a Basaltic Basemat: The SURC-4 Experiment", NUREG/CR-4994, SAND87-2008, Sandia National Laboratories, April 1989.

[83] R. E. Blose, J. E. Gronager, A. J. Suo-Anttila, J. E. Brockmann, "SWISS: Sustained Heated Metallic Melt/Concrete Interactions with Overlying Water Pools", NUREG/CR-4727, SAND85-1546, Sandia National Laboratories, July 1987.

[84] H Alsmeyer, "BETA-Experiments in Verification of the WECHSL Code: Experimental Results on the Melt-Concrete Interaction", *Nuclear Engineer Design*, February 6, 1987.